

REPORT DOCUMENTATION PAGE

AFRL-SR-BL-TR-98-

7
188
ources, gathering
this collection of
is Highway, Suite

Public reporting burden for this collection of information is estimated to average 1 hour per response, and maintaining the data needed, and completing and reviewing the collection of information. Send information, including suggestions for reducing this burden, to Washington Headquarters Services, Directorate for Information Operations and Reports, 1204, Arlington, VA 22202-4302, and to the Office of Management and Budget, Paperwork Reduction Project (0704-0188).

0801

1. AGENCY USE ONLY (Leave Blank)		2. REPORT DATE December, 1994	3. Final
4. TITLE AND SUBTITLE USAF Summer Research Program - 1994 Summer Faculty Research Program Final Reports, Volume 3A, Phillips Laboratory			5. FUNDING NUMBERS
6. AUTHORS Gary Moore			
7. PERFORMING ORGANIZATION NAME(S) AND ADDRESS(ES) Research and Development Labs, Culver City, CA			8. PERFORMING ORGANIZATION REPORT NUMBER
9. SPONSORING/MONITORING AGENCY NAME(S) AND ADDRESS(ES) AFOSR/NI 4040 Fairfax Dr, Suite 500 Arlington, VA 22203-1613			10. SPONSORING/MONITORING AGENCY REPORT NUMBER
11. SUPPLEMENTARY NOTES Contract Number: F49620-93-C-0063			
12a. DISTRIBUTION AVAILABILITY STATEMENT Approved for Public Release			12b. DISTRIBUTION CODE
13. ABSTRACT (Maximum 200 words) The United States Air Force Summer Faculty Research Program (USAF- SFRP) is designed to introduce university, college, and technical institute faculty members to Air Force research. This is accomplished by the faculty members being selected on a nationally advertised competitive basis during the summer intersession period to perform research at Air Force Research Laboratory Technical Directorates and Air Force Air Logistics Centers. Each participant provided a report of their research, and these reports are consolidated into this annual report. Reproduced From Best Available Copy			
14. SUBJECT TERMS AIR FORCE RESEARCH, AIR FORCE, ENGINEERING, LABORATORIES, REPORTS, SUMMER, UNIVERSITIES			15. NUMBER OF PAGES
			16. PRICE CODE
17. SECURITY CLASSIFICATION OF REPORT Unclassified	18. SECURITY CLASSIFICATION OF THIS PAGE Unclassified	19. SECURITY CLASSIFICATION OF ABSTRACT Unclassified	20. LIMITATION OF ABSTRACT UL

UNITED STATES AIR FORCE
SUMMER RESEARCH PROGRAM -- 1994
SUMMER FACULTY RESEARCH PROGRAM FINAL REPORTS

VOLUME 3A
PHILLIPS LABORATORY

RESEARCH & DEVELOPMENT LABORATORIES

5800 Uplander Way
Culver City, CA 90230-6608

Program Director, RDL
Gary Moore

Program Manager, AFOSR
Major David Hart

Program Manager, RDL
Scott Licoscas

Program Administrator, RDL
Gwendolyn Smith

Program Administrator
Johnetta Thompson

Submitted to:

AIR FORCE OFFICE OF SCIENTIFIC RESEARCH

Bolling Air Force Base

Washington, D.C.

December 1994

DTIC QUALITY INSPECTED 3

19981214 076

PREFACE

Reports in this volume are numbered consecutively beginning with number 1. Each report is paginated with the report number followed by consecutive page numbers, e.g., 1-1, 1-2, 1-3; 2-1, 2-2, 2-3.

Due to its length, Volume 3 is bound in two parts, 3A and 3B. Volume 3A contains #1-19. Volume 3B contains reports #20-39. The Table of Contents for Volume 3 is included in both parts.

This document is one of a set of 16 volumes describing the 1994 AFOSR Summer Research Program. The following volumes comprise the set:

<u>VOLUME</u>	<u>TITLE</u>
1	Program Management Report
	<i>Summer Faculty Research Program (SFRP) Reports</i>
2A & 2B	Armstrong Laboratory
3A & 3B	Phillips Laboratory
4	Rome Laboratory
5A & 5B	Wright Laboratory
6	Arnold Engineering Development Center, Frank J. Seiler Research Laboratory, and Wilford Hall Medical Center
	<i>Graduate Student Research Program (GSRP) Reports</i>
7	Armstrong Laboratory
8	Phillips Laboratory
9	Rome Laboratory
10	Wright Laboratory
11	Arnold Engineering Development Center, Frank J. Seiler Research Laboratory, and Wilford Hall Medical Center
	<i>High School Apprenticeship Program (HSAP) Reports</i>
12A & 12B	Armstrong Laboratory
13	Phillips Laboratory
14	Rome Laboratory
15A&15B	Wright Laboratory
16	Arnold Engineering Development Center

SFRP FINAL REPORT TABLE OF CONTENTS

i-xxi

1. INTRODUCTION	1
2. PARTICIPATION IN THE SUMMER RESEARCH PROGRAM	2
3. RECRUITING AND SELECTION	3
4. SITE VISITS	4
5. HBCU/MI PARTICIPATION	4
6. SRP FUNDING SOURCES	5
7. COMPENSATION FOR PARTICIPANTS	5
8. CONTENTS OF THE 1994 REPORT	6

APPENDICIES:

A. PROGRAM STATISTICAL SUMMARY	A-1
B. SRP EVALUATION RESPONSES	B-1

SRP Final Report Table of Contents

Author	University/Institution Report Title	Armstrong Laboratory Directorate	Vol-Page
Dr. James L Anderson	University of Georgia , Athens , GA Determination of the Oxidative Redox Capacity of	AL/EQC	2- 1
Dr. Hashem Ashrafiuon	Villanova University , Villanova , PA ATB Simulation of Deformable Manikin Neck Models	AL/CFBV	2- 2
DR Stephan B Bach	Univ of Texas-San Antonio , San Antonio , TX Pre-Screening of Soil Samples Using a Solids Inser	AL/OEA	2- 3
Dr. Suzanne C Baker	James Madison University , Harrisonburg , VA Rat Pup Ultrasonic Vocalizations: A Sensitive Indi	AL/OER	2- 4
DR Alexander B Bordetsky	Univ of Texas - Dallas , Richardson , TX Knowledge-Based Groupware for Geographically Distr	AL/HRGA	2- 5
DR. Michael J Burke	Tulane University , New Orleans , LA An Empirical Examination of the Effect of Second-O	AL/HRMI	2- 6
DR Yu-Che Chen	University of Tulsa , Tulsa , OK A Study of the Kinematics, Dynamics and Control AI	AL/CFBS	2- 7
DR Shashikala T Das	Wilmington College , Wilmington , OH The Benchmark Dose Approach for Health Risk Assess	AL/OET	2- 8
DR. Donald W DeYoung	University of Arizona , Tucson , AZ Noise as a Stressor: An Assessment of Physiologic	AL/OEBN	2- 9
DR Judy B Dutta	Rice University , Houston , TX Memory for Spatial Position and Temporal Occurence	AL/CFTO	2- 10
DR Paul A Edwards	Edinboro Univ of Pennsylvania , Edinboro , PA Fuel Identification by Neural Network Analysis of	AL/EQC	2- 11

SRP Final Report Table of Contents

Author	University/Institution Report Title	Armstrong Laboratory Directorate	Vol-Page
Dr. Daniel L Ewert	North Dakota State University , Grand Forks , ND Regional Arterial Compliance and Resistance Change	AL/AOCN	2- 12
Dr. Bernard S Gerstman	Florida International Universi , Miami , FL Laser Induced Bubble Formation in the Retina	AL/OEO	2- 13
DR Robert H Gilkey	Wright State University , Dayton , OH Relation Between Detection and Intelligibility in	AL/CFBA	2- 14
Dr. Kenneth A Graetz	University of Dayton , Dayton , OH Using Electronic Brainstorming Tools to Visually R	AL/HRGA	2- 15
Dr. Donald D Gray	West Virginia Unicersity , Morgantown , WV Improved Numerical Modeling of Groundwater Flow an	AL/EQC	2- 16
Dr. Pushpa L Gupta	University of Maine , Orono , ME Regression to the Mean in Half-Life Studies	AL/AOEP	2- 17
Dr. Thomas E Hancock	Grand Canyon University , Phoenix , AZ An Expanded Version of the Kulhavy/Stock Model of	AL/HR2	2- 18
DR. Alexis G Hernandez	University of Arizona , Tucson , AZ Preliminary Results of the Neuropsychiatrically En	AL/AOCN	2- 19
DR P. A Ikomi	Central State University , Wilberforce , OH A Realistic Multi-Task Assessment of Pilot Aptitud	AL/HRMI	2- 20
Dr. Arthur Koblasz	Georgia State University , Atlanta , GA Distributed Sensory Processing During Graded Hemod	AL/AOCI	2- 21
DR Manfred Koch	Florida State University , Tallahassee , FL Application of the MT3D Solute Transport Model to	AL/EQC	2- 22

SRP Final Report Table of Contents

Author	University/Institution Report Title	Armstrong Laboratory Directorate	Vol-Page
Dr. Donald H Kraft	Louisiana State University , Baton Rouge , LA An Exploratory Study of Weighted Fuzzy Keyword Eo	AL/CFHD	2- 23
Dr. Brother D Lawless	Fordham University , New York , NY Apoptosis Advanced Glycosylated End Products, Auto	AL/OER	2- 24
Dr. Tzesan Lee	Western Illinois University , Macomb , IL A Statistical Method for Testing Compliance	AL/OEM	2- 25
DR Robert G Main	California State Univ-Chico , Chico , CA A Study of Interaction in Distance Learning	AL/HRTT	2- 26
Dr. Augustus Morris	Central State University , Wilberforce , OH A Novel Design Concept for a Small, Force Reflecti	AL/CFBS	2- 27
DR Mark A Novotny	Florida State University , Tallahassee , FL Computer Calculation of Rate Constants for Biomole	AL/EQS	2- 28
Dr. Joseph H Nurre	Ohio University , Athens , OH A Review of Parameter Selection for Processing Cyl	AL/CFHD	2- 29
DR Edward L Parkinson	Univ of Tennessee Space Inst , Tullahoma , TN Improving the United States Air Force Environmenta	AL/EQS	2- 30
DR Malcom R Parks	University of Washington , Seattle , WA Communicative Challenges Facing Integrated Product	AL/AOE	2- 31
DR David R Perrott	California State Univ-Los Ange , Los Angeles , CA Aurally Directed Search: A Comparison Between Syn	AL/CFBA	2- 32
Dr. Edward H Piepmeier	University of South Carolina , Columbia , SC Dose Response Studies for Hyperbaric Oxygenation	AL/AOHP	2- 33

SRP Final Report Table of Contents

Author	University/Institution Report Title	Armstrong Laboratory Directorate	Vol-Page
DR Miguel A Quinones	Rice University , Houston , TX The Role of Experience in Training Effectiveness	AL/HRTE	2- 34
Dr. Ramaswamy Ramesh	SUNY, Buffalo , Buffalo , NY AETMS: Analysis, Design and Development	AL/HRAU	2- 35
DR Gary E Riccio	Univ of IL Urbana-Champaign , Urbana , IL REPORT NOT AVAILABLE AT PRESS TIME	AL/CFHP	2- 36
DR Kandasamy Selvavel	Clafin College , Orangeburg , SC Sequential Estimation of Parameters of Truncation	AL/AOEP	2- 37
DR David M Senseman	Univ of Texas-San Antonio , San Antonio , TX Multisite Optical Recording of Evoked Activity in	AL/CFTO	2- 38
DR Wayne L Shebilske	Texas A&M University , College Station , TX Linking Laboratory Research and Field Applications	AL/HRTI	2- 39
Dr. Larry R Sherman	University of Scranton , Scranton , PA Using The Sem-EDXA System at AL/OEA for Analysis o	AL/OEA	2- 40
Dr. Richard D Swope	Trinity University , San Antonio , TX Regional Arterial Complacance and Resistance Chang	AL/AOCI	2- 41
DR Steven D Tripp	The University of Kansas , Lawrence , KS Representing and Teaching a Discrete Machine: An	AL/HRTC	2- 42
DR Ryan D Tweney	Bowling Green State University , Bowling Green , OH Automated Detection of Individual Response Charact	AL/CFHP	2- 43
Dr. Brian S Vogt	Bob Jones University , Greenville , SC A Multiplexed Fiber-Optic Laser Fluorescence Spect	AL/EQW	2- 44

SRP Final Report Table of Contents

Author	University/Institution Report Title	Armstrong Laboratory Directorate	Vol-Page
DR Janet M Weisenberger	Ohio State University , Columbus , OH Investigation of the Role of Haptic Movement in Ta	AL/CFBA	2- 45

SRP Final Report Table of Contents

Author	University/Institution Report Title	Phillips Laboratory Directorate	Vol-Page
DR Behnaam Aazhang	Rice University , Houston , TX High Capacity Optical Communication Networks	PL/VTPT	3- 1
DR Nasser Ashgriz	SUNY-Buffalo , Buffalo , NY On The Mixing Mechanisms in a Pair of Impinging Je	PL/RKFA	3- 2
Dr. Raymond D Bellem	Embry-Riddle Aeronautical Univ , Prescott , AZ Radiation Characterization of Commerically Process	PL/VTET	3- 3
DR Gajanan S Bhat	Tennessee , Knoxville , TN Polyetherimide Fibers: Production Processing and	PL/RKFE	3- 4
DR Ronald J Bieniek	University of Missouri-Rolla , Rolla , MO Practical Semiquantal Modelling of Collisional Vib	PL/GPOS	3- 5
DR Jan S Brzosko	Stevens Institute of Tech , Hoboken , NJ Conceptual Study of the Marauder Operation in the	PL/WSP	3- 6
DR Ping Cheng	Hawaii at Manoa , Honolulu , HI Determination of the Interfacial Heat Transfer Coe	PL/VTPT	3- 7
DR Meledath Damodaran	University of Houston-Victoria , Victoria , TX Concurrent Computation of Aberration Coefficients	PL/LIMI	3- 8
Dr. Ronald R DeLyser	University of Denver , Denver , CO Analysis to Determine the Quality Factor of a Comp	PL/WSA	3- 9
DR Jean-Claude M Diels	University of New Mexico , Albuquerque , NM Unidirectional Ring Lasers and Laser Gyros with Mu	PL/LIDA	3- 10
Dr. David M Elliott	Arkansas Technology University , Russellville , AR REPORT NOT AVAILABLE AT PRESS TIME	PL/RKFE	3- 11

SRP Final Report Table of Contents

Author	University/Institution Report Title	Phillips Laboratory Directorate	Vol-Page
DR Vincent P Giannamore	Xavier University of Louisiana , New Orleans , LA An Investigation of Hydroxylammonium Dinitramide:	PL/RKA	3- 12
DR James E Harvey	University of Central Florida , Orlando , FL A New Mission for the Air Force Phillips Laborator	PL/LIM	3- 13
DR Stan Heckman	Massachusettes Inst of technol , Cambridge , MA REPORT NOT AVAILABLE AT PRESS TIME	PL/GPAA	3- 14
DR. James M Henson	University of Nevada , Reno , NV High Resolution Range Doppler Data and Imagery for	PL/WSAT	3- 15
Dr. San-Mou Jeng	University of Cincinnati , Cincinnati , OH Can Design for Cogging of Titanium Aluminide Alloy	PL/RKFA	3- 16
MR. Gerald Kaiser	University of Mass/Lowell , Lowell , MA Physical Wavelets fo Radar and Sonar	PI/GPOS	3- 17
MR Dikshitulu K Kalluri	University of Mass/Lowell , Lowell , MA Backscatter From a Plasma Plume Due to Excitation	PL/GP	3- 18
Lucia M Kimball	Worcester Polytechnic Inst. , Worcester , MA Investigation of Atmospheric Heating and Cooling B	PL/GPOS	3- 19
MR. Albert D Kowalak	University of Massachusetts/Lo , Lowell , MA Investigations of Electron Interactions with Molec	PL/GPID	3- 20
MR. Walter S Kuklinski	University of Mass/Lowell , Lowell , MA Ionspheric Tomography Using a Model Based Transfor	PL/GP	3- 21
Dr. Min-Chang Lee	Massachusetts Institute , Cambridge , MA Studies of Plasma Turbulence with Versatile Toroid	PL/GPSG	3- 22

SRP Final Report Table of Contents

Author	University/Institution Report Title	Phillips Laboratory Directorate	Vol-Pag
DR Kevin J Malloy	University of New Mexico , Albuquerque , NM REPORT NOT AVAILABLE AT PRESS TIME	PL/VTRP	3- 21
Dr. Charles J Noel	Ohio State University , Columbus , OH Preparation and Characterization of Blends of Orga	PL/RKA	3- 24
DR Hayrani A Oz	Ohio State University , Columbus , OH A Hybrid Algebraic Equation of Motion-Neural Estim	PL/VTSS	3- 25
DR Sudhakar Prasad	University of New Mexico , Albuquerque , NM Focusing Light into a Multiple-Core Fiber: Theory	PL/LIMI	3- 26
DR Mark R Purtill	Texas A&M Univ-Kingsville , Kingsville , TX Static and Dynamic Graph Embedding for Parallel Pr	PL/WSP	3- 27
DR Krishnaswamy Ravi-Chandar	University of Houston , Houston , TX On the Constitutive Behavior of Solid Propellants	PL/RKAP	3- 28
Dr. Wolfgang G Rudolph	University of New Mexico , Albuquerque , NM Relaxation Processes In Gain Switched Iodine Laser	PL/LIDB	3- 29
DR Gary S Sales	Univof Massachusetes-Lowell , Lowell , MA Characterization of Polar Patches: Comparison of	PL/GPIA	3- 30
DR I-Yeu Shen	University of Washington , Seattle , WA A Study of Active Constrained Layer Damping Treatm	PL/VTSS	3- 31
DR Melani I Shoemaker	Seattle Pacific University , Seattle , WA Frequency Domain Analysis of Short Exposure, Photo	PL/LIMI	3- 32
DR Yuri B Shtessel	University of Alabama-Huntsvil , Huntsville , AL Topaz II Reactor Control Law Improvement	PL/VTPC	3- 33

SRP Final Report Table of Contents

Author	University/Institution Report Title	Phillips Laboratory Directorate	Vol-Page
Dr. Alexander P Stone	University of New Mexico , Alburquerque , NM Impedances of Coplanar Conical Plates in a Uniform	PL/WSR	3- 34
DR Charles M Swenson	Utah State University , Logan , UT Reflected Laser Communication System	PL/VTRA	3- 35
Dr. Y. C Thio	University of Miami , Coral Gables , FL A Mathematical Model of Self Compression of Compac	PL/WSP	3- 36
DR Jane M Van Doren	College of the Holy Cross , Worcester , MA Investigations of Electron Interactions with Molec	PL/GPID	3- 37
DR Daniel W Watson	Utah State University , Logan , UT A Heterogeneous Parallel Architecture for High-Spe	PL/VTEE	3- 38
Dr. Wayne J Zimmermann	Texas Woman's University , Denton , TX Determination of Space Debris Flux Based on a Fini	PL/WS	3- 39

SRP Final Report Table of Contents

Author	University/Institution Report Title	Rome Laboratory Directorate	Vol-Page
DR Valentine A Aalo	Florida Atlantic University , Boca Raton , FL A Program Plan for Transmitting High-Data-Rate ATM	RL/C3BA	4- 1
DR Moeness G Amin	Villanova University , Villanova , PA Interference Excision in Spread Spectrum Using Ti	RL/C3BB	4- 2
Richard G Barakat	Tufts University , Medford , MA REPORT NOT AVAILABLE AT PRESS TIME	RL/EROP	4- 3
DR David P Benjamin	Oklahoma State University , Stillwater , OK Designing Software by Reformulation Using Kids	RL/C3CA	4- 4
DR Frank T Berkey	Utah State University , Logan , UT The Application of Quadratic Phase Coding to OTH R	RL/OCDS	4- 5
DR Joseph Chaiken	Syracuse University , Syracuse , NY A Study of the Application of Fractuals and Kineti	RL/ERDR	4- 6
Dr. Pinyuen Chen	Syracuse University , Syracuse , NY On Testing the Equality of Covariance Matrices Use	RL/OCTS	4- 7
DR. Julian Cheung	New York Inst. of Technology , New York , NY On Classification of Multispectral Infrared Image	RL/OCTM	4- 8
DR Ajit K Choudhury	Howard University , Washington , DC Detection Performance of Over Resolved Targets wit	RL/OCTS	4- 9
Dr. Eric Donkor	University of Connecticut , Stroes , CT Experimental Measurement of Nonlinear Effects in	RL/OCPA	4- 10
DR. Frances J Harackiewicz	So. Illinois Univ-Carbondale , Carbondale , IL Circular Waveguide to Microstrip Line Transition	RL/ERA	4- 11

SRP Final Report Table of Contents

Author	University/Institution Report Title	Rome Laboratory Directorate	Vol-Page
DR Joseph W Haus	Rensselaer Polytechnic Inst , Troy , NY Simulation of Erbium-doped Fiber Lasers	RL/OCP	4- 12
DR Yolanda J Kime	SUNY College-Cortland , Cortland , NY A Macroscopic Model of Electromigration: Comparis	RL/ERDR	4- 13
DR. Phillip G Kornreich	Syracuse University , Syracuse , NY Semiconductor Cylinder Fibers for Fiber Light Ampl	RL/OCP	4- 14
DR Guifang Li	Rochester Institute of Tech , Rochester , NY Self-Pulsation and Optoelectronic Feedback-Sustain	RL/OCP	4- 15
Dr. Beth L Losiewicz	Colorado State University , Fort Collins , CO Preliminary Report on the Feasibility of Machine S	RL/IR	4- 16
DR. Mohamad T Musavi	University of Maine , Orono , ME Automatic Extraction of Drainage Network from Di	RL/IR	4- 17
DR John D Norgard	Univ of Colorado-Colorado Sprg , Colorado Springs , CO Infrared Images of Electromagnetic Fields	RL/ERPT	4- 18
DR Michael A Pittarelli	SUNY Institute of Technology , Utica , NY Anytime Inference and Decision Methods	RL/C3CA	4- 19
DR Dean Richardson	SUNY Institute of Technology , Utica , NY Ultrafast Spectroscopy of Quantum Heterostructures	RL/OCP	4- 20
DR. Daniel F Ryder, Jr.	Tufts University , Medford , MA Synthesis and Properties of B-Diketonate-Modified	RL/ERX	4- 21
DR Gregory J Salamo	University of Arkansas , Fayetteville , AR Photorefractive Development and Application of InP	RL/ERX	4- 22

SRP Final Report Table of Contents

Author	University/Institution Report Title	Rome Laboratory Directorate	Vol-Page
Dr. Scott E Spetka	SUNY, Institute of Technology , Utica , NY The TkWWW Robot: Beyond Browsing	RL/IR	4- 23
DR James C West	Oklahoma State University , Stillwater , OK Polarimetric Radar Scattering from a Vegation Can	RL/ERC	4- 24
DR Rolf T Wigand	Syracuse University , Syracuse , NY Transferring Technology Via the Internet	RL/XP	4- 25
Dr. Xi-Cheng Zhang	Rensselaer Polytechnic Institu , Troy , NY Temperature Dependence of THz Emission for <111> G	RL/ERX	4- 26

SRP Final Report Table of Contents

Author	University/Institution Report Title	Wright Laboratory Directorate	Vol-Page
DR Sunil K Agrawal	Ohio Univeristy , Athens , OH A Study of Preform Design Problem for Metal Deform	WL/MLIM	5- 1
DR Michael E Baginski	Auburn University , Auburn , AL Calculation of Heating and Temperature Distributio	WL/MNMF	5- 2
Dr. William W Bannister	Univ of Massachusetts-Lowell , Lowell , MA Anomalous Effects of Water in Fire Firefighting:	WL/FIVC	5- 3
Mr. Larry A Beardsley	Athens State College , Athens , AL RFSIG Target Model Intergrated With the Joint Mode	WL/MNSH	5- 4
DR Thomas L Beck	McMicken Coll of Arts & Sci , , OH Multigrid Method for Large Scale Electronic Struct	WL/MLPJ	5- 5
DR Victor L Berdichevsky	Wayne State University , Detroit , MI Diffusional Creep in Metals and Ceramics at High T	WL/FIB	5- 6
DR. Steven W Buckner	Colullmbus College , Columbus , GA Quantitation of Dissolved O2 in Aviation Fuels by	WL/POSF	5- 7
DR. James J Carroll	Clarkson University , Potsdam , NY Development of an Active Dynamometer System	WL/POOC-	5- 8
Dr. Ching L Chang	Cleveland State University , Cleveland , OH Least-Squares Finite Element Methods for Incompres	WL/FIMM	5- 9
Dr. David B Choate	Transylvania University , Lexington , KY A New Superposition	WL/AAWP	5- 10
DR Stephen J Clarson	University of Cincinnati , Cincinnati , OH Synthesis of Novel Second and Third Order Nonlinea	WL/MLBP	5- 11

SRP Final Report Table of Contents

Author	University/Institution Report Title	Wright Laboratory Directorate	Vol-Page
Dr. Milton L Cone	Embry-Riddel Aeronautical Univ , Prescott , AZ The Sensor Manager Puzzle	WL/AAAS- _____	5- 12
DR Robert W Courter	Louisiana State University , Baton Rouge , LA A Research Plan for Evaluating Wavegun as a Low-Lo	WL/MNAA _____	5- 13
DR Vinay Dayal	Iowa State University , Ames , IA Longitudinal Waves in Fluid Loaded Composite Fiber	WL/MLLP _____	5- 14
DR Jeffrey C Dill	Ohio University , Athens , OH Discrete Wavelet Transforms for Communication Sign	WL/AAW _____	5- 15
DR Vincent G Dominic	University of Dayton , Dayton , OH Electro-Optic Characterization of Poled-Polymer Fi	WL/MLPO _____	5- 16
DR Franklin E Eastep	University of Dayton , Dayton , OH Influence of Mode Complexity and Aeroelastic Con	WL/FIBR _____	5- 17
DR Georges M Fadel	Clemson University , Clemson , SC A Methodology for Affordability in the Design Proc	WL/MTR _____	5- 18
Dr. Joel R Fried	University of Cincinnati , Cincinnati , OH Computer Modeling of Electrolytes for Battery Appl	WL/POOS- _____	5- 19
DR Paul D Gader	University of Missouri-Columbi , Columbia , MO Scanning Image Algebra Networks for Vehicle Ident	WL/MNGA _____	5- 20
DR Philip Gatt	University of Central Florida , Orlando , FL Laser Radar Performance Modelling and Analysis wit	WL/MNGS _____	5- 21
Dr. Richard D Gould	North Carolina State Univ , Raleigh , NC Analysis of Laser Doppler Velocimetry Data	WL/POPT _____	5- 22

SRP Final Report Table of Contents

Author	University/Institution Report Title	Wright Laboratory Directorate	Vol-Page
Dr. Raghava G Gowda	University of Dayton , Dayton , OH Issues Involved in Developing an Object-oriented S	WL/AAAS-	5- 23
DR Guoxiang Gu	Louisiana State University , Baton Rouge , LA Gain Scheduled Missile Autopilot Design Using Obse	WL/MNAG	5- 24
Dr Venkata S Gudimetla	OGI , Portland , OR Thermal Modeling of Heterojunction Bipolar Transis	WL/ELMT	5- 25
Dr. Raimo J Hakkinen	Washington University , St. Louis , MO Further Development of Surface-Obstacle Instrument	WL/FIMN	5- 26
DR Russell C Hardie	Univcity of Dayton , Dayton , OH Adaptive Quadratic Classifiers for Multispectral T	WL/AARA	5- 27
DR Larry S Helmick	Cedarville College , Cedarville , OH Effect of Humidity on Friction and Wear for Fombli	WL/MLBT	5- 28
DR Alan S Hodel	Auburn University , Auburn , AL Automatic Control Issues in the Development of an	WL/MNAG	5- 29
DR Vinod K Jain	University of Dayton , Dayton , OH Can Design for Cogging of Titanium Aluminide Alloy	WL/MLLN	5- 30
DR Jonathan M Janus	Mississippi State University , Mississippi State , MS Multidimensional Algorithm Development and Analysi	WL/MNAA	5- 31
DR Iwona M Jasiuk	Michigan State University , East Lansing , MI Characterization of Interfaces in Metal Matrix Com	WL/WLL	5- 32
Dr. Jack S Jean	Wright State University , Dayton , OH Reed-Solomon Decoding on Champ Architecture	WL/AAAT-	5- 33

SRP Final Report Table of Contents

Author	University/Institution Report Title	Wright Laboratory Directorate	Vol-Page
Dr. Ismail I Jouny	Lafayette College , Easton , PA Modeling and Mitigation of Terrain Scattered Inter	WL/AARM	5- 34
DR Tribikram Kundu	University of Arizona , Tucson , AZ Lamb Wave Scanning of a Multilayed Composite Plate	WL/MLLP	5- 35
DR. Jian Li	University of Florida , Gainesville , FL High Resolution Range Signature Estimation	WL/AARA	5- 36
DR. Chun-Shin Lin	University of Missouri-Columbi , Columbia , MO Prediction of Missile Trajectory	WL/FIPA	5- 37
Dr. Paul P Lin	Cleveland State University , Cleveland , OH Three Dimensional Geometry Measurement of Tire Def	WL/FIVM	5- 38
Dr. Juin J Liou	University of Central Florida , Orlando , FL A Model to Monitor the Current Gain Long-Term Inst	WL/ELRD	5- 39
Dr. James S Marsh	University of West Florida , Pensacola , FL Numerical Reconstruction of Holograms in Advanced	WL/MNSI	5- 40
DR Rajiv Mehrotra	Univ. of Missouri-St. Louis , St. Louis , MO Integrated Information Management for ATR Research	WL/AARA	5- 41
DR Douglas J Miller	Cedarville College , Cedarville , OH A Review of Nonfilled Intrinsically Conductive Ela	WL/MLBP	5- 42
DR Nagaraj Nandhakumar	University of Virginia , Charlottesville , VA Thermophysical Affine Invariants from IR Imagery	WL/AARA	5- 43
Dr. M. G Norton	Washington State University , Pullman , WA Surface Outgrowths on Laser-Deposited YBa ₂ Cu ₃ O ₇ Th	WL/MLPO	5- 44

SRP Final Report Table of Contents

Author	University/Institution Report Title	Wright Laboratory Directorate	Vol-Page
DR. James F O'Brien	Southwest Missouri State Univ. , Springfield , MO The Importance of Lower Orbital Relaxations in Po	WL/MLBP _____	5- 45
DR Krishna M Pasala	University of Dayton , Dayton , OH Performance of Music and Monopulse Algorithms in t	WL/AARM _____	5- 46
DR Robert P Penno	University of Dayton , Dayton , OH An Assessment of the WL/AAAI-4 Antenna Wavefront S	WL/AAAI- _____	5- 47
DR Marek A Perkowski	Portland State University , Portland , OR A Survey of Literature on Function Decomposition	WL/AAAT- _____	5- 48
DR Ramachandran Radharamanan	Marquette University , Milwaukee , WI A Study on Virtual Manufacturing	WL/MTI _____	5- 49
DR Ramu V Ramaswamy	University of Florida , Gainesville , FL Annealed Proton Exchanged (APE) Waveguides in LiTa	WL/MNG _____	5- 50
DR Stanley J Reeves	Auburn University , Auburn , AL Superresolution of Passive Millimeter-Wave Imaging	WL/MNGS _____	5- 51
Dr. William K Rule	University of Alabama , Tuscaloosa , AL <RESTRICTED DISTRIBUTION - CONTACT LABORATORY>	WL/MNM _____	5- 52
DR Arindam Saha	Mississippi State University , Mississippi State , MS Evaluation of Network Routers in Real-Time Paralle	WL/AAAT- _____	5- 53
DR John J Schauer	University of Dayton , Dayton , OH Turbine Blade Film Jet Cooling with Free Stream Tu	WL/POTT _____	5- 54
DR Carla A Schwartz	University of Florida , Gainesville , FL Neural Networks Identification and Control in Meta	WL/FIGC _____	5- 55

SRP Final Report Table of Contents

Author	University/Institution Report Title	Wright Laboratory Directorate	Vol-Pag
DR. James P Seaba	University of Missouri-Columbi , Columbia , MO Multiple Jet Mixing and Atomization in Reacting an	WL/POSF	5- 50
DR Sivanand Simanapalli	University of NC-Charlotte , Charlotte , NC HRR Radar Based Target Identification	WL/AARA	5- 57
DR. Terrence W Simon	University of Minnesota , Minneapolis , MN Documentation of Boundary Layer Characteristics Fo	WL/POTT	5- 58
DR Marek Skowronski	Carnegie Melon University , Pittsburgh , PA Mechanism for Indium Segregation In In _x Ga _{1-x} As Str	WL/ELRA	5- 59
DR Joseph C Slater	Wright State Univesity , Dayton , OH QFT Control of an Advanced Tactical Fighter Aeroel	WL/FIGS	5- 60
DR John A Tague	Ohio University , Athens , OH Performance Analysis of Quadratic Classifiers for	WL/AARA	5- 61
Dr. Barney E Taylor	Miami Univ. - Hamilton , Hamilton , OH Electroluminescence Studies of the Rigid Rod Polym	WL/MLBP	5- 62
DR Krishnaprasad Thirunarayan	Wright State University , Dayton , OH VHDL-93 Paser in Prolog	WL/ELED	5- 63
DR Robert B Trelease	University of California , Los Angeles , CA Developing Qualitative Process Control Discovery S	WL/MLIM	5- 64
DR. Chi-Tay Tsai	Florida Atlantic University , Boca Raton , FL A Study of Massively Parallel Computing on Epic Hy	WL/MNM	5- 65
DR James M Whitney	University of Dayton , Dayton , OH Stress Analysis of the V-Notch (Iosipescu) Shear T	WL/MLBM	5- 66

SRP Final Report Table of Contents

Author	University/Institution Report Title	Arnold Engineering Development Center Directorate	Vol-Page
DR Ben A Abbott	Vanderbilt University , Nashville , TN The Application Challenge	Sverdrup	6- 1
DR Theodore A Bapty	Vanderbilt University , Nashville , TN Development of Large Parallel Instrumentation Syst	Sverdrup	6- 2
Dr. Csaba A Biegl	Vanderbilt University , Nashville , TN Univeral Graphic User Inteface for Turbine Engine	Sverdrup	6- 3
DR Steven H Frankel	Purdue University , West Lafayette , IN Towards The Computational Modeling of Postall Gas	Sverdrup	6- 4
Dr. Peter R Massopust	Sam Houston State University , Huntsville , TX A Wavelet-Multigrid Approach To Solving Partial Di	Calspan	6- 5
DR Randolph S Peterson	University of the South , Sewanee , TN Infrared Imaging Fourier Transform Spectrometer	Sverdrup	6- 6
DR Roy J Schulz	Univ of Tennessee Space Inst , Tullahoma , TN Design of Soot Capturing Sample Probe	Sverdrup	6- 7
DR S A Sherif	College of Eng-Univ of Florida , Gainesville , FL A Model For Local Heat Transfer & Ice Accretion In	Sverdrup	6- 8
DR. Michael Sydor	University of Minnesota-Duluth , Duluth , MN Dimensional Analysis of ARC Heaters	Calspan	6- 9
Dr. John T Tarvin	Samford University , Birmingham , AL Ultraviolet Flat-Field Response of an Intensified	CALSPAN	6- 10

SRP Final Report Table of Contents

Author	University/Institution Report Title	Frank J Seiler Research Laboratory Directorate	Vol-Page
Dr. Gene O Carlisle	West Texas State University , Canyon , TX REPORT NOT AVAILABLE AT PRESS TIME .	FJSRL/NC	6- 11
DR John R Dorgan	Colorado School of Mines , Golden , CO Fundamental Studies on the Solution and Adsorption	FJSRL/NE	6- 12
DR Mary Ann Jungbauer	Barry University , Miami , FL Non-Linear Optical Properties of a Series of Linea	FJSRL/NC	6- 13
DR. Lawrence L Murrell	Pennsylvania State University , University Park , PA Catalytic Gasification of Pitch Carbon Fibers with	FJSRL/NE	6- 14
DR David E Statman	Allegheny College , Meadville , PA Charge Transport and Second Harmonic Generation in	FJSRL/NP	6- 15

SRP Final Report Table of Contents

Author	University/Institution Report Title	Wilford Hall Medical Center Directorate	Vol-Page
DR Walter Drost-Hansen	University of Miami , Coral Gables , FL Effects of Temperature on Various Hematological Pa	WHMC/RD	6- 16

1. INTRODUCTION

The Summer Research Program (SRP), sponsored by the Air Force Office of Scientific Research (AFOSR), offers paid opportunities for university faculty, graduate students, and high school students to conduct research in U.S. Air Force research laboratories nationwide during the summer.

Introduced by AFOSR in 1978, this innovative program is based on the concept of teaming academic researchers with Air Force scientists in the same disciplines using laboratory facilities and equipment not often available at associates' institutions.

AFOSR also offers its research associates an opportunity, under the Summer Research Extension Program (SREP), to continue their AFOSR-sponsored research at their home institutions through the award of research grants. In 1994 the maximum amount of each grant was increased from \$20,000 to \$25,000, and the number of AFOSR-sponsored grants decreased from 75 to 60. A separate annual report is compiled on the SREP.

The Summer Faculty Research Program (SFRP) is open annually to approximately 150 faculty members with at least two years of teaching and/or research experience in accredited U.S. colleges, universities, or technical institutions. SFRP associates must be either U.S. citizens or permanent residents.

The Graduate Student Research Program (GSRP) is open annually to approximately 100 graduate students holding a bachelor's or a master's degree; GSRP associates must be U.S. citizens enrolled full time at an accredited institution.

The High School Apprentice Program (HSAP) annually selects about 125 high school students located within a twenty mile commuting distance of participating Air Force laboratories.

The numbers of projected summer research participants in each of the three categories are usually increased through direct sponsorship by participating laboratories.

AFOSR's SRP has well served its objectives of building critical links between Air Force research laboratories and the academic community, opening avenues of communications and forging new research relationships between Air Force and academic technical experts in areas of national interest; and strengthening the nation's efforts to sustain careers in science and engineering. The success of the SRP can be gauged from its growth from inception (see Table 1) and from the favorable responses the 1994 participants expressed in end-of-tour SRP evaluations (Appendix B).

AFOSR contracts for administration of the SRP by civilian contractors. The contract was first awarded to Research & Development Laboratories (RDL) in September 1990. After completion of the 1990 contract, RDL won the recompetition for the basic year and four 1-year options.

2. PARTICIPATION IN THE SUMMER RESEARCH PROGRAM

The SRP began with faculty associates in 1979; graduate students were added in 1982 and high school students in 1986. The following table shows the number of associates in the program each year.

Table 1: SRP Participation, by Year

YEAR	Number of Participants			TOTAL
	SFRP	GSRP	HSAP	
1979	70			70
1980	87			87
1981	87			87
1982	91	17		108
1983	101	53		154
1984	152	84		236
1985	154	92		246
1986	158	100	42	300
1987	159	101	73	333
1988	153	107	101	361
1989	168	102	103	373
1990	165	121	132	418
1991	170	142	132	444
1992	185	121	159	464
1993	187	117	136	440
1994	192	117	133	442

Beginning in 1993, due to budget cuts, some of the laboratories weren't able to afford to fund as many associates as in previous years; in one case a laboratory did not fund any additional associates. However, the table shows that, overall, the number of participating associates increased this year because two laboratories funded more associates than they had in previous years.

3. RECRUITING AND SELECTION

The SRP is conducted on a nationally advertised and competitive-selection basis. The advertising for faculty and graduate students consisted primarily of the mailing of 8,000 44-page SRP brochures to chairpersons of departments relevant to AFOSR research and to administrators of grants in accredited universities, colleges, and technical institutions. Historically Black Colleges and Universities (HBCUs) and Minority Institutions (MIs) were included. Brochures also went to all participating USAF laboratories, the previous year's participants, and numerous (over 600 annually) individual requesters.

Due to a delay in awarding the new contract, RDL was not able to place advertisements in any of the following publications in which the SRP is normally advertised: *Black Issues in Higher Education*, *Chemical & Engineering News*, *IEEE Spectrum* and *Physics Today*.

High school applicants can participate only in laboratories located no more than 20 miles from their residence. Tailored brochures on the HSAP were sent to the head counselors of 180 high schools in the vicinity of participating laboratories, with instructions for publicizing the program in their schools. High school students selected to serve at Wright Laboratory's Armament Directorate (Eglin Air Force Base, Florida) serve eleven weeks as opposed to the eight weeks normally worked by high school students at all other participating laboratories.

Each SFRP or GSRP applicant is given a first, second, and third choice of laboratory. High school students who have more than one laboratory or directorate near their homes are also given first, second, and third choices.

Laboratories make their selections and prioritize their nominees. AFOSR then determines the number to be funded at each laboratory and approves laboratories' selections.

Subsequently, laboratories use their own funds to sponsor additional candidates. Some selectees do not accept the appointment, so alternate candidates are chosen. This multi-step selection procedure results in some candidates being notified of their acceptance after scheduled deadlines. The total applicants and participants for 1994 are shown in this table.

Table 2: 1994 Applicants and Participants

PARTICIPANT CATEGORY	TOTAL APPLICANTS	SELECTEES	DECLINING SELECTEES
SFRP	600	192	30
(HBCU/MI)	(90)	(16)	(7)
GSRP	322	117	11
(HBCU/MI)	(11)	(6)	(0)
HSAP	562	133	14
TOTAL	1484	442	55

4. SITE VISITS

During June and July of 1994, representatives of both AFOSR/NI and RDL visited each participating laboratory to provide briefings, answer questions, and resolve problems for both laboratory personnel and participants. The objective was to ensure that the SRP would be as constructive as possible for all participants. Both SRP participants and RDL representatives found these visits beneficial. At many of the laboratories, this was the only opportunity for all participants to meet at one time to share their experiences and exchange ideas.

5. HISTORICALLY BLACK COLLEGES AND UNIVERSITIES AND MINORITY INSTITUTIONS (HBCU/MIs)

In previous years, an RDL program representative visited from seven to ten different HBCU/MIs to promote interest in the SRP among the faculty and graduate students. Due to the late contract award date (January 1994) no time was available to visit HBCU/MIs this past year.

In addition to RDL's special recruiting efforts, AFOSR attempts each year to obtain additional funding or use leftover funding from cancellations the past year to fund HBCU/MI associates. This year, seven HBCU/MI SFRPs declined after they were selected. The following table records HBCU/MI participation in this program.

Table 3: SRP HBCU/MI Participation, by Year

YEAR	SFRP		GSRP	
	Applicants	Participants	Applicants	Participants
1985	76	23	15	11
1986	70	18	20	10
1987	82	32	32	10
1988	53	17	23	14
1989	39	15	13	4
1990	43	14	17	3
1991	42	13	8	5
1992	70	13	9	5
1993	60	13	6	2
1994	90	16	11	6

6. SRP FUNDING SOURCES

Funding sources for the 1994 SRP were the AFOSR-provided slots for the basic contract and laboratory funds. Funding sources by category for the 1994 SRP selected participants are shown here.

Table 4: 1994 SRP Associate Funding

FUNDING CATEGORY	SFRP	GSRP	HSAP
AFOSR Basic Allocation Funds	150	98 ^{*1}	121 ^{*2}
USAF Laboratory Funds	37	19	12
HBCU/MI By AFOSR (Using Procured Addn'l Funds)	5	0	0
TOTAL	192	117	133

*1 - 100 were selected, but two canceled too late to be replaced.

*2 - 125 were selected, but four canceled too late to be replaced.

7. COMPENSATION FOR PARTICIPANTS

Compensation for SRP participants, per five-day work week, is shown in this table.

Table 5: 1994 SRP Associate Compensation

PARTICIPANT CATEGORY	1991	1992	1993	1994
Faculty Members	\$690	\$718	\$740	\$740
Graduate Student (Master's Degree)	\$425	\$442	\$455	\$455
Graduate Student (Bachelor's Degree)	\$365	\$380	\$391	\$391
High School Student (First Year)	\$200	\$200	\$200	\$200
High School Student (Subsequent Years)	\$240	\$240	\$240	\$240

The program also offered associates whose homes were more than 50 miles from the laboratory an expense allowance (seven days per week) of \$50/day for faculty and \$37/day for graduate students.

Transportation to the laboratory at the beginning of their tour and back to their home destinations at the end was also reimbursed for these participants. Of the combined SFRP and GSRP associates, 58% (178 out of 309) claimed travel reimbursements at an average round-trip cost of \$860.

Faculty members were encouraged to visit their laboratories before their summer tour began. All costs of these orientation visits were reimbursed. Forty-one percent (78 out of 192) of faculty associates took orientation trips at an average cost of \$498. Many faculty associates noted on their evaluation forms that due to the late notice of acceptance into the 1994 SRP (caused by the late award in January 1994 of the contract) there wasn't enough time to attend an orientation visit prior to their tour start date. In 1993, 58% of SFRP associates took orientation visits at an average cost of \$685.

Program participants submitted biweekly vouchers countersigned by their laboratory research focal point, and RDL issued paychecks so as to arrive in associates' hands two weeks later.

HSAP program participants were considered actual RDL employees, and their respective state and federal income tax and Social Security were withheld from their paychecks. By the nature of their independent research, SFRP and GSRP program participants were considered to be consultants or independent contractors. As such, SFRP and GSRP associates were responsible for their own income taxes, Social Security, and insurance.

8. CONTENTS OF THE 1994 REPORT

The complete set of reports for the 1994 SRP includes this program management report augmented by fifteen volumes of final research reports by the 1994 associates as indicated below:

Table 6: 1994 SRP Final Report Volume Assignments

LABORATORY	VOLUME		
	SFRP	GSRP	HSAP
Armstrong	2	7	12
Phillips	3	8	13
Rome	4	9	14
Wright	5A, 5B	10	15
AEDC, FJSRL, WHMC	6	11	16

AEDC = Arnold Engineering Development Center
 FJSRL = Frank J. Seiler Research Laboratory
 WHMC = Wilford Hall Medical Center

APPENDIX A -- PROGRAM STATISTICAL SUMMARY

A. Colleges/Universities Represented

Selected SFRP and GSRP associates represent 158 different colleges, universities, and institutions.

B. States Represented

SFRP -Applicants came from 46 states plus Washington D.C. and Puerto Rico. Selectees represent 40 states.

GSRP - Applicants came from 46 states and Puerto Rico. Selectees represent 34 states.

HSAP - Applicants came from fifteen states. Selectees represent ten states.

C. Academic Disciplines Represented

The academic disciplines of the combined 192 SFRP associates are as follows:

Electrical Engineering	22.4%
Mechanical Engineering	14.0%
Physics: General, Nuclear & Plasma	12.2%
Chemistry & Chemical Engineering	11.2%
Mathematics & Statistics	8.1%
Psychology	7.0%
Computer Science	6.4%
Aerospace & Aeronautical Engineering	4.8%
Engineering Science	2.7%
Biology & Inorganic Chemistry	2.2%
Physics: Electro-Optics & Photonics	2.2%
Communication	1.6%
Industrial & Civil Engineering	1.6%
Physiology	1.1%
Polymer Science	1.1%
Education	0.5%
Pharmaceutics	0.5%
Veterinary Medicine	0.5%
TOTAL	100%

Table A-1. Total Participants

Number of Participants	
SFRP	192
GSRP	117
HSAP	133
TOTAL	442

Table A-2. Degrees Represented

Degrees Represented			
	SFRP	GSRP	TOTAL
Doctoral	189	0	189
Master's	3	47	50
Bachelor's	0	70	70
TOTAL	192	117	309

Table A-3. SFRP Academic Titles

Academic Titles	
Assistant Professor	74
Associate Professor	63
Professor	44
Instructor	5
Chairman	1
Visiting Professor	1
Visiting Assoc. Prof.	1
Research Associate	3
TOTAL	192

Table A-4. Source of Learning About SRP

SOURCE	SFRP		GSRP	
	Applicants	Selectees	Applicants	Selectees
Applied/participated in prior years	26%	37%	10%	13%
Colleague familiar with SRP	19%	17%	12%	12%
Brochure mailed to institution	32%	18%	19%	12%
Contact with Air Force laboratory	15%	24%	9%	12%
Faculty Advisor (GSRPs Only)	--	--	39%	43%
Other source	8%	4%	11%	8%
TOTAL	100%	100%	100%	100%

Table A-5. Ethnic Background of Applicants and Selectees

	SFRP		GSRP		HSAP	
	Applicants	Selectees	Applicants	Selectees	Applicants	Selectees
American Indian or Native Alaskan	0.2%	0%	1%	0%	0.4%	0%
Asian/Pacific Islander	30%	20%	6%	8%	7%	10%
Black	4%	1.5%	3%	3%	7%	2%
Hispanic	3%	1.9%	4%	4.5%	11%	8%
Caucasian	51%	63%	77%	77%	70%	75%
Preferred not to answer	12%	14%	9%	7%	4%	5%
TOTAL	100%	100%	100%	100%	99%	100%

Table A-6. Percentages of Selectees receiving their 1st, 2nd, or 3rd Choices of Directorate

	1st Choice	2nd Choice	3rd Choice	Other Than Their Choice
SFRP	70%	7%	3%	20%
GSRP	76%	2%	2%	20%

APPENDIX B – SRP EVALUATION RESPONSES

1. OVERVIEW

Evaluations were completed and returned to RDL by four groups at the completion of the SRP. The number of respondents in each group is shown below.

Table B-1. Total SRP Evaluations Received

Evaluation Group	Responses
SFRP & GSRPs	275
HSAPs	116
USAF Laboratory Focal Points	109
USAF Laboratory HSAP Mentors	54

All groups indicate near-unanimous enthusiasm for the SRP experience.

Typical comments from 1994 SRP associates are:

"[The SRP was an] excellent opportunity to work in state-of-the-art facility with top-notch people."

"[The SRP experience] enabled exposure to interesting scientific application problems; enhancement of knowledge and insight into 'real-world' problems."

"[The SRP] was a great opportunity for resourceful and independent faculty [members] from small colleges to obtain research credentials."

"The laboratory personnel I worked with are tremendous, both personally and scientifically. I cannot emphasize how wonderful they are."

"The one-on-one relationship with my mentor and the hands on research experience improved [my] understanding of physics in addition to improving my library research skills. Very valuable for [both] college and career!"

Typical comments from laboratory focal points and mentors are:

"This program [AFOSR - SFRP] has been a 'God Send' for us. Ties established with summer faculty have proven invaluable."

"Program was excellent from our perspective. So much was accomplished that new options became viable "

"This program managed to get around most of the red tape and 'BS' associated with most Air Force programs. Good Job!"

"Great program for high school students to be introduced to the research environment. Highly educational for others [at laboratory]."

"This is an excellent program to introduce students to technology and give them a feel for [science/engineering] career fields. I view any return benefit to the government to be 'icing on the cake' and have usually benefitted."

The summarized recommendations for program improvement from both associates and laboratory personnel are listed below (Note: basically the same as in previous years.)

- A. Better preparation on the labs' part prior to associates' arrival (i.e., office space, computer assets, clearly defined scope of work).
- B. Laboratory sponsor seminar presentations of work conducted by associates, and/or organized social functions for associates to collectively meet and share SRP experiences.
- C. Laboratory focal points collectively suggest more AFOSR allocated associate positions, so that more people may share in the experience.
- D. Associates collectively suggest higher stipends for SRP associates.
- E. Both HSAP Air Force laboratory mentors and associates would like the summer tour extended from the current 8 weeks to either 10 or 11 weeks; the groups state it takes 4-6 weeks just to get high school students up-to-speed on what's going on at laboratory. (Note: this same argument was used to raise the faculty and graduate student participation time a few years ago.)

2. 1994 USAF LABORATORY FOCAL POINT (LFP) EVALUATION RESPONSES

The summarized results listed below are from the 109 LFP evaluations received.

1. LFP evaluations received and associate preferences:

Table B-2. Air Force LFP Evaluation Responses (By Type)

Lab	Evals Recv'd	How Many Associates Would You Prefer To Get ?								(% Response)			
		SFRP				GSRP (w/Univ Professor)				GSRP (w/o Univ Professor)			
		0	1	2	3+	0	1	2	3+	0	1	2	3+
AEDC	10	30	50	0	20	50	40	0	10	40	60	0	0
AL	44	34	50	6	9	54	34	12	0	56	31	12	0
FJSRL	3	33	33	33	0	67	33	0	0	33	67	0	0
PL	14	28	43	28	0	57	21	21	0	71	28	0	0
RL	3	33	67	0	0	67	0	33	0	100	0	0	0
WHMC	1	0	0	100	0	0	100	0	0	0	100	0	0
WL	46	15	61	24	0	56	30	13	0	76	17	6	0
Total	121	25%	43%	27%	4%	50%	37%	11%	1%	54%	43%	3%	0%

LFP Evaluation Summary. The summarized responses, by laboratory, are listed on the following page. LFPs were asked to rate the following questions on a scale from 1 (below average) to 5 (above average).

2. LFPs involved in SRP associate application evaluation process:
 - a. Time available for evaluation of applications:
 - b. Adequacy of applications for selection process:
3. Value of orientation trips:
4. Length of research tour:
5.
 - a. Benefits of associate's work to laboratory:
 - b. Benefits of associate's work to Air Force:
6.
 - a. Enhancement of research qualifications for LFP and staff:
 - b. Enhancement of research qualifications for SFRP associate:
 - c. Enhancement of research qualifications for GSRP associate:
7.
 - a. Enhancement of knowledge for LFP and staff:
 - b. Enhancement of knowledge for SFRP associate:
 - c. Enhancement of knowledge for GSRP associate:
8. Value of Air Force and university links:
9. Potential for future collaboration:
10.
 - a. Your working relationship with SFRP:
 - b. Your working relationship with GSRP:
11. Expenditure of your time worthwhile:

(Continued on next page)

12. Quality of program literature for associate:
13. a. Quality of RDL's communications with you:
- b. Quality of RDL's communications with associates:
14. Overall assessment of SRP:

Laboratory Focal Point Responses to above questions

	<i>AEDC</i>	<i>AL</i>	<i>FJSRL</i>	<i>PL</i>	<i>RL</i>	<i>WHMC</i>	<i>WL</i>
<i># Evals Recv'd</i>	10	32	3	14	3	1	46
<i>Question #</i>							
2	90 %	62 %	100 %	64 %	100 %	100 %	83 %
2a	3.5	3.5	4.7	4.4	4.0	4.0	3.7
2b	4.0	3.8	4.0	4.3	4.3	4.0	3.9
3	4.2	3.6	4.3	3.8	4.7	4.0	4.0
4	3.8	3.9	4.0	4.2	4.3	NO ENTRY	4.0
5a	4.1	4.4	4.7	4.9	4.3	3.0	4.6
5b	4.0	4.2	4.7	4.7	4.3	3.0	4.5
6a	3.6	4.1	3.7	4.5	4.3	3.0	4.1
6b	3.6	4.0	4.0	4.4	4.7	3.0	4.2
6c	3.3	4.2	4.0	4.5	4.5	3.0	4.2
7a	3.9	4.3	4.0	4.6	4.0	3.0	4.2
7b	4.1	4.3	4.3	4.6	4.7	3.0	4.3
7c	3.3	4.1	4.5	4.5	4.5	5.0	4.3
8	4.2	4.3	5.0	4.9	4.3	5.0	4.7
9	3.8	4.1	4.7	5.0	4.7	5.0	4.6
10a	4.6	4.5	5.0	4.9	4.7	5.0	4.7
10b	4.3	4.2	5.0	4.3	5.0	5.0	4.5
11	4.1	4.5	4.3	4.9	4.7	4.0	4.4
12	4.1	3.9	4.0	4.4	4.7	3.0	4.1
13a	3.8	2.9	4.0	4.0	4.7	3.0	3.6
13b	3.8	2.9	4.0	4.3	4.7	3.0	3.8
14	4.5	4.4	5.0	4.9	4.7	4.0	4.5

3. 1994 SFRP & GSRP EVALUATION RESPONSES

The summarized results listed below are from the 275 SFRP/GSRP evaluations received.

Associates were asked to rate the following questions on a scale from 1 (below average) to 5 (above average)

- | | |
|--|----------|
| 1. The match between the laboratories research and your field: | 4.6 |
| 2. Your working relationship with your LFP: | 4.8 |
| 3. Enhancement of your academic qualifications: | 4.4 |
| 4. Enhancement of your research qualifications: | 4.5 |
| 5. Lab readiness for you: LFP, task, plan: | 4.3 |
| 6. Lab readiness for you: equipment, supplies, facilities: | 4.1 |
| 7. Lab resources: | 4.3 |
| 8. Lab research and administrative support: | 4.5 |
| 9. Adequacy of brochure and associate handbook: | 4.3 |
| 10. RDL communications with you: | 4.3 |
| 11. Overall payment procedures: | 3.8 |
| 12. Overall assessment of the SRP: | 4.7 |
| 13. a. Would you apply again? | Yes: 85% |
| b. Will you continue this or related research? | Yes: 95% |
| 14. Was length of your tour satisfactory? | Yes: 86% |
| 15. Percentage of associates who engaged in: | |
| a. Seminar presentation: | 52% |
| b. Technical meetings: | 32% |
| c. Social functions: | 03% |
| d. Other | 01% |

16. Percentage of associates who experienced difficulties in:

- | | |
|---------------------|-----|
| a. Finding housing: | 12% |
| b. Check Cashing: | 03% |

17. Where did you stay during your SRP tour?

- | | |
|----------------------|-----|
| a. At Home: | 20% |
| b. With Friend: | 06% |
| c. On Local Economy: | 47% |
| d. Base Quarters: | 10% |

THIS SECTION FACULTY ONLY:

18. Were graduate students working with you? Yes: 23%

19. Would you bring graduate students next year? Yes: 56%

20. Value of orientation visit:

- | | |
|-----------------|-----|
| Essential: | 29% |
| Convenient: | 20% |
| Not Worth Cost: | 01% |
| Not Used: | 34% |

THIS SECTION GRADUATE STUDENTS ONLY:

21. Who did you work with:

- | | |
|-----------------------|-----|
| University Professor: | 18% |
| Laboratory Scientist: | 54% |

4. 1994 USAF LABORATORY HSAP MENTOR EVALUATION RESPONSES

The summarized results listed below are from the 54 mentor evaluations received.

1. Mentor apprentice preferences:

Table B-3. Air Force Mentor Responses

		How Many Apprentices Would You Prefer To Get ?			
		<i>HSAP Apprentices Preferred</i>			
<i>Laboratory</i>	<i># Evals Recv'd</i>	<i>0</i>	<i>1</i>	<i>2</i>	<i>3+</i>
AEDC	6	0	100	0	0
AL	17	29	47	6	18
PL	9	22	78	0	0
RL	4	25	75	0	0
WL	18	22	55	17	6
Total	54	20%	71%	5%	5%

Mentors were asked to rate the following questions on a scale from 1 (below average) to 5 (above average)

2. Mentors involved in SRP apprentice application evaluation process:
 - a. Time available for evaluation of applications:
 - b. Adequacy of applications for selection process:
3. Laboratory's preparation for apprentice:
4. Mentor's preparation for apprentice:
5. Length of research tour:
6. Benefits of apprentice's work to U.S. Air force:
7. Enhancement of academic qualifications for apprentice:
8. Enhancement of research skills for apprentice:
9. Value of U.S. Air Force/high school links:
10. Mentor's working relationship with apprentice:
11. Expenditure of mentor's time worthwhile:
12. Quality of program literature for apprentice:
13.
 - a. Quality of RDL's communications with mentors:
 - b. Quality of RDL's communication with apprentices:
14. Overall assessment of SRP:

	<i>AEDC</i>	<i>AL</i>	<i>PL</i>	<i>RL</i>	<i>WL</i>
<i># Evals Recv'd</i>	6	17	9	4	18
<i>Question #</i>					
2	100 %	76 %	56 %	75 %	61 %
2a	4.2	4.0	3.1	3.7	3.5
2b	4.0	4.5	4.0	4.0	3.8
3	4.3	3.8	3.9	3.8	3.8
4	4.5	3.7	3.4	4.2	3.9
5	3.5	4.1	3.1	3.7	3.6
6	4.3	3.9	4.0	4.0	4.2
7	4.0	4.4	4.3	4.2	3.9
8	4.7	4.4	4.4	4.2	4.0
9	4.7	4.2	3.7	4.5	4.0
10	4.7	4.5	4.4	4.5	4.2
11	4.8	4.3	4.0	4.5	4.1
12	4.2	4.1	4.1	4.8	3.4
13a	3.5	3.9	3.7	4.0	3.1
13b	4.0	4.1	3.4	4.0	3.5
14	4.3	4.5	3.8	4.5	4.1

5. 1994 HSAP EVALUATION RESPONSES

The summarized results listed below are from the 116 HSAP evaluations received.

HSAP apprentices were asked to rate the following questions on a scale from 1 (below average) to 5 (above average)

1. Match of lab research to you interest:	3.9
2. Apprentices working relationship with their mentor and other lab scientists:	4.6
3. Enhancement of your academic qualifications:	4.4
4. Enhancement of your research qualifications:	4.1
5. Lab readiness for you: mentor, task, work plan	3.7
6. Lab readiness for you: equipment supplies facilities	4.3
7. Lab resources: availability	4.3
8. Lab research and administrative support:	4.4
9. Adequacy of RDL's apprentice handbook and administrative materials:	4.0
10. Responsiveness of RDL's communications:	3.5
11. Overall payment procedures:	3.3
12. Overall assessment of SRP value to you:	4.5
13. Would you apply again next year?	Yes: 88%
14. Was length of SRP tour satisfactory?	Yes: 78%
15. Percentages of apprentices who engaged in:	
a. Seminar presentation:	48%
b. Technical meetings:	23%
c. Social functions:	18%

HIGH CAPACITY OPTICAL COMMUNICATION NETWORKS

Behnaam Aazhang
Associate Professor
Department of Electrical and Computer Engineering

Rice University
6100 S. Main
Houston, Texas 77251-1892

Final Report for:
Summer Faculty Research Program
Phillips Laboratory

Sponsored by:
Air Force Office of Scientific Research
Bolling Air Force Base, DC

and

Phillips Laboratory

November 11, 1994

HIGH CAPACITY OPTICAL COMMUNICATION NETWORKS

Behnaam Aazhang
Associate Professor
Department of Electrical and Computer Engineering
Rice University
Houston, Texas 77251-1892

Abstract

Practical, very high speed networks are critical to support the next generation of information technology applications, such as high-performance computing environments, access to vast electronic libraries, and multimedia communication of voice, data, graphics, and video for business, medical, and industrial needs. This research program will design, prototype, and evaluate a multiuser optical communication network based on novel data encoding and decoding technology. This approach successfully meets the challenge of using the enormous bandwidths of optical channels by placing the burden of handling high bit rates on simple optics, rather than on ultrafast electronics or complex laser sources, making practical and economical implementation a real near-term possibility.

The approach is based on spread spectrum encoding in the optical frequency domain. The high bandwidth optical channel allows the assignment of codes to a large number of users, all of whom can access the channel simultaneously, asynchronously, and at different bit rates. User codes are sent and received in parallel, rather than in series, eliminating electronic bottlenecks and preserving the optical bandwidth advantage. Two innovative features of this technique account for its practical and performance advantages. First, the optical source for each user is extremely simple and rugged: a low power laser diode, similar to those in compact disc players, pumping a few meters of doped optical fiber. Second, highly effective data decoders, or smart receivers, based on integrated photodetector arrays and recent communication theory results, permit simultaneous use of the network by many users while maintaining low bit error rates.

HIGH CAPACITY OPTICAL COMMUNICATION NETWORKS

Behnaam Aazhang

Introduction

Optical networks have the potential of providing unprecedented low cost telecommunication capacity by dramatically reducing the cost per unit bandwidth. These gains will have the greatest impact as completely optical, local and metropolitan area networks, consisting of many users communicating simultaneously over a common, passive optical channel, replace traditional point-to-point links containing signal repeaters and switching electronics. Practical, very high speed networks are critical to support the next generation of information technology applications, such as high-performance computing environments, access to vast electronic libraries, and multimedia communication of voice, data, graphics, and video for business, medical, and industrial needs. This project is an interdisciplinary program to design, prototype, and evaluate a multiuser optical communication network based on novel data encoding and decoding technology that we have developed. This approach successfully meets the challenge of using the enormous bandwidths of optical channels by placing the burden of handling high bit rates on simple optics, rather than on ultrafast electronics or complex laser sources, making practical and economical implementation a real near-term possibility. Rapid development of this technology and the early implementation of optical networks will put industries in the U.S. in a unique competitive position during the next decade.

Methodology

The next generation of communication networks must be able to simultaneously serve many users and many types of applications with differing requirements for bandwidth, throughput, reliability, and security; capacities approaching a terahertz will be required. Despite the rapid progress of optical communications research, current optical communication systems utilize only a small fraction of the available bandwidth. Our approach is based on code division multiple access (CDMA), a dynamic and highly tolerant alternative to time and frequency division that has received considerable attention in the research community in the last few years [1, 2, 3, 4, 5, 6, 7]. In CDMA, each user is assigned a code as an address on a commonly shared channel. A high bandwidth channel allows the assignment of codes to a large number of users, all of whom can access the channel simultaneously, asynchronously, and at differing bit rates. In addition, CDMA provides security against unauthorized users, and reduces interference and

multipath problems.

In the radio frequency domain, CDMA, or spread spectrum, uses phase modulation coding. The phase of an optical signal, however, is quickly scrambled by fiber dispersion. We propose spread spectrum encoding in the optical frequency domain, which eliminates optical phase and pulse length as a source parameter, reduces dispersion as a channel constraint, and greatly increases the number of available codes and users. In addition, this technique, which we refer to as Optical Spectral Amplitude CDMA or OSA-CDMA, separates code elements or chips spatially, meaning that user codes are sent and received in parallel, rather than in series, eliminating electronic bottlenecks and preserving the optical bandwidth advantage.

There are two key reasons for the practical and performance advantages of our system relative to other approaches. First, the optical source for each user is extremely simple and rugged: a low power laser diode, similar to those in compact disc players, pumping a few meters of doped optical fiber. Second, we have developed highly effective data decoders, or smart receivers, based on integrated photodetector arrays and recent communication theory results. These decoders permit simultaneous use of the network by many users while maintaining low bit error rates. Our initial calculations indicate that these advances, in combination, will result in cost-effective optical networks serving thousands of users with total terahertz data capacities over tens of kilometers.

The objective of this program is to prototype an optical communication network based on these concepts; to evaluate the characteristics of the individual components, such as statistical variations and noise sensitivity; to incorporate that data into models and run simulations for design optimization; and to measure overall system performance under a variety of conditions.

Results

In this report, the tasks that have been completed with partial support from the Air Force Office of Scientific Research will be described. In addition to setting up the lab and ordering equipment, we have been working in three areas: experimental measurements to characterize the superfluorescence source (SFS), modulation and detection of bipolar sequences for optical systems, and constructing simulations of the proposed system using the SPW software package.

Experiment:

We have built and begun testing the neodymium-doped SFS that will be used in the initial prototype. It is a double core fiber pumped with a 500 mw multi-stripe diode laser at 810 nm. True spontaneous output power is about 3.5 mw; if one fiber end is left flat to form a weak reflector, the output increases

to more than 20 mw.

The output of an SFS results from amplified spontaneous emission and can be modeled as thermal light. Statistical modeling of a thermal source predicts that the signal-to-noise ratio (SNR) at the output of a photodetector should be constant and equal to the ratio of the source bandwidth and the detector electrical bandwidth. Noise measurements of the full bandwidth of the SFS with a fast photodiode reveals that the degree of output fluctuation is proportional to intensity, or that the SNR is constant, as expected. We are awaiting arrival of a new spectrometer to make similar measurements within the narrow spectral channel intervals, and to characterize the other spectral properties of the source.

Simulations:

Simulations of the multiuser system using the commercial software package SPW have begun. The SPW package is designed for RF systems, not optical systems, but we have constructed new blocks for this purpose. The determination of error rates for high performance systems is a difficult, or at least time consuming, problem, both in monte carlo simulations and in practice. We have had some initial successes in applying the analytical technique Importance Sampling to our SPW simulations. This has reduced the time for calculations for low error rate (10^{-6}) systems from about a day to 10 minutes. We are still investigating this approach and verifying its validity.

Bipolar coding:

In the radio frequency domain, simple correlation detectors work well because the code sequences are bipolar, consisting of $\{+1, -1\}$ elements. Such codes can be designed to have a very small, or zero, cross correlations and large autocorrelations. The success of RF CDMA systems have been well documented. Unfortunately, it has not been possible to transfer those practical results to the optical systems. Unipolar code sequences, consisting of $\{1, 0\}$ elements, lack the advantageous correlation properties of bipolar codes. For this reason, we originally studied more complex, but theoretically optimum, multiuser detectors described previously. These require a detector for each channel and knowledge of every user's code to perform an iterative algorithm to eliminate interference.

In this project, we developed a method to directly extend the RF CDMA techniques to the optical domain with no loss of performance. The technique involves recoding the bipolar codes into two channels of unipolar codes, and a new compound correlator for detection. As a consequence, all the well known system design techniques, codes, and performance results that have been demonstrated for the bipolar RF systems can be extended directly to the optical domain. The detector is quite simple, requiring only two detectors and no information about the other users; it can be implemented easily, especially

for spectral channel encoding. Our experimental work is now focused on this system, implemented at $1.55\mu m$ using an Er-doped fiber source.

The technique involves a recoding of the bipolar, RF codes to unipolar ones, coupled with a compound, unipolar, correlation detector. The structure of this detector arises naturally from considering the bipolar correlator as the combination of four unipolar correlations, as follows. Consider a bipolar sequence $s(n)$ that takes values from $\{-1, 1\}$. We observe that $s(n)$ can be expressed as the difference of two unipolar sequences $c(n)$ and $\bar{c}(n)$ where $c(n)$ is obtained from $s(n)$ by replacing each -1 with 0 and $\bar{c}(n)$ is the binary complement of $c(n)$. Then the correlation function $R_{12}(m)$ of two bipolar sequences $s_1(n)$ and $s_2(n)$ can be computed via their unipolar representations $(c_1(n), \bar{c}_1(n))$ and $(c_2(n), \bar{c}_2(n))$:

$$R_{12}(m) = \sum_{n=-\infty}^{\infty} [c_1(n)c_2(n-m) + \bar{c}_1(n)\bar{c}_2(n-m)] - \sum_{n=-\infty}^{\infty} [c_1(n)\bar{c}_2(n-m) + \bar{c}_1(n)c_2(n-m)] \quad (1)$$

Thus given any bipolar sequence of length N , this scheme recodes it as two unipolar sequences that can be represented as a single unipolar sequence of length $2N$. Practically, the two sequences, or channels, $c(n)$ and $\bar{c}(n)$ may be distinguished by polarization, time, or spectral properties. The proposed encoding and detection maintain all the correlation properties of the original bipolar system. As a consequence, all the well-known system design techniques, codes, and performance results that have been demonstrated for the bipolar RF systems can be extended directly to the optical domain.

The concepts, however, are general and applicable to any unipolar system, including those in the RF domain. The periodic unipolar codewords of length N modulate the transmitting source in two channels. The binary data source switches the modulator outputs such that if, say, symbol "1" is transmitted then c is on the \oplus channel and \bar{c} on the \ominus channel, and vice versa for symbol "0". The received signals are demodulated according to Eq. 1. The outputs of two unipolar correlators are summed optically and detected with a photodiode. The two photodiodes are operated in a balanced bridge connection so that their outputs (including dark current) are subtracted. The result is threshold-compared to zero to estimate the transmitted symbol.

In a time encoding system, the unipolar codewords are implemented with short optical pulses and the correlators can be implemented as fiber tapped-delay lines. Dual channel or time multiplexed transmissions can be used. The former can be done with two separate fibers, a dual wavelength source, or a single polarization preserving fiber so that the two orthogonal polarizations can be used. For time multiplexed transmission, the codewords are transmitted sequentially and only two correlators are required at the receiver.

Spectral encoding, however, offers several advantages. The codewords are implemented by encoding a broad optical source spectrum via dispersive devices and spectral amplitude masks. Single-channel

transmission at the symbol rate is feasible by concatenating the spectral masks, since the symbol rate is independent of the code length. Spectral encoding has the additional advantage that asynchronous transmission does not affect the correlation of the codewords. Thus if a length- N Gold code is used, the number of available codewords is $N(N+1)$ (since all N phase shifts of the $N+1$ codewords can be used), and the pool of subscribers can be much larger than the number of simultaneously active users. The receiver correlators are also realized via dispersive devices and spectral masks. We will present simple and practical designs for the required broadband sources, encoder and receiver.

The SNR performance of this scheme has been studied for comparison with the TDMA or WDMA system. By modeling the output of the photodetectors as two independent Poisson random variables, it can be shown that with length- N Walsh codes, the SNR of any one user in the presence of K simultaneous users is given by:

$$SNR \approx \frac{N\Lambda}{K} \quad (2)$$

where Λ is the code chip intensity of each user (assumed equal) and much larger than the photodetector dark currents. Since $1 \leq K \leq N$, the proposed system has the desirable property that its SNR is lower bounded by the comparable TDMA or CDMA system. Simulation results have been obtained using Importance Sampling techniques and show that the performance of the proposed scheme is much improved over the MAI-limited correlation detector in CDMA applications.

References

- [1] R. L. Pickholtz, D. L. Schilling, and L. B. Milstein, "Theory of spread-spectrum communications — a tutorial," *IEEE Trans. Commun.*, vol. COM-30, pp. 904–912, May 1982.
- [2] G. Foschini and G. Vannucci, "Using spread-spectrum in a high-capacity fiber-optic local network," *IEEE J. of Lightwave Tech.*, vol. 6, no. 3, pp. 370–379, March, 1988.
- [3] J. Hui, "Pattern code modulation and optical decoding - a novel code-division multiplexing technique for multifiber networks," *IEEE Journal Selected Areas in Commun.*, vol. SAC-3, no. 6, pp. 916–927, Nov 1985.
- [4] P. R. Prucnal, M. A. Santoro, and S. K. Sehgal, "Ultrafast all-optical synchronous multiple access fiber network," *IEEE J. on Sel. Areas in Commun.*, pp. 1484–1493, December, 1986.
- [5] J. A. Salehi, "Code division multiple access techniques in optical fiber networks: Part-I: Fundamental principles," *IEEE Trans. Commun.*, vol. COM-37, no. 8, pp. 824–833, Aug. 1989.

- [6] J. A. Salehi and C. A. Brackett, "Code division multiple access techniques in optical fiber networks: Part-II: Systems performance analysis," *IEEE Trans. Commun.*, vol. COM-37, no. 8, pp. 834-842, Aug. 1989.
- [7] A. Weiner, J. Heritage, and J. Salehi, "Encoding and decoding of femtosecond pulses," *Optics Letters*, vol. 13, no. 4, pp. 300-302, April 1988.

**ON THE MIXING MECHANISMS IN
A PAIR OF IMPINGING JETS**

Nasser Ashgriz

Associate Professor

Department of Mechanical and Aerospace Engineering

State University of New York

Buffalo, New York 14260

Final Report for:

Summer Faculty Research Program

Phillips Laboratory

Sponsored by:

Edwards Airforce Base

and

Phillips Laboratory

September 1994

On The Mixing Mechanisms In A Pair Of Impinging Jets

Nasser Ashgriz

1. Introduction

The performance of a biliquid propellant rocket motor is intimately dependent on the mixing and chemical reaction among the propellant or propellant combination in the combustor. Because of the restrictions on the physical size of the combustion chamber, certain limitations are set on the residence time of the reactants in the chamber. These limitations dictate requirement for a rapid mixing and chemical reaction between the propellants. Such requirements can be achieved by proper atomization of the liquid propellants and attainment of a certain mass distribution of each propellant across the injection surface for a stoichiometric and/or optimum heat release rate. The process of mixing in actual combustors is complicated due to the simultaneous action of the vaporization, diffusion, and gaseous turbulence. However, the first order effect seems to be the original physical mixing or the mass distribution generated by the injector.

One of the techniques for the attainment of proper mixing is by impinging two or more liquid jets at a common point. In rocket engines, liquid jets of fuel and/or oxidizer collide and breakup into a spray that vaporizes and combusts. There are numerous experimental as well as theoretical studies on the mechanism of the atomization of the impinging jets. These studies, exemplified by the works of Heidmann and Humphrey (1951), Heidmann *et al.* (1957), Rupe (1957), Taylor (1960), Dombrowski and Hooper (1963), Vassallo and Ashgriz (1992), and Anderson *et al.* (1992), show that when two jets collide they form a sheet in the direction perpendicular to the plane of jets. Waves form on the surface of the sheet and grow until the sheet breakups into small droplets. The generated spray has an elliptical cross-section with its major axis in the plane of the liquid sheet.

Studies on the mixing of the two streams are more scarce. There are several reports on the measurement of the spatial distribution of two components of a biliquid impinging stream spray. The most comprehensive experimental investigation of the mixing in impinging jets has been conducted at the Jet Propulsion Laboratory in 1950s (Rupe, 1953, 1956, and Elverum and Morey, 1959). Rupe (1953) has conducted the pioneering work in the jet mixing. Since it is very difficult to use actual liquid propellants in a systematic investigation of the mixing, alternative simulating fluids have been utilized. Mixing studies have been predominately by the use of immiscible liquids as the simulant. Immiscible liquids are preferred since the mixture ratio of the two liquids can be determined simply by measuring the volume of the two liquids in the sample. Whereas, if miscible liquids are used, one liquid has to be dyed and a technique, such as calibrated photometry, has to be used to measure the concentration of the dye in the sampled liquid. Immiscible liquids have also used because they allow the near duplication of the physical properties of some propellants. For instance, carbon tetrachloride and water have been used to simulate nitric acid-aniline propellant system. Nitric acid and aniline are believed to be immiscible.

The primary instrument to determine the mixing in sprays has been a Patterator. Patterator is basically

an array of test tubes which collects liquid samples from the spray cross-section and provides the local mixture fraction across the spray. The resolution of the mixing measurement depends on the number of tubes used. It is assumed that the ideal spray is one in which the local mixture ratio is constant and equal to the input mixture ratio. Then any actual spray may be compared with the ideal case by noting the departure of the local mixture ratio from the nominal value at a number of different points within the spray. Rupe (1953) defined the following coefficient to describe the degree of mixing in the impinging injectors:

$$Y' = \sum_0^N \frac{w}{W} \left(\frac{R-r}{R} \right) + \sum_0^{\tilde{N}} \frac{w}{W} \left(\frac{R-\tilde{r}}{R-1} \right) \quad (1)$$

In this equation, R is the nominal mixture ratio, $R = W_2/(W_1 + W_2)$, where W_i is the weight flow rate of stream i , r is the local mixture ratio, $r = w_2/(w_1 + w_2)$, \tilde{r} is the local mixture ratio for points where $r > R$, N is the number of samples with $r < R$, \tilde{N} is the number of samples with $r > R$, $w = w_1 + w_2$ is the total local weight flow rate of the spray, and $W = W_1 + W_2$ is the total weight flow rate or nominal weight flow rate of the spray. The percentage of this deviation represents the extent of mixing or mixing efficiency:

$$E_m = 100(1 - Y') \quad (2)$$

The investigators after Rupe have used this coefficient to characterize, evaluate, and compare sprays of different configurations produced under various conditions.

Experimental measurement of E_m for different values of momentum ratio by Rupe (1953) for a one-on-one, and Elverum and Morey (1959) for two-on-one, two-on-two, and four-on-one impinging jets, has shown that the maximum value of E_m occurs near $M_1/M_2 = 1.0$ and that the liquid-phase mixing is relatively insensitive to momentum ratio at or near a momentum ration of 1.0. Their results indicated that E_m did not change significantly in the range of 1.0 ± 0.2 .

Rupe's (1953) experimental results have indicated that a linear correlation exists between the impingement angle and E_m . Better mixing is obtained at lower impingement angles. This is in agreement with the actual rocket tests which show that the rocket performance increases as the impingement angle decreases from 90° to 45° . By extending the angle studies to 120° the actual rocket test results indicate that minimum perforce is obtained for $\alpha = 90^\circ$. The impact angle influences the mixing in two different manner. Higher impingement angles result in a higher impact-induced turbulence and, therefore, higher turbulence mixing. On the other hand, higher impingement angles will result in smaller contact time between the liquids of the two streams. The experimental results have revealed that the impingement angle of 45° results in the optimum mixing.

3. Experimental Apparatus and Procedure

The experimental system was consisted of a flow system, the injector setup, the Patternator, and the Diode Array Spectrophotometer. The flow system consisted of a driving force, a holding tank, and gages. A high pressure tank of Nitrogen with a regulator was used to drive the flow. This delivered a constant pressure to two 35 liter stainless steel tanks filled with water. A red dye (food coloring) was added to one of the tanks. The steady flow was monitored by a pressure gage. The flow rate was calibrated with a graduated cylinder

and stopwatch. The precision of the gage allowed the flow rate to be set to within $0.03\text{ml}/\text{sec}$ of the desired flow rate and as a result the jet velocity was determined to within $0.1\text{m}/\text{sec}$.

The injectors were mounted onto a stand. Since the characteristics of the spray change with position, it is important to have the same reference point for each test. The origin of the coordinate axis, $z = 0$, for the experiment was the point at which the jets impinge. The y -axis was chosen to be the direction perpendicular to the incoming jets (along the major axis of the spray), and the x -axis was in the same direction as the jets (along the minor axis of the spray) (see Fig. 1). The injectors were a plain faced orifice type. The orifice diameters used were $330\mu\text{m}$, $508\mu\text{m}$, and $711\mu\text{m}$, with orifice length to diameter ratios of 1, 5.4, and 7, respectively. The range of jet velocities was from $8.0\text{m}/\text{sec}$ to $27.6\text{m}/\text{sec}$.

A linear Patternator was built by using 20, $3.175\text{mm} \times 3.175\text{mm}$ square brass tubing, held linearly by a fixture. One end of these tubes was used for liquid collection, and their other end was bent and set into an array of test tubes. Before the start of each experiment the Patternator was completely cleaned. A shutter was set on top of the Patternator, so that the transient effects at the start and stop of the flow were eliminated. After a steady flow was achieved, the shutter was removed, and the liquid was collected by the Patternator. The time of filling was measured by a stop watch. The fluid volume as well as the concentration of the dye in each test tube was measured.

The concentration of the dye was measured by an HP 8450 UV/VIS Spectrophotometer. This instrument passes 200 to 800 nm bandwidth UV/VIS radiation alternately through the sample and reference cells twice in each one-second measurement period. A holographic grating linearly disperses the radiation to the 200 individual diode detectors in each of the UV and VIS detector arrays for a total of 401 resolution elements. Direct visualizations of the impinging process were made by using the Green Field instrument.

4. Experimental Results

4.1. The Stream Characteristics

The flow characteristics of the liquid streams before impingement have a significant effect on the mixing process. Typical jet characteristics for a nozzle with $711\mu\text{m}$ diameter and length to diameter ratio of $L/D = 16$ are shown in Fig. 2 for three jet velocities of $V_j = 8, 13.5, \text{ and } 20\text{m}/\text{s}$. Although no detailed measurement of the flow conditions are made, direct visualization of the jet behavior reveals the following characteristics.

Both large and small scale disturbances are observed. Small scale disturbances appear close to the orifice, whereas large scale disturbances develop downstream. Small scale disturbances damp out, while the large scale disturbances grow along the jet axis. As the jet velocity is increased the large scale disturbances are delayed to a further distance downstream of the nozzle. On the other hand, the frequency of the fluctuations on the jet surface increases with increasing the jet velocity. Figure 2a for $V_j = 8\text{m}/\text{s}$ shows that the jet surface does not contain small scale, high frequency fluctuations, and only contains large scale, low frequency fluctuations. As the jet velocity is increased to $V_j = 20\text{m}/\text{s}$ in Fig. 2c, the jet surface close to the nozzle contains small scale high frequency fluctuations, which damp further downstream, and transform into similar

type of fluctuations as in low velocity jet close to the nozzle. This fluctuations arise from the previously reported helical disturbances which result in the entire jet assuming a helical form. Hoyt and Taylor (1977) indicated that the helical disturbances grow due to the aerodynamic form drag, since jets discharging into surrounding air moving at the same speed as the jet remained relatively stable, compared with the case when the jet is discharged into stagnant air. Our observations of the streams indicate that, if the impingement point is approximately 20 diameters downstream of the nozzle, the small scale, high frequency fluctuations are damped and only large scale helical disturbances control the impingement process. As the jet velocity increases the amplitude of these low frequency, helical disturbances at the impingement point increases. The helical disturbances have a significant effect on the mixing processes in the impinging jets since they cause that two jets do not collide head-on. This results in the fluctuations of the stagnation point which will be discussed in the next section.

4.2 Atomization Process

Impinging jet atomization process has been extensively investigated previously. Here we provide some new findings on the mechanism of the atomization which had not been reported before. The overall behavior of the atomization process is presented in Fig. 3 for three different jet velocities and at impingement angle of 60° . When two jets impinge, a liquid sheet is formed in the plane perpendicular to the plane of impingement. The liquid sheet becomes unstable and breaks into liquid ligaments, which consequently break into small drops. The formation of the liquid ligaments are mainly due to the so called "impact waves," which radially propagate from the point of impingement. The actual mechanism of the formation of these waves is not known, and their study is not the subject of the present investigation.

The typical photographs shown in Fig. 3 reveal an interesting feature which, although existed, it has not been reported previously. The waves are not exactly symmetric, yet have a zig-zag type structure. We have observed similar zig-zag type structures on the photographs reported by the other investigators. This structure is due to the helical disturbances which result in fluctuation of the stagnation point at the plane of impinging jets. These fluctuations are more pronounced by observing the plane of impingement as shown in Fig. 4. Any fluctuation in the location of the stagnation point causes that the collision impact parameter between the two jets changes. The collision impact parameter is defined in Fig. 5a as half of the distance between the uninteracting surfaces along the major axis minus the mean jet diameter. The larger the impact parameter, a larger percentage of the two jets will not interact and tend to follow their initial trajectory. This will result in the formation of the liquid stretches. A schematic presentation of this effect is given in Fig. 5 in order to clarify the mechanism. This mechanism modifies the atomization models which are purely based on the instability of a liquid sheet. Obviously, more complex three dimensional effects are responsible for the actual atomization.

Figure 4 clearly shows that as the jet velocity increases the spreading in the x -axis increases. This is due to an increase in the kinetic energy of the uninteracted part of the two jets, which stretches the liquid until the surface tension forces stop the motion. It is believed that the increased stretching of the liquid along the x - axis will result in better atomization, since the drops can be sheared off of the thin liquid sheets formed by this stretching effect. This effect explains the observed increase in the spray angle in the plane of

the impinging jets with increasing the jet velocity.

Another effect which is evident from Fig. 4 is the increase in the frequency of the observed stretches with increasing the jet velocity. As discussed above, this is due to the increase in the frequency of the helical disturbances of each stream. This increase in frequency causes that the impact waves become more intermixed and harder to identify as observed in Fig. 3.

4.3 Mixing Mechanisms

The extent of mixing is measured by adding a dye (food color) to one of the jets and collecting the liquid on the impingement plane (x -axis) using the linear Patternator. The concentration of the dye is then measured using a spectrophotometer. Figures 6-8 show the mixture fraction on the impingement plane for three different jet diameters, and several jet velocities.

A very distinct feature is evident. At low jet velocities, when the two jets impinge and atomize, the liquid from each jet tends to stay in the same plane as the original jet. The two jets seem to bounce off each other. For instance, in Fig. 6a ($D_j = 330\mu\text{m}$ and $V_j = 20\text{m/s}$) the jet on the left (negative x -axis) is dyed, and the mixture fraction, measured at 9.21cm downstream of the impingement point, continuously reduces from left to right. Similar results are obtained for jets with larger diameters, as shown in Fig. 7a for $D_j = 508\mu\text{m}$ at $V_j = 13\text{m/s}$, and in Fig. 8a for $D_j = 711\mu\text{m}$ at $V_j = 8\text{m/s}$. As the jet diameter is increased the bouncing type impingement occurs at lower jet velocities. When the jet velocity is increased, totally different distribution of the mixture fraction is obtained. The results indicate that the dyed jet crosses to the side of the undyed jet. This is evident from the plots of mixture fraction in Figure 6b, 7b, and 8b,c, where the mixture fraction increases from left to right. Because of the turbulent nature of the flow, there is always some liquid from one jet which transmits to the other side. Therefore, we have not been able to find the limiting concentrations, i.e., zero and one, at the two extremum.

The observation that at low jet velocities, the two jets basically bounce off of each other after impingement, however, at high jet velocities they cross through each other, can be explained by dividing the mixing process into two different regions: Mixing in the liquid sheet, i.e., pre-atomization zone; and mixing in the spray region, i.e., post-atomization zone.

If two liquid jets with equal diameters collide head-on, and the liquid in each stream is 'completely' deflected, two jets will not cross and a bouncing or 'reflecting type' atomization is obtained. A schematic representation of such impingement is shown in Fig. 11a. The mixing is then governed by the turbulent dispersion in the spray zone. (The micromixing in the liquid sheet is relatively small.) One explanation of the observed stream crossing may be as follow. As the jet velocity increases, the sheet breaks up in a shorter distance from the impingement point and streams do not deflect completely. Therefore, one can assume a sheet with converging mean velocities, rather than parallel ones for the complete deflection. Figure. 11b shows a schematic of this process. After atomization, the trajectory of each drop will be governed by the trajectory of the stream which has contributed the most to the liquid in that drop. Therefore, shortly after atomization, the drops segregate, and it appears that the two jets cross each other.

The above explanation of the mixing process is based on a head-on impingement of two jets. However, due to the turbulent nature of the streams, head-on impingement hardly ever occurs in a continuous fashion. In order to achieve proper atomization (relatively small drop sizes), the jets should have high velocities and turbulent conditions. Turbulent liquid jets have a very unique characteristics. They develop a helical disturbances due to the form drag, the amplitude of which is entirely a function of the relative velocity between the jet and the surrounding gas. Such helical disturbances have also been reported by the experiments of Hoyt and Taylor (1977) and predicted by the analytical studies of Batchelor and Gill (1962). The helical characteristics of the streams cause that the two jet do not collide head-on. Therefore, at the collision point part of the liquid of each stream which is not interacting with the other stream tends to follow its own initial trajectory. The consequence of this process is a stretching and oscillation of the liquid sheet shown in Fig. 4. Figure 5b shows the region of interaction between two jets when the collision is not head-on. The parameter which governs the extent of this interaction is the amplitude of the helical disturbances at the time of impingement.

The above description of the impinging jets, explain the experimental observations. Our results show that increasing the jet velocity and/or the impingement angle, enhances the liquid crossing. Since the region of each stream which does not interact with the opposing stream is assumed to be responsible for the crossing of the two stream, all the parameters which increase the horizontal component of the kinetic energy of this region (component perpendicular to the direction of the resultant velocity vector of the two stream) control the crossing process: $\frac{\pi}{8}\rho_l V_j^3 D_j^2 \sin(\alpha/2)$.

Both the reflective and crossing types of impingements result in poor mixing, however, in the former the liquid from each stream stays on the its own side, yet in the latter it crosses to the other side. Therefore, at certain jet velocity optimum mixing can occur. In other words the curves of mixing should show a maximum with jet velocity. However, at low jet velocities the spray dispersion in the plane of the jets (x -axis) was small and the resolution of our Patternator was not sufficient to capture small variations in the jet velocity. Therefore, the results of the reflective type impingement are not at sufficiently small velocities, and they are already close to the optimum mixing condition as shown in Fig. 6a. Any increase from this condition reduces the mixing extent. Generally, higher jet velocities were needed for smaller jet diameters in order to obtain large enough dispersion in the plane of the jets for accurate measurement of the mixing.

Since almost all of the previous work on the mixing in the impinging jets have been conducted by using immiscible liquids, we have performed one experiment with such liquids as well, in order to confirm the general nature of the mixing characteristics described above. The results of these experiments are shown in Fig. 9. Two immiscible liquids, one water and one kerosene, RP-1, are used. The ratio of the volumes of each liquid in a test tube represents the local mixture fraction. Similar results to the miscible jet impingements are observed: At low jet velocities, the two jets bounce with minimum mixing as shown in Fig. 9a. Here, the jet on the left is RP-1 and the one on the right is water. As the jet velocity is increased the two jets cross each other, and a transmission type mixing process is observed (see Fig. 9b).

The effect of increasing the impingement angle on the mixing is shown in Fig. 10. An increase in the impingement angle from 60° to 90° enhances the transmission, and the extent of mixing reduces. Rupe (1953) had explained this effect by noting that higher impingement angles result in a higher impact-induced

turbulence and, therefore, higher turbulence mixing. On the other hand, higher impingement angles will result in smaller contact time between the liquids of the two streams. However, our results indicate that it is the higher momentum which enhance the stream crossing and results in poor mixing. As the impingement angle increases the component of the momentum in the horizontal direction increases, increasing the liquid crossing.

Plots mixing extent E_m with the jet velocity, given in Fig. 12, show that the mixing reduces with the velocity. There is one data point for $D_j = 508\mu m$ which indicates that increase in V_j increases E_m . However, similar measurements closer to the injector (upstream) show that E_m decreases with increasing V_j . This result indicates that the mixing in the post-atomization region plays a significant role in the extent of mixing. Similar results are observed for a jet with $D_j = 711\mu m$.

The enhancement of mixing in the post-atomization region is better realized by plotting the variation of E_m along the spray axis z , as shown in Fig. 13. In all the cases, except one, E_m increases downstream of the impingement point. If the jets are significantly segregated, by either crossing or reflecting type impingement, the segregation increases downstream of the spray. The turbulent dispersion may not be significant enough to compensate for this segregation and overall extent of mixing, E_m reduces. This effect is shown for the jet with $D_j = 508\mu m$ and $V_j = 13m/sec$. In the post-atomization region, the turbulent dispersion controls the mixing of the two streams. Therefore, a mixing layer is developed in the central region of the spray, which grows along the spray axis. This explains the observed improvement of the mixing downstream of the impingement point. A schematic of the enhancement of mixing in the post-atomization region is shown in Fig. 11c by representing the mixture fraction with colored drops.

5. Concluding Remarks

The mixing process in impinging jet atomizers is controlled by different processes in the pre-atomization and post-atomization regions. In the pre-atomization region upon impingement, two liquid jets may reflect or cross-through each other. The former type occurs at low jet velocities with steady and smooth surfaces. As the jet velocity increases, the jet becomes non-smooth and develops helical disturbances on its surface. Since at the impingement point the helical disturbances of each stream are not in phase, part of each stream does not interact with the other. The uninteracted part of the stream tends to stretch the liquid to the other side of the impingement plane, which after atomization, it appears that the streams have crossed through each other. The degree of stream crossing increases with the jet diameter, jet velocity, and the impingement angle. The jet velocity increases both the amplitude of the helical disturbance and the kinetic energy of the uninteracted region; the jet diameter and the impingement angle increase the component of the kinetic energy normal to the plane of the liquid sheet. In the post-atomization region the turbulent dispersion develops a mixing layer along the axis of the spray which enhances the mixing. The overall results can be expressed in terms of the extent of mixing which decreases with increasing the jet velocity and increasing the jet diameter, and it increases along the spray axis.

Acknowledgment: This work was completed during the author's tenure at the Phillips Laboratory, Edwards Airforce Base. I am indebted to Dr. D. Talley for inviting me to the laboratory and supporting me through

out the course of this research, Mr. W. Brocklehurts for taking the experimental measurements, Mr. T. Christensen in building the experimental set up, and finally Dr. J. Levin, without whom this work would have not been completed.

6. References

- Anderson, W.E., Ryan, H.M., Pai, S., and Santoro, R.J., "Fundamental studies of Impinging Liquid Jets," AIAA Paper No. 92-0458, 1992.
- Elverum, Jr., G.W., and Morey, T.F., "Criteria for Optimum Mixture-Ratio Distribution Using Several Types of Impinging-Stream Injector Elements," Jet Propulsion Laboratory, Memorandum No. 30-5, 1959.
- Foster, H.H., and Heidmann, M.F., "Spatial Characteristics of Water Spray Formed by Two Impinging Jets at Several Jet Velocities in Quiescent Air", NASA Tech Note D-301, July 1962.
- Hautman, D.J., "Spray Characterization of Like-on-Like Doublet Impinging Rocket Injectors", AIAA 29th Aerospace Sciences Meeting, Reno NV. Jan 7-10, 1991, pp. 1-8, AIAA Paper 91-0687
- Heidmann, M.F., Priem, R.J., and Humphrey, J.C., "A Study of Sprays Formed by Two Impinging Jets", NACA Tech Note 3835, March 1957.
- Heidmann, M.F., and Humphrey, J.C., "Fluctuations in a Spray Formed by two Impinging Jets", NACA Tech Note 2349, April 1951.
- Heidmann, M.F., and Foster, H.H., "Effect of Impingement Angle on Drop-Size Distribution and Spray Pattern of Two Impinging Water Jets", NASA Tech Note D- 872, July 1961.
- Hoehn, F., and Rupe, J., "Flow Cavitation Effects on the Mixing Characteristics of Bipropellant Doublets," 8th JANNAF Combustion Meeting, CPIA Pub. 220, Nov. 1971, Vo. 1, pp. 569-582.
- Hoyt, J.W., and J.J. Taylor, "Waves on Water Jets," *J. Fluid Mech.* vol. 83, paper 1, pp. 119-127, 1977.
- Rupe, J.H.. "The Liquid-Phase Mixing of a Pair of Impinging Streams," Progress Report No. 20-195, Jet Propulsion Laboratory, Pasadena, Calif., Aug. 6, 1953.
- Rupe, J.H., "A Corelation Between the Dynamic Properties of a Pair of Impinging Streams and the Uniformity of Mixture-Ratio Distribution in the Resulting Spray," Progress Report No. 20-209, Jet Propulsion Laboratory, Pasadena, Calif., Mar. 28, 1956.
- Taylor, G., "Formation of thin flat sheets of water," Vassallo, P., Ashgriz N., and Boorady, F.A., "Effect of Flow Rate on the Spray Characteristics of Impinging Water Jets", AIAA Journal of Propulsion and Power, Vol. 8, No. 5, Sept-Oct, 1992.

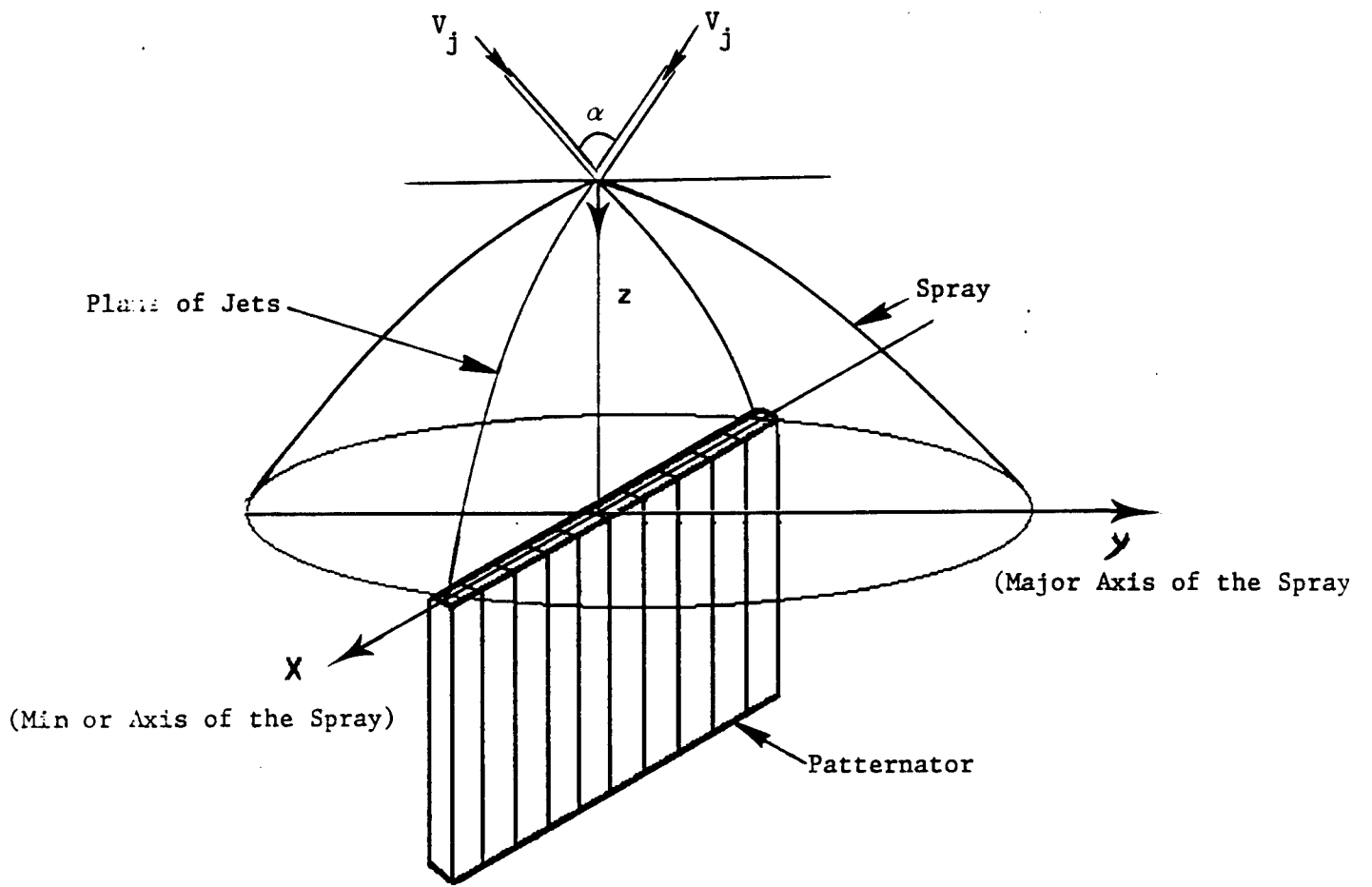
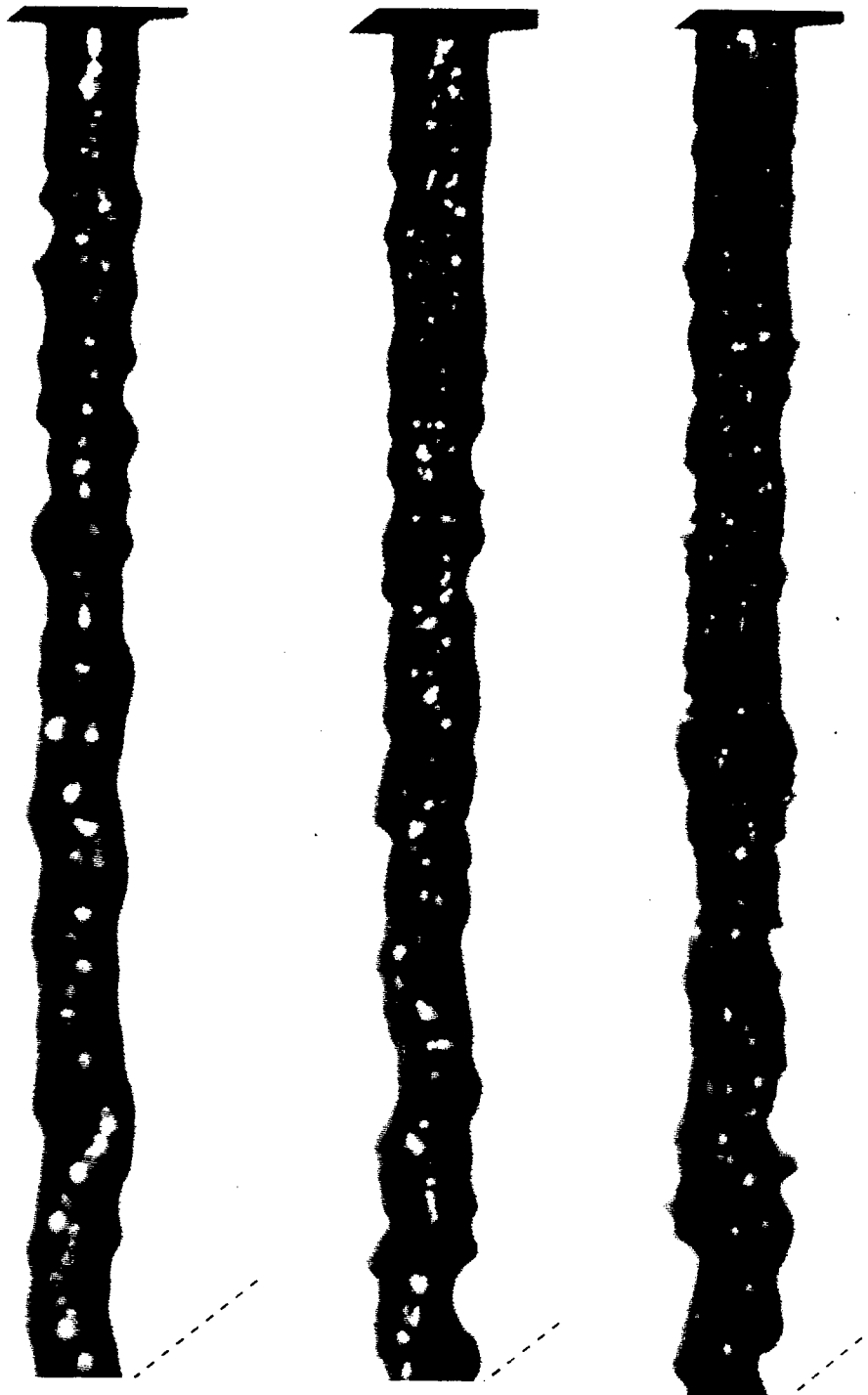


Figure 1: Schematic of the Linear Patterning Setup.



$V_j = 8 \text{ m/s}$	13.5 m/s	20 m/s
$Re = 5690$	9601	14224
$we = 615$	1752	3844
(a)	(b)	(c)

Figure 2: Closeup images of a stream with $D_j = 711 \mu\text{m}$ and for three different jet velocities.

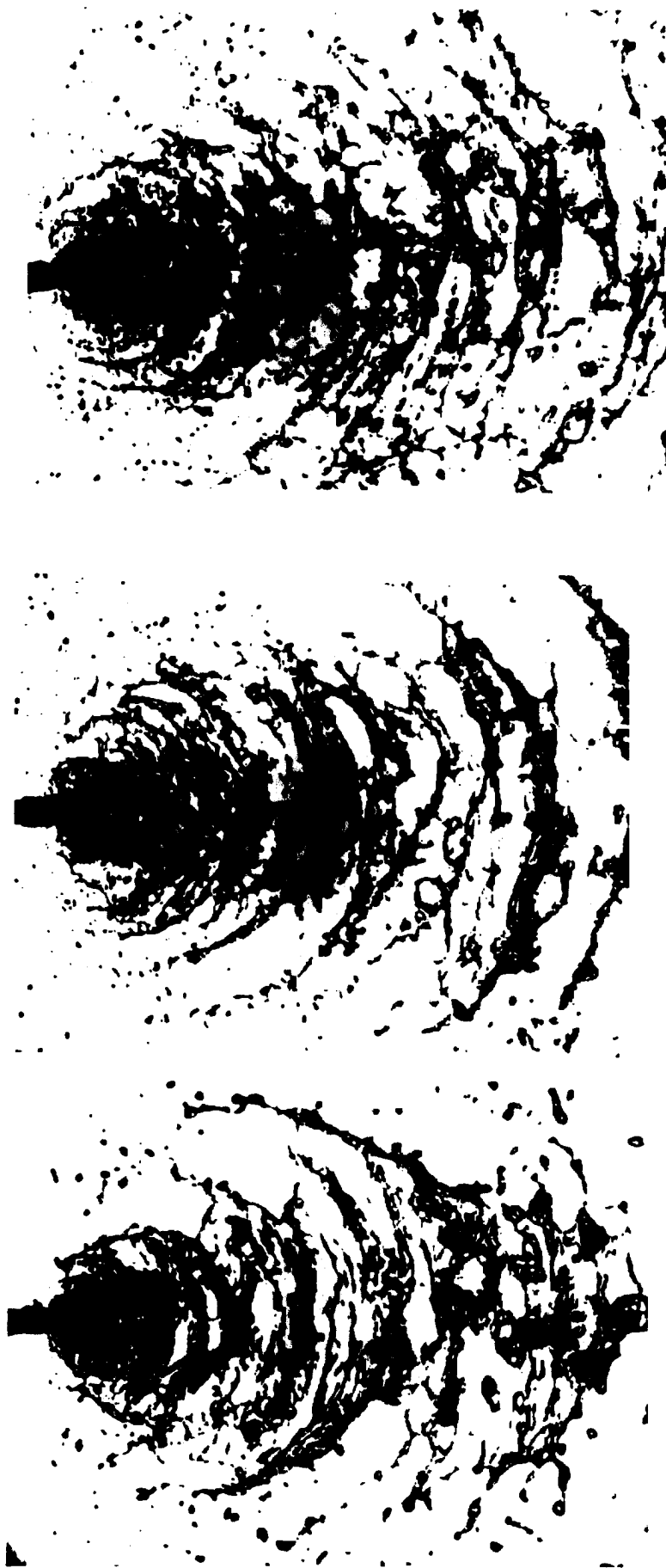
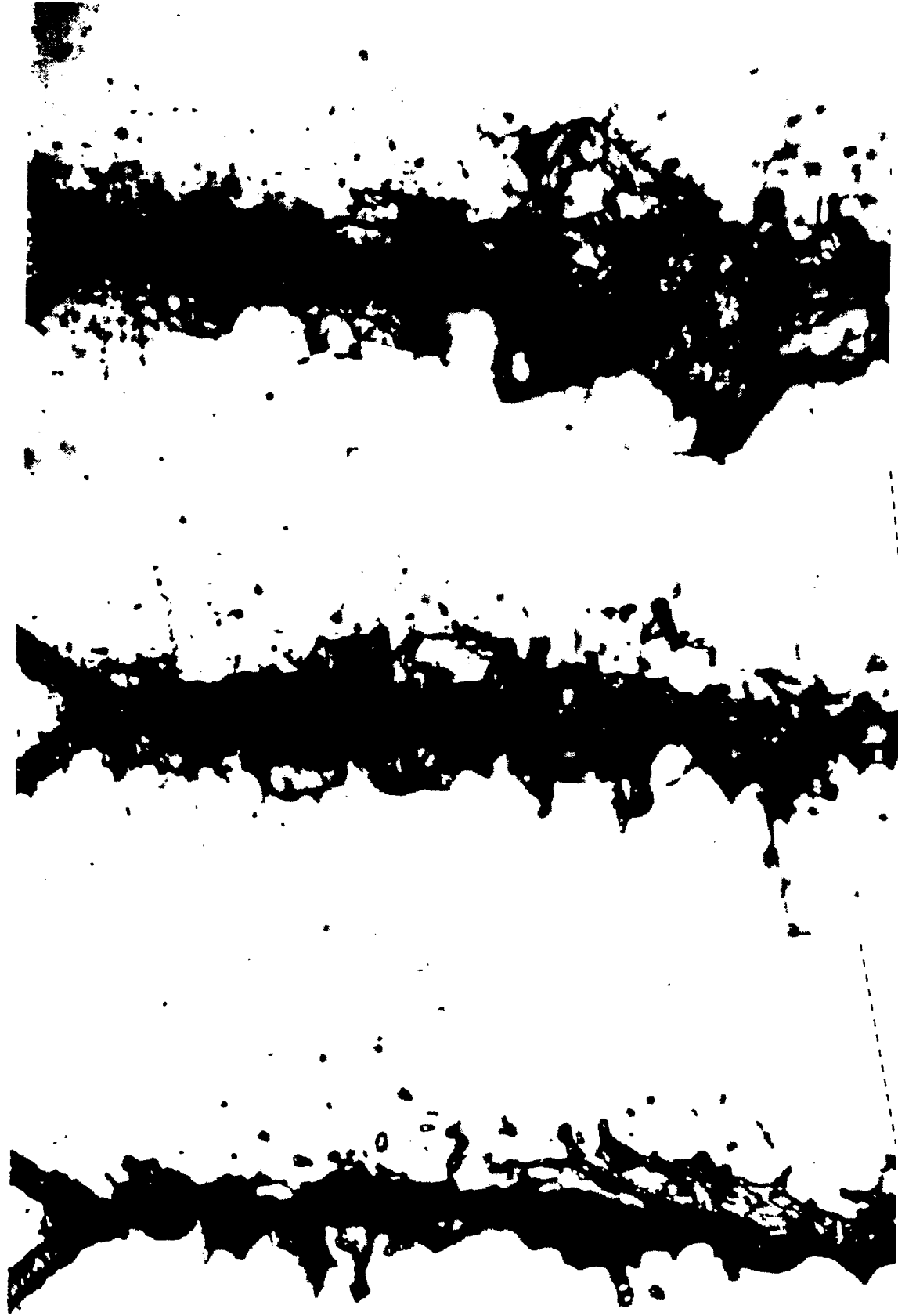


Figure 3.: Atomization of an impinging doublet with
 $D_j = 711 \mu\text{m}$, $\alpha = 60^\circ$

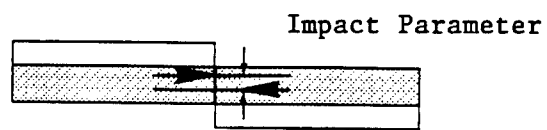


(a) $V_j = 8$ m/s

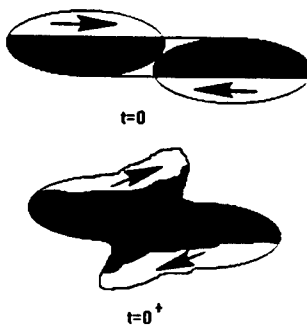
(b) $V_j = 13.5$ m/s

(c) $V_j = 20$ m/s

Figure 4: Atomization of an impinging doublet with $D_j = 711 \mu\text{m}$, $\alpha = 60^\circ$ and for three jet velocities.



(a) Top View of the Impingement Point.



(b) Cross-sectional view of the jets shortly after impingement.

Figure 5: Off Head-on impingement of two jets.

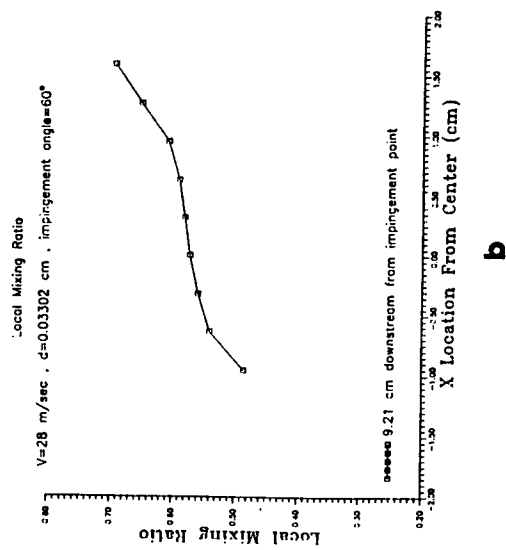
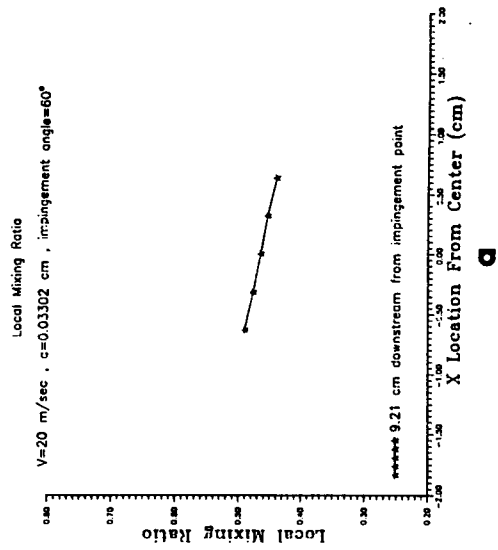


Figure 6

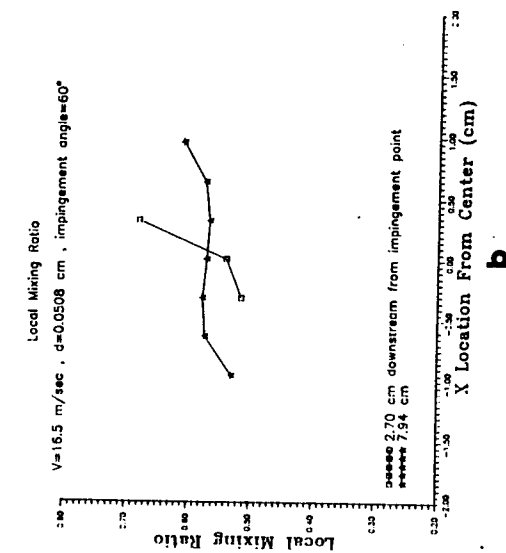
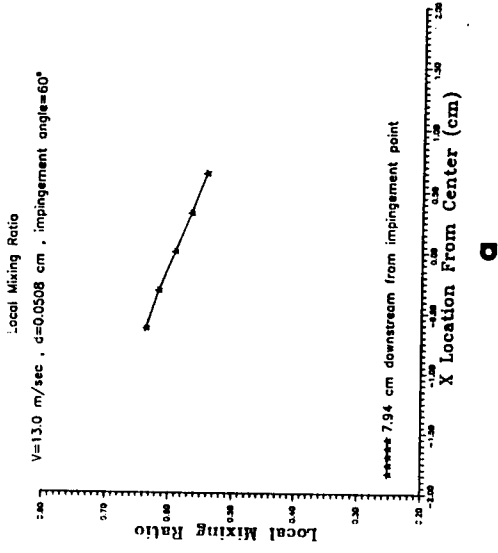


Figure 7

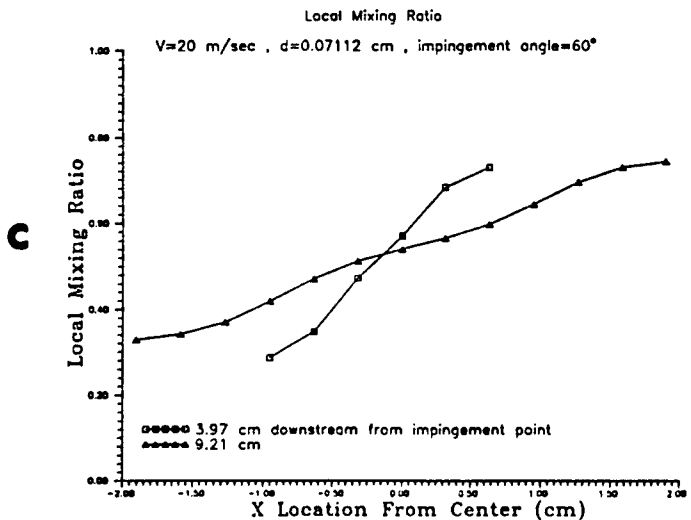
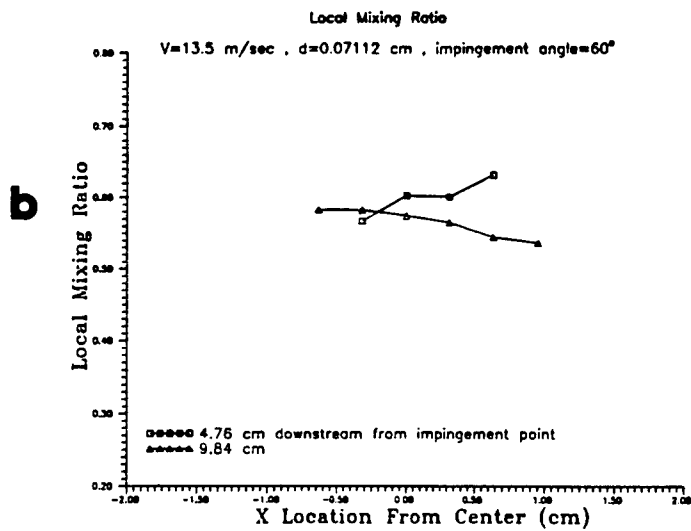
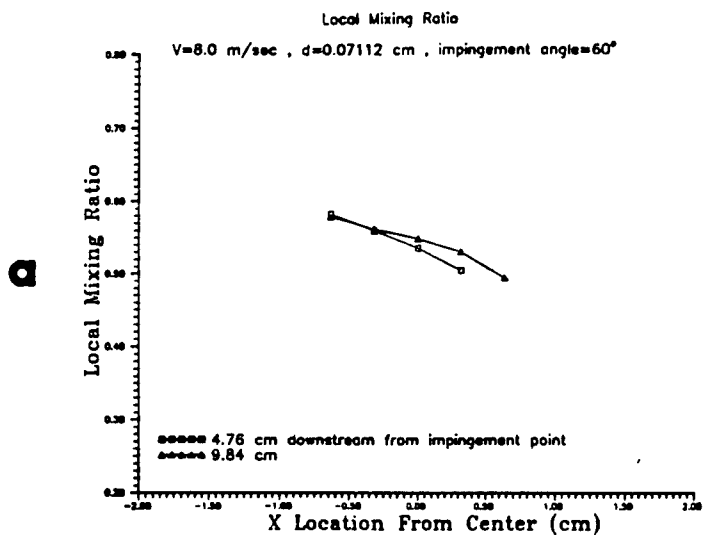


Figure 8

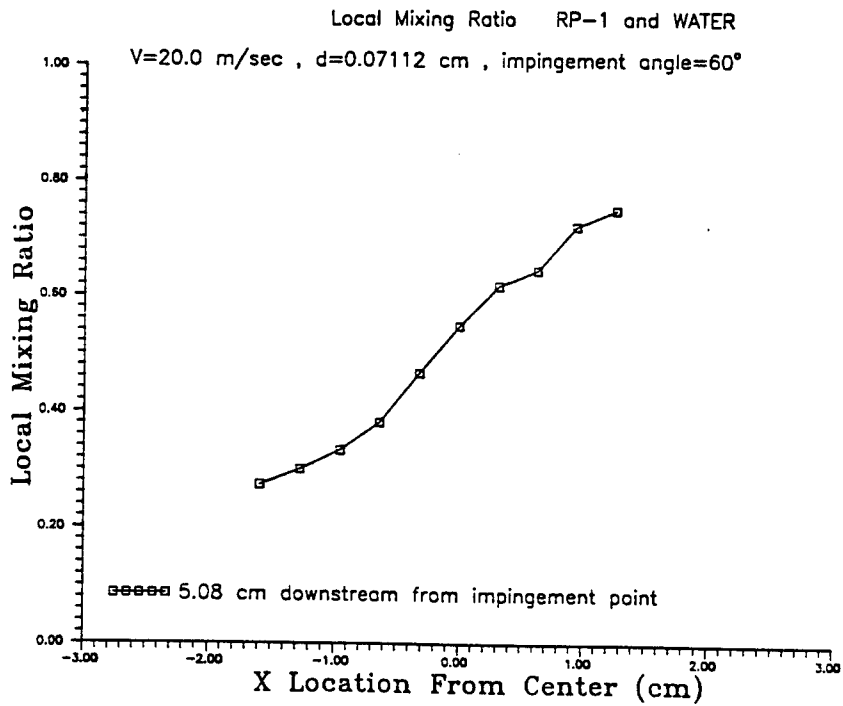
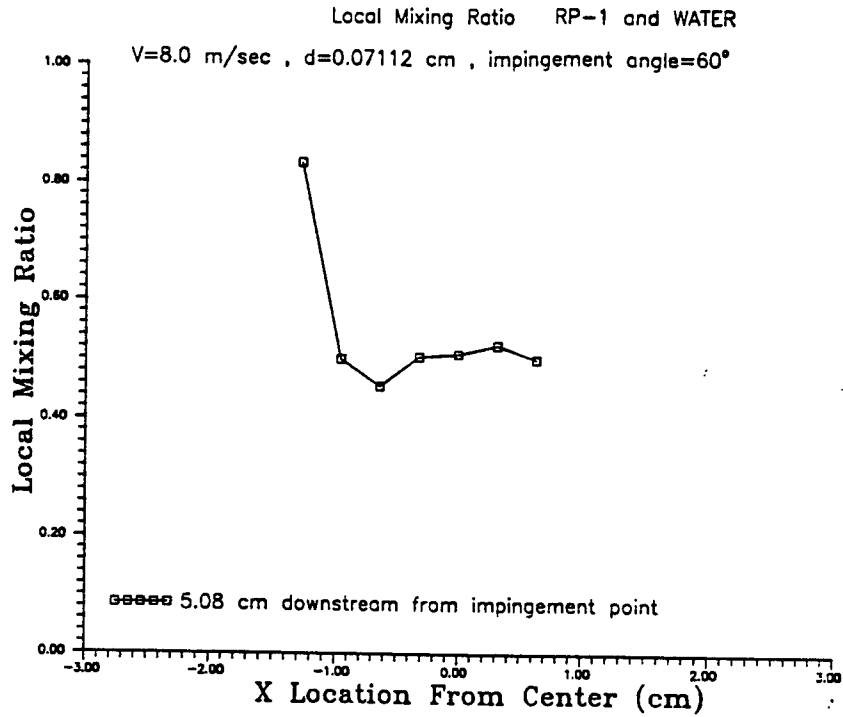


Figure 9

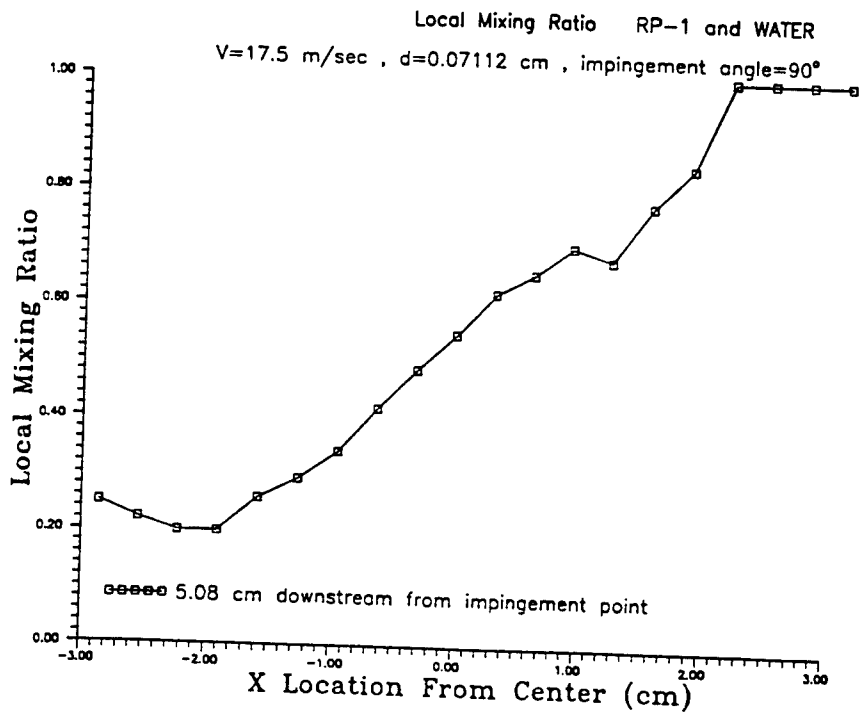
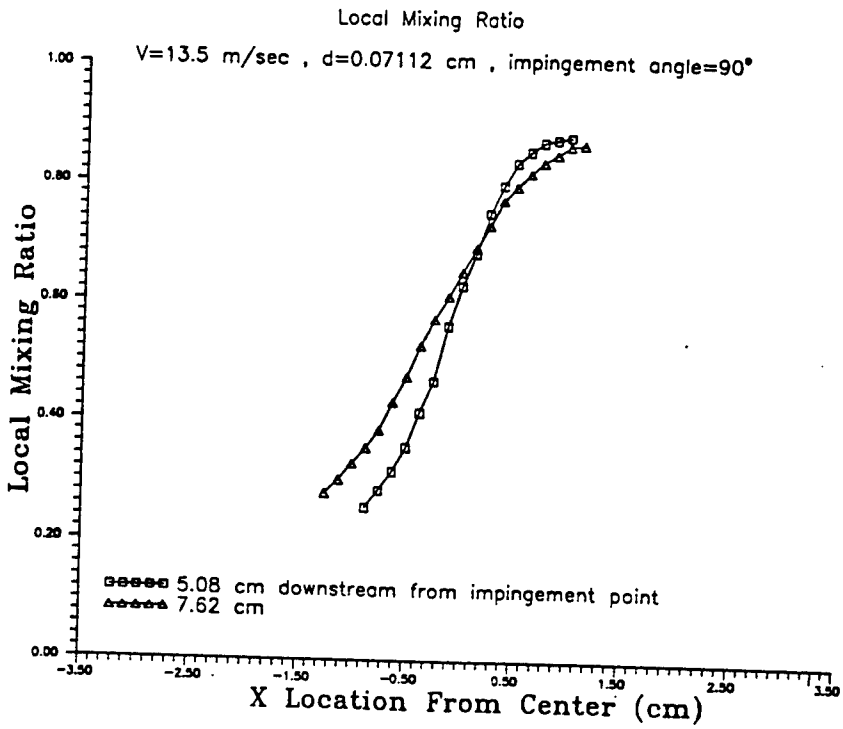
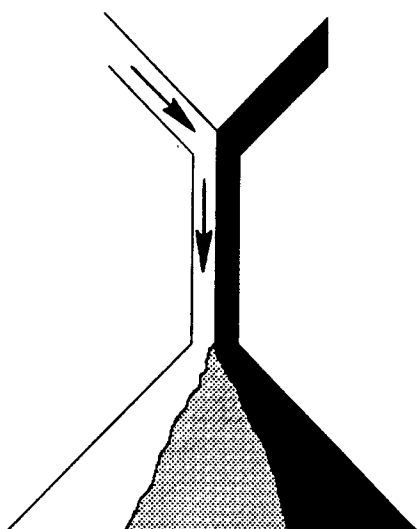
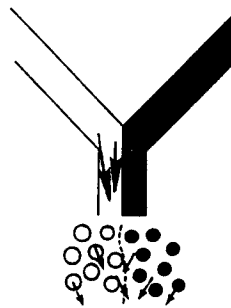


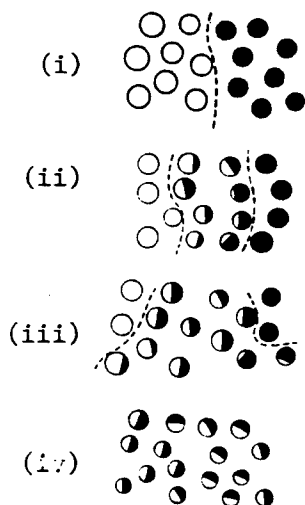
Figure 10



(a) Reflective Impingement



(b) Transmitting Impingement



(c) Mixing by Turbulent Dispersion.

Figure 11: Schematic of mixing in Pre-atomization and Post-atomization Regions.

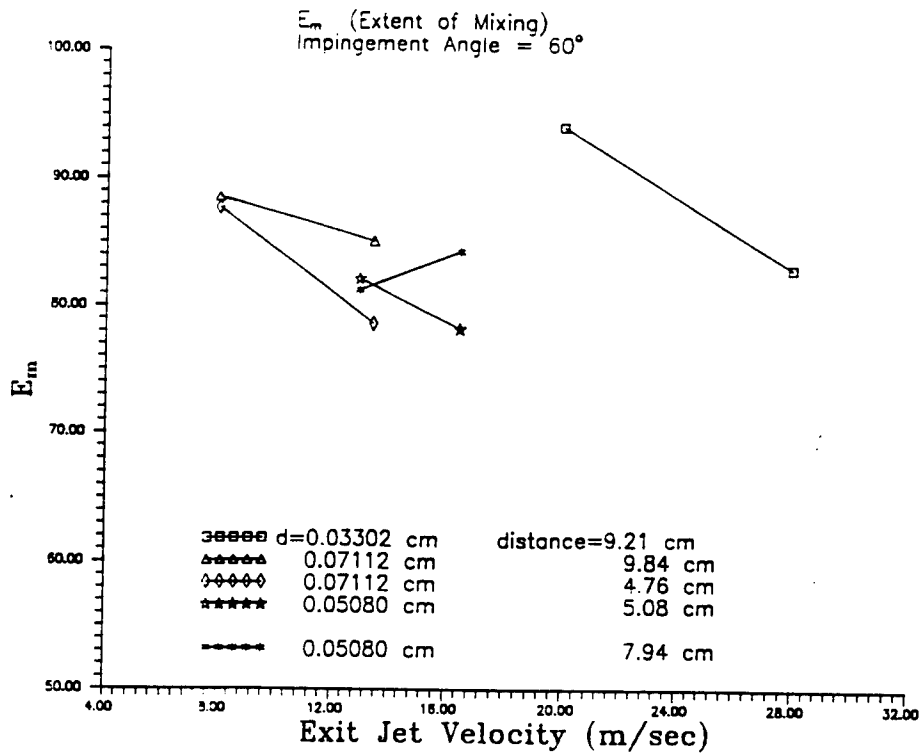


Figure 12

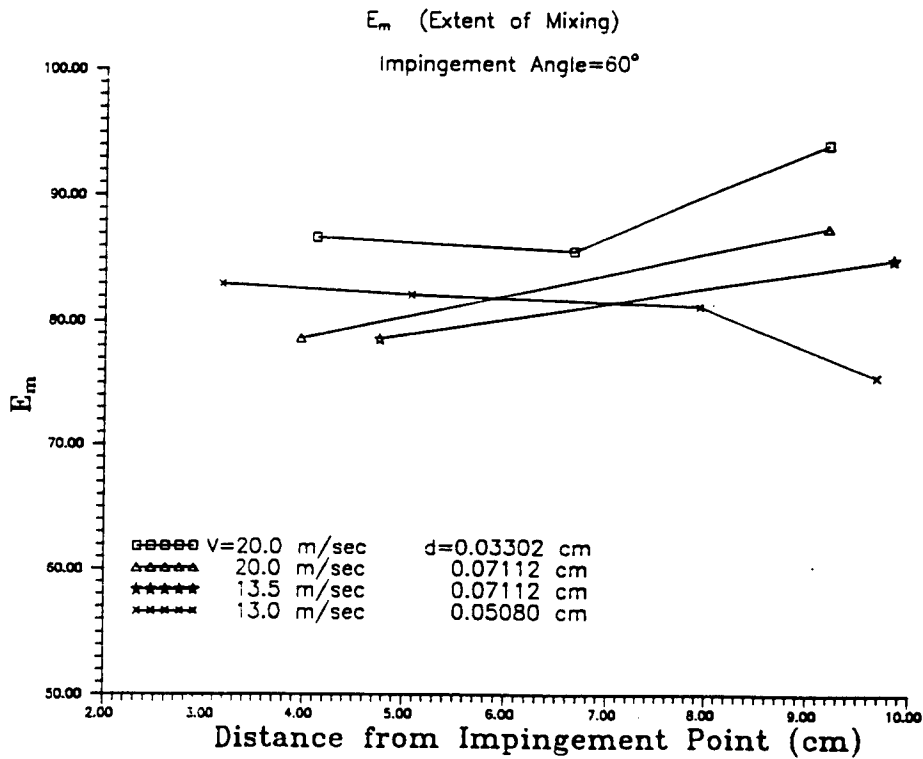


Figure 13

RADIATION CHARACTERIZATION OF COMMERCIALY PROCESSED
1.2 MICRON CMOS DEVICES

Raymond D. Bellem
Associate Professor
Department of Electrical Engineering

Embry-Riddle Aeronautical University
3200 Willow Creek Rd.
Prescott, AZ 86301

Final Report for;
Summer Faculty Research Program
Phillips Laboratory

Sponsored by:
Air Force Office of Scientific Research
Bolling Air Force Base, Washington, D.C.

and

Phillips Laboratory

September 1994

RADIATION CHARACTERIZATION OF COMMERCIALY PROCESSED 1.2 MICRON CMOS DEVICES

Raymond D. Bellem
Associate Professor
Department of Electrical Engineering
Embry-Riddle Aeronautical University

Abstract

This paper describes a program to study the effects of ionizing radiation on integrated circuits which were fabricated using standard commercial Complementary Metal Oxide Semiconductor (CMOS) processing steps. A test chip was designed using a hardened circuit design methodology which yield radiation tolerant IC's when using a standard commercial CMOS fabrication process such as resident in a facility such as a MOSIS IC foundry. Several CMOS test circuits and a variety of P and N-channel MOS devices were irradiated up to dose levels of 300krad(SiO₂) at a dose rate of 100 rad/sec in accordance with MIL-STD-883D, Test Method 1019.4 and ASTM F-1467. A 10keV mean energy X-ray source was used to provide an ionizing radiation environment. Radiation test data is presented on the three circuits - a 21 gate delay chain, an XROM sense amplifier and a 4-bit shift register. All test circuits operate effectively through 100krads and show less than 20% degradation after 300krads. Reentrant (annular) structures show very little threshold shift or leakage current after 300krads. Edge transistors show little threshold shift at 100krads with increasing shifts up to 0.3 volts at 300krads with leakage currents increasing several orders of magnitude up to 1 nanoamp. Field oxide devices show significant leakage current after 100krads and are the limiting factors in applying commercial processes to radiation tolerant IC's.

RADIATION CHARACTERIZATION OF COMMERCIALY PROCESSED

1.2 MICRON CMOS DEVICES

R.D. Bellem

INTRODUCTION

The use of commercial technologies in military systems has received a great deal of attention and evaluation by the DoD over the past several years. Budgetary constraints and technological requirements brought on by the changing threat and mission requirements of the military have led to a reevaluation of investments in mil spec equipments for many applications. This has led to R&D efforts within DoD to adapt semi-tolerant commercial and dual-use technologies wherever possible in military electronic systems. This approach will not only have tremendous cost advantages but will also draw upon the strengths of rapid advances in commercial electronic technologies, especially those experienced in integrated circuits.

The radiation hardening requirements on both space and missile systems has changed due to recent changes in the threat scenario and the strategic posture of the United States. Radiation tolerant integrated circuits however, continue to be a challenge for certain well-defined hostile environments such as the natural radiation environments of space. With advances in IC technologies has come an increased sensitivity to the space environment. This growing sensitivity of electronics to natural radiation is due to device and density scaling inherent in miniaturization, as well as radiation introduced during state-of-the-art integrated circuit processing steps. These factors are also becoming a major concern for commercial vendors of IC's as well. Therefore, radiation effects on electronics research has shifted from the arena of high total dose and high dose rates to low dose rates, moderate total dose and single event effects.

CMOS technology finds widespread application in military systems. Most signal and data processing functions along with memory are implemented using CMOS. The use of commercial CMOS circuits for application in military systems such as satellites is of great interest. The research being done in this effort looks at the effects of ionizing radiation on devices and circuits fabricated with a standard commercial CMOS process. The goal of this research is to determine the radiation tolerance of integrated circuits designed using a circuit design methodology while using standard IC CMOS fabrication techniques.

RADIATION EFFECTS IN THIN OXIDE MOS DEVICES

Ionizing Radiation Effects

The trend in commercial MOS devices is toward smaller line geometries and a proportional scaling of most device dimensions and processes. As devices become smaller, the gate oxide thickness becomes very-thin (<20nm). As the oxide thickness decreases, the amount of interface-trap and oxide-trap charge decreases with slightly less than a $(t_{ox})^2$ relationship. Thus, the total-dose hardness of commercial gate oxides should improve as the gate oxide thickness is decreased.

Field oxides of advanced commercial technologies may however be very soft to ionizing radiation. Field oxides are much thicker than gate oxides, ranging from 200nm to 1000nm. Unlike gate oxides, field oxides are produced using a wide variety of deposition techniques such as CVD. Thus, the trapping properties of a field oxide may be poorly controlled and can be considerably different than for a thermally grown gate oxide. As radiation induced oxide charge builds up in a field oxide, it causes the threshold voltage of the field oxide to tend to go toward depletion mode for field oxides over a p substrate (equivalent to an n-channel field oxide transistor). If the buildup of charge is large enough, excessive leakage current can flow from the source to drain of the gate-oxide transistors and between transistors. The field-oxide leakage significantly adds to the drain-to-source current at zero gate voltage. Thus, the field-oxide leakage prevents the transistor from being completely turned off. This will greatly add to the static supply leakage current of an IC. Field oxide leakage current limits the radiation hardness of most commercial integrated circuits and it is a major problem for advanced hardened technologies, both at high and low dose rates.

Single Event Effects

Single Event Effects have been getting increased attention in the commercial sector, especially with respect to Single Event Upset(SEU). High energy cosmic rays can cause bit upsets in memory devices or create latchup conditions which may result in permanent damage to an IC. Radioactive decay of impurities in the chip package material can also lead to SEU phenomena resulting in soft memory errors. Commercial non-hardened memories are not suitable for space applications due to the high upset rates and latchup conditions which occur. Special design precautions must be used before a commercial process can be used in memory chips destined for use in a high SEU environment.

TEST SAMPLES AND EXPERIMENTAL DETAILS

Test Samples

Parts used in this work were designed and developed under a Phillips Laboratory contract with the Mission Research Corp. in Albuquerque. Radiation tolerant design techniques were incorporated where possible without affecting the IC processing steps. The layout rules are for the standard MOSIS 1.2 micron MOSIS process. The Hewlett Packard facility in Corvallis, Oregon was used for fabrication. The test chip incorporates the building block devices and circuits which are representative of those found in a high speed signal processor. The chip can be used to study a variety of radiation environments: total dose ionizing; single event effects (SEE); high dose rate upset and latchup. This study will only look at total dose ionizing. The test structures selected, designed and fabricated on each chip are as follows:

- * 5-NMOS GOX (Gate Oxide) Transistors for total dose characterization.
- * 5-PMOS GOX Transistors for total dose characterization.
- * 4-NMOS & PMOS Reentrant (annular) Transistors for total dose characterization.
- * 3-NMOS FOX (Field Oxide) Transistors for total dose characterization.
- * 3-Photodiodes for photocurrent studies.
- * 2-PNPN Latchup paths with max. gain and max. gate resistance for latchup susceptibility evaluation.
- * 1-4-bit Shift register for SEU testing of register latches.
- * 2-Tristate buffers for dose rate evaluation.
- * 1-Sense amplifier for total dose and dose rate evaluation.
- * 1-Delay chain for total dose performance.

The HP MOSIS process uses a standard CMOS process with a thermal gate process and a LOCOS field oxidation process. The structure is an n-well process with a p-p+ epi starting material. The gate oxide (GOX) has a nominal thickness of 182 angstroms. The field oxide thickness is estimated to be 5-8000 angstroms. Both poly and Al gate processes were used. The metal interconnect pattern is two-level. Devices were bonded out in a 40 pin DIP. The lids were not sealed in order to allow radiation exposure and failure analysis. Anti-static handling techniques were strictly adhered to in order to prevent device damage due to static electricity.

Experimental Set-up

The devices were irradiated in a 10keV mean energy X-ray source. An illustration of the X-ray chamber and test set-up is shown in Figure 1.

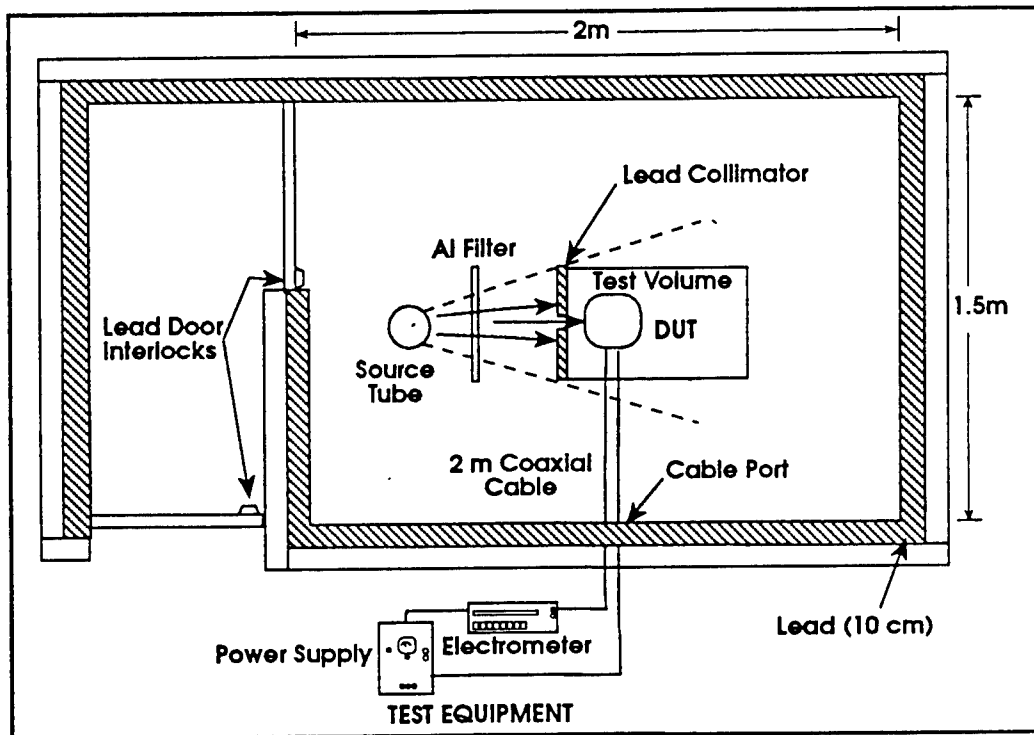


Figure 1. X-Ray Test Chamber with instrumentation

Dose rate was measured by a calibrated PIN diode detector to assure highly accurate dosimetry. Following irradiation, the devices were removed from the test chamber and electrically characterized. Standard subthreshold characteristics and drain characteristics were obtained on each device with a computer controlled HP 4145 Semiconductor Parameter Analyzer. Data is recorded on disc for further review and analysis. The three circuits, delay line, shift register and sense amplifier were then dynamically tested using an HP 85000. Clock frequency, timing and waveform patterns can be accurately measured up to 200 MHz with the HP 85000. Frequencies above 100 MHz are unlikely in these circuits. A random bit pattern generator is used to detect errors in the shift register as the clock frequency is increased. Delay time and low-high threshold voltage are measured for the sense amplifier. A measurement of the delay time of the delay line at moderate frequency clock is used for analysis.

RESULTS

Reentrant Transistors

The reentrant transistor is annular in structure with the drain at the center. The drain has dimensions of 5x5 microns. The gate width is approximately 3 microns. Two n-channel reentrant transistors were tested per the discussion above. Figures 2.1 and 2.2 are plots of the subthreshold characteristics of each device. The threshold voltage could be found from the subthreshold data using a simple computer program which also calculates the charge separation. The threshold voltage was measured as 0.55v with a threshold shift of only 0.03v at a dose of 100 krad(SiO₂). The post-rad leakage current for these devices is also observed to remain very low ($< 10^{-10}$ amps) at a gate voltage of zero volts.

N-Channel Gate Oxide (NGOX) Transistors

Two n-channel NGOX transistors were tested. The dimensions of the device measured $W = 18$ microns and $L = 1.2$ microns. Figures 3.1 and 3.2 are plots of the subthreshold characteristics of each device. The threshold voltage was measured at .585v with a threshold shift of 0.53v at a dose of 300 krad. The leakage current remained low ($< 10^{-10}$ amps) at 100 krad then increases to 10^{-9} amp at 300 krad at a gate voltage of zero volts.

N-Channel Field Oxide (NFOX) Transistors

Two n-channel NFOX transistors were tested per the discussion above. The dimensions of the devices were $W = 50$ microns and $L = 5$ microns. Figures 4.1 and 4.2 show the subthreshold characteristics of each device. The threshold voltage is rather meaningless in the case of the NFOX devices. The threshold voltage is < 40 v in both cases. The leakage currents however are very important for the NFOX. At a gate voltage of 5volts, the leakage is approximately 10^{-10} amp at 100 krad. At 300 krad, the leakage is $> 10^{-9}$ amps which would be intolerable in most IC's.

P-Channel Gate Oxide (PGOX) Transistors

Two p-channel PGOX transistors were tested. The dimensions of these devices were $W = 18$ microns and $L = 1.2$ microns. Figures 5.1 and 5.2 are plots of the subthreshold voltage. The threshold voltage measured was -1.69 volts with a shift of -0.67 volts at 300 krad. The leakage currents remained low ($> 10^{-10}$) at 300 krad at a gate voltage of zero volts.

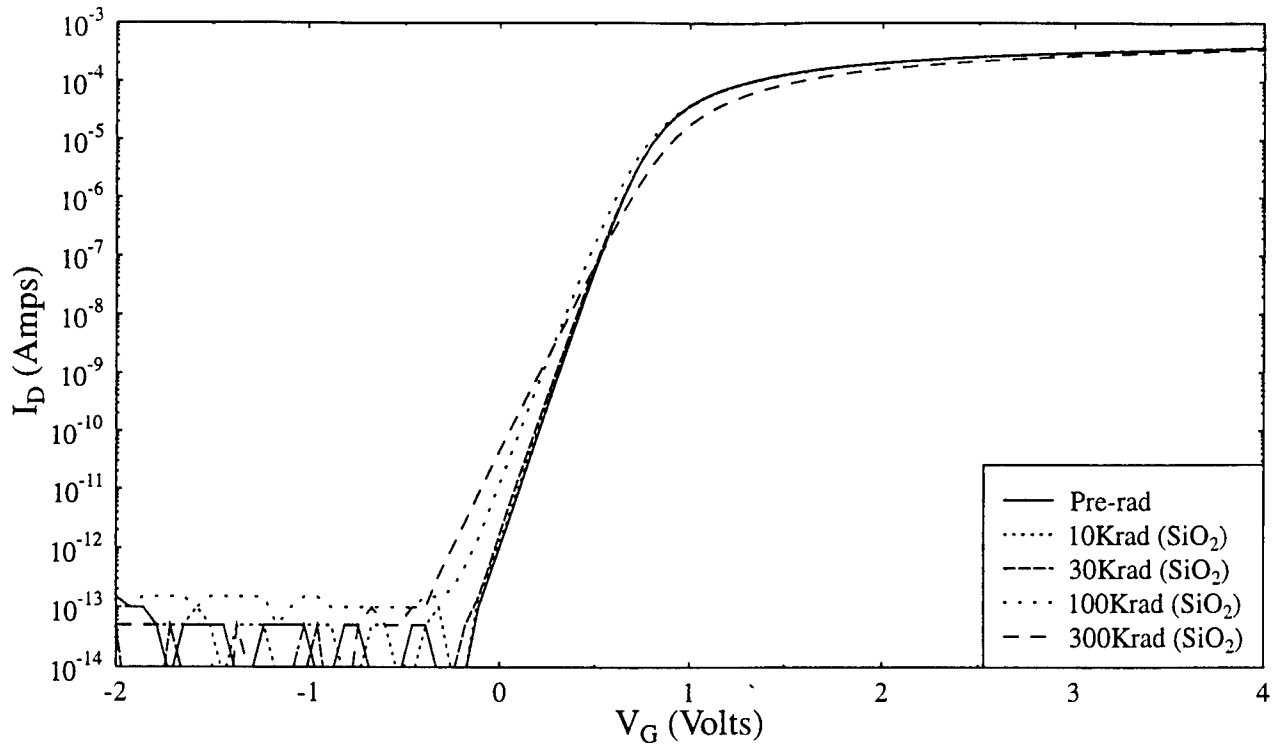


Figure 2.1: Subthreshold Characteristics for Reent 1-3 Following Ionizing Radiation Exposure

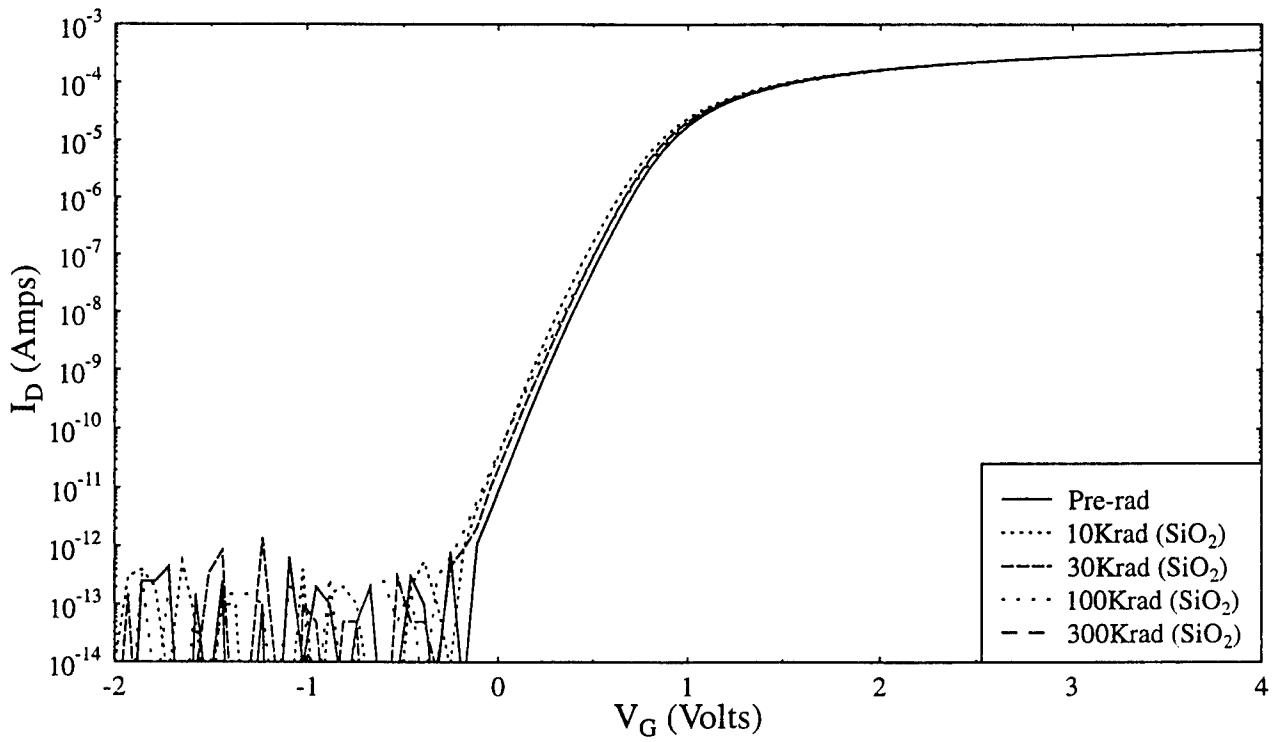


Figure 2.2: Subthreshold Characteristics for Reent 2-3 Following Ionizing Radiation Exposure

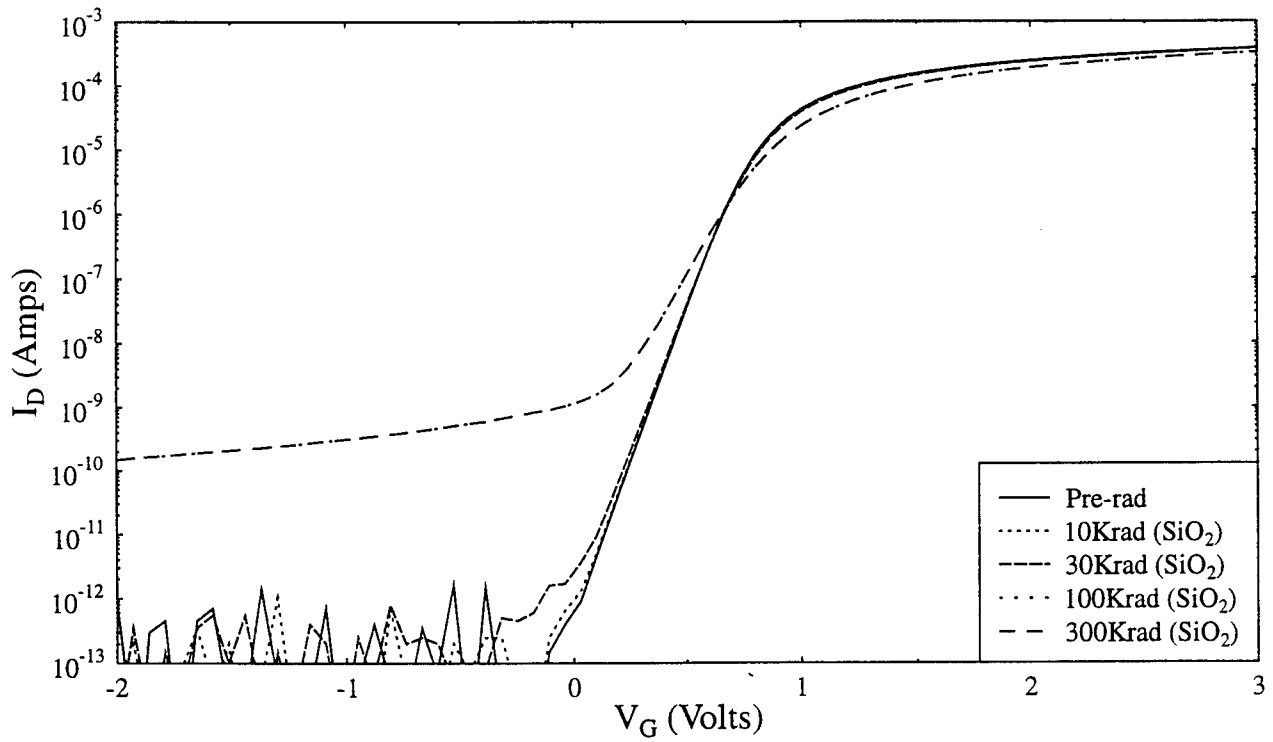


Figure 3.1: Subthreshold Characteristics for NGOX 1-3 Following Ionizing Radiation Exposure

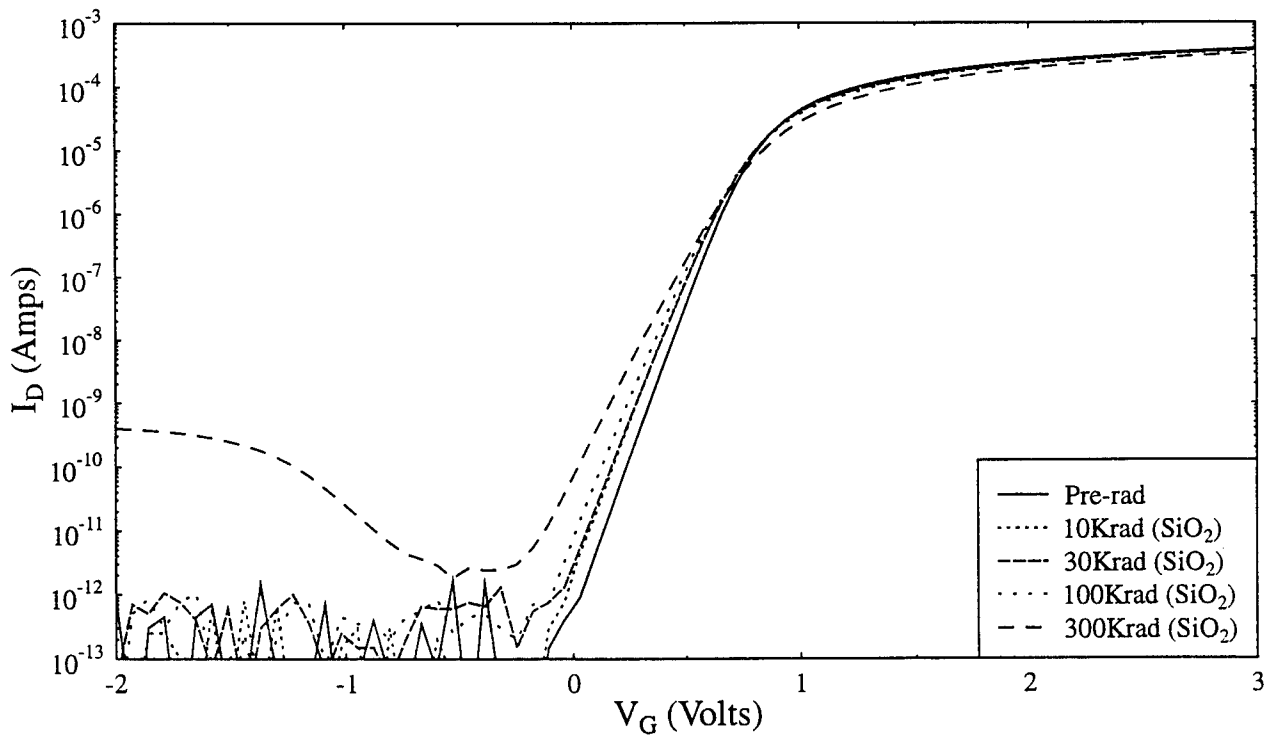


Figure 3.2: Subthreshold Characteristics for NGOX 3-3 Following Ionizing Radiation Exposure

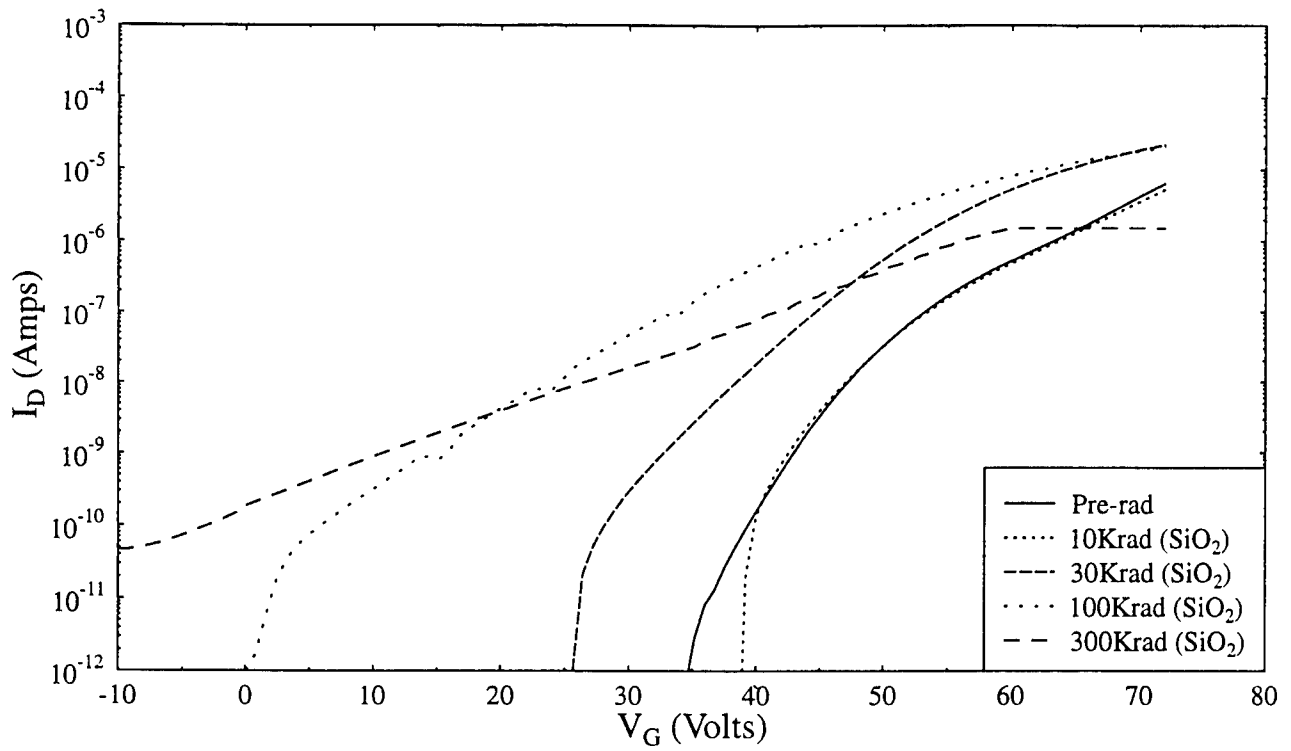


Figure 4.1: Subthreshold Characteristics for NFOX 1-3 Following Ionizing Radiation Exposure

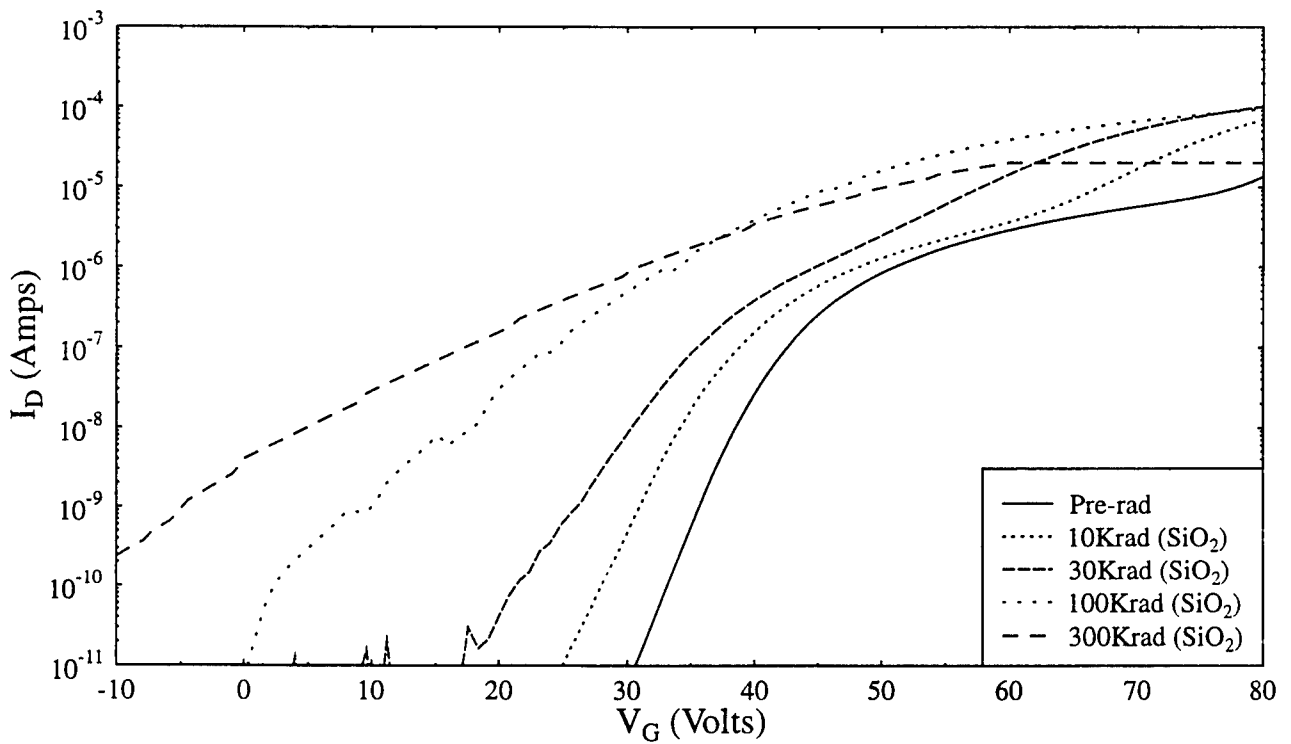


Figure 4.2: Subthreshold Characteristics for NFOX 4-3 Following Ionizing Radiation Exposure

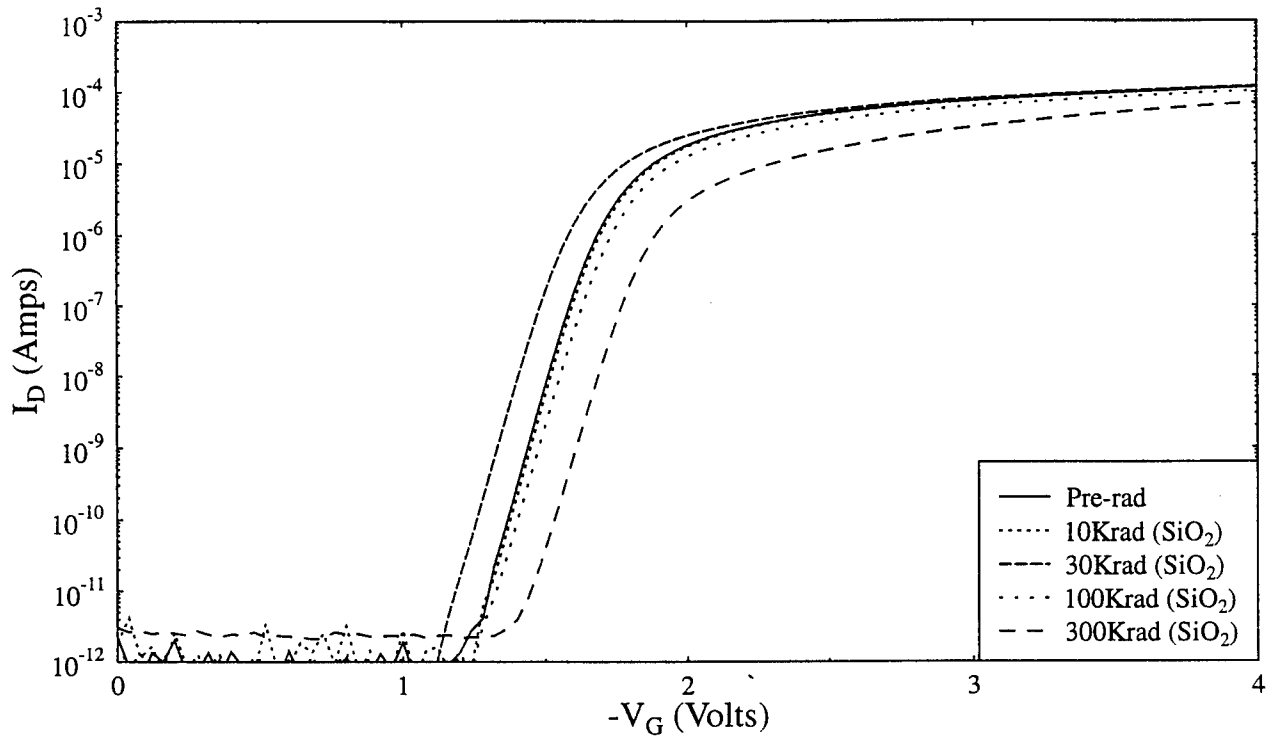


Figure 5.1: Subthreshold Characteristics for PGOX 2-3 Following Ionizing Radiation Exposure

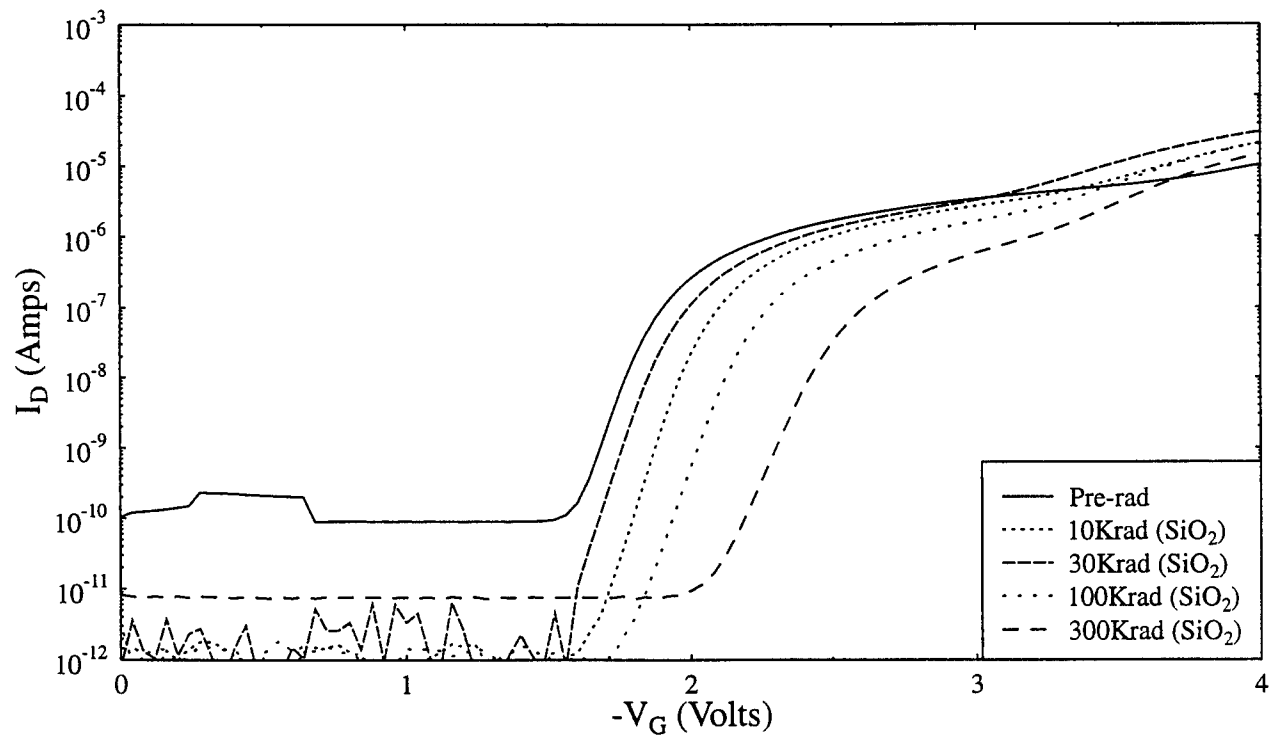


Figure 5.2: Subthreshold Characteristics for PGOX 4-3 Following Ionizing Radiation Exposure

Shift Register

The four bit shift register was designed such that serial shifting is possible with a single two phase clock. Two inverters were added to the circuit to get the two clock pulses. The input to the shift register has diode protection and the output is buffered with a pad driver cell. The shift register was characterized using the HP 85000 network analyzer. A random bit pattern was generated by the HP85000 and the failure conditions defined as the frequency at which errors began to appear in any one of the bit patterns. A scope trace showing the operation of the shift register is shown in Figure 6. Testing of the shift register was performed after each radiation exposure. The shift register operates at 110 MHz at pre-rad with no degradation appearing after 30krad. Errors began appearing after 100krad at 90 MHz with further degradation to 70 MHz after 300 krad.

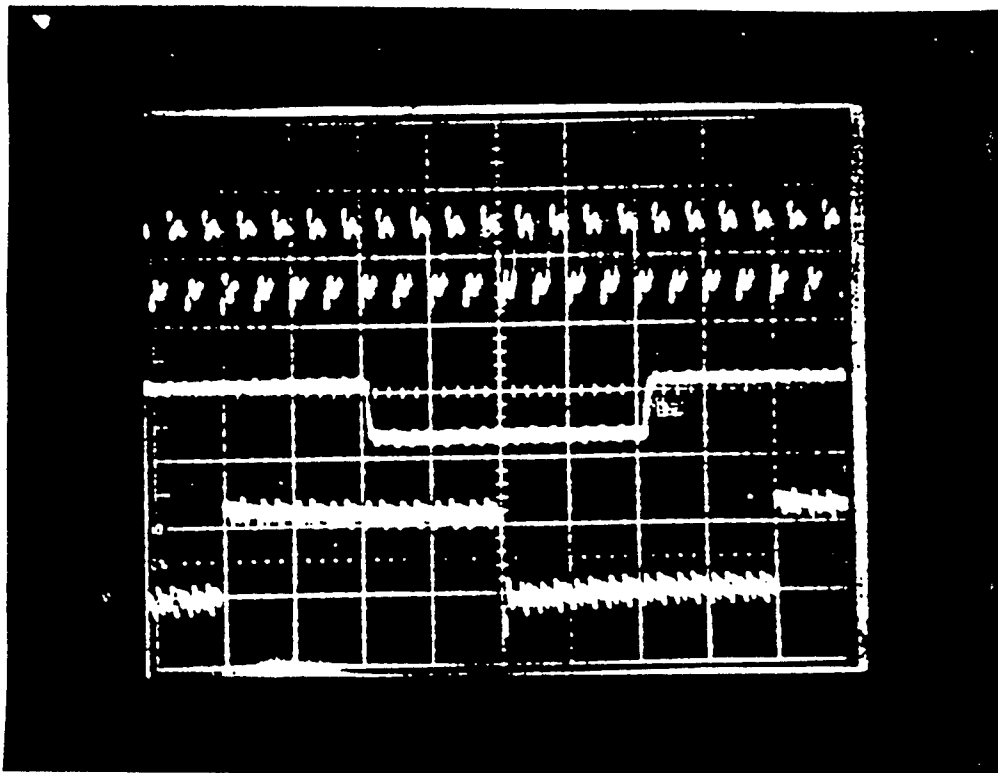


Figure 6. Shift Register Performance (5 volts/div, 500 nsec/div)

Delay Chain

The delay chain consists of 21 3-input NOR gates each constructed with n and p type reentrant transistors. The delay output signal is the result of gating the chain input with the chain output to create a pulse which has a width equal to the chains delay and is not dependent on delays induced in any other associated circuitry. A high to low transition on the input initiates a delay pulse at the output. The delay chain was characterized using the HP 85000. Delays were measured with supply voltage varied from 4.5 to 5.5v. The prerad delay was measured at 14.6 nsec. with $V_{dd} = 5v$. The gate delay shows little change after 30 krad then increases to 17.3 nsec after 300 krad. A typical Shmoo Plot of the 85000 output shows gate delay vs. V_{dd} is shown in Figure 7.

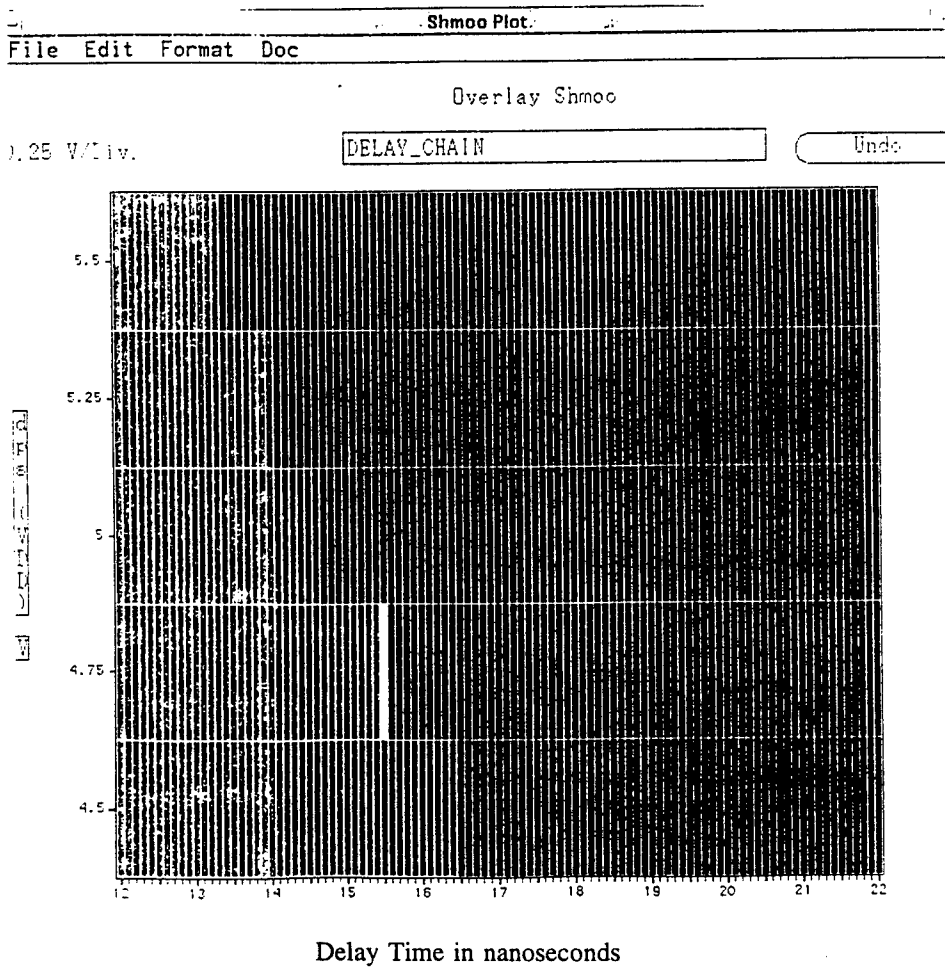


Figure 7. Shmoo Plot For Delay Chain

Sense Amplifier

The XROM Sense Amplifier was characterized using the HP 85000. An input pulse with a 20 nanosecond pulse width and a 0 - 5 volt rise time of 3.5 nanoseconds was used to measure the low-to-high trigger voltage of the sense amplifier. Figure 8 shows a Shmoo Plot of the sense amplifier output voltage vs. delay time for the input pulse trigger described above. The light colored area represents a high output on the sense amp while the dark area is low. The sense amplifier should transition at an input level of 2.5 volts. Measurements show the sense amp triggering between 2.5 and 2.7 volts for radiation levels up through 100 krad. At 300 krad, errors appear in the output state.

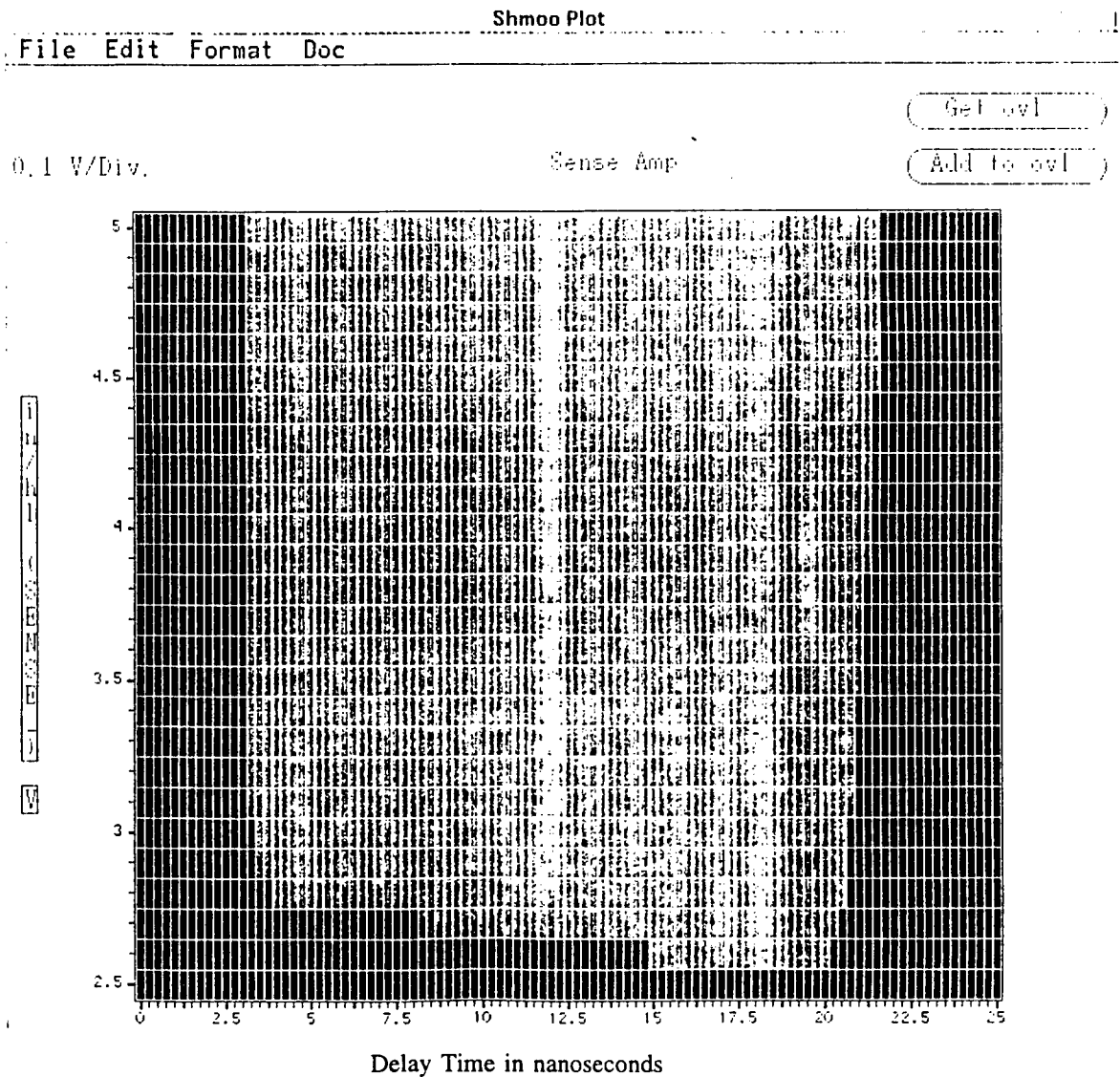


Figure 8. Shmoo Plot For Sense Amplifier

CONCLUSIONS

This work represents the initial phase of a larger program to completely characterize commercial CMOS processes. The results being reported are incomplete at this time. Nevertheless, the results of the radiation response of the devices and circuits were very encouraging. The reentrant and the edge devices show excellent radiation tolerance at 100 krad. Threshold shifts are tolerable in most circuit design applications and the leakage currents will not significantly degrade the operation of most circuits of interest. The field oxide devices show that surface inversion will be a problem above 100 krad. Each of the circuits are operational at 100 krad and again degrade significantly at 300 krad. It appears that circuitry can be designed which will be radiation tolerant to ionizing radiation up to levels of 100 krad using standard commercial CMOS fabrication techniques. Most study in this area is needed and is being accomplished at this time.

ACKNOWLEDGEMENTS

The author would like to thank Dave Alexander and Mike Williams of MRC, Albuquerque for valuable advise and assistance. Bill Kemp, Paul Duggin and Nathan Nowlin of the Phillips Lab assisted in some of the measurements and provided invaluable advise.

**POLYETHERIMIDE FIBERS: PRODUCTION PROCESSING AND
CHARACTERIZATION**

Gajanan S. Bhat
Assistant Professor
Department of Textiles

University of Tennessee
230 Jessie Harris Building
Knoxville, TN 37996

Final Report for:
Summer Faculty Research Program
Phillips Laboratory

Sponsored by:
Air Force Office of Scientific Research
Bolling Air Force Base, DC

and

Phillips Laboratory

August 1994

POLYETHERIMIDE FIBERS: PRODUCTION PROCESSING AND CHARACTERIZATION

Gajanan S. Bhat, Assistant Professor
Department of Textiles
University of Tennessee, Knoxville

Abstract

Polyetherimide is a copolyimide, which unlike most polyimides which are thermosets is a thermoplastic polymer. This means that polyetherimide can be melt spun. A melt spinning set-up was built to produce fibers from this polymer. Polyetherimide fibers were produced in different diameters by melt spinning of the Ultem resin. The as-spun fibers were subsequently drawn to different extents to achieve required diameters. The fibers were characterized for fiber diameter, as well as mechanical and thermal properties. Also, fibers spun from the same resin at other facilities were characterized. Shrinkage behavior of these fibers and their usefulness in fabrication of certain products was studied.

The fibers showed a significant amount of shrinkage tendency depending on the conditions of processing. It was shown that the shrinkage tendency of PEI can be significantly reduced by heat setting. The tensile properties indicated that the fiber can be drawn further by the appropriate selection of drawing temperatures and rates. It was also observed that the thermomechanical response of the fibers was dependent on their processing history.

POLYETHERIMIDE FIBERS: PRODUCTION PROCESSING AND CHARACTERIZATION

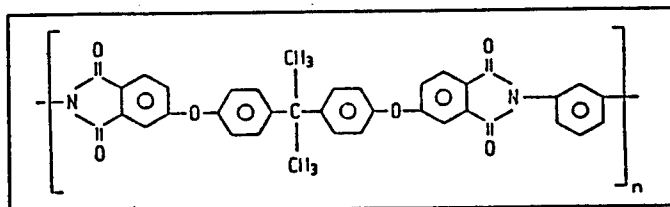
Introduction

Polyimide is a high temperature resistant polymer with excellent mechanical properties. Polyimide fibers have excellent thermal and chemical stability as well as good mechanical properties [1-3]. The very fact that they have good chemical stability means that they neither dissolve in simple solvents nor melt, and this creates problem for fabrication of products. It is because all the polyimides are chemically crosslinked.

Copolyimides on the other hand have better tractability and can be dissolved in less exotic solvents. Several copolyimides have been tried for the production of fibers and other products due to the ease of fabrication. One such example is the P84 fiber manufactured and marketed by Lenzing Co., Austria, from the 80/20 copolymer produced by Dow Chemical Company [1, 4]. However, even this fiber is partially crosslinked and thus can be dissolved only in aprotic solvents. The polyimide/amide copolymer manufactured by Amoco chemical company, although easily processable, on heat treatment becomes crosslinked [5, 6].

Polyetherimide Fibers

Polyetherimide (PEI) is a new resin introduced in 1982 by General Electric Company under the Tradename Ultem. It is a copolymer with ether molecules between imide groups with a structure as shown below:



The fully reacted polyimide with the imide group being part of the linear polymer chain makes this polymer thermoplastic and easily dissolvable. Being an amorphous thermoplastic polyimide, the Ultem resin combines the high performance associated with exotic specialty polymers and the good processability of typical engineering plastics [7]. In addition to high strength and modulus, and heat

resistance, the polymer has high dielectric strength, broad chemical resistance, transparency and good processability. Another advantage is that this polymer dissolves readily in methylene chloride.

GE has been marketing this polymer mainly for aerospace, marine, automotive, dielectric and electrical applications, where their long-term high temperature capabilities meet the stringent requirements [8]. Polyimide films are used as electrical insulation for electric motors, magnet wires, and aircraft and missile wiring. Because of their inherent flame resistance, polyimide films are also used as fire barriers in aircraft and marine applications. Polyetherimide exhibits this exceptional balance of properties without sacrificing processability, providing a material capable of meeting the difficult design requirements of many applications [9]. Many grades of this resin are available, each suitable for certain applications. The lower viscosity material of the available grades was used for fiber spinning.

Although possibility of spinning fibers from Ultem [10] has been reported, it is not commercially being produced. It was demonstrated that Ultem can be extruded into fibers and filaments, and then can be drawn and subsequently processed to textiles in conventional ways. The textile like properties of these fibers enables ultem to be used in several applications including hot gas filtration and thermoplastic composites. The major advantage of PEI fibers is their ability to retain tensile properties at temperatures above 150 °C.

Experimental Procedure

Materials

For this work, Ultem 1000 series resin, which is the low viscosity grade polymer, was selected since fiber spinning demands much lower viscosity compared to typical molding processes. The properties of the polymer are listed in **Table 1**. The effect of temperature on melt viscosity of the polymer is shown in **Figure 1**. Although the glass transition temperature of the polymer is about 215 °C, the viscosity data suggests that the spinning temperature should be above 350 °C. The spinning equipment and the processing conditions used are detailed in the next section. In addition to the fibers spun at Phillips Laboratory, fibers produced at two other laboratories, Center for Advanced Fiber Research, Clemson University (UL1), and Hoechst Celanese Company, Charlotte, NC (UL2), were used for characterization.

Table 1. Properties of Ultem 1000

Glass Transition Temperature (°C)	215
Vicat Softening Point (°C)	209
Melt Flow Rate	8.9
Density (g/cc)	1.28
Moisture regain (%)	0.25

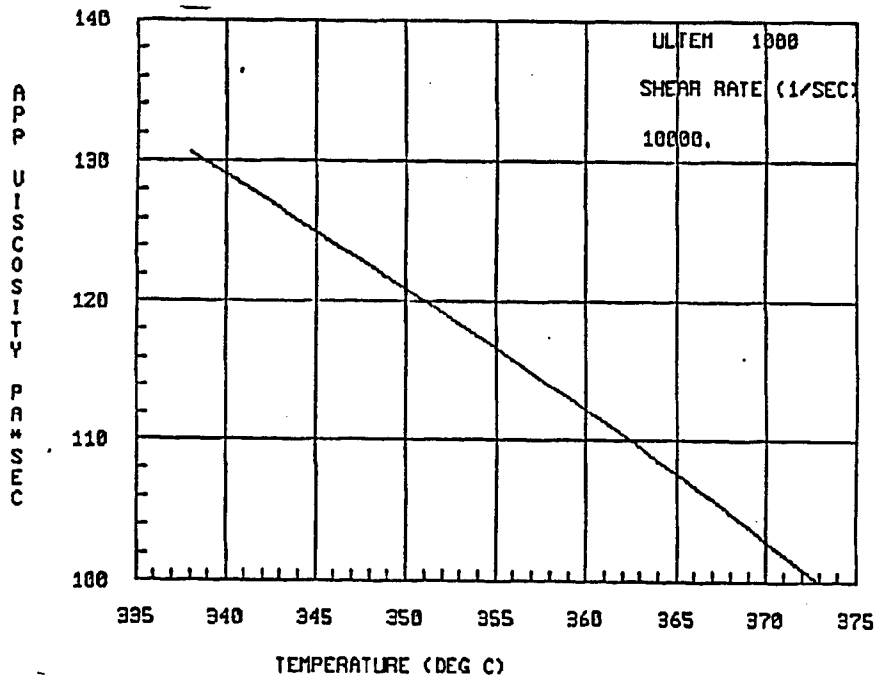


Figure 1. Melt Viscosity of Ultem 1000 Resin.

Melt Spinning

Melt spinning of the polymer was done using a home-built spinning unit. The spinning unit was built during the course of this tour. The schematic of the spinning apparatus is shown in **Figure 2**. The major parts of the set up are, melting pot, extrusion of the polymer and winding of the fibers. The spin-pack, consisting of melting pot, distributor, filter and spinneret is shown in **Figure 3**. As can be seen from the figures, the ultem polymer is placed in the melt chamber. The spinning unit fits inside the heating chamber. The molten polymer is pushed down by pressure generated through a high pressure cylinder. The polymer melt, before coming out of the spinneret, is filtered by special filters for removing any contaminants or unmelted polymer that may be in the melt. The fiber coming out of the spinnerets is quenched by the ambient air and then wound on a bobbin.

The important variables in spinning are, melt temperature, melt pressure, spinneret (no. and shape of holes and their dimensions), quenching conditions and winding speed. At the time of this research, a positive feeding unit for the melt (metering pump) was not installed and the polymer feed rate was determined only by temperature and pressure.

Fiber Characterization

Fiber Diameter. Diameter of the fibers was determined using a Panavise digital micrometer. It was assumed that the fibers had a circular cross section.

Thermal Analyses. Thermal analyses of the fibers were done at the Textile Materials Research Laboratory of the University of Tennessee, Knoxville. A Mettler DSC25 was used for the differential scanning calorimetry (DSC) and the Mettler TMA40 was used for the thermo-mechanical analysis (TMA). DSC and TMA scans were done at a heating rate of 10 °C per minute. For TMA, the gauge length used was 10 mm, and two levels of tensions were used. Both the DSC and TMA scans were done in the nitrogen environment.

Tensile Properties. Breaking strength and elongation of the fibers were measured with a home built tensile tester. The tensile tester was assembled using the Oriel motor mike, an Oriel Single Controller Model 18007, Scorensen regulated DC power supply and a Beckman Model 3020B multimeter. The load response on stretching of the fibers glued to fixed and variable jaws was measured in mV from the multimeter, was converted to gm force using previous calibrations, and

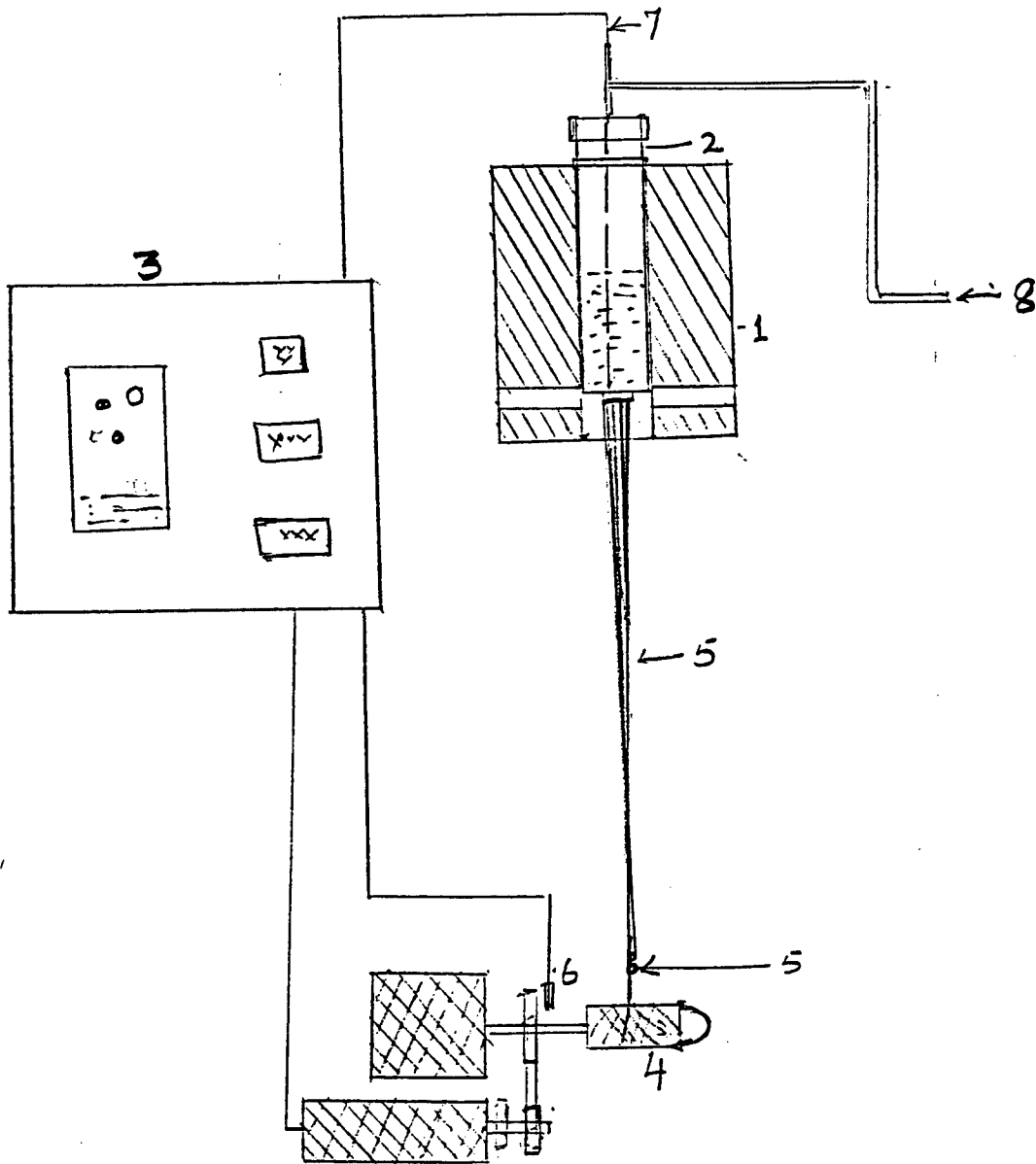


Figure 2. Schematic of the Melt Spinning Unit: 1-Heating Chamber; 2-Spin Pack; 3- Control Panel; 4- Take-up; 5- Threadline; 6- Tachometer Probe; 7- Thermocouple; 8- Pipe to Gas Cylinder

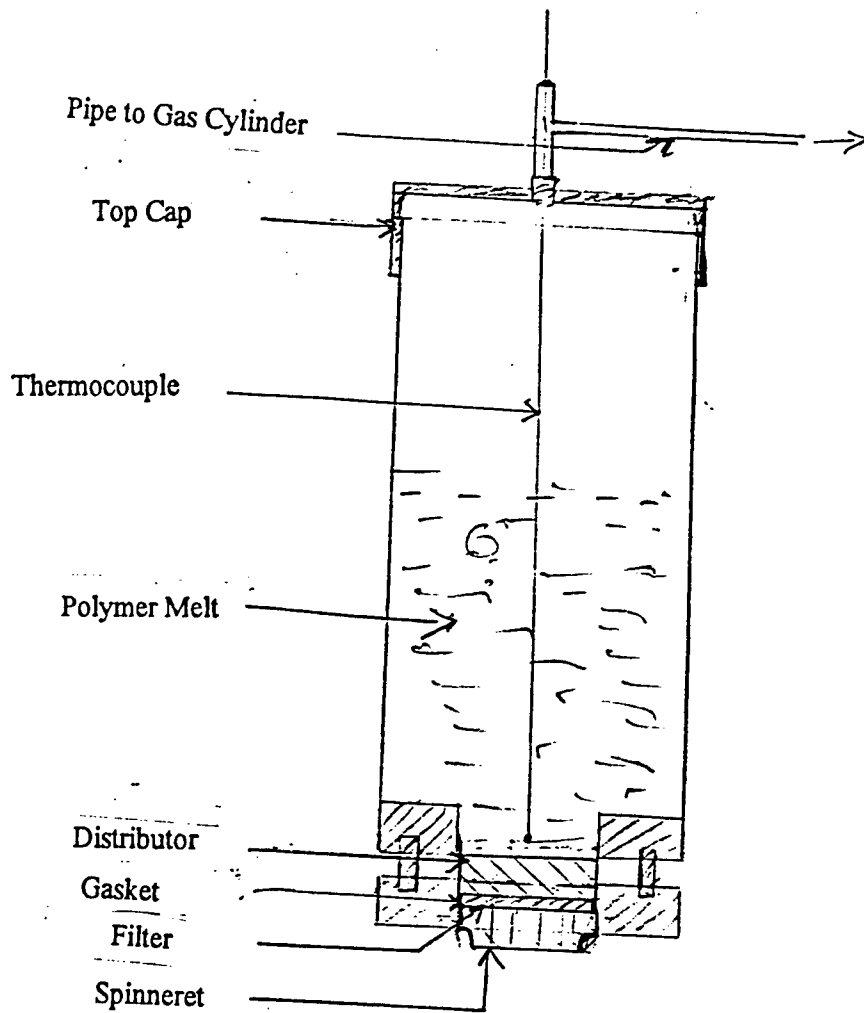


Figure 3. Description of the Spin Pack.

the tenacity was calculated. Elongation was calculated from the extension readings in micron from the controller. Although several data points were recorded during the course of the extension experiment, only breaking strength and elongation are reported.

Annealing Studies

Annealing studies were done using a Fisher Model 497 Isotemp furnace. Temperature inside the furnace, where the fibers were placed, was checked with a separate thermocouple and temperature indicator. Thus it was possible to estimate the heat setting temperature for different isothermal temperatures of the furnace. In this report, the actual temperature of annealing is reported. The temperature of the oven was maintained within ± 5 °C of the set point. For each set of fibers, four samples mounted on a suitably bent steel plate using kapton adhesive films, were used. For free length annealing (FLA), while one end was fixed, the other end was pretensioned with a piece of kapton film. For constant tension annealing (CTA), at the free end, in addition to kapton film, a suitable weight was hung using alligator clips. Change in length of the fibers on annealing was measured and reported as per cent extension or shrinkage. All the samples were heat set for about four minutes. The drop in temperature of the oven on opening and closing the door to place the samples was about 10 °C, and the temperature reached the set point within 45 sec.

Results and Discussion

Melt Spinning

Melt spinning was done with Ultem 1000 to produce fibers of different diameters. The melt spinning conditions used are shown in **Table 2**. The melt temperature was varied in a narrow range. At lower temperatures there was not enough melt coming out and on increasing the temperature, there was extensive breakage. The pressure was set at a level to maintain a consistent flow of the melt. Spinning speeds were rather slow as the cooling length was small and quenching was only by ambient air. Attempts were made to increase the take-up speed without breaking a lot of filaments.

Although fibers were collected under some processing conditions, spinning was not without problems. Obviously the temperature of the melt to achieve flow through the spinneret was very high. This is because of the very high viscosity of the polymer, as the resin was not made for fiber

Table 2. Melt Spinning Conditions and Fiber Samples.

<u>Spinning Conditions</u>	<u>Sample</u>					
	1	2	3	4	5	6
Heater Temp. (°C)	390	390	390	389	389	389
Melt Temp. (°C)	379	379	379	376	376	376
Melt pressure (psi)	700	700	700	580	700	700
Spinneret hole dia (u)	200	200	200	200	200	200
L/D ratio	2	2	2	1	1	1
Take-up Speed (ft/min)	4.5	7.5	9.0	15	15	22
Fiber Diameter	95	85	65	75	80	70

spinning, but for molding. It is hoped that the use of Ultem 1010 which has a viscosity slightly lower than that of Ultem 1000 would process better. In fact, this resin has been ordered and will be tried as a candidate for fiber spinning.

Another problem was that of air bubbles coming with the melt. While the melt coming out in the initial periods seemed to be free of air bubbles, after some time, the melt had a lot of bubbles leading to filament breakages. A practical way of getting rid of entrapped air from the melt needs to be implemented to achieve continuous spinning without breakage.

The spinneret used in this study had L/D ratios of 1 or 2, while typical melt spinning for fibers uses spinnerets with L/D of 10 or more. Higher L/D helps in reducing the die swell and this can help in achieving higher draw and orientation, as well as finer fibers. The throughput was not positively controlled as mentioned in the earlier section. Use of metering pumps would ensure a uniform throughput, which will help in achieving uniform diameter of the fibers. Incorporation of cooling system to provide additional cooling of the fiberline would increase the flexibility of processing conditions. While the polymer was heated in the furnace, the top of the melt chamber was much cooler since it was not insulated. This might have been responsible for higher heat loss from the top and nonuniform melt temperature profile within the chamber. Insulating the top of the spinpack might help in improving the melting efficiency.

Fiber Properties

Since the melt spinning was done towards the end of the tour, the fibers spun at Phillips Laboratory could not be characterized. As a result, only the properties of the other two sets of Ultem filaments (UL1 and UL2) that were characterized earlier are included in this report.

The fibers were not uniform and the diameters varied considerably, at some points as much as 50 per cent. Average diameters of the fibers are used in all the calculations. The tensile properties of the two as-spun fibers (Table 3) indicates that they have a good drawing potential. The breaking elongation was above 100 per cent. However, on hand stretching, the filaments had their stretching potential reduced to less than half of the as-spun fibers. This was not a controlled drawing and probably the fibers could be drawn further. This decrease in elongation was also accompanied by an increase in tenacity which is consistent with drawing of any filament.

Table 3. Tensile Properties Polyetherimide Fibers

Sample	Diameter (u)	Tenacity (gpd)	Br. Elongation (%)
UL1	38	1.3	126
UL1 - hand stretched	26	4.5	54
UL2	40	0.8	93
UL2 - hand stretched	25	3.5	22

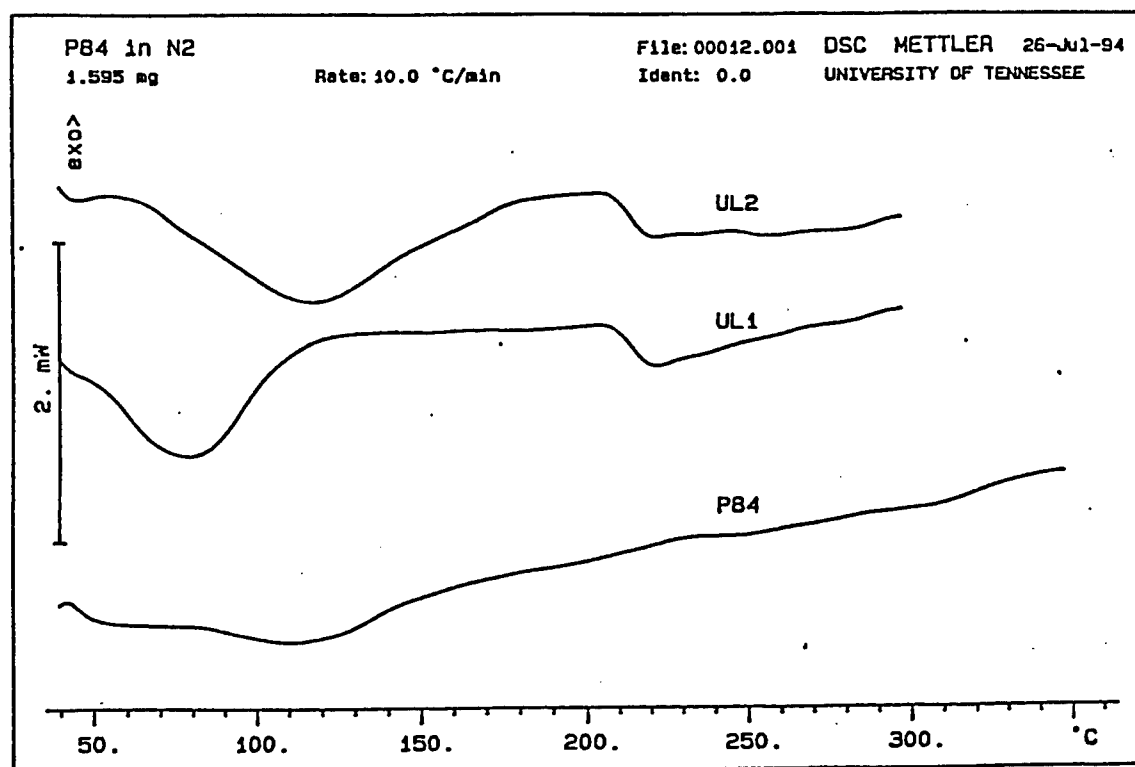


Figure 4. DSC Scans of Ultem and P84 Fibers.

The DSC scans of the two fibers and that of a P84 fiber are shown in **Figure 4**. Both of the ultem fibers show a glass transition around 215 °C, while P84 does not show Tg till 300 °C. The higher transition temperature of the P84 copolyimide fiber is because of its crosslinked structure. Obviously the DSC does not show any difference in structure of the two ultem fibers. Thermal shrinkage values (**Table 4**) indicated that the fibers were quite stable till about 180 °C. However at 200 °C, the fibers showed significant level of shrinkage. For both the fibers, hand-stretched filaments showed higher shrinkage than as-spun fibers. This is a clear indication of the differences in the orientation of the two filaments. Again, low level of shrinkage for as-spun fibers indicates that the orientation achieved in spinning is not very high, which is determined by the spinning conditions used. It was observed that on heat setting, even the hand-stretched fibers did not show any shrinkage.

The shrinkage tendency of the as-spun fibers can also be seen from the TMA scans (**Figure 5**). From **Figure 5A**, it appears that the two fibers are quite similar, and the deformation is seen at a temperature around the Tg. This was the case at very low loads. However, TMA scans done at a higher tension show the difference in structures of the two as-spun fibers as shown **Figure 5B**. There was a difference of almost 30 °C in the temperature of onset of shrinkage. UL2 seemed to be more stable than UL1, which shrank at a lower temperature. This is due to the differences in spinning conditions of the two fibers and is consistent with the difference in breaking elongation of the two fibers. This difference in TMA response is also an indication of the difference in drawability of the two fibers.

Annealing studies of the filaments indicated that shrinkage potential of the fibers can be completely reduced. In fact, even hand-stretched fibers that showed a shrinkage of above 50 per cent at 200 °C, showed almost negligible shrinkage when heat set at 150 °C. Because of the lack of suitable facilities, annealed fibers could not be thoroughly characterized.

Conclusions

A simple melt spinning unit was built to spin fibers from thermoplastic polymers, especially the Ultem resin. The ultem resin was spun into fibers of different diameters. The structure and properties of the as-spun fibers were dependent on the spinning conditions used. The structure of

Table 4. Shrinkage Behavior of Polyetherimide Fibers.

Sample	Setting Temp. °C	Shrinkage, %
UL1	180	1.1
Hand-stretched UL1	180	15.6
UL2	180	1.3
Hand-stretched UL2	180	15.7
UL1	200	0.8
Hand-stretched UL1	200	53.6
UL2	200	16.1
Hand-Stretched UL2	200	54.7

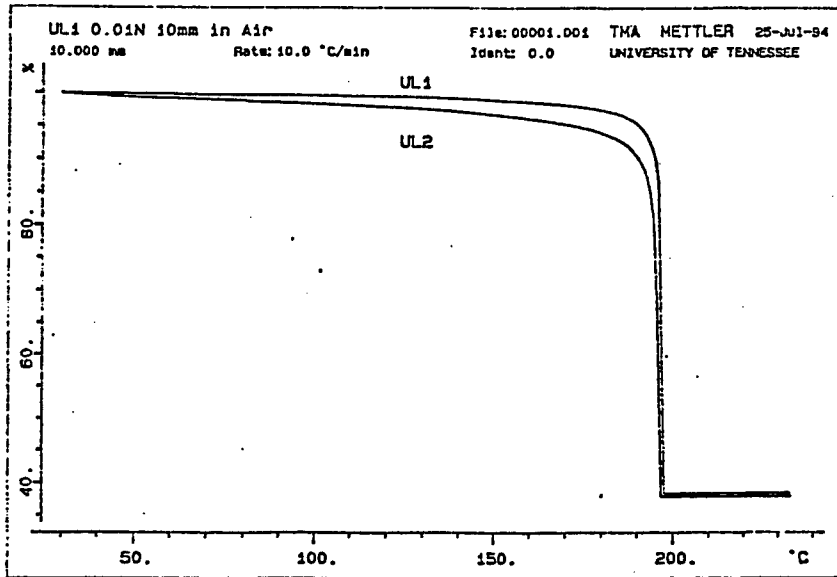


Figure 5a. TMA of Ultem Fibers Under 0.01 N Load.

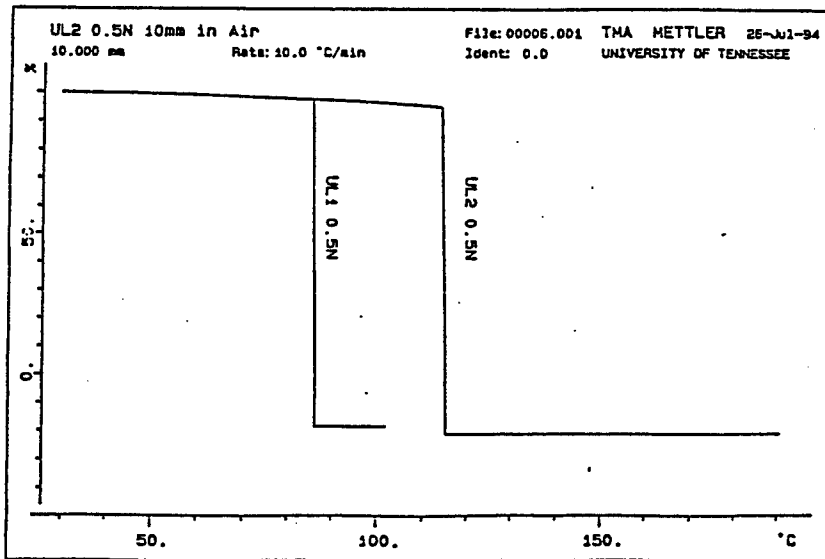


Figure 5b. TMA of Ultem Fibers Under 0.5 N Load.

as-spun fibers determine the drawability of these fibers. The fibers showed almost same level of shrinkage, but deformation under stress occurred at different temperatures for the two fibers characterized. It was also observed that heat-setting can be used to reduce the shrinkage tendency of the oriented ultem fibers. Thus, heat-setting can be a useful technique to set the stretched fibers in different shapes, if desired. The shrinkage behavior of the fibers is important in setting of fibers in different shapes. When exposed to higher temperatures under some constraint, the fibers tend to shrink, but can not do so leaving a permanent set in that shape.

Recommendations for Future Work

Although it was possible to spin fibers from the Ultem resin, some problems were observed in extruding of this polymer. The presence of air bubbles was a problem. Alternate use of vacuum and pressure may be helpful in getting rid of the air bubbles. Also providing means to improve the temperature profile to ensure complete melting inside the chamber before use of pressure/vacuum will be of greater help.

There is no rheological data on these resins with respects to fiber spinning conditions. Melt rheology of this polymer needs to be studied to determine the viscosity behavior at shear rates comparable to that used in melt spinning. Also the die-swell and the effects of channel length to diameter of the spinneret on die swell needs to be investigated. This will give an idea about the elasticity of the polymer melt and the role of spinneret design on spinning performance.

Structure and properties of the as spun fibers are very important in determining their processability (such as drawing and heat-setting) and usefulness. Fibers have to be characterized for birefringence, stress-strain behavior, DSC, TMA, thermal shrinkage and thermal stress analysis to get a better idea of the structure of the fibers. The information will also be useful in knowing the drawability of the fibers and suitable drawing temperatures that can be used.

When it comes to achieving small diameters in fibers, the combination of optimizing spinning conditions and drawing has to be done. By maximizing the draw ratio, small diameters can be realized. For this, suitable draw conditions have to be determined. In fact, use of some special

techniques, such as plasticized drawing may be required. This needs to be investigated by an in-depth study of drawability of the fibers in varying processing conditions.

Heat setting is a very important process in determining the properties of, and in fabricating products from fibers. A detailed investigation of the effect of heat setting on these fibers needs to be done. Changes in the structure and properties of the fibers on annealing at different temperatures, and both with and without stress should be studied.

Acknowledgments

The author would like to sincerely acknowledge the guidance, support and encouragement of Dr. West Hoffman of Phillips Laboratory. Dr. Philip Wapner of Hughes STX Corporation is greatly acknowledged for his help and advise through out the course of the tour, both inside the laboratory and outside. Mr. Dong Zhang of University of Tennessee, Knoxville helped in getting the DSC and TMA data. Other colleagues at the laboratory, Drs. Pete Pollock, I. K. Ismail, N. S. Abhyankar, Mr. Martin Burmeister, Mrs. Hong Phan, Mr. Tim Naughton and many others helped in making my stay more enjoyable and fruitful.

Of course this tour would not have been possible without the financial support of AFOSR. A great deal has been accomplished during this summer and the tour exposed the author to some of the exciting research at the Laboratory. In fact, some of this research will be continued at UTK using the facilities and expertise available there to complement the activities at the Phillips Laboratory. RDL and its employees in charge of the summer program are greatly acknowledged for their timely help and guidance, and making sure that the tour went very well from the beginning.

Bibliography

1. M. S. Reisch, *C & E News*, February 2, 9 (1987).
2. H. H. Yang, 'Aromatic High Strength Fibers,' John Wiley and Sons, New York (1989).
3. T. Kaneda, T. Katsura K. Nakagawa, H. Makino and M. Horio, *J. Appl. Polym. Sci.*, 2, 32, 3133; 32, 3151 (1986).
4. P-84 High Performance Products, Company literature, Lenzing AG.
5. G. V. Cekis, *Modern Plastics Encyclopedia*, mid October issue, 32 (1993).
6. Applications Bulletin, Amoco AI-10 Polymer, Amoco Performance Products, Inc., Atlanta, GA.
7. H. R. Penton, *Modern Plastics Encyclopedia*, mid October issue, 87 (1993).
8. Ultem Polyetherimide Resin, Company literature, GE Plastics.
9. I. W. Serfaty, in *Polyimides*, ed. by K. L. Mittal, Plenum Press, New York (1988).
10. 'Textile Applications of Performance Polymers,' *Textile Month*, July, 20 (1991).

PRACTICAL SEMIQUANTAL MODELLING OF COLLISIONAL
VIBRATIONAL RELAXATION OF DIATOMIC MOLECULES

Ronald J. Bieniek
Associate Professor
Department of Physics

University of Missouri - Rolla
Rolla, MO 65401-0249

Final Report for:
Summer Faculty Research Program
Phillips Laboratory, Geophysics Directorate
Hanscom Air Force Base

Sponsored by:
Air Force Office of Scientific Research
Bolling Air Force Base, DC

and

Phillips Laboratory, Geophysics Directorate

August, 1994

PRACTICAL SEMIQUANTAL MODELLING OF COLLISIONAL
VIBRATIONAL RELAXATION OF DIATOMIC MOLECULES

Ronald J. Bieniek
Associate Professor
Department of Physics
University of Missouri - Rolla

Abstract

To model and interpret emission spectra and energy budgeting in infrared-active molecules in the atmosphere, such as OH and NO, the rates for vibrational relaxation through collisions must be known. This project successfully produced practical, easily applied semiquantal analytic formulae that accurately simulated relaxation rates determined both by brute-force quantum mechanical computations (e.g., HF(n) + He) and also by laboratory measurements (e.g., OH(n) + O₂). The one-parameter required for the semiquantal expressions (the exponential slope of the collisional repulsive core) can be determined for a specific collision system from a known interaction potential or, as is usually the case, from a limited set of experimental rates. In all systems studied, the one-parameter fits passed through all error bars. These handy expressions were also able to predict the extreme sensitivity of relaxation rates to molecular anharmonicity and collisional temperature, accurately tracking the rates over changes of many order of magnitude. Furthermore, a perturbation expansion for the scattering matrix, coupled with computed values, clearly demonstrated that relaxation to the next lower level dominates all other transitional paths. A simple formula was derived that estimates an upper bound for the relative strengths of these paths.

PRACTICAL SEMIQUANTAL MODELLING OF COLLISIONAL VIBRATIONAL RELAXATION OF DIATOMIC MOLECULES

Ronald J. Bieniek

INTRODUCTION

Vibrationally excited molecules play an important and well-known role in the chemistry and energy budget of the upper atmosphere, as well as in combustion processes. A kinetic model of energy pathways and energy conversion processes in these systems requires knowledge of the rate constants for collisional deactivation of vibrational excitation. However, in many cases experimental measurements of these rates are limited to very few vibrational rates, and more are required in order to model a system adequately. Empirical descriptions of this vibrational dependence as simple powers of the vibrational quantum number n have been attempted, but these have been found to be unsatisfactory. Furthermore, to produce emission models, it is important to know whether single ($n \rightarrow n-1$) or multi-quanta (e.g., $n \rightarrow n-2$) transitions dominate in the establishment of level populations. Common wisdom holds that single quanta transitions are the most important, but theoretical justification needs to be supplied.

This problem is illustrated by the vibrational relaxation of hydroxyl (OH) and nitric oxide (NO) in the upper atmosphere.^{1,2,3} OH($n=1-9$) is formed by the reaction of O_3 and H in the mesopause region, and collisional relaxation of the $n=1-9$ levels plays an important role in determining the steady-state OH population distributions. This, in turn, strongly affects the chemistry and energy budgets of the mesopause. Separate measurements have been made of the relaxation of OH($n=1-6$)³ and OH($n=9,12$)^{4,5} by O_2 . This raises the dual problem of ascertaining whether these measurements for different vibrational levels are mutually consistent, and how to properly interpolate for other levels not yet experimentally measured.

In the case of the relaxation of NO(n) by O_2 , rates have been measured for $n=1-7$,⁶ while NO can be formed from the $N(^2D) + O_2$ reaction up to $n=18$. NO(n) can be chemically produced as a result of both solar and auroral energy deposition, ultimately leading to infrared emission from NO(n). Due to these emissions, NO is a key infrared emitter in the lower thermosphere, and dominates the cooling of that region of the atmosphere. Therefore, in order to model these phenomena, once again a reliable method of extrapolating from known vibrational relaxation measurements is highly desirable.

The purpose of the present project (undertaken at the Phillips Laboratory, Geophysics Directorate, at Hanscom Air Force Base) was to devise general, practical methods of predicting unknown or uncertain rates needed for analysis and modelling, from known experimental values. Furthermore, it was also important to ascertain if one could rightfully ignore multi-quanta transitions in the interpretation of relaxation phenomena. All goals were achieved.

BASIC PERTURBATION EXPANSION

To compute vibrational relaxation rates, particularly multi-quanta ones, it is generally advisable to employ a perturbation expansion. Since we are interested only in vibrational transitions, summed over all final rotational states, we will apply the breathing-sphere approximation, though which the collisional interactions are averaged over molecular orientations.^{7,8} In an earlier study of vibrational transitions in HF(n) + He collisions, the numerical quantal results from the breathing-sphere approximation were quite accurate when compared to results obtained from the full orientation-dependent potential⁹ using a quantal adiabatic distorted-wave infinite-order approximation.¹⁰

If H is the total hamiltonian and H_0 is a hamiltonian with known solutions, then $V = H - H_0$ is the perturbation interaction. These will generally be functions of the molecular stretch coordinate r and the collisional separation R . In this work, we use diabatic molecular vibrational states $\phi_n(r,R)$ of energy ϵ_n , and continuum atom-diatom scattering states $u_n(K,R)$ of asymptotic kinetic energy K . These are the eigenstates of H_0 .

We can produce a convenient, insightful perturbation expansion⁸ for the S-matrix in terms of first-order

T-matrix elements in the following way. The formal S-matrix is given by:

$$S(\xi) = 1 - i 2 \pi T \delta(\xi - H_0) = 1 - i 2 \pi T(\xi) \quad (1)$$

where ξ is the total energy. The T-matrix on the total energy shell can be written as an expansion in powers of the perturbation interaction V and the scattering Green's function G^{out} :

$$T(\xi) = T^{(1)} + T^{(2)} + T^{(3)} + \dots = \sum_{n=1}^{\infty} T(\xi)^{(n)} \quad (2a)$$

where

$$T^{(n)} = V (G^{out} V)^{n-1} \quad (2b)$$

We will employ a spectral decomposition using a complete set of first-order distorted-wave scattering states:

$$1 = \sum_j \int_0^{\infty} |\psi_j(K)\rangle \langle \psi_j(K)| dK \quad (3a)$$

where

$$|\psi_j(K)\rangle = |u_j(K, R)\rangle \cdot |\phi_j(r, R)\rangle \quad (3b)$$

The general form of coupling terms in the perturbation expansion is:

$$W_{jn}(K, \kappa) = (1 - \delta_{jn}) \int_0^{\infty} u_j(K, R) V_{jn}(R) u_n(\kappa, R) dR \quad (4a)$$

where

$$V_{jn} = \langle \phi_j | V | \phi_n \rangle \quad (4b)$$

These can be used to produce a perturbation series expansion of the T-matrix on the total energy (ξ) shell:

$$T_{if}^{(1)} = W_{if}(K_i, K_f) \quad (5)$$

where $K_n = \xi - \epsilon_n$. We now look at higher-order elements. In second-order:

$$T_{if}^{(2)} = \sum_j \int_0^{\infty} \frac{W_{ij}(K_i, K) W_{jf}(K, K_f)}{K_j - K + i \cdot \epsilon} dK \quad (6a)$$

This is equivalent to:

$$T_{if}^{(2)} = \sum_j \mathcal{P} \int_{-\infty}^{\infty} \frac{W_{ij}(K_i, K) W_{jf}(K, K_f)}{K_j - K} dK - i \pi \sum_j W_{ij}(K_i, K_j) W_{jf}(K_j, K_f) \quad (6b)$$

The first set of terms on the right, involving the principal-part integrals, can generally be neglected because of the approximate odd symmetry of the integrand $(K_j - K)$. This essentially excludes terms that arise from channels off the energy shell.

The first-order distorted-wave T-matrix elements are then simply given by:

$$t(\xi)_{jn} = W_{jn}(K_j, K_n) = (1 - \delta_{jn}) \int_0^{\infty} u_j(K_j, R) V_{jn}(R) u_n(K_n, R) dR \quad (7)$$

These can be used to compute the T-matrix (and thereby the S-matrix) to all orders:

$$T_{if}^{(1)} = t(\xi)_{if} \quad T(\xi)^{(1)} = t(\xi) \quad (8a)$$

$$T_{if}^{(2)} = (-i \pi) \sum_j t_{ij} t_{jf} \quad T^{(2)} = (-i \pi) t^2 \quad (8b)$$

$$T_{if}^{(3)} = (-i \pi)^2 \sum_n \sum_j t_{ij} t_{jn} t_{nf} \quad T^{(3)} = (-i \pi)^2 t^3 \quad (8c)$$

This gives a simple expansion series for the S-matrix, in terms of first-order T-matrix

$$S = 1 - i 2 \pi \left[t + (-i \pi) t^2 + (-i \pi)^2 t^3 + \dots \right] = 1 + 2 \sum_{n=1}^{\infty} (-i \pi t(\xi))^n \quad (9)$$

This matrix forms demonstrates the role of transitional paths through virtual states. For instance, for a two-quanta vibrational relaxation from the ground state ($n = 2 \rightarrow 0$),

$$S_{20} = -2\pi i t_{20} - 2\pi^2 (t_{21} t_{10} + t_{23} t_{30} + \dots) + 2\pi^3 i (t_{20} t_{01} t_{10} + t_{23} t_{31} t_{10} + \dots) + \dots \quad (10)$$

The first term in (10) represents a "direct" double-quanta transition, while the second term represents single-quantum transitions ($2 \rightarrow 1$ then $1 \rightarrow 0$) through energy-conserving virtual states. The third term is a mixture of multi-quanta transitions through virtual states. As will be argued, paths made up single-quanta steps dominate most vibrational collision processes as long as the perturbation interaction is small. This implies that reasonable distorted-wave states be used.

We can produce a formal operator expression for this expansion in the following way:

$$S = \mathbf{1} + 2 \sum_{n=1}^{\infty} (-i \pi t)^n = 2 \left[\mathbf{1} + \sum_{n=1}^{\infty} (-i \pi t)^n \right] - \mathbf{1} = \frac{2 \mathbf{1}}{1 + i \pi t} - \mathbf{1} \quad (11)$$

The final compact result is:

$$S(\xi) = \frac{1 - i \pi t(\xi)}{1 + i \pi t(\xi)} = (1 - i \pi t(\xi)) (1 + i \pi t(\xi))^{-1} \quad (12)$$

The last form clearly shows that this is a unitary expression, a gratifying result for an approximate form of the S-matrix.

Within the breathing-sphere approximation, we do not need to worry about the angular momenta of the molecule, for that has been subsumed by the averaging of the potential over orientations. This implies that the vibrational transition rates R from vibrational levels n to f at a collisional energy E (and total energy $\xi = E + \epsilon_n$) can be written as a sum over collisional partial waves L:

$$R(E)_{n,f} = \sqrt{\frac{2 E}{\mu}} \left[\frac{\pi \hbar^2}{2 \mu E} \sum_L (2L+1) \left(|S(\xi, L)_{n,f}| \right)^2 \right] \quad (13)$$

THE EXPONENTIAL MODEL

We use a few simplifying approximations to obtain the desired practical scaling relations that accurately fit a wide range of experimental data. The first assumption is that vibrational excitation and relaxation is mainly caused when the molecule strikes the repulsive wall of the atom-diatom interaction potential, and that this region is adequately described by a repulsive exponential potential. This gives a perturbation interaction of the form:

$$V(r, R) = a e^{(-\alpha R + \gamma \Delta r)} - \zeta \quad (14)$$

where $\Delta r = r - r_e$, with r_e the equilibrium separation of the diatom, and ζ is on the order of the depth of the attractive well of the atom-diatom interaction.

Fortunately, the first-order distorted-wave elements t for this exponential potential can be evaluated analytically:¹¹

$$t(\xi, L)_{n,f} = \frac{\alpha}{16} \left[\left(1 - \delta_{n,f} \right) \frac{V_{n,f}}{V_{f,f}} \left(\frac{V_{n,n}}{V_{f,f}} \right)^{i \cdot 0.5 q(L)_n} \right] \frac{\sqrt{\sinh(\pi q(L)_f) \sinh(\pi q(L)_n)} \left[(q(L)_f)^2 - (q(L)_n)^2 \right]}{\sinh[0.5 \pi (q(L)_f + q(L)_n)] \sinh[0.5 \pi (q(L)_f - q(L)_n)]} \\ \times \sqrt{\frac{q(L)_f q(L)_n}{k_f k_n}} F \left[1 + 0.5i (q(L)_f + q(L)_n), 1 - 0.5i (q(L)_f - q(L)_n), 2, 1 - \frac{V_{n,n}}{V_{f,f}} \right] \quad (15a)$$

where

$$k_j = \sqrt{\frac{2\mu}{\hbar^2} (\xi - \epsilon_j)} \quad (15b)$$

$$q(L)_j = \frac{2}{\alpha} \sqrt{\frac{2\mu}{\hbar^2} (\xi - \epsilon_j + \zeta) - \frac{L(L+1)}{R_c(j, \xi)^2}} \quad (15c)$$

$$R_c(j, \xi) = \alpha^{-1} \left(\ln\left(\frac{a}{E + \xi}\right) + \gamma r_e \right) \quad (15d)$$

and

$$F(a, b, c, z) = \frac{\Gamma(c)}{\Gamma(a)\Gamma(b)} \sum_{n=0}^{\infty} \frac{\Gamma(a+n)\Gamma(b+n)}{\Gamma(c+n)} \frac{z^n}{n!} \quad (15e)$$

is a confluent hypergeometric function. R_c is essentially the collisional turning point. Because this solution is based on a distorted-wave solution of the Schroedinger wave-equation, it can be properly looked upon as a *semi-quantal* method.

This hard-core simulation of vibrational changing collisions has proved to be very good at reproducing more elaborate quantal computations in a variety of systems, e.g., HF + He and CO + He. However, those tests were always at super-thermal collisional energies, typically on the order of electron volts. In the present study, we pushed the test to much lower energies. Because there is extensive theoretical information on the HF(n) + He collision system, it was chosen for initial evaluations of the methods and computer codes developed in this project. A very good double-exponential analytic fit to the *ab initio* breathing-sphere potential is available (in atomic units):¹¹

$$V_{\text{HF-He}}(r, R) = 54.3723 e^{(-1.80 R + 0.23718 \Delta r)} - 33.3464 e^{(-1.70 R + 0.21099 \Delta r)} \quad \text{hartrees} \quad (16)$$

A fairly accurate single-exponential fit to this is:

$$V_{\text{exp}}(r, R) = 31.545 e^{(-2.20 R + 0.340 \Delta r)} - 0.000926 \quad \text{hartrees} \quad (17)$$

Numerical computations were conducted for vibrational excitation and relaxation in HF(n) + He from temperatures of 300 K to 30,000 K. Since it has proved accurate in the past,¹¹⁻¹³ the adiabatic distorted-wave approximation was employed for the quantal computations; these used the full double-exponential fit to the interaction potential. Analytic matrix elements and rates, based on the single-exponential model of Eqs. 15 and 17, were computed using the single-exponential fit to the *ab initio* potential. Both utilized the expansion (9) in t to compute the S-matrix for several orders.

The first thing observed was that the only significant term in the series expansion for the S-matrix came from the unique path from initial to final vibrational levels through single-quantum transitions, as discussed above; for

example, $S_{20} = -2\pi^2 t_{21} t_{10}$, with the direct ($-2\pi i t_{20}$) and all other multiple-quantum paths (e.g., $2\pi^3 i t_{20} t_{01} t_{10}$) comparatively insignificant. The second result noted was that the relaxation rate to the next lower level was always much greater than the rates to still lower levels. This latter result is easily explained by the fact that the rates for multi-quanta transitions are governed by products of single-quantum matrix elements ($t_{j,j-1}$), that are all inherently much smaller than unity. Thus the transition to the next lower level is much larger than the others because only a single element appears, rather than a product of them as in the multi-quanta case.

Since the main thrust of this report is the explication of accurate, practical scaling relations, we will cut to the additional approximations required without dwelling on the detailed numerics of these points. The energy of a vibrational level v is given by

$$\epsilon_v = \hbar \omega_e (v + 0.5) [1 - x_e (v + 0.5)] \quad (18)$$

where ω_e is the fundamental spectroscopic frequency and $x_e = \omega_e x_e / \omega_e$ is the anharmonicity, both of which can be readily obtained from standard reference literature.¹⁴ In the context of this discussion, we have noted that single-quantum transitions from some initial level n to the next lower level $n-1$ dominates the relaxation process. Since the change in kinetic energy in the V-T process equals the change in vibrational energy, the change in kinetic energy is given by:

$$|\Delta K_n| = \epsilon_n - \epsilon_{n-1} = \hbar \omega_e (1 - 2 x_e n) \quad (19)$$

The last major approximation is that the first-order T-matrix elements $t(\xi, L)$ are a smooth, uniform function of L that is fairly independent of the incident collisional energy at thermal temperatures, and can thereby be easily characterized by the s-wave ($L=0$) element:

$$t(\xi, L)_{jf} = F(L)_j t(\xi, 0)_{jf} \quad (20)$$

This is actually quite reasonable, if one examines the analytic first-order distorted matrix elements. The angular momentum L will not have much of an effect until it gets large. However, at that time, the summation will be near termination because of the cut-off by the centrifugal barrier. In deference to compactness of presentation, we will now just note that extensive numerical computations were done on both the HF(n) + He and OH(n) + Ar systems that demonstrate the validity of this approximation. Furthermore the smooth function $F(L)$ varied little over the partial waves that matter, typically by only tens of percent.

This allows a very significant simplification. For the dominate single-quantum transitions to the next lower level, we achieve a simple expression for the partial wave summation in the rate:

$$\sum_L (2L+1) \left(|S(\xi, L)_{n,n-1}| \right)^2 = B \alpha^{-2} \left[\left(|t(\xi, 0)_{n,n-1}| \right)^2 \langle F \rangle (E + \zeta) \right] \quad (21)$$

where B is a constant for given collision partners. The factor $(E + \zeta)$ arises from the approximation that the number of partial waves in the sum is cut off by the centrifugal barrier.

The final issue to be dealt with is the evaluation of the vibrational coupling matrix elements $V_{n,f}$. Analytic

expressions are available for harmonic oscillator and for Morse oscillator basis sets. Generally, both basis sets produce coupling terms that are within a few percent of one another. However, computations undertaken in this project confirm an extensive study¹⁵ by Mies that the full distorted-wave matrix element t_{nf} can differ significantly between harmonic and Morse oscillator sets, due to the extreme sensitivity of the confluent hypergeometric function to its last argument, $1 - V_{n,n}/V_{f,f}$. Since γ is generally much smaller than unity, we would expect the diagonal elements to be nearly equal, making this argument very small. Indeed, it is. If it were zero, the hypergeometric function would be identically one. But the small differences in basis set produced nearly a factor of two difference in total rates between harmonic and Morse oscillator basis sets. Morse oscillators are much more natural to use than harmonic because the Morse-oscillator vibrational eigenenergies are identically (18). However, the relevant transitional coupling term $V_{n,f}/V_{f,f}$ has a much more appealing approximate expression in the harmonic oscillator basis for single-quantum transitions:

$$\left(\left| \frac{V_{n,n-1}}{V_{n-1,n-1}} \right| \right)^2 = n \frac{\hbar}{2m} \left[\frac{\gamma^2}{\omega (1 - 2 x_e n)} \right] \quad (22)$$

where m is the reduced mass of the diatom and $\omega = \omega_e$. In this, the anharmonicity x_e is accounted for by forcing the harmonic oscillator to have an vibrational energy spacing given by (18). Since we will produce scaling relations, the constant factor differences between harmonic and Morse oscillator basis sets will cancel out in the end by taking ratios. The harmonic oscillator coupling factor above allows the cancellation in ratio of the stretch-dependence γ of the rates.

One can achieve the main result of this paper with the simplifying approximations above, and noting that the arguments of the hyperbolic sines are much larger than unity. By taking the ratios of the analytic single-exponential rates, we can compute a predicted rate $R_{pre}(E)_n$ for dominant single-quantum vibrational relaxation path from some initial level n , at a collisional energy E , if we know a single rate $R(E_s)_{s \rightarrow s-1}$, at the same or a different energy E_s , and the effective exponential slope α of the repulsive core for that collisional energy. Because of its handy simplicity of form, experimentalist colleagues affectionately dubbed the scaling relation as the *Handy Relation*, R_{hdy} . After *much* algebra, "one can show that":

$$R_{pre}(E)_n = \frac{R_{hdy}(n, E)}{R_{hdy}(s, E_s)} \cdot R(E_s)_s \quad (23a)$$

where

$$R_{hdy}(n, E) = A \alpha^{-6} f(n, E) \exp\left(\frac{\chi(n, E)}{\alpha}\right) \quad (23b)$$

$$f(n, E) = n \omega (1 - 2 x_e n) \frac{\mu^{1.5} (E + \zeta)^{1.5}}{m E} \sqrt{1 + \frac{\zeta}{E + \hbar \omega (1 - 2 x_e n)}} \quad (23c)$$

$$\chi(n, E) = -2 \pi \sqrt{\frac{2 \mu}{\hbar^2}} \left| \sqrt{E + \zeta} - \sqrt{E + \zeta + \hbar \omega (1 - 2 x_e n)} \right| \quad (23d)$$

where A is a constant for the collision system under study.

To use this *a priori*, one would need to know the exponential slope α . This is not generally the case, though. However, if a set of data is available, such as experimental measurements of relaxation from several different initial vibrational states for the same collisional energy, then simple regression methods can yield a fit for the best values of α and A. To see how this is done, assume one has a data set of rates $D_n = R(E_n)_{n \rightarrow n-1}$. (Generally, the collisional energies E_n will all be the same.) The exponential form of $R_{\text{hdy}}(n, E)$ yields a simple linear expression to be fitted by standard least-squares routines:

$$\ln\left(\frac{D_n}{f_n}\right) = (\alpha_{\text{fit}})^{-1} \chi_n + \ln\left[\frac{A_{\text{fit}}}{(\alpha_{\text{fit}})^6}\right] \quad (24)$$

where $f_n = f(n, E_n)$ and $\chi_n = \chi(n, E_n)$. This is in the form $y_n = a x_n + b$. The least squares fit for a gives the exponential slope α_{fit} , which can in turn be used along with b to obtain the constant A_{fit} . (If one is using experimental data with error bars δ_n , one can use standard expressions¹⁶ for the weighted least squares fit by approximating the standard deviations as $\sigma_n = 0.5[\ln(D_n + \delta_n) - \ln(D_n - \delta_n)]$.) Once this is done, prediction of unknown rates can be made from the fit.

The analytic scaling relation has a particularly appealing form if we only need to predict rates at a single temperature. (In all that follows we will assume the collisional energy for a gas at temperature T is given by $E = 3kT/2$. Assume that we know the fundamental rate $1 \rightarrow 0$, i.e., $s=1$. Because the well depth ζ is generally small compared to the vibrational spacing, the scaling relation for $n \rightarrow n-1$ transitions reduces to:

$$R_{\text{hdy}}(E)_n = \frac{n(1 - 2x_e n) \exp\left[\frac{2\pi}{\alpha} x_e \sqrt{\frac{2\mu\omega}{\hbar}} (n-1)\right]}{(1 - 2x_e)} R(E)_1 \quad (25)$$

We only need to make a one-parameter (α) fit of rates known for only a few different initial vibrational states to obtain the exponential slope α . Once this is done, rates at the same temperature can be easily interpolated or extrapolated.

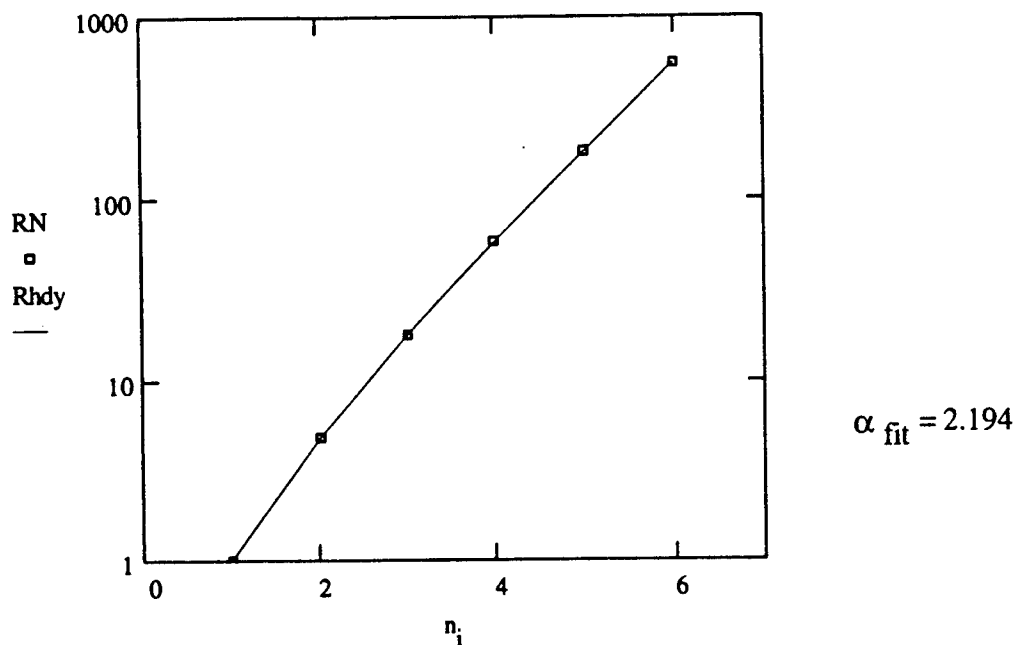
TESTS ON WELL CHARACTERIZED SYSTEMS

To test the efficacy of such handy expressions, extensive numerical tests were done on systems for which reasonable potentials can be exactly specified. The first is the HF(n) + He system cited above. Fully quantal, adiabatic distorted-wave calculations were made for $n \rightarrow n-1$ relaxation rates using the accurate double-exponential potential given above. The collisional energy was set to $E_T = 3kT/2$. Terms up to t^4 of the expansion for S were included in the computation of these quantal rates. All rates are normalized to the fundamental rate at $T = 300$ K. This rate was computed to be $R(300 \text{ K})_{1 \rightarrow 0} = 1385 a_0^3/\text{sec}$. These normalized rates are:

$$RN_n = \frac{R(E_T)_{n \rightarrow n-1}}{R(E_{300})_{1 \rightarrow 0}} \quad (26)$$

Quantum mechanical rates were computed for $n=1-6$ at a variety of temperatures. The quantal results at $T=300$ K, normalized to the fundamental $1 \rightarrow 0$ rates, are displayed in Figure 1 below, as small squares. At this temperature, the local kinetic energy is about 10% of the vibrational spacing. Note that the rates increase by a factor of about 70 as the initial level goes from $n=1$ to $n=6$. Simple harmonic oscillator arguments predict only a factor of 6 increase. It is the anharmonicity ($x_e=0.0218$ for HF), found in the exponentials of the $Rhdy(n,E)$ scaling function, that generates this sensitivity to initial quantum number. The solid line is the least squares fit to the quantal points, using the procedure (24) outlined to obtain α_{fit} . At this thermal collisional energy, the fit gives $\alpha = 2.194 a_0^{-1}$. This is extremely gratifying, since the best fit to the potential (17) has an $\alpha_{ab initio} = 2.20 a_0^{-1}$. This is a strong indication that all the approximations that led up to $Rhdy(n,E)$ are, at least, viable.

Figure 1: Normalized Quantal Rates RN for, and $Rhdy$ Fit of, HF($n \rightarrow n-1$) + He Relaxation Rates at $T = 300$ K

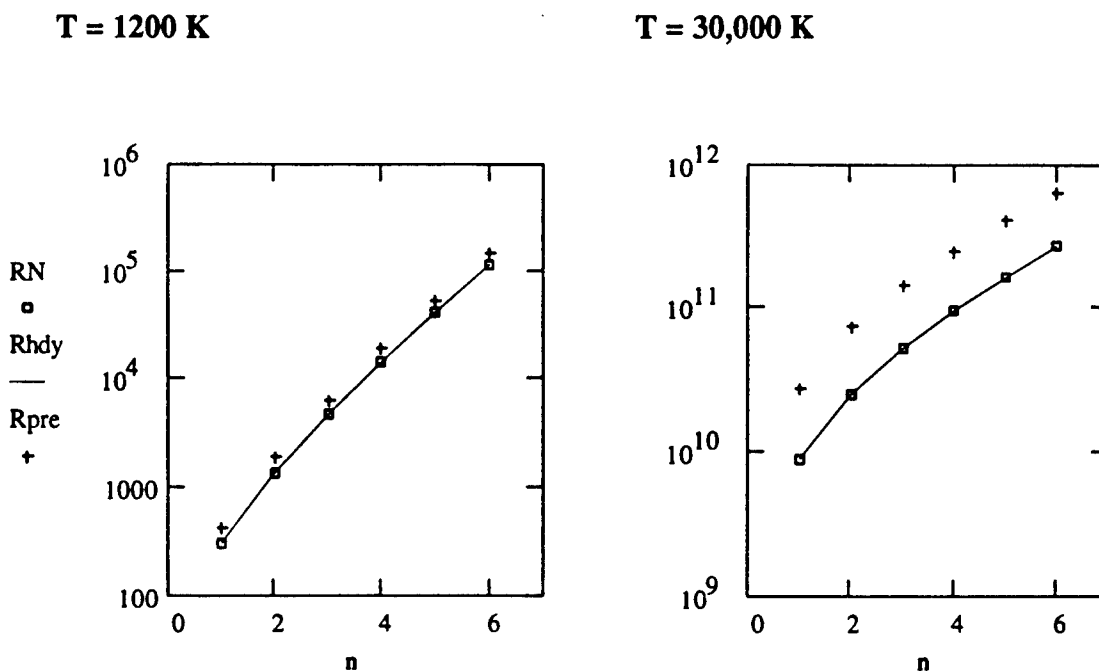


However, the viability of $Rhdy$ is more stunningly confirmed by calculations at higher kinetic energies. Figure 2 below shows results for temperatures of $T = 1,200$ K and $30,000$ K. In the former case, the collisional energy is about 30% of the vibrational spacing, while it is a factor of 7 larger at the higher temperature. All rates are normalized to the fundamental $1 \rightarrow 0$ rate at 300 K. Note that the rates are many orders of magnitude larger than the fundamental one. Again most of this can be directly traced to the anharmonicity of HF; for harmonic diatoms, the rates should be approximately a linear function of collisional energy. Note that the solid lines showing the fits produced by $Rhdy(E_c)$ hit the quantal points right on. For a given collisional energy, each is essentially a one parameter fit, the parameter being the exponential slope α_{fit} . The fact that the value of α_{fit} is slowly decreasing with increasing collisional energy (2.19 at 300 K, 2.15 at 1200 K, and $1.90 a_0^{-1}$ at 30000 K) is probably just a reflection of the slightly different exponential slopes of the potential that the collision samples as the turning points progress in. It should be recalled

that the quantal computations are based on the double exponential potential, and a single α cannot describe it everywhere. Again, it must be remembered that α is the effective exponential slope that the collision feels at a given collisional energy.

The most gratifying results are those predicted at 1200 and 30000 K, based solely on $\alpha_{\text{fit}}=2.194 \text{ a}_0^{-1}$ obtained for $T=300 \text{ K}$ transitions. These predicted rates $R_{\text{pre}_{n \rightarrow n-1}}$ are displayed as crosses in Figure 2. Consider the $6 \rightarrow 5$ relaxation at 30,000 K. The quantal normalized rate at 30000K is 2.68×10^{12} larger than the fundamental $1 \rightarrow 0$ at 300 K! Simple harmonic (as opposed to anharmonic) arguments predict only a factor of 600 larger, which is ten order-of-magnitude in error. However the rate predicted from the 300 K data is only off by a factor of about three. Thus the simple *Rhdy*(n,E) formula tracks the sensitivity of relaxation rates (to initial state vibrational state and collisional energy) accurately over twelve orders of magnitude.

Figure 2: Normalized Quantal Rates RN for, and Predictions of, HF(n) + He Vibrational Relaxation at Higher Temperatures

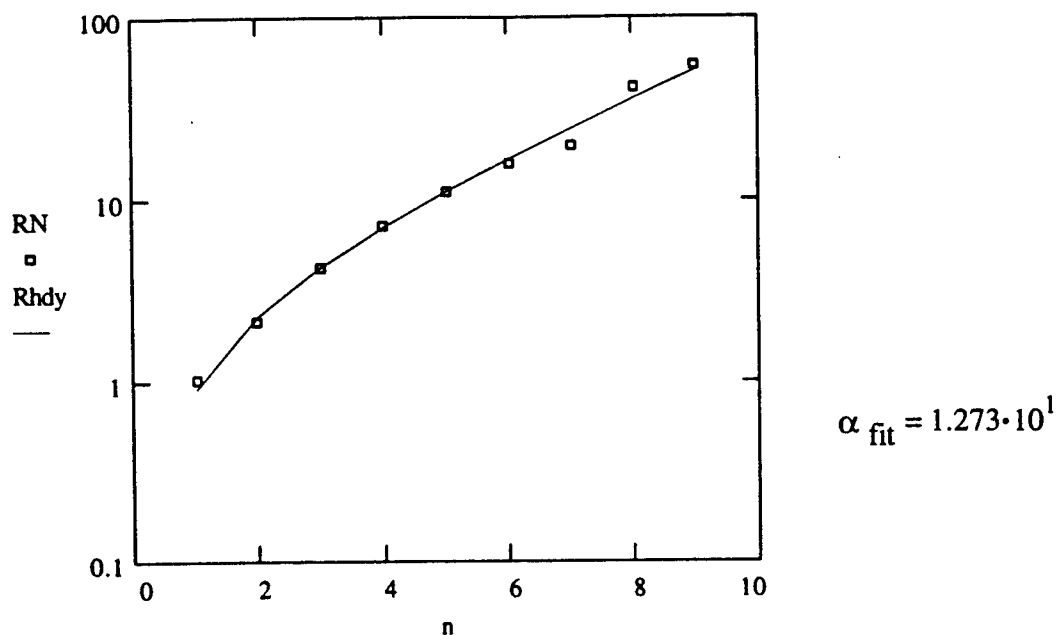


To make sure this result was not just a quirk of the HF + He system, a similar range of tests were conducted on the OH(n) + Ar. Although not a significant player in the atmospheric IR problem, the interaction potential between these two should be somewhat similar to a much more important OH collision partner: O₂. Eposti and Werner have computed an *ab-initio* orientation-dependent potential surface for the rigid-rotor OH + Ar system;¹⁷ i.e., only for the equilibrium separation of the diatom ($\Delta r = 0$). From this, the spherically averaged potential surface, $V(r_e, R)$ was determined, and to which a Morse potential was fitted. To get a breathing-sphere potential, the molecular stretch dependence needed for vibrational transitions was modelled by an exponential prefactor; i.e., $V_{\text{OH-Ar}}(r,R)=V(r_e,R) \exp(\gamma \Delta r)$. Since γ was not known for this system, it was simply set to 0.2 a_0^{-1} , a typically value in molecular systems. However, it should be noted that the handy relationships imply that the value for γ value should cancel out in the ratio of normalized rates. The numerical form of the potential is (in atomic units):

$$V(r, R)_{\text{OH}-\text{Ar}} = (91.16 \cdot \exp(-1.791 \cdot R) - 0.338 \cdot \exp(-0.896 \cdot R)) \exp(0.2 \Delta r) \quad (27)$$

Figure 3 below shows the normalized rates for OH($n \rightarrow n-1$) at a temperature of $T=300$ K, for $n=1-9$. Note that, as in the HF + He, the rates rise rapidly with initial vibrational excitation. And, as before, the exponential model approximations, inherent in *Rhdy* function (25), produce a very satisfactory fit to the quantal points, with $\alpha_{\text{fit}} = 12.73$. This value for the exponential slope is considerably larger than the one for the HF + He system. However, as we shall see, the experimental data on OH + O₂ imply a similar result.

Figure 3: Normalized Quantal Rates RN for, and *Rhdy* Fit of, OH($n \rightarrow n-1$) + Ar Relaxation Rates at $T = 300$ K



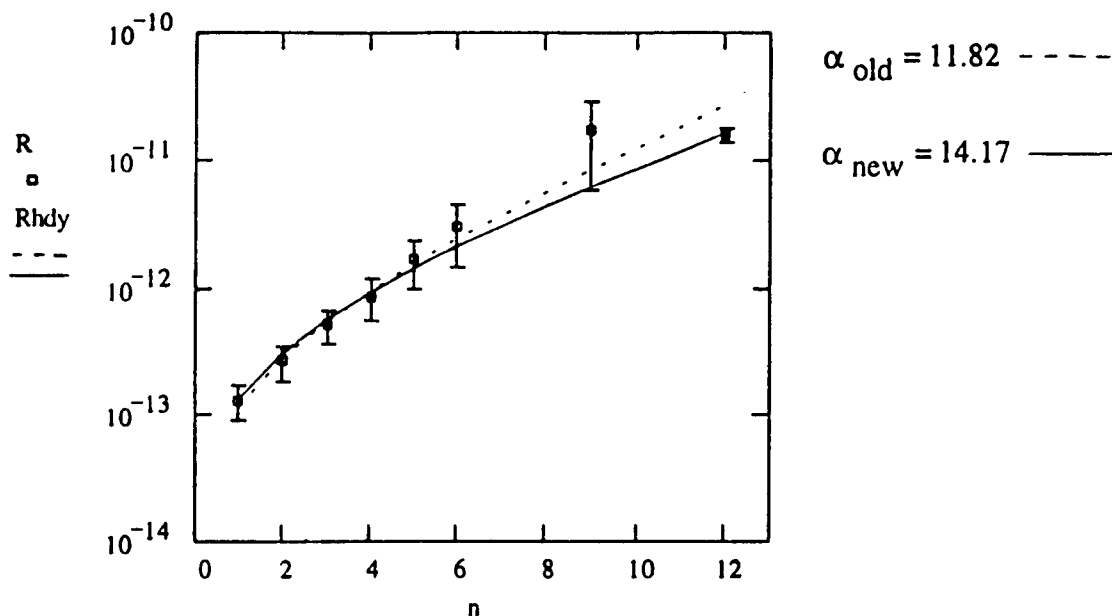
The ability of the simplified exponential model, as embodied in *Rhdy*(n, E), to mimic the quantal computations both in the HF + He and in the OH + Ar systems, and direct examination of products of T-matrix elements, confirm that virtual paths involving multi-quanta transitions are insignificant compared to the unique path involving single-quantum transitions. With confidence then, we can apply the *Rhdy* expressions to the fitting of experimental rates of interest for IR-active molecules in the atmosphere.

RATES FOR VIBRATIONAL RELAXATION OF OH AND NO IN COLLISIONS WITH O₂

The LABCEDE group at the US Air Force Geophysics Directorate has measured the vibrational relaxation for OH(n) due to collisions with O₂ at a temperature of $T=300$ K, for $n=1-6$.³ Other groups measure the OH rate for $n=9$,^{12,4,5} These are important processes in interpreting the level populations of OH and NO produced in the atmosphere.

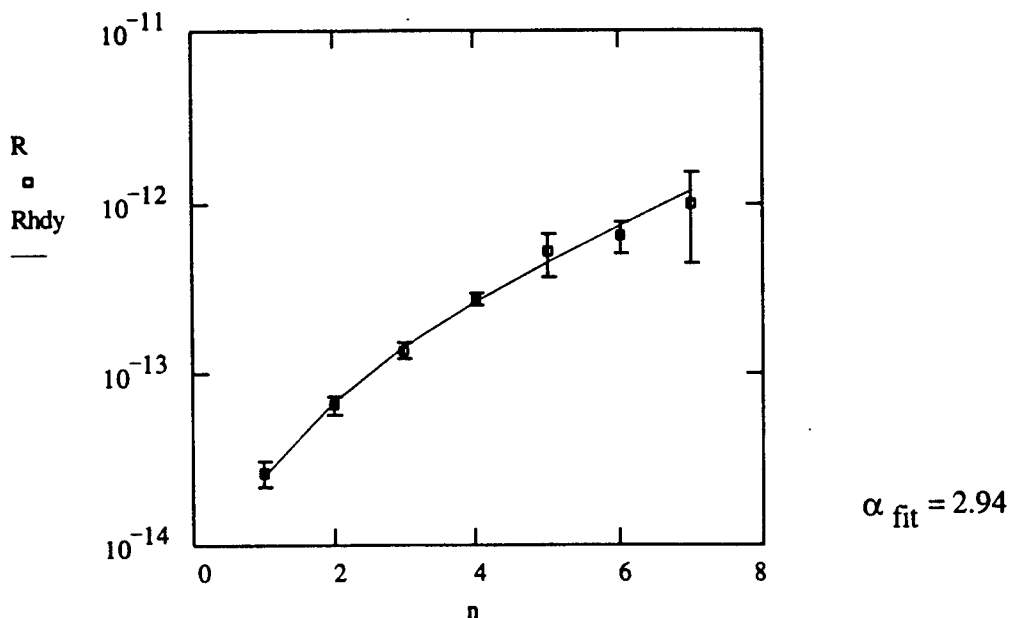
Because the data is all at the same energy, the simplified version of Rhdy (25) could be used to fit the data. Figure 4 shows the OH(n) + O₂ results. Experimental data are indicated by small squares, along with their associated error bars. The dashed line is the "old" fit that would result if only the LABCEDE data (n=1-6) were employed, giving an $\alpha_{old} = 11.82 \text{ a}_0^{-1}$. Note that it quite adequately predicts the "unknown" rates at n=9,12. If the full set of data is used, the "new" least-squares fit (solid line) indicates an exponential slope of $\alpha_{new} = 14.15 \text{ a}_0^{-1}$. Note that the "new" fit successfully goes through all the error bars, even though the rates increase over this range of vibrational levels by two orders of magnitude in a non-linear, non-exponential manner. Finally, the exponential slope obtained for the theoretical OH+Ar system ($\alpha_{OH-Ar} = 12.73 \text{ a}_0^{-1}$) is quite consistent with the value obtained for the experimental OH+O₂ system.

Figure 4: Rhdy Fit to Experimental OH(n) + O₂ Relaxation Rates at T=300 K
(rates are in cm³/sec; dashed line is α_{old} fit and solid line is α_{new} fit)



The final experimental system to be examined was the NO(n) + O₂ collision. The experimental relaxation rates come from the USAF LABCEDE Group.⁶ These rates and the exponential-model fit is shown in Figure 5. The value for the exponential slope is $\alpha_{NO-O_2} = 2.94 \text{ a}_0^{-1}$. As with the OH + O₂ relaxation process, Rhdy generates relaxation rates that go through all of the error bars.

Figure 5: *Rhdy* Fit to Experimental NO(n) + O₂ Relaxation Rates at T=300 K
(rates are in cm³/sec)



RELATIVE IMPORTANCE OF DOUBLE-QUANTA TRANSITIONS

In analyzing experimental data, it is useful to know if the relaxation rate out of a particular vibrational level is dominated by the single quantum transition $n \rightarrow n-1$, or if multiple-quanta transitions (e.g., $n \rightarrow n-2$) are significant. As already demonstrated, the dominate term is always the path through single-quantum virtual transitions in the perturbation expansion (9) for the S-matrix in terms of the first-order distorted-wave T-matrix (i.e., t).

If the spirit of the handy relationships, the double-quanta rate can be shown to be related to single quantum rate by:

$$R(E_c)_{n \rightarrow n-2} = RD(\alpha)_n R(E_c)_{n \rightarrow n-1} \quad (28)$$

where $RD(\alpha)_n$ is the relative strength of the double-quanta transition given by:

$$RD(\alpha)_n = \pi^2 |t(\xi, L=0)_{n-1 \rightarrow n-2}|^2 \quad (29)$$

Note that this involves the single-quantum coupling *from* the next level down. The analytic evaluation of the s-wave matrix element will depend upon the value α chosen for the exponential slope. Because this is evaluated at the common total energy $\xi = E_c + \epsilon_n$, this s-wave T-matrix element associated with an asymptotic exit collisional kinetic energy of $K_n = \xi - \epsilon_{n-1} = E_c + h\omega(1 - 2x_e n)$. Since the vibrational spacing is so large compared to thermal kinetic energies ($E_c \ll h\omega$), we see that $K_n \gg E_c$ for thermal collisions.

If we give the stretch perturbation parameter γ a conservative typical value of 0.5, we can produce an expression for the relative strength that depends *only* upon the α exhibited at the high kinetic energy K_n :

$$RD(\alpha)_n = \frac{\pi^2 \mu}{\alpha^4 m} \left(\frac{2\mu}{\hbar^2} \right) (n-1) \hbar \omega [1 - 2x_e(n-1)] (0.5)^2 \quad (30)$$

$$\times \exp \left[-\frac{2\pi}{\alpha} \sqrt{\frac{2\mu}{\hbar^2}} \left[\sqrt{E_c + 2\hbar\omega(1 - 2x_e n + x_e)} - \sqrt{E_c + \hbar\omega(1 - 2x_e n)} \right] \right]$$

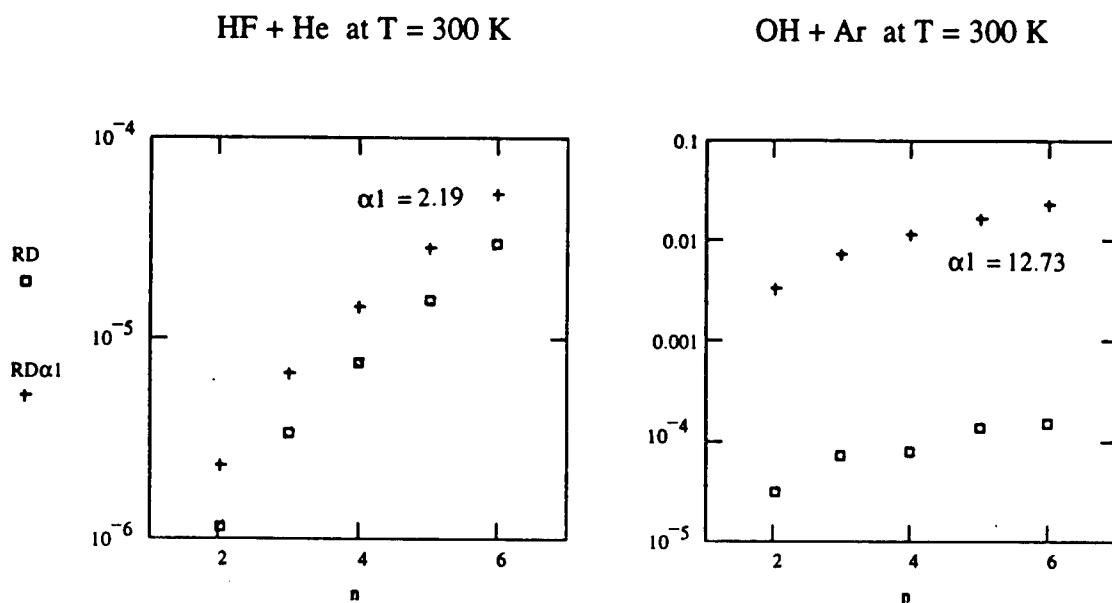
Alas, we do not typically know the value of α for high kinetic energies. But we do "know" that the effective exponential slope $\alpha(E)$ usually decreases with incident kinetic energy E . If we define $\alpha_1 = \alpha(E_c)$ and $\alpha_2 = \alpha(E_c + \hbar\omega)$, then we know that $\alpha_2 < \alpha_1$. From this we can infer that the true strength for a double-quanta relaxation ($n \rightarrow n-2$), relative to the single-step relaxation to the next lower level ($n \rightarrow n-1$):

$$RD = R(E_c)_{n \rightarrow n-2} / R(E_c)_{n \rightarrow n-1} \quad (31)$$

will satisfy the condition $RD < RD(\alpha_2) < RD(\alpha_1)$. Since we know α_1 from our fit to the rates at a collisional energy E_c , $RD(\alpha_1)$ is an upper-bound estimate to the true relative strength of double-quanta transitions.

This can be tested on the HF + He and OH + Ar systems at $T=300$ K. The results are displayed in Figure 6. Note that the relative strengths of the quantum mechanical double-quanta rates RD are very small. That is the reason that only vibrational relaxation to the next lower level needs to be considered in the analysis of experimental data. The expression for $RD(\alpha_1)$ gives a very good estimate for the double-quanta strength in HF + He. It is significantly less good in the OH + Ar case; the reason for this is still unclear. However, in each system the simple expression for $RD(\alpha_1)$ does a useful job in giving upper-bound values for the relative importance of double-quanta relaxation rates. Any laboratory investigator can employ this simple formula to check, in most applications, if he or she needs to consider the role of double-quanta transitions.

Figure 6: Ratio of Double-Quanta ($n \rightarrow n-2$) to Single-Quantum ($n \rightarrow n-1$) Rates



SUMMARY

The primary purpose of this project was to develop handy, yet accurate formulae to determine desired, but unknown vibrational relaxation rates from a limited set of experimental values or theoretical information. The major results of this effort are:

1) Single-quantum transition paths are the only ones that need to be considered in relaxation computations.

The scattering matrix can be written as a relatively straight-forward power series expansion in terms of first-order distorted-wave matrix elements of the transition coupling. Matrix elements that couple states differing by more than one vibrational quanta are much smaller than elements that differ by only a single quantum. In the series expansion for the S-matrix, the dominate term that determines the strength of transitions between any two real levels that differ by more than one quantum is the path through virtual states that is made of the minimal number of single-quantum first-order elements [e.g., see (10)].

2) Transitions to the next lower vibrational level dominate the relaxation process.

Because of the result cited above, one can readily argue that transitions to the next lower level dominate the relaxation process out of a given excited vibrational state of the molecules of interest in this study. Products of small coupling single-quantum elements will always be less than the single one describing the direct transition to the next lower level. Thus, multi-quanta transitions (e.g., $n \rightarrow n-2$) will be insignificant compared to single-quantum relaxations ($n \rightarrow n-1$) from the same excited vibrational level.

3) Handy formulae that are easy to employ can accurately predict vibrational relaxation rates.

Formulae for vibrational relaxation were derived that accurately track vibrational relaxation over many orders of magnitude. The one major parameter in the model is the exponential slope of the repulsive core of the atom-diatom interaction potential. Their simple form (23 and 25) make them handy expressions for fitting known experimental data (24) to interpolate or extrapolate to desired, but unknown or uncertain rates. The accuracy of these handy semiquantal formulae to describe vibrational relaxation were demonstrated in several collisional systems: $\text{HF}(n) + \text{He}$, $\text{OH}(n) + \text{Ar}$, $\text{OH}(n) + \text{O}_2$, and $\text{NO}(n) + \text{O}_2$.

REFERENCES

1. See, for example, J.A. Dodd, S.J. Lipson, J.R. Lowell, P.S. Armstrong, W.A.M. Blumberg, R.M. Nadile, S.M. Adler-Golden, W.J. Marinelli, K.W. Holtzclaw, and B.D. Green, *J. Geophys. Res.* **99**, 3559 (1994) and references therein.
2. See, for example, S.J. Lipson, P.S. Armstrong, J.A. Dodd, W.A.M. Blumberg, J.R. Lowell, and R.M. Nadile, "Thermospheric Nitric Oxide Number Densities and vibrational Distributions from High Resolution Earthlimb Spectra", manuscript in preparation.
3. J.A. Dodd, S.J. Lipson, and W.A.M. Blumberg, *J. Chem. Phys.* **95**, 5752 (1991).
4. B.R. Chalamala and R.A. Copeland, *J. Chem. Phys.* **99**, 5807 (1993).
5. A.D. Sappey and R.A. Copeland, *J. Chem. Phys.* **93**, 5741 (1990).
6. B.D. Green, J.E. Caledonia, R.E. Murphy, F.X. Robert, *J. Chem. Phys.* **76**, 2441 (1982).
7. D. Rapp and T. Kassal, *Chem. Rev.* **69**, 61 (1969); R.B. Bernstein (ed.), *Atom-Molecule Collision Theory: A Guide for the Experimentalist* (Plenum, New York, 1979).
8. T.F. Ewing and R.W. Conn, *Chem. Phys.* **26**, 201 (1977).
9. T.F. Ewing, J. Detrich, and R.W. Conn, *J. Chem. Phys.* **69**, 4662 (1978).
10. R.J. Bieniek, *J. Chem. Phys.* **79**, 3738 (1983).
11. T.F. Ewing and R.W. Conn, *Chem. Phys.* **36**, 407 (1979).
12. R.J. Bieniek, *J. Chem. Phys.* **73**, 851 (1980).
13. R.J. Bieniek and S. Green, *Astrophys. J. Lett.* **265**, L29; and (E) **270**, L101 (1983).
14. K.P. Huber and G. Herzberg, *Molecular Spectra and Molecular Structure. IV: Constants of Diatomic Molecules* (Van Nostrand Reinhold, New York, 1979)
15. F.H. Mies, *J. Chem. Phys.* **40**, 523 (1964).
16. W.H. Press, B.P. Flannery, S.A. Teukolsky, and W.T. Vetterling, *Numerical Recipes* (Cambridge University Press, Cambridge, 1986).
17. A. Degli-Esposti and H.-J. Werner, *J. Chem. Phys.* **93**, 3351 (1990).

CONCEPTUAL STUDY OF THE MARAUDER OPERATION
IN THE NEUTRON PRODUCTION MODE

by

Jan S. BRZOSKO
Research Professor
Department of Physics and Engineering Physics
Stevens Institute of Technology
Castle Point Station
HOBOKEN, NJ 07030

Final Report for:
Summer Faculty Research Program
Phillips Laboratory, Kirtland AFB

Sponsored by:
Air Force Office of Scientific Research
Bolling Air Force Base, DC
and
Phillips Laboratory

August 1994

CONCEPTUAL STUDY OF THE MARAUDER OPERATION
IN THE NEUTRON PRODUCTION MODE

by

Jan S. BRZOSKO
Department of Physics and Engineering Physics
Stevens Institute of Technology

A b s t r a c t

The potential use of the MARAUDER facility, operational at SHIVA-STAR capacitor bank, for D-D and D-T neutron production were studied. Three schemes of neutron production were considered: (a) compact toroid (CT) collision against a solid target; (b) use of the CT as opening switch for the plasma focus action; and (c) MARAUDER operation in the plasma focus mode (without CT formation). All three schemes are promising a possibility of producing E(18)/shot of 14 MeV neutrons (for W=9 MJ). This is the yield necessary for nuclear explosion simulation and advanced material technology. The above estimates were done keeping in mind the use of existing hardware at the PL/WSP. This opens an exciting opportunity to challenge the Russian projects presently on an advanced level of execution.

N o t e : This report is a summary of concepts that the author developed during his 12-weeks stay at Phillips Laboratory. Many elements presented here were already "circulating" in the High Energy Plasma Division PL. Other concepts were developed following long hours of discussion with HEPD/PL colleagues, to whom the author is truly grateful. Special thanks are extended to Dr. James H. Degnan and Dr. Gerry Kiuttu for the introduction to MARAUDER physics and technology, Dr. Robert Peterkin and Dr. Norman F. Roderick for the explanation of CT-acceleration and target collision phenomena and to Maj. Allen Chesley for the computer visualization of PF/MARAUDER operation principles in the neutron mode.

CONCEPTUAL STUDY OF THE MARAUDER OPERATION
IN THE NEUTRON PRODUCTION MODE

by
Jan S. BRZOSKO

1. INTRODUCTION

Recently, Phillips Laboratory had performed studies (experimental and theoretical) on the magnetized plasma structures known as Compact-Toroids (CTs). These plasmas are axially symmetric, donut-shaped low-beta configurations with both poloidal and toroidal magnetic fields. Due to field relaxation to its minimum energy state between concentric electrodes, CT is MHD stable and can be accelerated and compressed in a coaxial gun configuration. This research program with its facility installed on the 9.4 MJ SHIVA-STAR fast capacitor bank, has been named MARAUDER. Its goal is to compress toroids to high mass density and magnetic field intensity, and to accelerate the toroids to high speed [1-3]. So far, using 1 MJ of stored energy, CT (mass of 1-5 mg of H, N, Ne or Ar) was accelerated to 40 cm/us (speed defined at electrodes muzzle). Factor nine in simultaneous compression in radius and thickness each was achieved (40cm/us with factor 3 compression at 1 MJ operation; 15cm/us extraction with factor 9 compression at 1MJ operation).

There are a variety of applications for compressed and accelerated toroids that are under vigorous studies at Phillips Laboratory. There are: X-ray sources, fast opening switches, radio-frequency compressors, charge-neutral ion beam sources and inertial confinement fusion option. In this report we discuss the potential use of the MARAUDER facility as a neutron source. We are also going to identify questions that should be answered before experimental program definition.

The Government's demand for a neutron sources of high yield in fast neutrons ($> E_{18}$ neutrons/s of 2.5 MeV and/or 14 MeV), required for advanced material technology and nuclear weapon simulation, has yet remained without a feasible solution. The review of the literature shows that existing (or almost existing) neutron sources are based on the following concepts:

- (a) use of the electrostatic accelerators (limited at E_{11} to E_{13} n/s [4,5] depending on the design);
- (b) use of the Q-machines (promise of E_{13} n/s), and
- (c) use of the plasma sources of plasma-focus type (capable of producing E_{14} neutrons (14 MeV) in 200-500ns pulses with Hz frequency potentials [6]).

The review of the conceptual designs of hyper-intense neutron sources ($> E_{18}$ n/s) [7-9] reveal that this type of enterprise will cost at least 500 M\$. Many of the proposed solutions will deliver fast neutrons (>10 MeV) distributed on a very broad energy range clearly limiting the material studies. The only proposal that tends toward less expensive solutions, while oriented on 14 MeV neutron production (with option for 2.5 MeV) is the CAPT-10 [10]. This is

the advanced concept of what is known as plasma focus device. The projects of hyper-intense neutron sources which have passed prototype stage and are in the final design stage of machine are in Russia, e.g.

- (i) Gas Dynamic Trap at Novosibirsk [11,12] which still has to solve problems with the superconducting magnet [13], and
- (ii) Filipov-type plasma focus using 1-GJ magnetic storage located in Troitsk (common effort with Kurchatov Inst.At.En., and VNIIEF-Arzamas [14]).

In present situation where some military research facilities are joining pro-industry effort in development of competitive technologies, it is legitimate to examine whether MARAUDER facility can be turned to hyper-intense neutron source prototype. In fact it may become useful for nuclear weapon simulations while simultaneously serve in material research (as an example see Refs.7-9) or serve as facility for the brain cancer treatment (as an example see Ref.15).

2. BRIEF INTRODUCTION TO THE PRESENT SCHEME OF MARAUDER OPERATION

The design concept and some details of the existing MARAUDER hardware are shown in Fig.1. A basic sequence of physical phenomena are as follows (also see Fig.2):

(1) A slowly rising magnetic field (radial) feed by external magnetic field coils is imposed in the coaxial gun electrode gap above the formation bank transmission line.

(2) When the radial magnetic field reaches its peak value (see Fig.2a), neutral gas (mono- or multi- elemental) is injected into electrodes gap by a set of fast gas valves distributed evenly around the circumference.

(3) Voltage from the formation bank is applied (between the inner and outer conductor) with controlled delay related to opening of the gas valves.

(4) The breakdown in the injected gas develops, producing a highly conductive plasma. This "freezes" the radial magnetic field together with the toroidal (azimuthal) field, B , produced by the current flowing across the plasma (between electrodes).

(5) The $B \times J$ forces push the plasma and its embedded radial fields into the formation region. The initially radial magnetic field lines became stretched (see Fig.2b) and are given a twist by the toroidal field from the formation discharge.

(6) A bubble of mass (1-5mg) and magnetic fields (poloidal and toroidal) moves from the gas injection region toward the expansion region. The stretched helical magnetic field lines reconnect at the neck of the toroidal bubble on a time scale that is short compared with that of classical diffusion. Thus a toroidal plasma with nonzero magnetic helicity, i.e. with closed poloidal magnetic field lines linked with closed toroidal magnetic field lines is formed. The object produced in this way relax to a minimum free energy state (Woltier-Taylor state) and is called "Compact Toroids" (CTs). The poloidal component of magnetic fields and mass distribution at

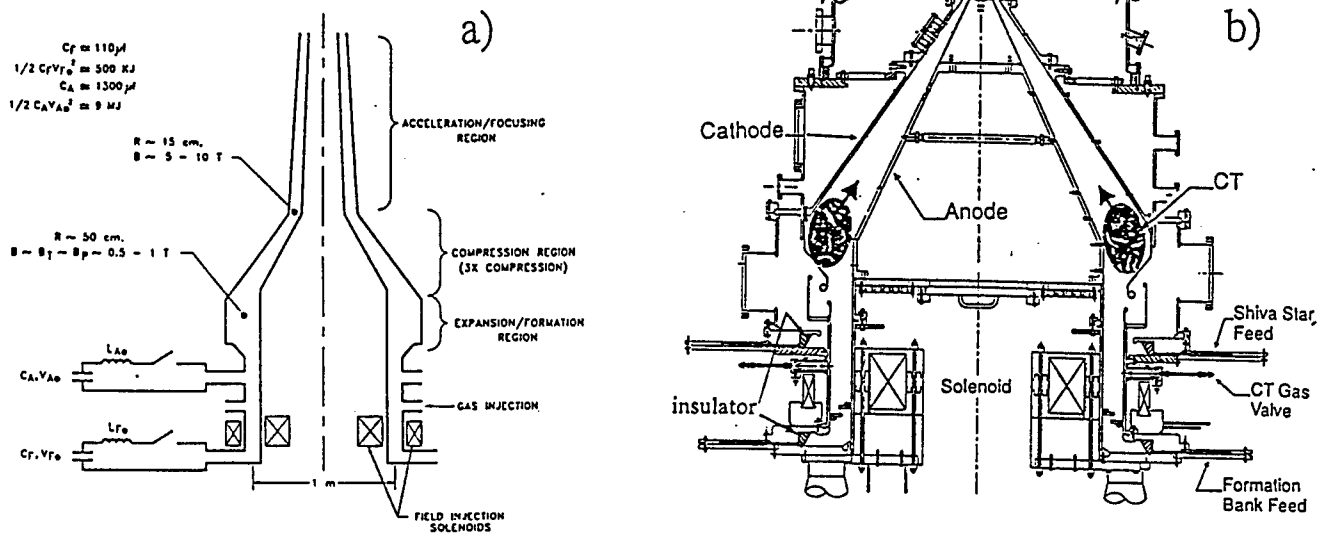


Fig.1. MARAUDER design concept (a) [see Ref.1] and some hardware details (b) [see Ref.3] relevant to the discussion of the operation principles.

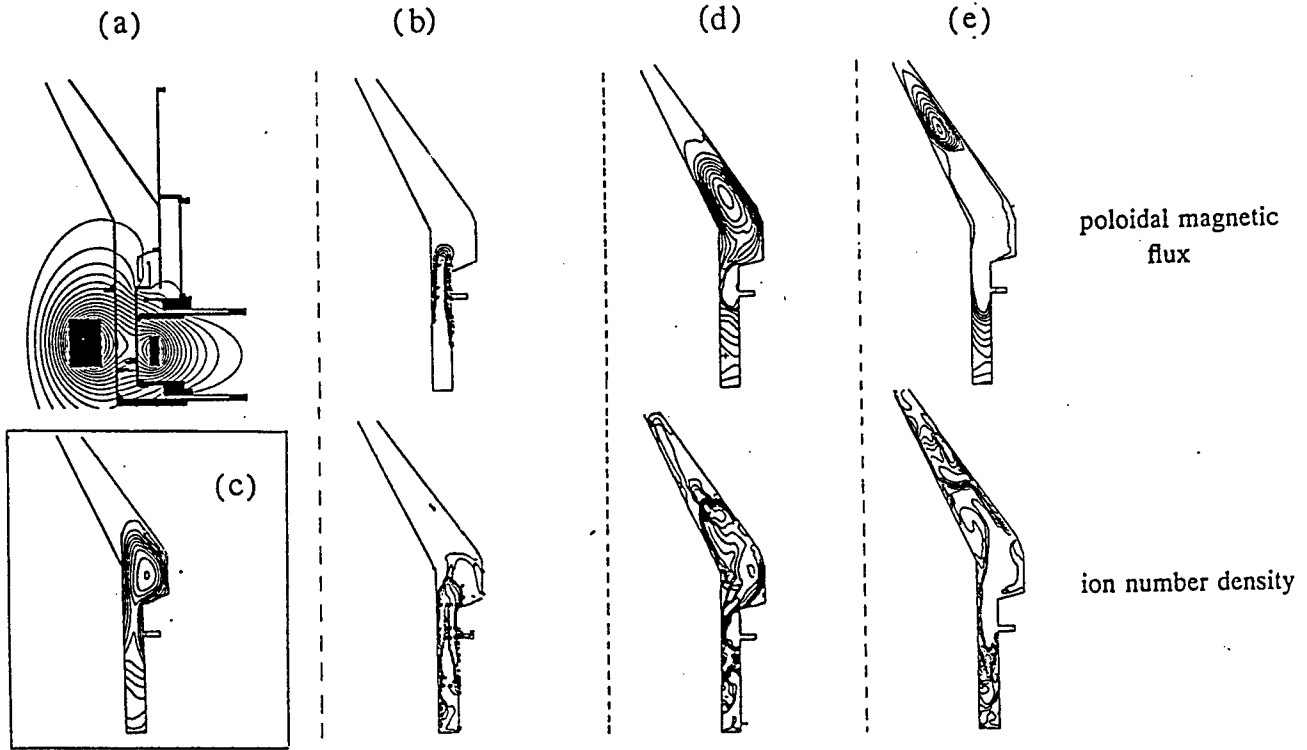


Fig.2. Sequence of physical phenomena occurring in MARAUDER facility operating with conical electrodes. Most of the pictures are copied from published papers. Some of them (when applicable) are adopted from the studies of coaxial geometry. The geometry corresponds to the right-hand side of Fig.1. Poloidal magnetic fields and mass density profiles shown here were calculated with 2 1/2 dimensional magnetohydrodynamic code MACH2.

- (a) The initial bias magnetic flux distribution at the instant of gas injection.
- (b) Poloidal fields and atomic density before relaxation to equilibrium state. The iso-contour lines are at 0.1T step for the fields ($B_{max}=0.7T$), and two contours per decade of ion density ($N_{max}=5 \times 10^{15}/\text{cm}^3$).
- (c) CT at the state of equilibrium.
- (d) CT at the beginning of acceleration/compression phase.
- (e) CT at arrival to the electrodes muzzle.

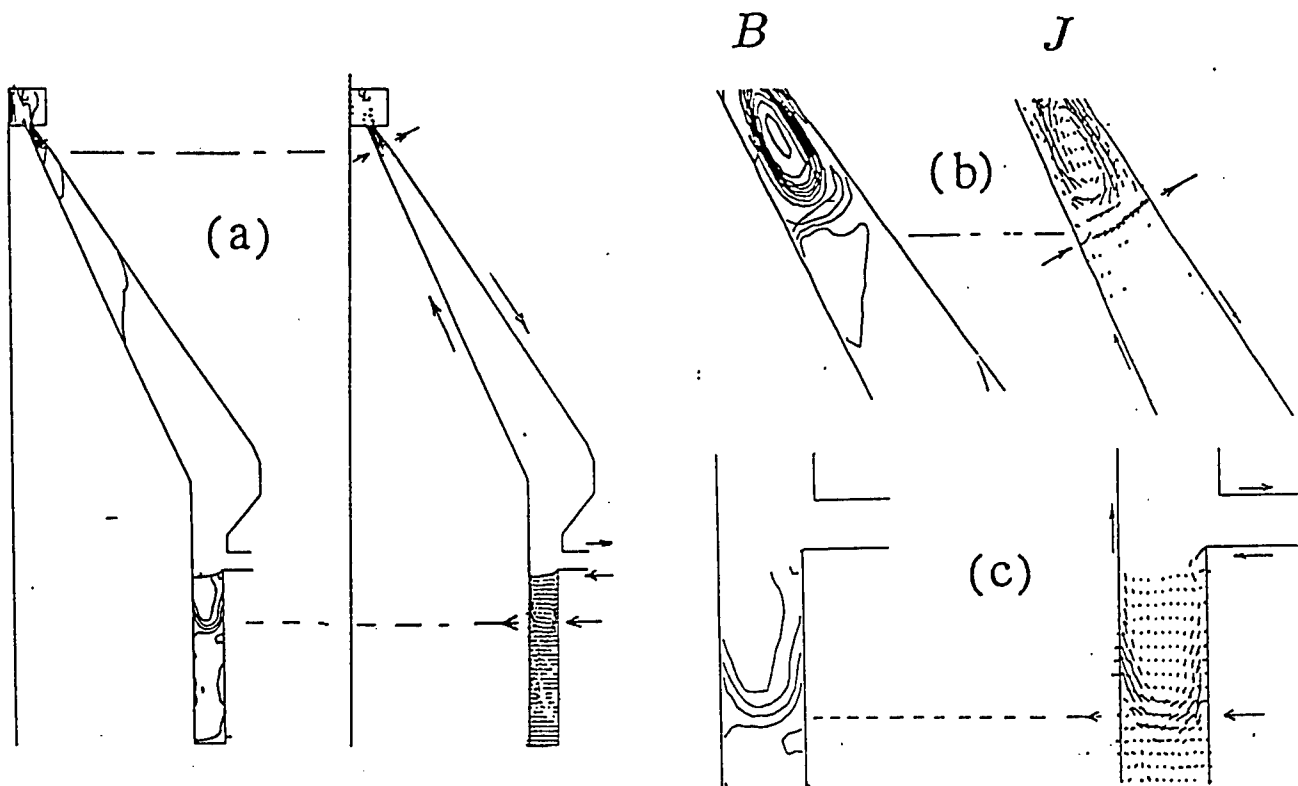


Fig.3. Comparison of the magnetic fields (left column; B) and current density (right column; J) for $T=3.05 \text{ E}(-5) \text{ s}$. (a) is the snap-shot of the whole interelectrode gap, (b) and (c) are magnification of the near muzzle and below Shiva-Star feed regions, respectively. Simulations [16] were done for 1.5 mg of neon formed CT at 0.6 MJ Shiva-Star feed. Poloidal field of about 0.6 T holds during the entire sequence of snap-shots. Arrows outside the electrodes point in the direction of current flow in the electrodes. Horizontal dashed lines show altitude at which diffused current flows between electrodes, and long/short dashed lines mark the position of current in the plasma sheath associated with the accelerating piston.

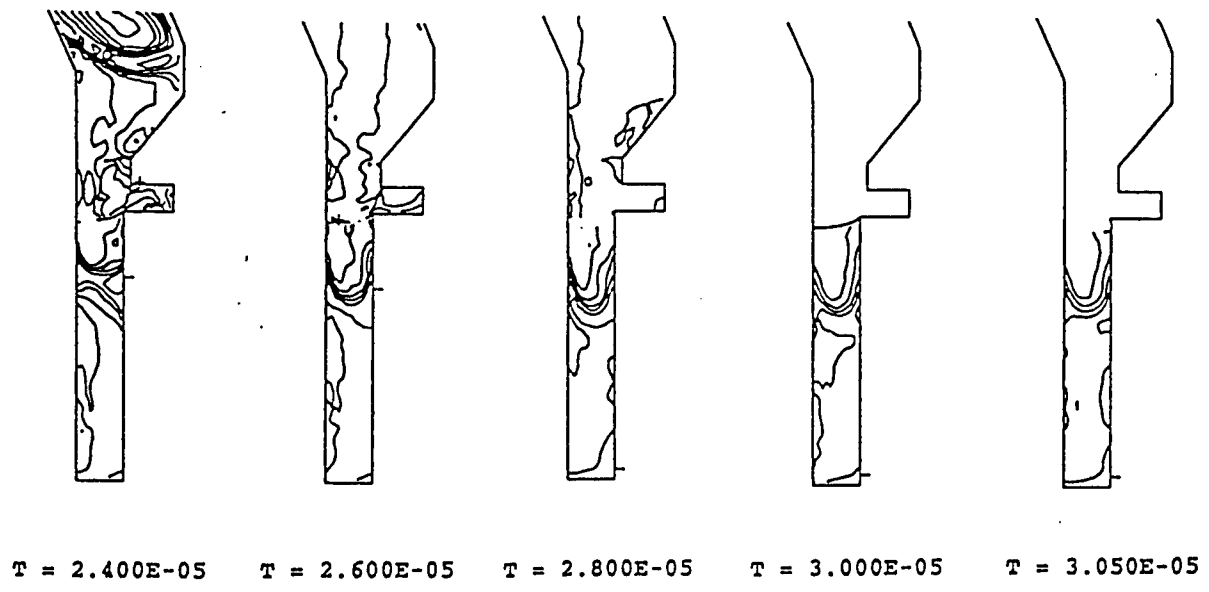


Fig.4. Pattern of the magnetic fields in the formation region during acceleration/compression phase. Time T from the formation discharge is given in [s]. For other information see Fig.3.

this stage are shown in Fig.2c.

(7) When the CT is formed, the SHIVA-STAR bank is fired. The discharge pushes the CT down stream, out of formation volume, accelerating and compressing it (see Fig.2 d and e). The CT acts like a gasket, within the compression region, as it maintains contact with the conducting walls and keeps magnetic flux from the compression discharge behind it. The magnetic piston fields pushing the CT cannot exceed the CT fields, to avoid blow-by of piston field and enable self-similar compression of the CT.

(8) The next step of operation (and fine tuning of CT parameters) depends on the considered application. Therefore it shall be discussed as part within the variety concepts pertaining to the neutron mode of MARAUDER operation.

The current loop (see Fig.3) that supplies energy to the magnetic piston has a trajectory composed of the following paths: (i) from the SHIVA-STAR feed, via outer electrode to actual piston position, (ii) across the electrodes through a thin plasma sheath forming CT-pushing piston, (iii) from the piston position returning via inner electrode to the altitude of radial fields injection, (iv) across the electrodes gap through diffused plasma, trapped in the region of maximum radial magnetic fields produced by coils, (v) to the SHIVA-STAR feed via the external electrode.

One has to recognise that the current reconnecting electrodes at the level of the coils (source of poloidal fields) is diffuse. It is also well held in the same position through the entire time of the acceleration/compression and the utility (post compression) phases (see Fig4).

3. BRIEF INTRODUCTION TO FUSION PHENOMENON IN THE PLASMA FOCUS DEVICES

When comparing different plasma fusion devices and accelerators, one can find that plasma focus (PF) machines are the most economically feasible source of neutrons (see Ref.10), provided that operation commences at MJ capacitor bank level. However, a draw back of PF-machines resides in their discharge being initiated on the insulator's surface, due to: (i) restrikes on the insulator during PF maximum compression; (ii) exposure of the insulator to large mechanical stresses during discharge formation; and (iii) exposure of insulator to high radiation doses during the nuclear reactivity phase.

If one can initiate discharges in the gap between electrodes (without current flow at insulator surface) while preserving the formation of a thin, dense and impenetrable to magnetic fields plasma sheath, then such a design will have potentials to become a hyper-intense neutron source machine.

Design and operation concept of Plasma-Focus is shown in Fig.5. The discharge chamber is usually prefilled with D2 or D2+T2 gas at $p = 0.5-15$ Torr depending on PF-mode of operation. For the neutron mode of operation this pressure is $p > 3$ Torr, while for the beam mode $p < 2$ Torr. The particular pressure interval is dependent on circuit-parameters of the energy supplying system. It is

important to recognise that in the neutron optimized mode the yield (Y_n) dependence on the filling gas pressure is flat in the wide range of gas pressure ($\Delta p/p_{av} > 0.5$) and rapidly decreases outside of it. The following text refers mainly to the Mather-type PF, since neutron yield (from shot-to-shot) is relatively stable (10-25%) for long periods of operation [17].

The plasma focus operation can be divided into the following phases:

(1) Initiation of the discharge i.e. breakdown, sheath formation and take-off. The breakdown occurs along a cylindrical insulator and is governed by a modified version of the Paschen's law [18,19]. Stable and unified plasma sheath (PS) is formed under conditions that: (a) driving magnetic pressure is sufficient to provide the necessary work for ionization and plasma heating [$B^2/2\mu_0 > 2N_0(Q_d+Q_i)$]; and (b) surface energy density (on insulator) does not exceed the experimentally determined limit ($\{N_e kT_e + N_0(Q_d+Q_i)\} * d < 100 \text{ J/cm}^2$, [18]), where N_e and N_0 are the electron and filling densities respectively, Q_d and Q_i are the dissociation and ionization energies, respectively, and d is the sheath thickness.

(2) Run-down phase of the plasma sheath (PS). After its formation, the PS begins a lift-off from the insulator surface due to the $B \times J$ magnetic forces and accelerates in the direction of the electrode muzzle. The current sheath moving with the velocity ca. $E(7) \text{ cm/s}$ into unperturbed deuterium gas region generates a shock front (thickness typically $< 1 \text{ mm}$ corresponding to the free mean path of neutrals) as its Mach number at that point is of the order of 100. Deuterium molecules go through this front in about 1 ns. This time is about two orders of magnitude less than the ionization relaxation time. Therefore, a nonequilibrium transition region, with a temperature of several eV, exists. It gradually develops into a plasma layer, where 100% of ionization ($kT_e > 20 \text{ eV}$, $N_e \sim E(18)/\text{cm}^3$) and equilibrium is established. The dynamics of the run-down (and compression) phase is pretty well described by the second Newton's law and the circuit equation. For a well operating system three conditions are fulfilled: (i) almost all momentum increase is allocated in the increase of the PS-mass, (ii) ohmic resistivities of the external circuit and plasma are negligible, and (iii) inductance of the electric circuit is comparable or smaller than plasma inductance.

(3) Radial compression phase. When plasma sheath arrives at the end of the electrode muzzle it changes the direction of motion from axial to radial, forming an inward moving funnel type sheath. The radial compression is described well by the similar equations as in the rundown phase. Here however the driving magnetic force has $B \sim 1/r$ dependence instead of the position independent B occurring in the axial phase. This allows for a rapid acceleration (up to $E(8) \text{ cm/s}$) of the funnel-shaped plasma sheath before the funnel itself reaches a radius comparable with the plasma sheath thickness ($r < 3 \text{ mm}$). For $r < 3 \text{ mm}$ collision of sheaths have to be included in the description of the process. At the maximum of compression (pinch instant) plasma achieves density of $n = 1 E(19)/\text{cm}^3$ and electron

temperature of $kT_e = 0.1 \text{ keV}$ [20,21] but neutron emission is negligible as compared to the following phase i.e. plasma column formation and disruption phase.

(4) Nuclear activity phase. Collision of quasi-cylindrical plasma sheaths on the PF axis leads to the heating of plasma and initiates its reverse movement. This soon (within 30 ns) stagnates due to magnetic pressure outside of the plasma, compensating the expansion momentum. The column itself may be 1-2 cm in dia. and 10 cm long, remaining stable for 50-100 ns. After this time instabilities begin developing, leading to plasma decompression. The strong neutron and hard X-ray signal accompanies the disruption of the plasma column. At that point the plasma is characterized by $kT_e=0.3-0.6 \text{ keV}$ and $n=2-4 \text{ E}(18)/\text{cm}^3$, only. Fig.6 shows the sequence of Schlieren pictures recording plasma evolution and the relation to neutron yield, Y_n . It is well established [22] that Schlieren images and X-ray (1-3 keV) pinhole images, taken simultaneously, have the same pattern. Experimental data [25] reveal that ca. 75% of $D(d,n)3\text{He}$ reaction yield in plasma focus is induced by D^+ ions with average energy $E_d = 100-200 \text{ keV}$ trapped in the volume well represented by that recorded through Schlieren pictures. The remaining 25% of neutrons have their origin in submillimeter size plasma domains (PDERs) of solid state-like density and life time $< 10 \text{ ns}$. PDERs trap ions of energy (observed) up to 10 MeV [24,25].

The plasma fusion in the PF-device has an outstanding fusion efficiency. This is a consequence of the fact, that its fusion is based on subpopulation of fast ions embedded in moderately heated plasma target and not associated with the thermonuclear conditions (requiring high kT for high Y_n). In this scheme, the radiation losses do not play an important role.

Present know-how in the PF-fusion allows one to easily estimate theoretically:

(a) sequence of plasma phenomena (in macro-scale) from the breakdown until the column formation, using existing MHD codes (2D-Potter-code, MACH-2, etc.) and

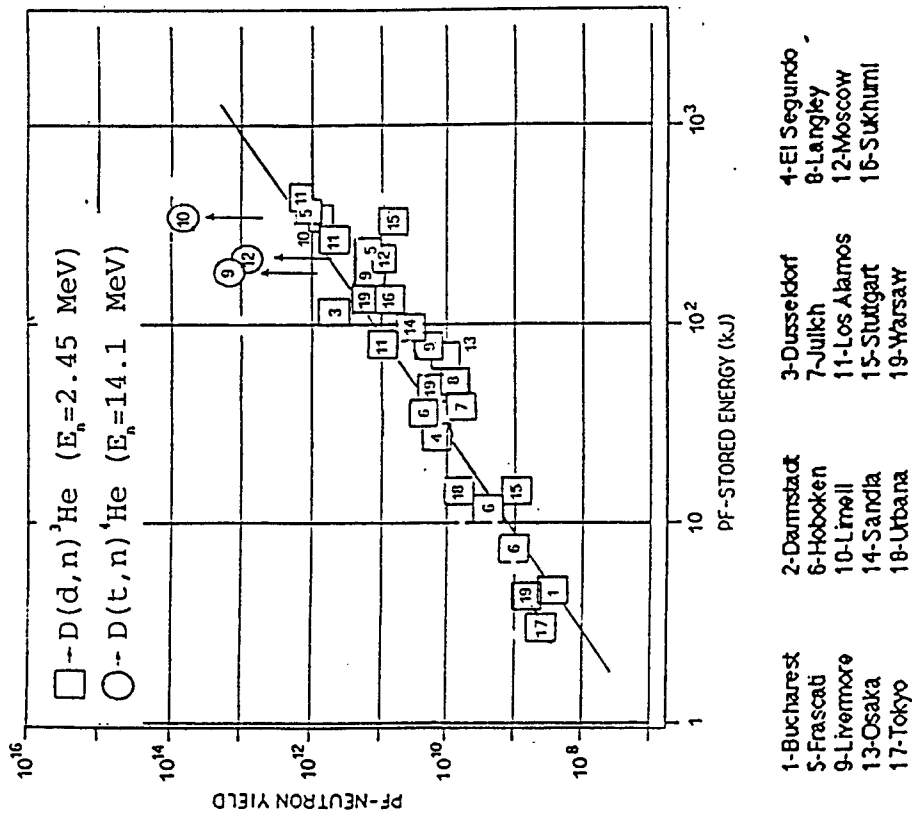
(b) sequence of nuclear phenomena (in macro- and micro- scale) beginning with empirical plasma characteristics relevant for nuclear phase (spectra of fast ions, kT_e , n) [26,27]. However, there is no satisfactory theoretical model linking development of the column instabilities with ion acceleration and trapping process.

Fortunately, the neutron yield produced in one PF-discharge, Y_n , scales smoothly locally (i.e. for the same PF operating with bank charged to different energy W) as well as geographically (for PF build by different teams and with banks operating at different W). Fig.7 shows compilation of published neutron yields (average) from different PF devices operating with D_2 and T_2+D_2 gas mixtures. Fig.7a shows engineering scaling

$$Y_n(E_n=2.5\text{MeV}) = 1.2 \text{ E}(7) * W^2 ; \quad [W]=[kJ] \quad (1a)$$

that holds for PF-devices operating in $5\text{kJ} < W < 500\text{kJ}$ capacitor bank energy range for $D(d,n)3\text{He}$ reaction and confirms that the scaling for $T(d,n)4\text{He}$ neutrons is similar, however with the scaling

(a)



(b)

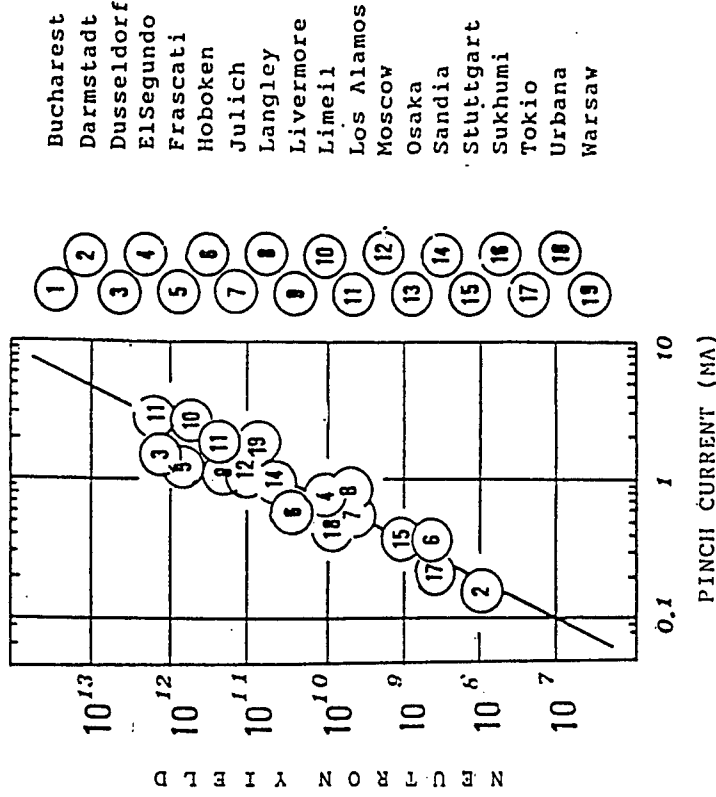


Fig. 7. Neutron yield (Y_n) scaling for different PF-devices for deuterium and deuterium-tritium gas fillings. All considered devices were operating in the neutron optimized mode but often with different optimization concept. (a) scaling versus capacitor bank energy, W. (b) scaling versus plasma pinch current, I.

constant two orders of magnitude higher. Fig.7b shows the scientific scaling:

$$Y_n(E_n=2.5\text{MeV}) = 1 E(11) * I^k ; 3.3 < k < 4 ; [I] = [\text{MA}] \quad (1b)$$

where: I is the current flowing through plasma at the pinch instant. One can notice that not all laboratories listed in Fig.7a appear in Fig.7b, this is because pinch current diagnostics were not installed on every device or were not used for the whole operational regime or particular PF-device. In addition, the FWHM of the neutron signal, t , can be approximated as:

$$t = 16 * W^{0.6} . \quad [t] = [\text{ns}], [W] = [\text{kJ}] \quad (1c)$$

The scientific scaling is the one to be considered if we (as in this study) search for PS-delivery to the compression phase in the scheme different from classical.

4. SOME OPTIONS OF MARAUDER OPERATION IN THE NEUTRON PRODUCTION MODE

Brief presentation of MARAUDER and Plasma-Focus features, point towards challenging opportunities of using MARAUDER facility as technologically reliable system for delivery of plasma sheath to the electrode muzzle and then using the plasma focus scheme for acceleration/trapping of ions in dense plasma with outstanding efficiency of fusion (neutron production).

In the present report we shall briefly discuss the following schemes of MARAUDER facility operation:

- (a) CT composed of neon/deuterium mixture colliding against solid target,
- (b) CT (composed of neon or deuterium) working as a switch for D-plasma compression at the muzzle, and
- (c) use of MARAUDER hardware in the plasma-focus mode with D2 gas differential filling.

Presented study are based on the knowledge and current understanding of MARAUDER performance, general schemes of plasma fusion and on know-how of PF focalized discharges. Conclusions have the character of preliminary selection of the different options. As such they can be considered as reference point to quantitative studies and toward-prototype projects.

4.1. CT COLLISION AGAINST A SOLID TARGET

One of the present MARAUDER program goals is the production of intense X-ray radiation by the process of CT stagnation. The broad calculations [28], based on the nonequilibrium radiation diffusion model (performed with MACH-2 [29]) show that: for the nominal 1 cm diameter of the CT and 10 mg of Ne mass at velocity of 100 cm/us (equivalent to 5 MJ of kinetic energy), collisions with a solid target will lead to the emission of 4.6 MJ electromagnetic power in 10 ns period.

Ref.28 shows that by changing the CT velocity, mass, Z, and its ratio of direct to magnetic field energy one can manipulate the efficiency of the ion-ion, ion-electron and electron radiation

coupling. Therefore manipulating the conversion of kinetic energy of ions into ion thermal energy. Additionally, by decreasing Z the material experiences "burn through" and the electron-radiation coupling drops significantly.

The goal of this chapter is different from the aim of Ref.28. Present study does examine the upper limit and the consequences of D+ (or D+ and T+ mixture) heating. In that sense, we are interested in cases of inefficient ion-electron and electron-radiation coupling while at the same time efficient transfer of direct energy to D+ with long deuterium burning time. Assuming that proper conditions (mass, HZ/D mixture, compression ratio, velocity; HZ is the high Z element) of MARAUDER operation were established, allowing us to consider a 100% of kinetic energy to ion temperature conversion, then the D-D neutron yield will be expressed in the following way:

$$Y_n = 0.5 * [(M/M_d)^2] * V * t * F(kT) / (1+n*Z)^2 \quad (2)$$

$$M = M_d * N_d + M_z * N_z; n = N_z / N_d; Z = M_z / M_d; F(kT) = \langle \sigma v \rangle \quad (2a)$$

$$kT = 1.05E(-15) * (v^2) * (1+n*Z) / (1+n); [kT] = [keV]; [v] = [cm/s] \quad (2b)$$

where: M_d , M_z and N_d , N_z are masses and atomic densities in the stagnated plasma of deuterium and high-Z atoms; V is the volume of the "hot" plasma where fusion occurs in the time interval "t"; kT is the ion temperature assuming 100% efficiency of kinetic to thermal energy conversion; $\langle \sigma v \rangle$ is the nuclear reactivity taken from Ref.30 (average product of fusion reaction cross-section and ion velocity).

Reviewing trends of the CT-plasma [28] in the high density stage, where directed kinetic to thermal energy conversion occurs, one can note that the plasma density peak of compression is near proportional to the initial plasma density. In the mean time FWHM of the plasma density time dependence is near-inversely proportional to the initial directed-velocity. This leads us to conclude that it is fairly sufficient to consider the $(V*t)$ term in Eq.2 as a constant. Additionally, for constant CT directed-velocity, the peak density of plasma also increases near proportionally with its initial CT-mass.

For estimates of Y_n in CT-stagnation fusion-scheme one can take mass of the CT $m(CT) = 10$ mg and $V*t = 2E(-8)$ cm³*s to be good representation of the future experiment. Thus leaving only the task of optimizing the composition ratio for different initial CT directed velocities ($Y_n \sim F(kT) / (1+n*Z)^2$). Fig.8b shows the dependence of expected neutron yield on the composition ratio of plasma $n = N_z / N_d$ (for D+T fusion $n = N_z / (N_d + N_t)$). In result, for low CT-velocities the 50%/50% mixtures give the maximum neutron production. This is because the gain in deuteron temperature from high-Z ions is more important than the decrease of D+ density associated with it. For high velocities, where $\langle \sigma v \rangle$ becomes saturated with the increase in kT , the governing factor in Y_n becomes D+ density and there is no need anymore for high-Z admixture.

In summary one can expect for present hardware and 1MJ SHIVA-STAR operation ($20\text{cm/us} \geq v \geq 10\text{cm/us}$):

$$7.2 * E(11) \geq Y_n(2.5\text{MeV}) \geq 4 * E(8), \text{ and}$$

$$8 * E(13) > Y_n(14\text{MeV}) \geq 2.3 * E(10).$$

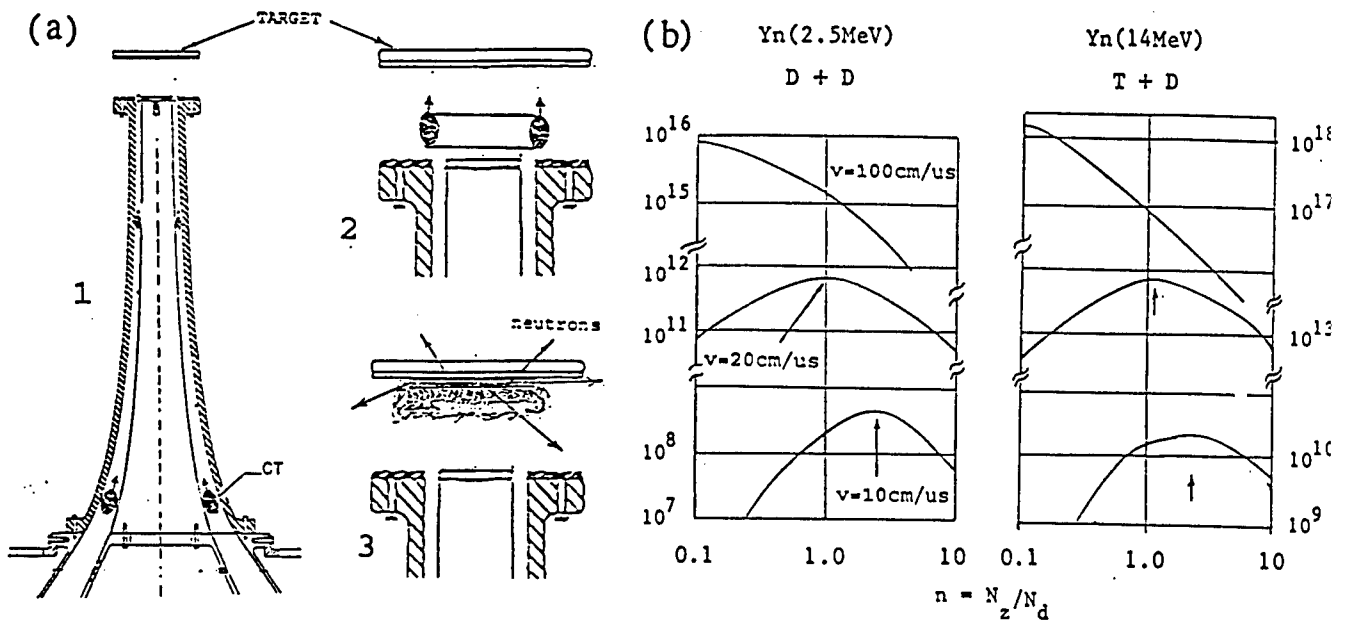


Fig.8. (a) The design of the muzzle for the CT stagnation experiment and sequence of the CT positions, and (b) dependence of the neutron yield (Y_n) on the CT composition $n=N_z/N_d$ (CT-mass=10 mg, $V \cdot t = 2E(-8) \text{ cm}^3 \cdot \text{s}$) for the CT-velocity $v=10-20 \text{ cm/us}$ (1MJ SHIVA-STAR operation) and $v=100 \text{ cm/us}$ (expected for 9.6 MJ); arrows show Y_n maximum.

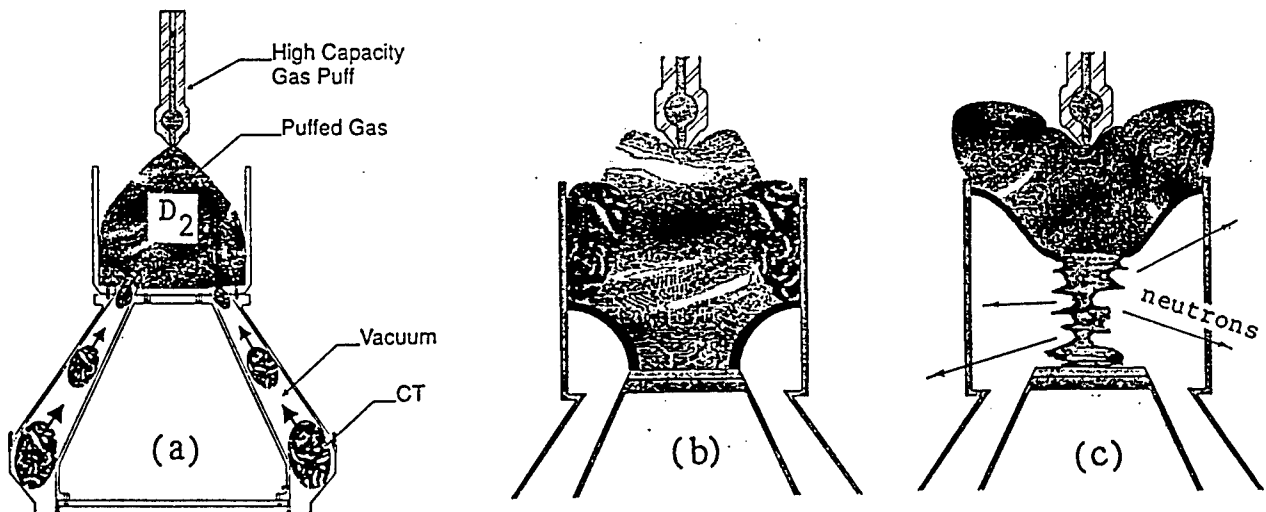


Fig.9. The main concept of the CT/DPF MARAUDER operation mode and the sequence of main events leading to neutron production. Alternation of the external electrode (at the muzzle) shows the concept of efficient reconnection of the current carrying plasma sheath from CT to the axially injected D_2 gas. (a) CT run-down (CT shown at three consecutive positions), current ramp-up phase, (b) Current transfer and beginning of radial compression phase, (c) Instability of plasma column enhancing D+D fusion.

All estimates for this scheme rely on calculations done in Ref.28 that are based on theoretical model not yet proven. One can consider that these obtained values give us the upper limit of the estimated Y_n , and it would be a mistake to disregard other options based on solid empirically proven schemes.

It is in fact reasonable to consider the CT collision with a grid-type target. Passing through a grid, CT-plasma will induce strong instabilities that may, as it happens in the PF, strongly enhance the acceleration of ions subpopulation and result in the increase of the fusion yield.

4.2. CT AS OPENING SWITCH FOR PLASMA FOCUS ACTION

The main concept in the CT/DPF mode of MARAUDER operation and its sequence of events are shown in Fig.9. One can see some alteration of the external electrode (at the muzzle) and the installation of fast D2-gas puff-valve.

As it was shown in Ch.2 (see Figs.1a and 2) the CT is driven into compression stage by the magnetic piston, generated due to the compression discharge current. The CT acts like a gasket as it maintains contact with the conducting walls and keeps magnetic flux from the compression discharge behind it. When CT leaves the central electrode muzzle, the current sheath switches from the inner electrode to the gas column and compresses it radially in a conventional plasma focus fashion (see Ch.3). From now on one can expect a classical sequence of events leading to efficient neutron production. The numerical simulations (confirmed by experimental data) for 1MJ SHIVA-STAR load, predict a maximum current of 3 MA that can be translated to following neutron yields:

$$4 * E(12) \leq Y_n(2.5\text{MeV}) \leq 8 * E(12) \quad \text{for D2 puffed gas, and/or}$$
$$4 * E(14) \leq Y_n(14.7\text{MeV}) \leq 8 * E(14) \quad \text{for D2+T2 puffed gas;}$$

see Fig.7 and Eq.2.

Coincidence of CT arrival at the muzzle of electrodes with the maximum current (from the SHIVA-STAR) instant can be easily obtained by choosing properly the CT-mass and the capacitor bank voltage. Proper D2-gas distribution is the issue that has to be taken care of empirically and will depending on the valve performance.

As it was stated previously we have the know-how in driving CT up to the muzzle as well as the know-how of driving compression once plasma funnel is formed. The major numerical studies have to be devoted to the transient phase when the current sheath switches from accelerating the CT to compressing the plasma funnel. At this transient phase, it is very important that the rearranging plasma sheath does not incorporate the magnetized plasma of the CT fragments into the funnel formation. If it does occur, then compression of the D2-plasma funnel will become inefficient. One can anticipate future solution by taking into account the existing studies on "magnetically-confined plasma opening switch", McPOS [2]. Using findings of Ref.2 one can consider an increase in the radius of the cylindrical external electrode part at the muzzle (see Fig.9). Also a choice of the proper ratio of compressing to

self-field of the CT at the muzzle should be considered. The toroidal field of the magnetic piston is a function of the cylindrical radius and discharge current: $B \sim I/r$. Hence, the field is larger near the inner electrode than near the outer one. In properly chosen scenario, as the CT approaches the muzzle, the magnetic piston field will push the CT aside to the outer electrode - a process that is called "blow-by". The phenomenon occurs when the compression field exceeds the self-field of the CT and supports the CT decompression due to shallow outer electrode.

The gas injected axially at the muzzle has to be composed of deuterium or deuterium/tritium mixture since the goal of the analysis is to produce fusion neutrons. CT works as a gasket, its mass and composition has to be numerically verified to assure optimum of the McPOS operation. However, one has to remember that if Ne composed-CT is considered, the neon component will mix itself with the PF-pinch and may influence the nuclear phase. From recent study [25,30] done with conventional DPF it is known that admixture of different gases ($Z \geq 6$) into deuterium decreases neutron yield in the following way:

$$Y_n \sim (N_d/N_{tot})^2 \quad \text{for } N_d/N_{tot} > 0.85 \quad (3)$$

where: N_d and N_{tot} are deuterium and total atomic densities in the plasma, respectively. Admixture larger than 20% of heavy gases introduces a severe cut in Y_n . This is due to rapid increase in slowing-down of fast-D⁺-ions (0.1-0.3 MeV) that in quasi pure deuterium plasma ($N_d/N_{tot} > 0.85$) is insignificant during the short fast-ions confinement time. It is therefore very probable that a deuterium-CT should be considered as a solution to this problem.

4.3. MARAUDER OPERATION IN THE PLASMA FOCUS MODE

One can consider using the MARAUDER hardware as a coaxial plasma gun without initially injecting the radial fields (see Ch.2 phase-1). This will in consequence prevent CT-forming. In such a scenario, the injection of gas (deuterium) and a sequential application of the formation voltage from the SHIVA-STAR banks will allow us to initiate the run-down phase of the deuterium plasma sheath, PS.

4.3.1. Design of the Electrodes and Axial Distribution of Filling Gas

Design of MARAUDER operation in the plasma focus mode should be performed under guidance derived from the MACH-2 simulations. At the conceptual level of these studies the simplified (analytical) model of the run-down phase was used. The parameters were similar to those of the Frascati PF (operated at 0.5 MJ energy level). It was also taken into consideration to use the existing sets of MARAUDER electrodes. The resulting design, as shown in Fig.10a, is supposed to fulfil the basic requirements for the efficient delivery of PS to the muzzle and the execution of the compression phase. To assure proper conditions for the PS-forming discharge and the following run-down (based on SHIVA-STAR

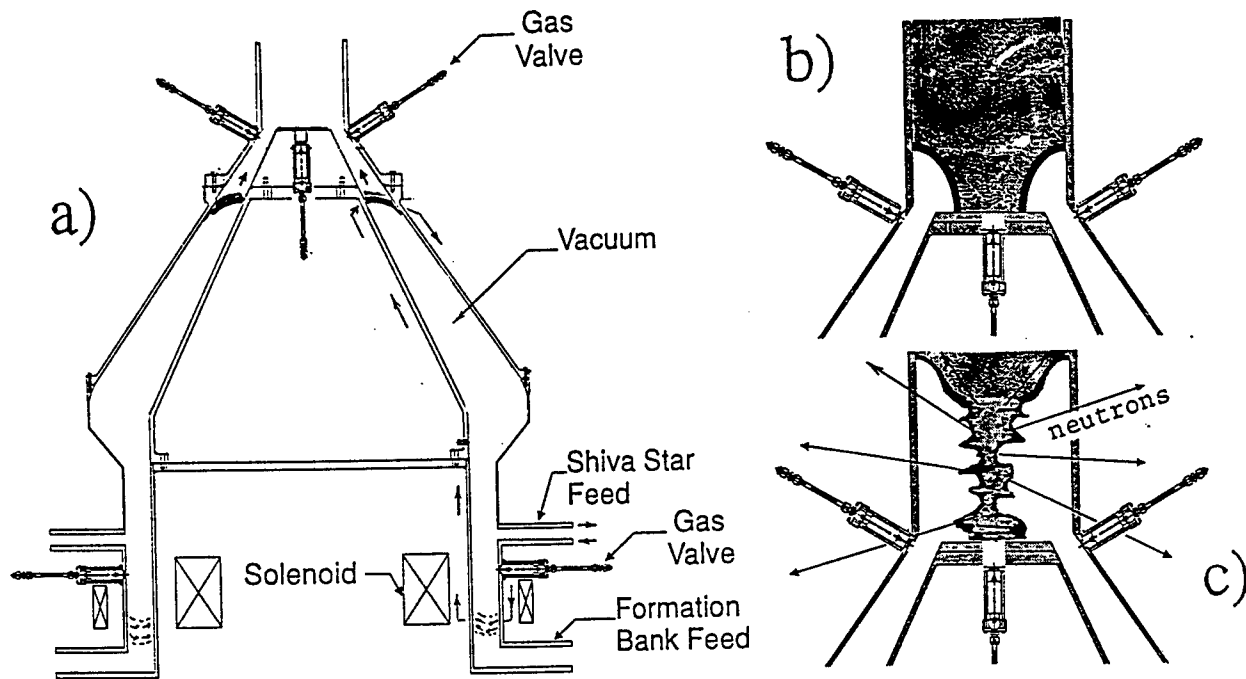


Fig.10. MARAUDER alternation for PF-mode of MARAUDER operation. (a) The modified electrodes and the main current path during the run-down phase. (b) Beginning of radial compression phase, (c) Instability of plasma column enhancing D+D fusion.

discharge) two sets of gas injectors are considered (see Fig.10a). They should produce the required gradients of the deuterium density. The length adjustment of the cylindrical external electrode (in form of rods) should be chosen experimentally. This will have as its function the proper shaping of the plasma funnel during the compression phase.

The run-down phase is well described by two equations:

(a) The second Newton's principle:

$$\frac{d}{dt} \left[\pi \rho (b^2 - a^2) z \frac{dz}{dt} \right] = \frac{\mu I^2}{4\pi} \ln \frac{b}{a} \quad \left(\int_a^b \frac{B^2}{2\mu} 2\pi r dr = \frac{\mu I^2}{4\pi} \ln \frac{b}{a} \right) \quad (4)$$

where: ρ is the mass-density of filling gas, a and b are radiuses of inner (outer dimension) and outer (inner dimension) electrodes, respectively, I is the current flowing in the interelectrode gap and z is the axial coordinate of the PS.

From experiments we do know that, soon after its take-off, the PS maintain a constant velocity (dz/dt) of order of $E(7)$ cm/s. This translates to the allocation of the momentum increase via increase of the PS mass.

(b) The circuit equation:

$$\frac{d}{dt} [(L + L_p + L_{ex})I] = V_0 - \frac{Q}{C_0} \quad (5)$$

where: L_p , L_{ex} and L are the inductances of plasma, adjusting element and the electrical circuit of SHIVA-STAR, respectively, V_0 is the voltage to which SHIVA-STAR capacitor bank (C_0) is charged. In circuit analysis the resistivities of an external circuit and plasma are neglected ($R < 5$ mohm, $R_p < 1$ mohm). The L_{ex} element is

installed to control the coincidence of compression phase initiation with the occurrence of maximum current delivery to PS.

To create PS run-down with the existing MARAUDER electrodes and create similar conditions to those of 1 MJ Frascati [31,32] it seems that, the best compatibility would be attained for the electrodes used in the nine-times-compression mode (M9) with shortened electrodes at the muzzle. Indeed, when one compares geometrical parameters relevant for Eqs. 4 and 5 the following is observed : (i) $\ln(b/a)$ is 0.3 for PF and 0.39 for M9, (ii) 'a' is 8 cm for PF and 8 cm for M9 at the muzzle and (iii) the electrode length is 56cm for PF and 67cm for M9. Electric characteristics of both installations are comparable also: the capacitance of bank Co is 1.25 mF for PF-Frascati and 1.31 mF for M9-Phillips while inductance of electric circuit and vacuum for both installations is about 100 nH. So to make Eq. 5 almost identical (for both devices) one has to assure that, for both installations, terms $\rho \cdot (b^2 - a^2)$ have the similar value, i.e. swept mass of deuterium per unit of trajectory in z-direction is the same. For PF, ρ , 'a' and 'b' are constant, for M9 constant value of $\rho \cdot (b^2 - a^2)$ term will be achieved by gradient of deuterium density along z-direction:

$$\rho(z) = \rho_0 \cdot [Bo^2 - Ao^2] / [(Bo - z \cdot ctgB)^2 - (Ao - z \cdot ctgA)^2] \quad (6a)$$

$$(z > Zo) = \rho_0 \quad (Zo) \quad \text{for } z < Zo = 67 \text{ cm} \quad (6b)$$

where: ρ_0 , Ao and Bo are the density, radius of inner electrode and radius of outer electrode at the base of the conical electrodes, respectively. A and B are the slopes of the inner and outer electrodes, respectively; "z" is measured from the cone base to the PS position. Depending on capacitor bank energy fired, ρ_0 has to be adjusted to give $\rho(Zo)$ at the muzzle as required for PF operation. For example when W is about 1 MJ then $\rho(Zo) = 10-20$ Torr has to be considered.

4.3.2. Phases of Marauder Operation in the Plasma Focus Mode

The following phases of operation should be considered:

(1) Injection of neutral gas (deuterium). Injection should take place at two different z-altitudes. One being at the level of the coils, exactly as for the MARAUDER. The other one can be at the altitude of the muzzle from the external electrode. It must be arranged however in such a way as to insure that a very particular z-distribution of pressure will be achieved (see comments above for the proper development of the run-down phase.

(2) Application of voltage from the formation bank (between the inner and outer conductor) with controlled delay related to the opening of MARAUDER gas valves.

(3) The breakdown in the injected gas, producing a highly conductive plasma. The BxJ forces pushing the plasma along the axis, form two diverging plasma sheaths PS. At the time when PS moving in the direction of the muzzle passes the SHIVA-STAR feed (the other PS moves in the direction of a lower baffle) a slowly

rising magnetic field (fed by external magnetic field coils) is injected into PS, near the lower baffle. This will cause a stagnation of the diffuse discharge for the whole duration of the PF operation, same as during classical MARAUDER discharge (see Ch.2 and Fig.3).

(4) When PS passes Shiva-Star feed (PS arrives to the altitude at which normally CT was formed) the bank is fired and a regular run-down phase of plasma focus begins.

(5) From now on one has to assure discharge conditions close to those of the PF (see Ch.3). We expect regular compression phase.

(6) In the following nuclear activity phase (see Fig.10c) for 1 MJ operation one can expect a plasma target of $kT_e=0.3-0.6$ keV and $n=2-4 \times 10^{18}/\text{cm}^3$, and neutron emission (due to trapped 0.1-0.3 MeV D+ions) signal of $t=500$ ns with total yield of

$Y_n(2.5\text{MeV}) = 2 \times E(13)$ for D2 puffed gas, and/or

$Y_n(14.7\text{MeV}) = 2 \times E(15)$ for D2+T2 puffed gas;

see Eqs.1 and 2.

5. SUMMARY

We analyzed here three schemes of neutron production. One based on the CT stagnation and two variants of the PF phenomenon. The most challenging one is the operation of MARAUDER in the plasma focus mode CH.3.3). This however would give, for nominal energy of the capacitor bank $W=9$ MJ, a $E(18)$ yield of 14 MeV neutrons per shot i.e. yield required for nuclear weapon simulation and advanced material technology. All estimates have the meaning of the conceptual study. They are based on the use of rational analogies and common sense therefore should be considered as initial stage for quantitative analysis with available MHD codes. Extremely important advantage of the presented results is that all schemes do consider the use of modified MARAUDER hardware. It means that parallel to numerical studies one can make current experimental cross-checks of the theory and adapt hardware accordingly. Author of this report believes that initiating this line of research will allow us to compete with already advanced Russian projects.

REFERENCES

1. J.H.Degnan et.al., Phys. Fluids B5(1993)2938;
2. R.E.Peterkin Jr., J.H.Degnan, T.W.Hussey, N.F.Roderick and P.J.Turchi, IEEE Trans.-PS 21(1993)522;
3. G.F.Kiuttu et al., Proc. 94ICOP (Santa Fe, USA, 1994), IEEE Conf.Record 94CH3465-2, p.104 (2B1-2);
4. T.D.Hayward, T.Armstrong and D.H.Epperson, Nucl.Instr. and Meth., B10/11(1985)1077;
5. G.Peto, R.Pepelnik, Nucl.Sci. Engineering, 106(1990)219;
6. V.Nardi and J.S.Brzosko, "Plasma Focus Sources" Los Alamos Nat. Lab. Report LA-11393-C (UC414), 1989;
7. Summary Rep. of Workshop on Requirements for an International Fusion Materials Irradiation Facility, San Diego, 1988, Ed.

- D.G.Doran, Publ. Battelle Pacific Northwest Lab., Richland, Washington, (1988);
8. Proc. Japan-USA Workshop (P119) on 14 MeV Neutron Source for Material R&D Based on Plasma Devices, Osaka (Japan), 1988, (Publ. by Nagoya Univ. as Report IPPJ-T-37);
 9. LANL, Intense Neutron Sources Meeting July 21-22, 1992, LANL Report LA-11393 Suppl. Conf. UC414, 1992;
 10. V.Nardi and J.S.Brzosko: (a) "Plasma focus: CAPT-10 (I)" in Ref.8, p.225; (b) "Plasma focus: CAPT-10 (II)" in Ref.9, p.213; (c) "Neutron Sources of the Advanced Plasma Focus Type for Demonstration Tests of Safe Reactors", in Ref.10;
 11. A.A.Ivanov and D.D.Ryutov "The GDT-Based Neutron Sources and Related Issues" Publ. by Budker Inst. Nucl. Phys., Novosibirsk (1993) Russia;
 12. Proc. of Int. Conf. on Neutron Sources for Material Sci., Obinsk (Russia), Sept. 1994;
 13. B.V.Robouch, L.Ingrosso and J.S.Brzosko, "Neutron Radiation Effects in Hevily Shilded Superconducting Magnets of the Novosibirsk GDT" in Ref.12;
 14. N.V.Filippov, Kurchatov Inst. At. Energy, Moscow, private communication (1994);
 15. F.Flam, Science 265(1994)468;
 16. R.E.Peterkin Jr. private communication, from set of simulations done with MACH-2 at PL/WSP (1994);
 17. J.S.Brzosko, B.V.Robouch and J.Klobukowska, Fusion Techn., 12(1987)71;
 18. W. Kies, Plasma Phys. Contr. Fusion 28(1986)1645-1657;
 19. J.S.Brzosko and J.Klobukowska, IEEE Trans. EI-18(1983)420;
 20. H.Herold et.al., IAEA-CN-44/D-III-6-3;
 21. J.Ehrhardt, P.Kirchesch, K.Hubner and J.P. Rager, Phys. Lett. 89A(1982)285;
 22. H.Schmidt, et al., Atomkernenergie 44(1984)191;
 23. J.S.Brzosko, V.Nardi, J.R.Brzosko and D.Goldstein, Phys. Lett. A (1994) in press, see also 1994 IEEE Int. Conf. on Plasma Phys., Santa Fe; Conf.Record 94CH3465-2, p.131 (3A6);
 24. V.Nardi, J.Brzosko et al., IEEE Trans. PS-16(1988)368;
 25. J.S.Brzosko, V.Nardi, J.R.Brzosko and D.Goldstein, 1992 IEEE Int. Conf. on Plasma Phys., Miami; Conf.Record 93CH3334, p.188;
 26. U.Jager and H.Herld, Nuclear Fusion, 27(1987)407;
 27. J.S.Brzosko and V.Nardi, Phys.Lett. A155(1991)162;
 28. M.R.Douglas "Radiation Production from Stagnating Compact Toroids Employing a Nonequilibrium Radiation Diffusion Model" PhD Diss. at The Univ. of New Mexico, Albuquerque, July, 1994;
 29. H.M.Frese, "MACH-2:17" Mission Res.Corp.Report AMRC-R-874, 1987;
 30. H.S.Bosch and G.M.Hale, Nucl. Fusion, 32(1992)611;
 31. C.Gourlan et al., 2-nd Int.Conf. on Energy Storage, Compr. and Switching, 1978, p.221; Publ. Plenum Press, New York;
 32. J.S.Brzosko, J.R.Brzosko, B.V.Robouch, L.Ingrosso and K.Hubner, "Triton Burn-up in Plasma Focus Plasmas" submitted to Plasma Phys. (1994);

**DETERMINATION OF THE INTERFACIAL HEAT TRANSFER COEFFICIENT
IN A REGENERATOR OF A CRYOCOOLER**

**Ping Cheng
Professor and Chair
Department of Mechanical Engineering
University of Hawaii
Honolulu, Hawaii 96822**

**Final Report for
Summer Faculty Research Program
Phillips Laboratory**

**Sponsored by:
Air Force Office of Scientific Research
Bolling Air Force Base, DC**

and

**Phillips Laboratory
Kirtland Air Force Base, NM**

September 9, 1994

DETERMINATION OF THE INTERFACIAL HEAT TRANSFER COEFFICIENT
IN A REGENERATOR OF A CRYOCOOLER

Ping Cheng
Professor and Chair
Department of Mechanical Engineering
University of Hawaii

Abstract

Correlation equations for the interfacial heat transfer coefficient, the effective axial thermal conductivity, and the pressure drop of an oscillating and reversing flow through a stack of screens are needed for an optimum design of a regenerator in a cryocooler. At the present time, the design of these regenerators is based on the correlation equations obtained for steady flow in a compact heat exchanger. In this report, relevant literature on the transport processes occurring in the regenerator, heat exchangers, and the pulse tube of an orifice pulse-tube refrigerator is reviewed. Experimental work initiated at the Phillips Laboratory in cooperation with the University of Hawaii for the determination of the correlation equations of the heat transfer and fluid flow characteristics in a regenerator under periodically reversing flow conditions is discussed. A method for the analysis of the experimental data is described.

DETERMINATION OF THE INTERFACIAL HEAT TRANSFER COEFFICIENT
IN A REGENERATOR OF A CRYOCOOLER

Ping Cheng

1. Introduction

A basic pulse-tube refrigerator, consisting of a compressor, heat exchangers, a regenerator and a close end tube, was invented by Gifford and Longworth in 1964 [1]. During the ensuing twenty years, however, not much interest has been given to this type of refrigerator because of its small refrigeration capacity and low thermal efficiency compared to Stirling refrigerators. In 1983, an improved design of this refrigerator was made by Mikulin et al. [2] who installed an orifice at the closed end of the basic pulse tube that greatly increases its thermal efficiency. This new design has attracted immediate attention and has been referred to as the "orifice pulse tube (OPT) refrigerator" in the literature. Recently, a great deal of effort has been devoted to the development of miniature orifice pulse tube (OPT) cryocoolers for military and space applications. Because of their high reliability and relatively free of vibration and noise, the miniature orifice pulse tubes are ideal devices for cooling of infrared detectors in night vision and missile guidance systems, as well as for infrared sensors aboard satellites [3]. The orifice pulse tube cryocoolers are also currently being considered for the cooling of superconducting devices and micro-chips in electronic devices.

At the present time, transport phenomena occurring in an orifice pulse tube cryocooler are poorly understood. In particular, correlation equations for heat transfer and pressure drop under oscillating flow conditions such as those occurring in a regenerator and a pulse tube have not yet been obtained. For this reason, the design of regenerators and the pulse tubes is based on steady-flow correlation equations. In this report, we

shall review the literature pertinent to the transport phenomena occurring in an orifice pulse-tube cryocooler. Research work currently being carried out at the University of Hawaii and at the Phillips Laboratory on the determination of the interfacial heat transfer coefficient and the effective axial thermal conductivity of a regenerator under periodically reversing flow conditions will be described.

2. Survey of Literature

In this section, we shall review relevant literature on the fluid flow and heat transfer processes occurring in the regenerator, the heat exchanger, and the pulse tube of an orifice pulse tube cryocooler.

2.1 Regenerator

The regenerator in a cryocooler acts as a heat storage device that absorbs energy when the hot fluid enters at one end during the first half cycle and gives up energy when the cold fluid enters from the other end during the second half cycle. A regenerator is usually made of a stack of stainless steel screens which can be considered as a special form of porous media. Thus, a qualitative behavior of transport phenomena in a regenerator can be inferred from existing literature for heat and mass transfer in porous media.

2.1.1 Fluid Flow in Porous Media

Fluid flow and heat transfer characteristics in a porous medium have been the subject of intensive studies during the past forty years because of its important applications in the recovery of oil [5], the development of geothermal energy [6], and chemical processing

industries. However, most of the investigations in this field are limited to a steady incompressible (or a slightly compressible) flow in a packed-sphere bed. It has been well established that the pressure drop in a packed-sphere bed for a steady flow at low Reynolds numbers obeys the Darcy law, which states that the pressure drop is linearly proportional to the velocity [5,6]. At higher Reynolds numbers where inertia force becomes important, the pressure drop in a packed-sphere bed is proportional to the velocity square that is known as the Forchheimer equation [5,6]. Recently, a number of investigators have attempted to derive Darcy's law and the Forchheimer equation from the Navier Stokes equations by a spatial averaging process [7] akin to the time-averaging procedure in the turbulent flow. This leads to a number of closure problems that require modeling at the pore level. For example, the interfacial drag force term in the momentum equation for flow past a packed bed can be obtained within a constant factor by considering a steady flow over a sphere. Using this model, it can be shown that the skin friction gives rise to the Darcy frictional term while the form drag gives rise to the Forchheimer frictional term [7]. Although the Reynolds number dependency of the interfacial drag force term can be determined by such a model, the undetermined constant in the drag force term (which reflects the effect of interference of spheres) can only be determined by a comparison of the model with experimental data obtained for a packed bed. Tanaka et al. [8] have shown that by suitably defining the permeability, the pressure drop in a steady flow at low Reynolds numbers through a stack of screens is also governed by Darcy's law.

2.1.2 Heat Transfer in Porous Media

Since a stack of screens can be considered as a special form of porous media, knowledge gained in the research work on heat transfer in porous media can also be applied to the heat transfer process occurring in the regenerator. For example, the effective thermal

conductivity of a porous medium is known to be consisting of the stagnant thermal conductivity of the solid phase and the fluid phase (k_m^*) plus the dispersive thermal conductivity (k_T^*), the latter is due to the deflection of fluid owing to the presence of solid particles. Thus, the dispersive thermal conductivity in a porous medium is akin to the eddy thermal conductivity in the classical turbulent flow. The axial dispersive thermal conductivity of fluid in a packed-sphere bed is known to be linearly proportional to the Reynolds number as

$$k_T^* = C Pr Re_d \quad (1)$$

where Pr is the Prandtl number of the fluid, Re_d is the Reynolds number based on the particle diameter, and $C= 0.7$ is an empirical constant for steady flow in a packed-sphere bed. It is anticipated that Eq.(1) can also be applied to flow passes a stack of screens if a different value of C is used to take into consideration of the difference in the geometry. It has been established that the thermal dispersion effect is important in forced convection in porous media at high Reynolds numbers.

Another concept that is of special importance to oscillatory flow in a porous medium is the interfacial heat transfer coefficient between the solid phase and fluid phase of the medium. However, most of the previous research work on heat transfer in porous media focuses on steady flow problems where the temperature of the solid phase equals to that of the fluid phase. In other words, the interfacial heat transfer coefficient between the solid phase and the fluid is infinite. As a result, the energy equation for the fluid phase can be added to that of the solid phase to give a single energy equation for the study of the heat transfer process in a porous medium. In the catalytic reactor's community, however, it has been recognized for some time that the temperature of the fluid phase may not be equal to that of the solid phase. Therefore, a separate energy equation for

each phase is needed. This is the so-called two-temperature model where the interfacial heat transfer coefficient is finite. This interfacial heat transfer coefficient is usually measured by the so-called single blow technique in the compact heat exchanger literature [9].

2.1.3 Fluid Flow and Heat Transfer in a Regenerator

Transport phenomena occurring in a regenerator are much more complicated than those discussed in the porous media literature because of the following reasons: (1) the flow is periodically reversing and not steady unidirectional, (2) the flow is undergoing rapid pressure fluctuations and it can no longer be considered as incompressible, and (3) the porous medium is made of a stack of screens rather than spherical particles, the former is much more complicated from a geometrical point of view.

To investigate whether the Darcy law is valid in an oscillating flow in a regenerator, Roach and Bell [10] designed and constructed a test facility for the study of pressure drop through a stack of screens under the condition of a rapidly reversing flow. They found that the frequency of oscillation has no effects on the pressure drop. A similar conclusion was reached recently by Gedeon and Wood [11]. However, Tanaka et al. [8] found that the frequency of oscillation does increase the pressure drop in a regenerator. In a recent paper, Huang and Lu [12] show numerically that a phase difference between the inlet and outlet mass flow rates does exist in a compressible flow if the mesh size of the screens in the regenerator is greater than 100.

Early theoretical study on heat transfer in a regenerator is based on a thermodynamic analysis of enthalpy flow [13]. Recently, a number of computer codes have been developed to solve the transient one-dimensional partial differential equations of heat,

mass, and momentum for the design of a regenerator [14] and an orifice pulse-tube refrigerator [15]. In these computer codes, however, the correlation equations for pressure drop and the interfacial heat transfer coefficient are based on steady flow. Furthermore, the effect of thermal dispersion is neglected in these models.

2.2 Heat Exchanger

Oscillatory and reversing flow in an empty pipe has been a subject of investigation for the past fifty years because of its important bioengineering applications to human airways. Richardson and Tyler [16] were among the first ones to observe the so-called annular effect in a pipe where the maximum velocity is not at the center of the pipe as in the case of steady flow but occurs near the wall of the pipe when the frequency of oscillation is high. Subsequently, Uchida [17] obtained an analytical solution for velocity profiles in a fully-developed oscillating flow. Early experimental work focused on the critical Reynolds numbers for the occurrence of turbulence in an oscillatory and reversing flow [18]. Recently, Simon and Seume [19] measured velocity profiles in an oscillating and reversing flow, and observed that turbulence occurs only during the deceleration stroke at high Reynolds numbers. Isabey et al. [20] found that oscillation has no effect on the pressure drop at a frequency less than 10 Hz; however, the effect of oscillation increases the pressure drop at a frequency greater than 10 Hz.

Relatively little research work has been performed on the corresponding problem of oscillatory heat transfer in a pipe. Iwabuchi and Kanzaka [21] investigated oscillatory heat transfer in a heat exchanger for a specific prototype Stirling engine. They presented their heat transfer data in terms of rpm, mean pressure and phase difference between the opposing pistons but did not attempt to correlate the data in terms of dimensionless parameters. Hwang and Dybbs [22] presented their experimental data

graphically in terms of Nusselt number versus Reynolds number at selected oscillating amplitudes. Wu et al. [23] investigated oscillating flow resistance and heat transfer in a gap heat exchanger of a cryocooler; they found that the value of the cycle-averaged Nusselt number is constant and is independent of the oscillatory frequency over a wide range of Reynolds numbers.

2.3 Pulse Tube

Gifford and Lonsworth [24] discussed the surface heat pumping effect in a pulse tube. Lee et al. [25] used a visual smoke-wire technique to observe flow patterns in a pulse tube; they also obtained an analytical solution for a two-dimensional incompressible oscillating flow in a diverging tube to approximate the compressible flow problem in the limit of very small pressure ratios. Huang et al. [26] developed a simplified one-dimensional analysis for the performance of a pulse tube by assuming the convective heat transfer between the gas and the pulse-tube wall as the controlling heat transfer mechanism. Steady state forced convection correlation equations between the gas and the walls were used in the mathematical formulation of the problem. By integrating the transient one-dimensional conservation equations of mass and energy over a half-cycle, Huang et al. [25] solved the resulting ordinary equations analytically.

3. Determination of Pressure Drop and Heat Transfer in a Regenerator

As mentioned earlier, no correlation equations have been obtained so far for the interfacial heat transfer coefficient and the friction factor in a regenerator under periodically reversing flow conditions; these correlation equations are needed for an optimum design of Stirling or pulse-tube cryocoolers. In the remaining of this report,

we shall discuss the research work to be carried out at the University of Hawaii and at at the Phillips Laboratory to obtain these correlation equations.

3.1. Drag Force and Heat Transfer about a Sphere in a Periodically Reversing Flow

As discussed earlier, the functional dependency of the Reynolds number for the interfacial drag force term (within an undetermined constant) in the momentum equation for a steady flow through a packed-sphere bed can be modeled as steady flow over a single sphere. Similarly, we shall use the same approach to obtain the interfacial drag force term in the momentum equation and the interfacial heat transfer coefficient in the energy equation for a periodically reversing flow through a stack of screens. To this end, a finite difference solution will first be carried out at the University of Hawaii for an oscillatory and reversing flow past a sphere. Correlation equations will be obtained for the friction factor and Nusselt numbers as a function of oscillatory frequency, Reynolds number, and dimensionless time. These correlation equations multiplied by an unknown constant will be used as the correlation equations for friction factor and Nusselt number for an oscillating flow passes a stack of screens. The unknown constants in these correlation equations can then be determined by a comparison of theory and experiments that will be described in the following paragraphs.

3.2 Friction Factor of a Periodically Reversing Isothermal Flow Through a Regenerator

The test facility at the University of Hawaii's Thermal Engineering Laboratory will be used for the experimental investigation of pressure drop in an isothermal periodically reversing flow through a regenerator with a length L^* and a diameter D^* . The regenerator is made of a stack of stainless steel screens. The experimental set-up consists of a double-acting piston and a long tube that contains a regenerator. Air,

driven by the piston, oscillates periodically and reversibly in the tube. The pressure drop across the regenerator will be measured by a pressure transducer while the mass flow rates at the inlet and outlet of the regenerator will be measured by a hot-wire anemometer. Temperatures at the inlet and outlet of the regenerator will be measured by thin thermocouples with a fast response time. Data for dimensionless pressure drop versus Reynolds number will be plotted. The magnitudes and phase differences in the mass flow rates at the inlet and outlet of the regenerator will be examined. Any deviation from the Darcy law will be examined in the light of the correlation equations obtained numerically in Sec. 3.1.

3.3 Interfacial Heat Transfer Coefficient in a Periodically Reversing Incompressible Flow Through a Regenerator

After the pressure drop experiment has been completed, the same apparatus will be modified to perform the heat transfer experiment in a regenerator under atmospheric pressure. A heater and a cooler will be added to the two ends of the regenerator. Temporal variations of temperatures, pressures, and mass flow rates at the inlet and outlet of the regenerator will be measured. The interfacial heat transfer coefficient can be determined by a simplified model if an incompressible plug flow is assumed. Under this assumption, the energy equation for the fluid phase is

$$\rho_f^* c_{p,f}^* \left(\phi \frac{\partial T_f^*}{\partial t^*} + u^* \frac{\partial T_f^*}{\partial x^*} \right) = \phi k_f^* \frac{\partial^2 T_f^*}{\partial x^{*2}} + h^* (T_s^* - T_f^*) \quad (2)$$

where T_f^* and T_s^* are the temperatures of the fluid phase and solid phase respectively; ϕ is the porosity of the matrix screens; h^* is the interfacial heat transfer coefficient between the fluid and the matrix screens that is an unknown function of velocity for an

oscillatory flow; t^* is time and x^* is the distance measured from left-hand side of the regenerator. The velocity u^* in Eq.(2) is given by

$$u^* = u_{\max}^* \cos(\omega t^* + \psi) \quad (3)$$

where u_{\max}^* is the maximum Darcy velocity during a cycle, ω is the frequency of oscillation, and ψ is the phase angle between velocity and inlet temperature variations.

The energy equation for the solid phase is

$$(1 - \phi)\rho_s^*c_{ps}^* \frac{\partial T_s^*}{\partial t^*} = (1 - \phi)k_s^* \frac{\partial^2 T_s^*}{\partial x^{*2}} + h^*(T_f^* - T_s^*) \quad (4)$$

where ρ_f^* and c_{pf}^* are the density and specific heat of the fluid while ρ_s^* and c_{ps}^* are the corresponding properties of the solid phase. Boundary conditions for Eqs.(2) and (4) depend on whether the fluid enters from the left-hand side ($x^* = 0$) or from the right-hand side ($x^* = L^*$) of the regenerator as follows:

(i). During the first half-cycle when the hot fluid enters from the left-hand side ($x^* = 0$), the boundary condition for the fluid phase is

$$T_f^*(t^*) = T_{fi}^*(t^*) \quad (5a)$$

where $T_{fi}^*(t^*)$ is fluid temperature at $x^* = 0$ obtained from the experiment (see Sec.

3.4). The boundary condition for the solid phase at the hot end is

$$T_s^*(0, t^*) = T_{fi}^*(t^*) \quad (5b)$$

where $T_{ii}^*(t^*)$ is temperature of the screens of the regenerator at $x^* = 0$ obtained from the experiment. The boundary conditions for the fluid and solid phases at the exit ($x^* = L^*$) are:

$$\frac{\partial T_f^*}{\partial x^*}(L^*, t^*) = 0, \quad T_s^*(L^*, t^*) = T_{so}^*(t^*) \quad (6a,b)$$

where $T_{so}^*(t^*)$ is temperature of the screens of the regenerator at $x^* = L^*$ obtained from the experiment.

(ii) During the second half cycle when the cold fluid enters from the right-hand side ($x^* = L^*$) of the regenerator, the inlet boundary conditions are

$$T_f^*(L^*, t^*) = T_{fo}^*(t^*) \quad (7a)$$

where $T_{fo}^*(t^*)$ is fluid temperature at the cold end obtained from the experiment. The boundary condition for the solid phase at the inlet is

$$T_s^*(L^*, t^*) = T_{so}^*(t^*) \quad (7b)$$

where $T_{so}^*(t^*)$ is the temperature of the screen at the cold end obtained from the experiment. The outlet boundary conditions at $x^* = 0$ are:

$$\frac{\partial T_f^*}{\partial x^*}(0, t^*) = 0, \quad T_s^*(0, t^*) = T_{si}^*(t^*) \quad (8a,b)$$

where $T_{si}^*(t^*)$ is the temperature of the screens at the hot end obtained from the experiment.

Numerical solutions for the outlet fluid temperature variations for each half cycle can be obtained if the values of h^* and k_T^* are known. Conversely, the values of h^* and k_T^* can be determined simultaneously by matching the predicted and experimentally determined outlet fluid temperature variations.

3.4 Interfacial Heat Transfer Coefficient in a Regenerator of an Orifice Pulse Tube

The design of an experimental setup for the determination of the interfacial heat transfer coefficient in a regenerator of an orifice pulse tube was completed during the summer of 1994. The experimental setup, currently under construction at the Phillips Laboratory, is shown in Fig. 1. It consists of a MTI compressor, heat exchangers, a regenerator and a pulse tube that is connected to a reservoir through an orifice. Helium gas will be used as a working medium. Temporal variations of temperatures of the gas and the screens at the inlet and outlet of the regenerator will be measured by a cold wire

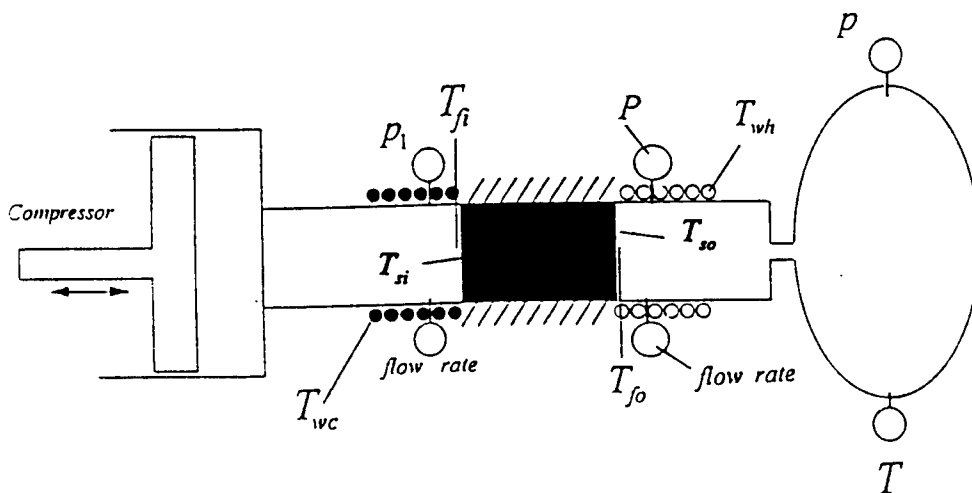


Fig. 1 Schematic diagram of the experimental setup

anemometer. Temporal variations of mass flow rates and pressures at the inlet and outlet of the regenerator will be measured by a hot-wire anemometer and by pressure transducers. Effects of the screen mesh size, mean pressure in the system, swept volume and oscillatory frequency of the MTI compressor, and the opening of the orifice valve will be examined.

For data analysis, the model presented in Section 3.3 will be extended to take into consideration of the compressibility effect of the gas. The conservation equations of mass and momentum for a compressible fluid are:

$$\phi \frac{\partial \rho_f^*}{\partial t^*} + \frac{\partial}{\partial x^*} (\rho_f^* u^*) = 0 \quad (9)$$

$$\frac{1}{\phi} \frac{\partial}{\partial t^*} (\rho_f^* u^*) + \frac{1}{\phi^2} \frac{\partial}{\partial x^*} (\rho_f^* u^{*2}) = - \frac{\partial p_f^*}{\partial x^*} + \frac{D_{fs}^*}{\phi} \quad (10)$$

where D_{fs}^* is the interfacial drag force that is given by Darcy's law for a steady flow.

This term may be suitably modified after the analysis of experimental data obtained from Section 3.2 has been completed. The energy equation for the gas phase is

$$\phi c_{pf}^* \frac{\partial}{\partial t^*} (\rho_f^* T_f^*) + c_{pf}^* \frac{\partial}{\partial x^*} (\rho_f^* u^* T_f^*) = \phi k_f^* \frac{\partial^2 T_f^*}{\partial x^{*2}} + h^* (T_s^* - T_f^*) + \frac{\partial p_f^*}{\partial t^*} + u^* \frac{\partial p_f^*}{\partial x^*} \quad (11)$$

while the energy equation for the solid phase is

$$(1 - \phi) \rho_s^* c_{ps}^* \frac{\partial T_s^*}{\partial t^*} = (1 - \phi) k_s^* \frac{\partial^2 T_s^*}{\partial x^{*2}} + h^* (T_f^* - T_s^*) \quad (12)$$

The ideal gas law gives

$$\rho_f^* = \frac{p_f^*}{R^* T_f^*} \quad (13)$$

where R^* is the gas constant. Substituting Eq.(13) into Eqs.(9)-(11), the resulting equations together with Eq.(12) constitute four equations for the four unknowns, $T_f^*(x^*, t^*)$, $T_s^*(x^*, t^*)$, $p_f^*(x^*, t^*)$, and $u^*(x^*, t^*)$. Boundary conditions for these equations are also given by Eqs.(5)-(8). The model described above differs from Radebough et al's third order model [14] in the following aspects:

1. The interfacial heat transfer coefficient is a function of time, Reynolds number and the kinetic Reynolds number with an unknown constant. Thus, the interfacial heat transfer coefficient is to be determined rather than assumed to be given by the steady flow correlation equation.
2. The effective axial thermal conductivity is not assumed to be negligibly small, but is to be determined by matching the predicted and measured outlet temperature variations. It is relevant to note that Sarangi and Baral [27] found that the axial heat conduction of the gas phase in a regenerator is not negligibly small.
3. Different thermal boundary conditions at the two ends of the regenerator are specified which was discussed in Section 3.3.

Solutions for the above four nonlinear transient partial equations and boundary conditions can be carried out by the finite different method if the values of h^* and k_T^* are known. The numerical solution is expected to be more difficult than the corresponding

incompressible flow problem discussed in Section 3.3. The procedure for the determination of the values of h^* and k_T^* in this problem is similar to those discussed in Section 3.3 for the corresponding incompressible flow problem.

4. Concluding Remarks

In this report, research work performed during the summer of 1994 on the determination of the interfacial heat transfer coefficient of a regenerator is presented. A new method is proposed for data analysis in order to obtain the correlation equations for the interfacial heat transfer coefficient and effective axial thermal conductivity in a regenerator under periodically reversing flow conditions. These correlation equations are needed for an optimum design of a regenerator in a cryocooler.

References

1. Gifford, W. E. and Longworth, R. C., (1964), "Pulse-Tube Refrigeration," J. of Engineering for Industry, Trans. ASME, Series B, v. 86, 264-265.
2. Mikulin, E. I., Tarasov, A. A., and Shrebyonock, M. P. (1983), "Low-Temperature Expansion Pulse Tubes", Adv. in Cryo. Eng., v.29, 629-637.
3. Radebaugh, R., "Progress in Cryocoolers", Applications of Cryogenic Technology, v.10, 1-14 (1991).
4. Radebaugh, R., Zimmerman, J., Smith, D. R., and Louie, "A Comparison of Three Types of Pulse Tube Refrigerators: New Methods for Reaching 60 K," Adv. Cryogenic Eng., v.31, p. 779 (1986).
5. Bear, J., Dynamics of Fluid Flow in Porious Media (1972).
6. Cheng, P., "Heat Transfer in Geothermal Systems," Adv. in Heat Transfer, v.14, p.1-105 (1978).
7. Hsu, C. T. and Cheng, P. (1990), "Thermal Dispersion in Porous Media," Int. J. Heat Mass Transfer, v. 33, pp. 1587-1597.

8. Tanaka, M. Yamashita, I. and Chisaka, F.(1990), Flow and Heat Transfer Characteristics of the Stirling Engine Regenerator in an Oscillating Flow, *JSME International J.*, v.33, p.283.
9. Kays, W. M. and London, A. L., Compact Heat Exchangers, McGraw-Hill Book Company (1984).
10. Roach, P. D. and Bell, K. J., (1988),"Analysis of Pressure Drop and Heat Transfer Data from the Reversing Flow Test Facility," Rept. #ANL/MCT-88-2, Argonne National Laboratory, Argonne, Illinois.
11. Gedeon, D. and Wood, G., CSTR/OU Regenerator Oscillating Flow Test Rig Results, June 1992.
12. Huang, B. J. and Lu, C. W. (1992), "Dynamics Characteristics of Regenerators Used in Cryocoolers," Proc. of the 7th International Cryocooler Conference, p.1-
13. Storch, P. J., and Radebaugh, R. (1988), Development and Experimental Test of An Analytical Model of the Orifice Pulse Tube Refrigerator," Adv. Cryogenic Engineering, v.33, p.851.
14. Radebaugh, R., Gary, J., Marquardt, Louie, B., and Daney, D.(1992), "Measurement and Calculation of Regenerator Ineffectiveness for Temperatures of 5 to 40 K," Wright Laboratory, Report # WL-TR-92-3074.
15. Harpole, G. M. and Chan, C. K. (1990), Pulse Tube Cooler Modeling, Proc. of the Sixth Int. Cryocoolers Conference, pp. 91-101.
16. Richardson, E. G. and Tyler, E. (1929), "The Transverse Velocity Gradient near the Mouths of Pipes in Which an Alternating or Continuous Flow of Air is Established," Proc. Phys. Soc. London, v. 42, p.1-15.
17. Uchida, S. (1950), "The Pulsating Viscous Flow Superposed on the Steady Laminar Motion of a Incompressible Fluid in a Circular Pipe, ZAMP, v.7, pp.403-422.
18. Hino, M., Sawamoto, M., and Takasu, S., (1976), "Experiments on Transition to Turbulence in an Oscillatory Pipe Flow," J. Fluid Mech., v.75, pp.193-207.
19. Simon, T. W. and Seume, J. R.(1988), "A Survey of Oscillating Flow in Stirling Engine Heat Exchanger," NASA Contract Report 182108.
20. Isabey, D., Chang, H. K., Delpuech, C., Harf, A., and Hatzfeld, C. (1986), "Dependence of Central Airway Resistance on Frequency and Tidal Volume: a Model Study," The American Physiological Society, p.113-126.
21. Iwabuchi, M., and Kanzaka, M. (1982), "Experimental Investigation into Heat Transfer Under the Periodically Reversing Flow Condition in a Heated Tube," I. Mech. Engineers, C24/82,135.
22. Hwang, M. F. and Dybbs, A.(1983), "Heat Transfer in a Tube with Oscillatory Flow," ASME Paper #83-WA/HT-90.

23. Wu, P., "Investigation of Oscillating Flow Resistance and Heat Transfer in the Gap Used for Cryocoolers" 13th IECEC.
24. Gifford, W. E. and Longworth, R. C. (1966), "Surface Heat Pumping", Adv. in Cryo. Engg., v.11, 171-179.
25. Huang, B. J., Lee, L. T. and Lu, C. W. (1990), System Design Analysis of Pulse-Tube Cryocooler, Proceedings of the 6th International Cryocoolers Conference, v.1, p.77.
26. Lee, J. M., Kittel, P. Timmerhaus, K. D., and Radebaugh, R. (1992), "Flow Patterns Intrinsic to the Pulse Tube Refrigerator," Proc. of 7th International Cryocooler Conference, 125-139.
27. Sarangi, S. and Baral, H. S. (1987), Effects of axial conduction in the fluid on cryogenic regenerator performance, Cryogenics, v.27, 505-509.

CONCURRENT COMPUTATION OF ABERRATION COEFFICIENTS

Meledath Damodaran
Associate Professor
Division of Arts & Sciences

University of Houston - Victoria
2506 E. Red River
Victoria, Texas 77901

Final Report for:
Summer Faculty Research Program
Phillips Laboratory

Sponsored by:
Air Force Office of Scientific Research
Bolling Air Force Base, D.C.

and

Phillips Laboratory

August 1994

8-1

CONCURRENT COMPUTATION OF ABERRATION COEFFICIENTS

Meledath Damodaran
Associate Professor
Division of Arts & Science
University of Houston - Victoria

Abstract

The method of Phase Diversity is useful to measure the aberrations caused by distortions by atmosphere and other media. Two images are taken: one at a focused position and the other at a defocused position. By minimizing the Con-salves metric, the Zernike aberration coefficients are estimated and thus the aberration that produced the distortion in the original image is obtained. Being a nonlinear optimization technique involving several variables, the method is very compute intensive. We introduce a method using nonlinear optimization involving only a single variable to independently, hence potentially concurrently, evaluate the different Zernike coefficients. The method of independent evaluation of Zernike coefficients can be further speeded up by using parallel processing and neural network techniques. Our method works both for point source objects as well as extended objects.

CONCURRENT COMPUTATION OF ABERRATION COEFFICIENTS

Meledath Damodaran

1. INTRODUCTION

The presence of aberration in an optical system can be represented by a generalized pupil function

$$P(x,y) = P(x,y) \exp[i k W(x,y)]$$

where P is the pupil function which is 1 inside and 0 outside the aperture, and W is an effective path length error at (x,y) in the exit pupil [Goodman 1968]. The Zernike decomposition provides a simple way to include in W the effects of higher order aberrations in an orderly fashion [Kim 1987]. The Zernike polynomials are usually described in terms of the radial variable and the angular variable in the pupil. For the purpose of correcting atmospheric aberrations it may be necessary to estimate several coefficients in the Zernike decomposition of the wave front function. In [Carreras 1994] a method using Phase Diversity to extract higher order Zernike coefficients is introduced, along with a laboratory implementation. The method makes heavy use of nonlinear optimization involving several variables.

The Phase Diversity method may be summarized as follows. Two images are acquired: one at the focal plane and the other with some known aberration (typically focus aberration). The first image is corrupted by the unknown aberration, whereas the second image (known as the diversity image) is much more corrupt, as it contains not only the unknown phase errors of the system but also the additional diversity phase error. Using the optical transfer functions of the system with and without the added defocus, and the Fourier transform O of an estimate of the object, an error metric is set up between the measured and diverse images. This error metric, originally due to Gonsalves [Gonsalves 1982] is independent of the original object estimate. An excellent source of derivation of the Gonsalves metric is [Miller 1993]. A non-linear optimization technique such as the gradient descent method is then used to estimate the Zernike coefficients that would minimize the above error metric. Carreras et al [Carreras 1994] used the conjugate gradient method for non-linear optimization, using finite difference methods to calculate the gradients.

Even though the above method is attractive, it is computationally a very formidable task to calculate the several Zernike coefficients for a given system. In order to get a reasonably accurate approximation of the coefficients, a large number of iterations have to be carried out. Each iteration involves time-consuming calculations of the error function and its gradients. These could not be done in real time,

to correct images on the fly. Therefore, it is natural to consider ways to speed up the computational task.

In this paper we show that all the Zernike coefficients may be computed in parallel. Our method uses nonlinear optimization of a single variable only. The advantages of such a method are self-evident. Independent evaluation of the coefficients implies the possibility of using a parallel processor or a network of processors to speed up the computation. The number of iterations needed with our method are significantly less than what was required in [Carreras 1994] in the case of gradient descent involving several variables. Also, each iteration in our case took a fraction of the corresponding duration of time for the multivariate algorithm. The possibility of independent evaluation of the aberration coefficients also opens up other possibilities for their efficient evaluation, the prominent being the method of neural networks. This will be the subject of our future investigation.

2. METHOD

We start with a pupil function P in the form of a 64 X 64 matrix representing a circle. The circle itself is contained in a 32 X 32 submatrix. We then compute the generalized pupil function \mathbf{P}

$$\mathbf{P} = P \exp(i(a_1 \cdot Z_1 + a_2 \cdot Z_2 + a_3 \cdot Z_3 + a_4 \cdot Z_4 + a_5 \cdot Z_5)),$$

where a_1, \dots, a_5 are given values of Zernike coefficients representing simulated aberrations, and Z_1, \dots, Z_5 are Zernike polynomials, defined as follows and representing focus error, astigmatism in the x-direction, astigmatism in the y-direction, coma in the x-direction, and coma in the y-direction respectively:

$$Z_1 = 2r^2 - 1$$

$$Z_2 = r^2 \cos 2\theta$$

$$Z_3 = r^2 \sin 2\theta$$

$$Z_4 = (3r^2 - 2)r \cos \theta$$

$$Z_5 = (3r^2 - 2)r \sin \theta$$

It may be noted that for this experiment, we chose to use these five aberrations, but the method may be applied with any number of aberrations. We ignored the piston, x-tilt, and y-tilt aberrations, the first three aberrations, because they were not needed for our application.

We compute the optical transfer function H as

$$H = \mathbf{P} * \mathbf{P},$$

where * denotes 2-D convolution.

Similarly we compute the generalized pupil function and the transfer function for the diverse image as follows:

$$\mathbf{P}_d = \mathbf{P} \exp (i k Z_1)$$

$$H_d = \mathbf{P}_d * \mathbf{P}_d$$

Here, k is the coefficient of defocus in the diversity term.

Next, a computer-generated test object was chosen. This pristine object is also of size 64 X 64. The object is next blurred using the transfer function calculated for the optical system (H) to generate the in-focus measured image. In addition, an out-of-focus image was generated by using the transfer function H_d .

Let us call these images I and I_d . Then

$$I = O H$$

$$I_d = O H_d,$$

where O is the Fourier transform of the object o .

The non-linear optimization can start now. For each separate aberration we compute a \mathbf{P}^{\wedge} and a \mathbf{P}_d^{\wedge} as follows:

$$\mathbf{P}^\wedge = \mathbf{P} \exp(i \mathbf{a}_j^\wedge \mathbf{Z}_j)$$

$$\mathbf{P}_d^\wedge = \mathbf{P}^\wedge \exp(i \mathbf{k} \mathbf{Z}_1)$$

where $j = 1, \dots, 5$, and $^\wedge$ denotes estimates. We then take the 2-D convolutions of these to get the estimated transfer functions \mathbf{H}^\wedge and \mathbf{H}_d^\wedge :

$$\mathbf{H}^\wedge = \mathbf{P}^\wedge * \mathbf{P}^\wedge$$

$$\mathbf{H}_d^\wedge = \mathbf{P}_d^\wedge * \mathbf{P}_d^\wedge$$

To estimate the unknown aberrations (along with estimating the object), we minimize an error metric:

$$E = \sum \|\mathbf{I} - \mathbf{H}^\wedge \mathbf{O}^\wedge\|^2 + \|\mathbf{I}_d - \mathbf{H}_d^\wedge \mathbf{O}^\wedge\|^2,$$

where the summation is over all the matrix elements. But the object is unknown and difficult to estimate. Gonsalves used Parseval's theorem to perform this calculation in the spatial frequency domain. Following this suggestion, we can minimize E by choice of \mathbf{O}^\wedge as:

$$\mathbf{O}^\wedge = (\mathbf{I} \mathbf{H}^{\wedge*} + \mathbf{I}_d \mathbf{H}_d^{\wedge*}) / (\|\mathbf{H}^\wedge\|^2 + \|\mathbf{H}_d^\wedge\|^2)$$

where * denotes conjugates. Substituting this into the above, we get the Gonsalves error metric

$$E = \sum [|H_d^* - I_d H|^2] / [|H|^2 + |H_d|^2],$$

where the summation is over all the matrix elements.

The function E can be seen as a function of a_j^* alone, and is independent of the object. It is, furthermore, a smooth function.. In order to determine the value of a_j^* for which E is minimum, we used a quadratic interpolation method due to M. J. D. Powell, from the IMSL library of mathematical subroutines. We chose this routine as it uses only function evaluations and because it gave satisfactory results when we used double precision arithmetic. We found that the algorithm provides fast convergence. With single precision arithmetic, rounding errors in the calculations caused the existence of , and convergence to, other local minima nearby the sought-out minimum point.

3. RESULTS

The results of a typical run with an extended object are given in Table I

Actual aberration coefts. Estimated aberration coefts. Gonsalves metric

-1.25	-1.23	.1e-4
.66	78	.7e-4
1.5	-1.74	.66e-4
.44	.43	.77e-4
-.33	-.21	.77e-4

Average percentage error: 14.7

TABLE I

An average of 12 iterations was all that was required for convergence in the five instances of single variable optimizations of our experiment. The average percentage error of the computed values (a_j^{\wedge}) from the given values (a_j) was no more than 15 percent. This error may be attributed to the effect of round-off errors, and is unavoidable in minimization routines that use only function values [IMSL, 1989]. The error, however, is no more than similar runs in the multivariate case [Carreras 1994] and are well within expected norms. In fact, the image reconstruction with this level of accuracy is quite satisfactory, as illustrated in [Carreras 1994]. Explicit derivative evaluation is not practical, as the dependence of E on

a_j^\wedge is via a convolution; hence, optimization routines that explicitly require the derivative to be made available to the routine, cannot be employed.

However, when we used a point spread image instead of an actual image, the estimated Zernike coefficients were near perfect; the average error in this case was just 1.7 percent.

4. CONCLUSION

We were able to show that the estimation of the aberration coefficients may be done independent of each other using the same Gonsalves metric as in the normal case. That the accuracy of these estimates was comparable to, if not slightly better than, when they were calculated by the straightforward method of non-linear optimization involving several variables, demonstrates that the method of independent evaluation using a non-linear optimization of the Gonsalves metric with a single variable, is experimentally valid. It would be good to prove this theoretically as well. It is remarkable and somewhat surprising that when we consider only one aberration in the calculation of the Gonsalves metric, the terms I and I_d contain contributions from all the aberrations, whereas the estimates H^\wedge and H_d^\wedge only have

that one aberration under consideration, and still it does not seem to affect the minimum point.

The advantages of independent evaluation of the Zernike coefficients are many. The total amount of time required to calculate all the coefficients is dramatically shorter than in the multivariate case, as (i) the total number of iterations needed is less, and, more importantly, (ii) each iteration in our algorithm takes only a fraction of the time for the multivariate case, it being the case that it is easier for the function to move towards a minimum in the case of a function of a single variable. The fact that the calculation of the coefficients may be done independently, also means that we may easily partition the task into several nodes in an interconnected network of processors or in a parallel computer of the right type. Another case in point is the application of neural networks. If we have to compute n aberration coefficients, we may use n simpler neural networks rather than one complicated network that computes all the coefficients. The neural network implementation may also be a parallel one. It would then be possible to apply this method in a real-time image reconstruction scheme. We have already started looking into these possibilities.

5. REFERENCES

[Carreras 1994] Richard A. Carreras, Sergio Restaino, Dennis Duneman, “ A Laboratory Experiment Using Phase Diversity to Extract Higher Order Zernike Coefficients”, Proceedings of the SPIE International Symposium on Optics, Imaging and Instrumentation, July 1994

[Gonsalves 1982] R. A. Gonsalves, “Phase Retrieval and Diversity in Adaptive Optics”, Opt. Eng. 21 (5), 829-832, 1982

[Goodman 1968] J. W. Goodman, *Introduction to Fourier Optics*, McGraw-Hill, San Francisco, 1968

[IMSL 1989] Users Manual, FORTRAN Subroutines for Mathematical Applications, Vol.3, IMSL Inc, Houston, TX, 1989

[Kim 1987] C-J. Kim and R. R. Shannon, “Catalog of Zernike Polynomials”, Chapter 4, *Applied Optics and Optical Engineering*, Vol. X, pp 193-221, edited by R.R. Shannon and J.C. Wyant, Academic Press

[Miller 1992] Nancy A. Miller, *Nonlinear Optimization and Neural Networks for Phase Diversity: Simulation and Experiment*, Ph.D. Thesis, University of New Mexico, Albuquerque, NM, December 1992

ANALYSIS TO DETERMINE THE QUALITY
FACTOR OF A COMPLEX CAVITY

Ronald R. DeLyser
Assistant Professor of Electrical Engineering
Department of Engineering

Peyman Ensaf
Graduate Student
Department of Engineering

University of Denver
2390 S. York Street
Denver, CO 80208-0177

Final Report for:
Summer Faculty Research Program
Phillips Laboratory

Sponsored by:
Air Force Office of Scientific Research
Bolling Air Force Base, Washington, D.C.

September, 1994

ANALYSIS TO DETERMINE THE QUALITY
FACTOR OF A COMPLEX CAVITY

Ronald R. DeLyser
Assistant Professor of Electrical Engineering
Peyman Ensaf
Graduate Student
Department of Engineering
University of Denver

Abstract

The low frequency, preliminary analysis of a simplified model of a space craft sensor has been accomplished using CARLOS-3D™ (Code for Analysis of Radiators on Lossy Surfaces), a general purpose computer code using the Method of Moments (MoM.) Resonances of a cavity region have been identified by determining the cavity quality factor (Q) as a function of frequency. The Q is proportional to the total energy stored in the cavity and inversely proportional to the power lost from the cavity due to lossy materials and apertures. Even though this measure does not give an exact value for power density at a specific point in the system, it does give an indication of the representative power levels one will find in a similar system. An analysis approach for the high frequency range includes using GEMACS (General Electromagnetic Model for the Analysis of Complex Systems) which incorporates the geometrical theory of diffraction, MoM, and the finite difference method for multiple region problems. A comparison of the two methods (CARLOS-3D™ and GEMACS) at an intermediate frequency (~3 GHz) is proposed.

ANALYSIS TO DETERMINE THE QUALITY
FACTOR OF A COMPLEX CAVITY

Ronald R. DeLyser and Peyman Ensaf

Introduction

Determining the effects of high power microwaves (HPM) to satellite systems and subsystems is one of the missions of the Phillips Laboratory Satellite Assessment Center (SAC). HPM tests can not always be performed on these systems so that analytical techniques are necessary. One such analytical technique has been proposed [1] for the analysis of large complex cavities.¹ However, when the systems are not large, numerical techniques have to be used. When analyzing a single system or subsystem, it can be considered large at high frequencies and not large at the lower frequencies. One therefore has to use different analytical procedures depending on the frequency of interest.

We were tasked with analyzing a simplified model of a typical sensor over a frequency range of several hundred MHz to tens of GHz. Figure 1 shows a skeleton drawing of the model generated by GAUGE (Graphical Aids for User's of GEMACS) [2] which is discussed below. The model of the sensor consists of a lower mirror assembly, and an upper cavity region.

The ultimate goal of any analysis would be to find the power density incident on a particular part in the cavity. However, due to non-uniformity in the manufacturing process or changes in the internal configuration which accompanies field modifications or maintenance, all such sensors will not be alike. Therefore, any analysis of a specific system would be futile. So what should our calculated quantity be? We decided on the quality factor (Q) of the upper cavity region. As discussed in detail below, Q is proportional to the total energy stored in the cavity

¹ "Large" is to be taken in the sense that the dimensions of the cavity or object is large when compared to the wavelength of the radiation.

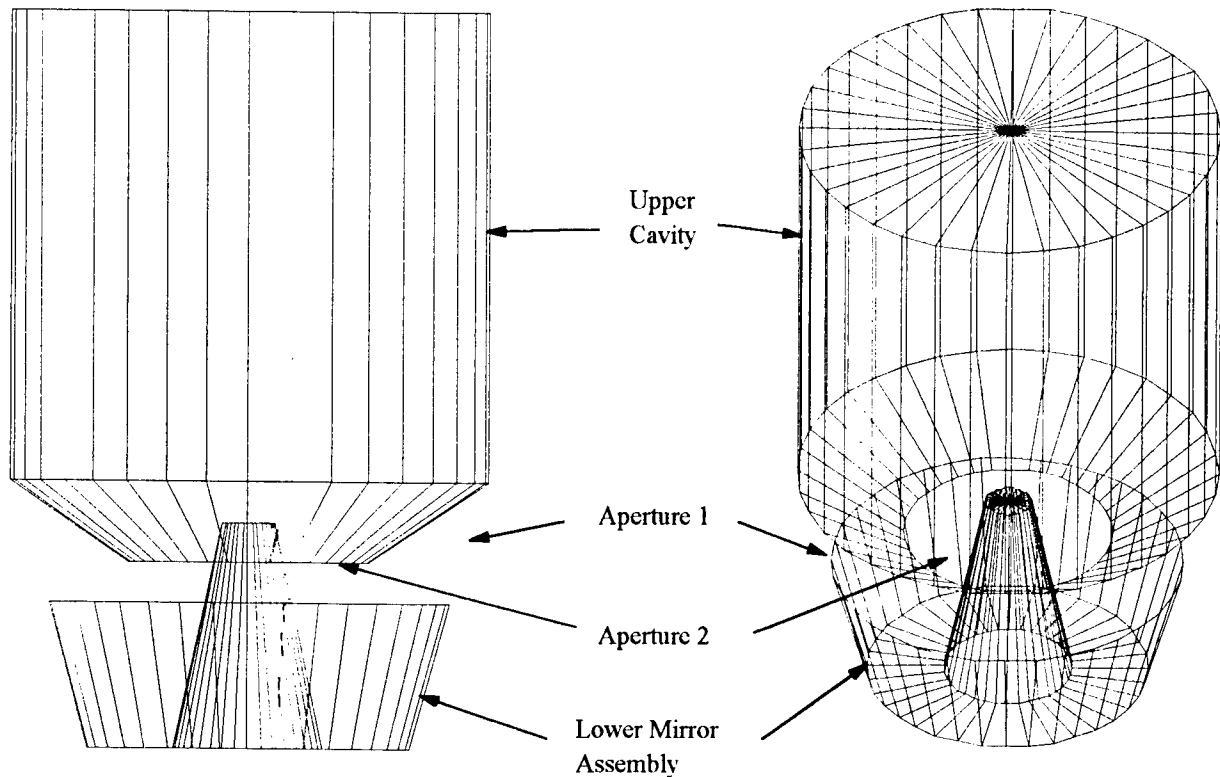


Figure 1. The symplified model of the sensor.

and inversely proportional to the power lost from the cavity due to lossy materials and apertures. Even though this measure does not give an exact value for power density at a specific point in the system, it does give an indication of the representative power levels one will find in a similar system.

The Software

The programs available at the SAC which are appropriate for this project are CARLOS-3D™ (Code for Analysis of Radiators on Lossy Surfaces) [3], a general purpose computer code using the Method of Moments (MoM) and GEMACS (General Electromagnetic Model for the Analysis of Complex Systems) [4], which solves electromagnetic radiation and scattering problems using MoM and Geometrical Theory of Diffraction (GTD) for exterior analysis, and a Finite Difference (FD) formulation for solution of interior problems.

CARLOS-3D™

The CARLOS-3D™ software utilized in this project implements the method of moments (MoM) solution for fully arbitrary three-dimensional complex scatterers. These solutions are obtained for perfectly electrically conducting (PEC) bodies as well as fully or partially penetrable ones. The electromagnetic scattering formulation used in this software (hence in this project) is based on surface integral equations (SIE) spanning the entire external surface of the body and the internal boundaries between penetrable and PEC regions. The analysis and software are extended to boundaries (or surfaces) which may be characterized by resistive or magnetic sheets as well as impedance boundary conditions.

CARLOS-3D™ operates on a triangularly-faceted body that may be composed of the following types of surfaces:

- (1) Conducting (PEC)
- (2) Conducting/Penetrable
- (3) Multi-Region Penetrable
- (4) Resistive Boundary Condition (RBC)
- (5) Magnetically Conducting Boundary Condition (MBC)
- (6) Impedance Boundary Condition (IBC)
- (7) Global or Local RBC and IBC

CARLOS-3D™ implements the MoM solutions for a variety of SIE formulations associated with the classes of 3-D geometries described above. A combined-field formulation is available to overcome the ill-conditioning with the electric and magnetic field integral equations (EFIE and MFIE) for closed conducting bodies at internal resonances.

The following options are available in this code:

- (1) EFIE/PMCHW (after Poggio, Miller, Chu, Harrington, and Wu) formulation for coated conductors (symmetric system matrix)
- (2) EFIE, MFIE and CFIE (Combined Field Integral Equation) on closed conductors
- (3) PMCHW on dielectric boundaries

(4) CFIE for combination of open/closed geometries

The analysis and the implementing software permits the following specific options to be considered for the foregoing classes of 3-D problems:

- (1) Mono- and bistatic scattering,
- (2) far field calculation,
- (3) body symmetry option to minimize storage and execution time,
- (4) automatic modeling of junctions where two or more surfaces intersect,
- (5) infinitesimally thin conducting, resistive, and magnetic surfaces,
- (6) surface current computation,
- (7) infinite ground plane, adjacent to or intersecting the body,
- (8) analytical green's function evaluation using singularity extraction,
- (9) near field calculations,
- (10) radar cross-section,

Specifics of the use of CARLOS-3D™ for this project

For penetrable bodies the boundary conditions are generally complicated and depend on geometry and material composition. Integral formulations of Maxwell's equations provide an attractive formulation for these problems, since the necessary boundary conditions are easily incorporated. The resulting equations can then be solved by the Method of Moments technique.

The EFIE and MFIE exhibit an internal resonance phenomenon that is due to the non-uniqueness of the solution in these integral equations at and near the resonance frequencies of the interior problem [5]. These non-unique solutions arise from the fact that the resonant frequency can be achieved in the absence of an excitation source. Therefore, at these particular frequencies, the EFIE and MFIE formulations can lead to non-physical, spurious results. The CFIE remedies this non-uniqueness in results by adding a supplementary integral to eliminate spurious

solutions. In this method it is recognized that at interior resonance frequencies an electric current on the surface that produces no tangential electric field on the surface can exist. This is overcome by placing both an electric current J_s and a magnetic current M_s on the surface S . In this case the combined field integral equation can be written as [5],

$$\hat{n} \times [E^i + E^s (J_s, M_s)] = 0 \quad (1)$$

where $E^s(J_s, M_s)$ denotes the electric field E^s radiated by the sources J_s and M_s and n is the unit vector. The CFIE formulation results in a well-posed problem and provides robust solutions at resonances. Therefore in accordance with this approach, a set of calculations will be conducted using the EFIE technique in parallel with a set conducted using the CFIE at these particular internal resonances. Hence, the results obtained from both approaches will be compared and any discrepancies will be acknowledged.

Application of Mathematica to the problem.

CARLOS-3D™ requires an input file in which one or more geometrical data files are incorporated. The input file along with the geometrical data files need to be prepared in accordance with the CARLOS-3D™ code. This consists of a descriptive title line followed by the frequency of operation, number of dielectric regions (if any) and then the name of each data file under study along with indications of whether a particular data file represents a perfect electric conductor or a dielectric and also whether it's a closed or an open structure. CARLOS-3D™ recognizes a few different data files such as

- (1) ACAD-facet
- (2) AGM
- (3) IGES

Of many different interfaces compatible with CARLOS-3D™, the one available at the Satellite Assessment Center was Mathematica [6]. Mathematica is not necessarily the best user interface software (this will be discussed below), however, it has some features that made it unique. Mathematica enables the user to write a program generating input data files that incorporate triangular surfaces along with nodal values that describe each triangular surface and also identifies the X,Y,Z coordinates accordingly, providing compatibility with the CARLOS-3D™ code. In order

to generate these structures, Mathematica uses functions such as Surface Of Revolution and Parametric Plot3D. A particularly useful feature in Mathematica is its ability to create a complicated structure by generating sub-structures and ultimately joining each of those together, forming the desired composite structure. In generating the structure of the sensor, it was necessary to keep in mind that the body of each structure must be segmented into a number of cells in which each cell side is taken to be at most one-tenth of the operating wavelength. Therefore, using Mathematica the appropriate number of segmentations was calculated and implemented for each operating frequency range (wavelength).

Calculation Of The Quality Factor (Q)

Once the geometry of the sensor was fully generated using the above techniques, the appropriate data files were formed into a compatible input file. At lower frequencies below internal resonances, namely 0.6 GHz-1.6 GHz, the input files dictated the EFIE technique. The next step was to create a grid of points in the interior of the upper cavity of the sensor for the calculation of the near fields. A rectangular grid was chosen.

In general the fields inside the chamber are nonuniform. However, in this analysis, uniformity was assumed for individual cubic cells of 1.5 cm ($< 0.1\lambda$) in each dimension. These grid points (a total of 963) were prescribed in the input file to CARLOS-3D™ for near-field calculations. Ultimately, CARLOS-3D™ calculated the near fields and the Z-directed power at each declared grid point. The power calculations of interest were those into and out of the inlet to the upper chamber of the model. CARLOS-3D™ provides the X,Y,Z components of the fields at each grid point. Knowing these field values, the electric and magnetic energy at each point are calculated using [2]

$$e = \frac{1}{4} \iiint \epsilon |E|^2 dx dy dz \quad (2)$$

$$m = \frac{1}{4} \iiint \mu |H|^2 dx dy dz \quad (3)$$

The integrals in equations (2) and (3) are quite trivial to solve. Since it is assumed that the fields within each cell are constant, the E and the H terms along with the corresponding material properties can be brought out of the integrals leaving only a volume integral with respect to the dimensions of the cell. Keeping in mind that the dimensions of each cell are 1.5 cm on each side, equations (2) and (3) become

$$e = \frac{1}{4} \epsilon |E|^2 (.015m)^3 \quad (4)$$

$$m = \frac{1}{4} \mu |H|^2 (.015m)^3 \quad (5)$$

Equations (4) and (5) correspond to the electric and magnetic energy for one cell. Now, the same calculations for each cell corresponding to each grid point must be done and then sum the total for both electric and magnetic energies and the sum of their total would be the total energy for each of the θ and ϕ polarizations. The chosen incidence angles were θ and ϕ at 90° and 0° respectively (figure 1). Once the fields are calculated, the power [2] going out from the chamber can also be calculated, using the Poynting theorem. Hence, power is calculated using

$$\vec{P} = \iint (\vec{E} \times \vec{H}^*) \cdot d\vec{s} \quad (6)$$

Since the outgoing power is in the negative Z- direction, we can calculate the power using

$$\vec{P} = - \iint [(\hat{a}_x E_x + \hat{a}_y E_y + \hat{a}_z E_z) \times (\hat{a}_x H_x + \hat{a}_y H_y + \hat{a}_z H_z)] \cdot dx dy \cdot \hat{a}_z \quad (7)$$

$$\vec{P} = - \iint [\hat{a}_z (E_x H_y) - \hat{a}_z (E_y H_x)] dx dy \quad (8)$$

We are only concerned with the power out of the chamber so power calculations at a height of 0.075 m, which is at the inlet of the chamber, were accomplished. Once again, since the fields within each designated cell are constant, equation (8) can be modified to

$$\vec{P} = - (E_x H_y - E_y H_x) (0.015)^2 \cdot \hat{a}_z \quad (9)$$

Once the energy and power are calculated, Q is given by

$$Q = \omega \frac{U}{P} \quad (10)$$

where U and P are the total energy stored and power exiting the cavity calculated separately for θ and ϕ polarizations.

Summary Of Results

Recall that the extent of these calculations is to a high frequency of 1.6 GHz. Calculations at higher frequencies will be conducted at a later time. Figures 2, 3 and 4 are plots of Q, energy, and power versus frequency for both polarizations. At aperture 1 of figure 1a, the θ polarized electric field will be more easily maintained because the field lines will terminate on the top and bottom edges of the aperture. However, the ϕ polarized electric fields (in

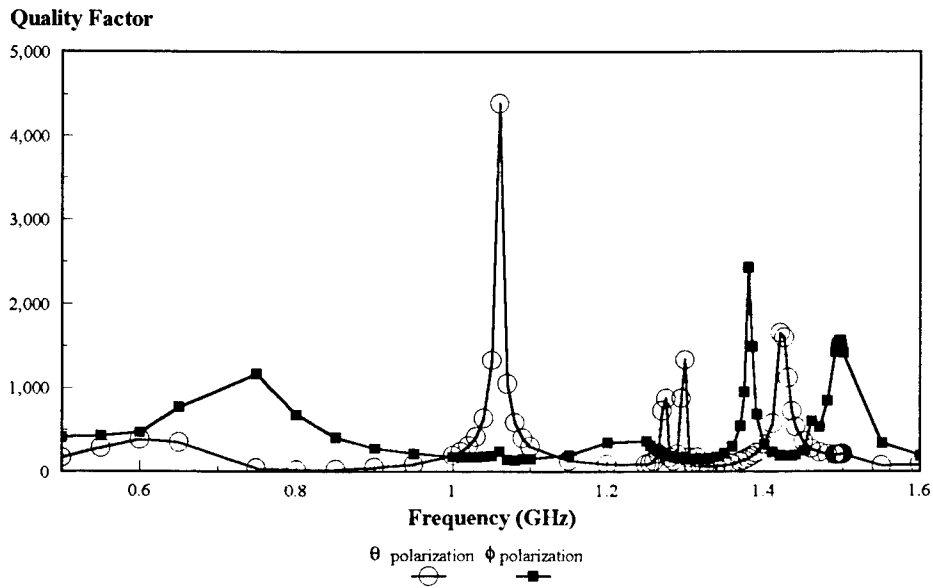


Figure 2. Q of the upper cavity region.

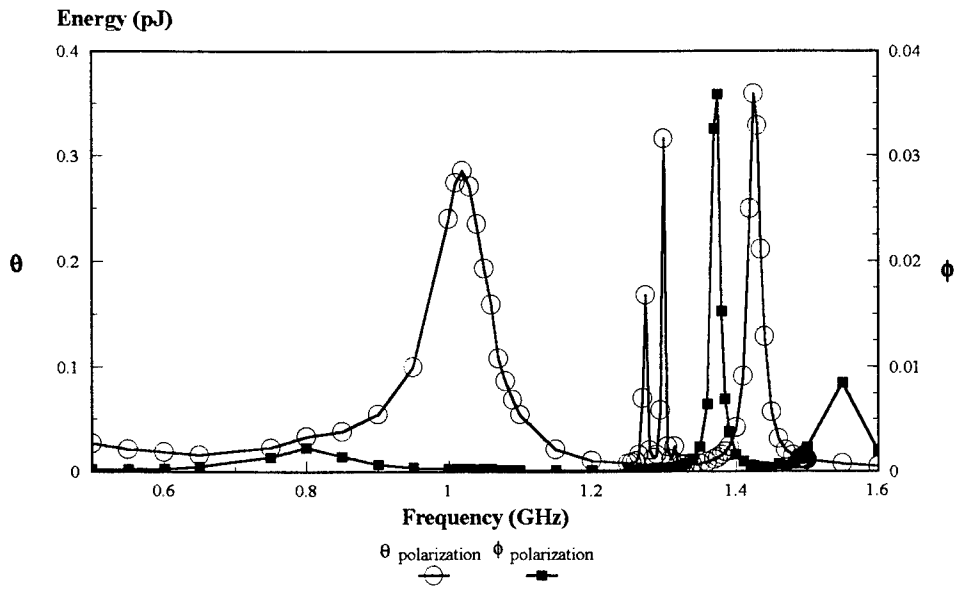


Figure 3. Energy in the upper cavity region.

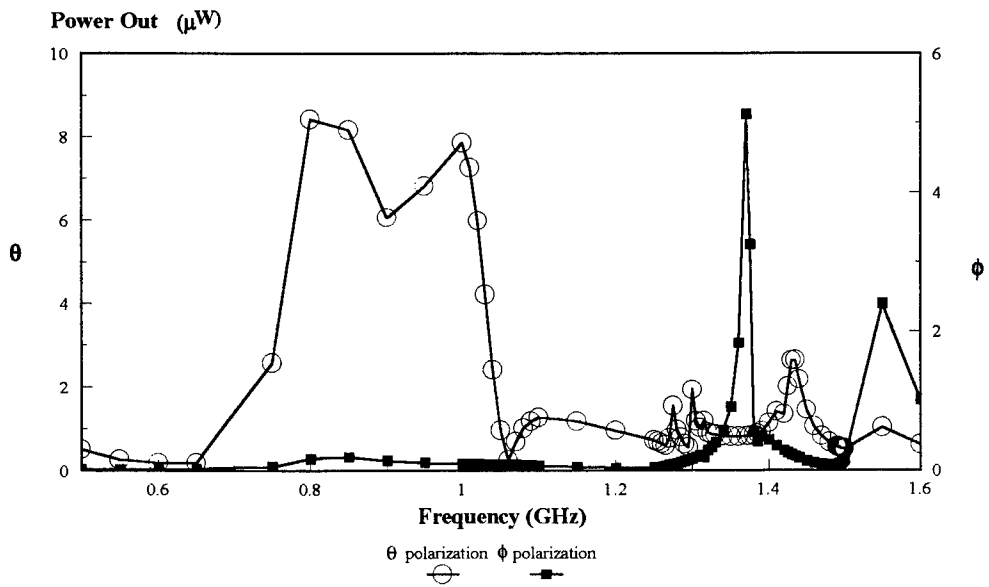


Figure 4. Power leaving the upper cavity region.

the low frequency domain) create ϕ directed currents on the surfaces and hence the aperture fields are not as pronounced. Therefore, as observed in Figure 3, the energy values due to the θ polarized fields are much higher than those for the ϕ polarized fields. In Figure 3, one can also observe that at some higher frequencies increases in energy due to the ϕ polarized fields occur. Table II provides resonant frequencies for a frequency sweep over the range of 0.5 GHz - 1.6 GHz. Table II also compares the measured resonant frequencies with those analytical calculations assuming a cylindrical cavity of 8.6 cm supporting TM modes.

The TE_{mnp} and TM_{mnp} modes provided in Table II are given respectively by,

$$f_{mnp}^{TEz} = \frac{1}{2\pi\sqrt{\mu\epsilon}} \sqrt{\left(\frac{\chi'_{mn}}{a}\right)^2 + \left(p\frac{\pi}{h}\right)^2} \quad \begin{cases} m=0, 1, 2, 3, \dots \\ n=1, 2, 3, \dots \\ p=1, 2, 3, \dots \end{cases} \quad (11)$$

$$f_{mnp}^{TMz} = \frac{1}{2\pi\sqrt{\mu\epsilon}} \sqrt{\left(\frac{\chi_{mn}}{a}\right)^2 + \left(p\frac{\pi}{h}\right)^2} \quad \begin{cases} m=0, 1, 2, 3, \dots \\ n=1, 2, 3, \dots \\ p=0, 1, 2, 3, \dots \end{cases} \quad (12)$$

Table II. Resonant frequencies.

Resonant Frequency (GHz)	Quality θ polarization	Quality ϕ polarization	Analytical for the upper Cavity Region
1.06	4392.108		
1.126			TEM(λ)
1.275	872.1293		
1.30	1337.026		
1.33			TM ₀₁₀
1.38		2433.935	
1.42	1659.651		
1.496		1566.211	
2.127			TM ₁₁₀
2.639			TE ₀₁₁

Where κ'_{mn} represents the n th zero of the derivative of the m th order Bessel function. According to equations (11) and (12), the lowest mode is the TM_{010} proceeding with TM_{110} which are well below the first TE mode (TE_{011}). The subscript p in equation (12) will remain zero for the lowest TM modes, therefore, guarantee the TM modes to be independent of the height of the cavity. Therefore, the analytical values in Table II are for the TM_{mnp} modes. Also due to the presence of the coaxial like structure below the chamber, there may exist TEM modes, and hence these are also presented in Table II. The remaining data provided in Table II correspond to CARLOS-3D™ calculations. Differences with the numerical results are due to the fact that we have a much more complex cavity.

Radar cross-section (RCS) for the model was also calculated and is shown in figure 5 as a function of frequency. It was hoped that there would be a correlation between resonances and this quantity. Other than a small indication in the region of the 1.3 GHz resonance, there is no correlation. Evidently this is due to the fact that a much greater

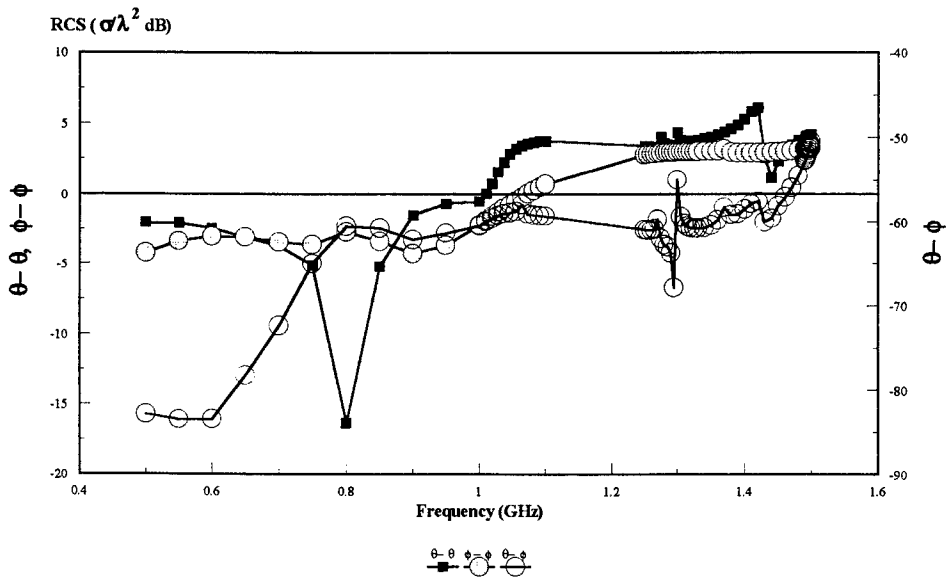


Figure 5. Radar cross-section for the sensor.

amount of energy is scattered than is stored in the cavity. Any dip in the RCS versus frequency graph would have to be due to a much greater amount of energy stored in the cavity relative to that which is scattered.

Problems using CARLOS-3D™ and Mathematica

A list of some problems encountered with Mathematica and CARLOS-3D™ follows:

a) Generating complicated structures using Mathematica, requires many tedious operations which could most likely be avoided with a well designed interface.

b) As the measurements escalate to higher frequencies, the cell sizes become much smaller. For problems of circular symmetry, the cells near the center of circles become exceedingly small. Mathematica only allows a symmetric gridding like that shown in Figure 6a. Since in this geometry, at a radius of half the outer radius the cells have sides half as large, a simple transition such as that shown in Figure 6b can be used to maintain reasonable cell

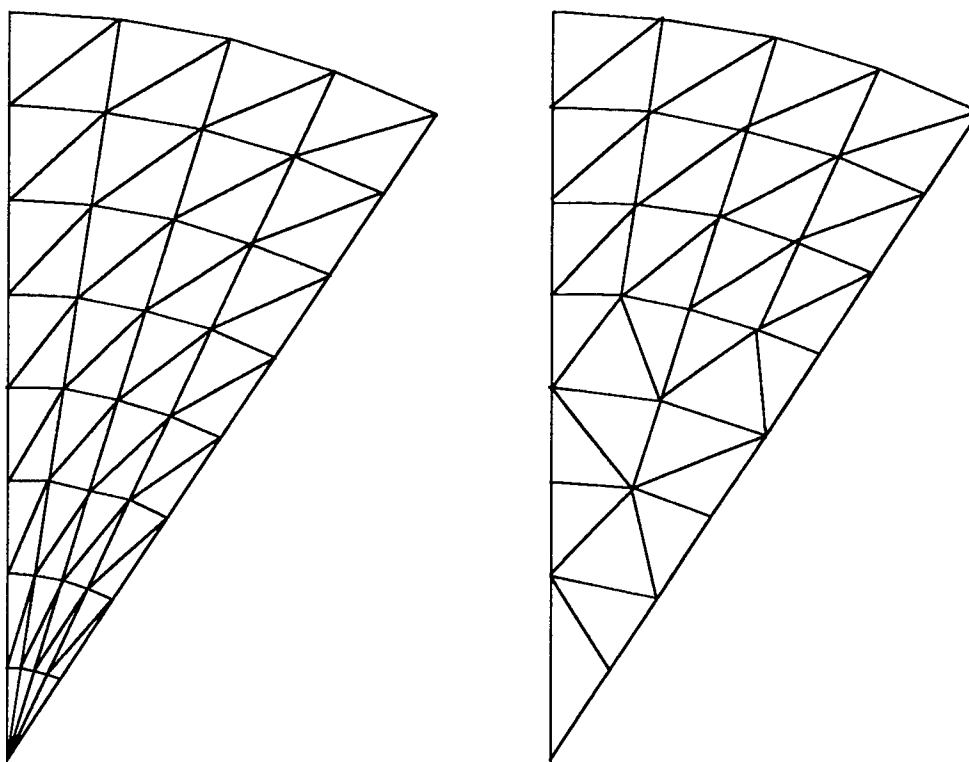


Figure 6. Alternate gridding scheme for circular geometry.

sizes. This is not now possible with the software available at the Phillips SAC.

(c) The largest input files used for calculations were for a frequency of 1.6 GHz. At this frequency, there exists a total of 3990 unknowns. This corresponds to approximately 16 million complex numbers in the impedance matrix. Each complex number requires 8 bytes, which means that at a frequency of 1.6 GHz, the user requires approximately 128 Mbytes of random access memory (RAM). The work station that we were using has this much RAM, but a larger problem will require that the work station do disk swapping. It has been our experience that this slows down the process significantly. Without disk swapping, this large problem has an approximate running time of 1 hour on an IBM RS6000 570 Powerstation. As a test at 3 GHz and approximately 8000 unknowns, CPU time was reduced to 25% of the total process time and it was anticipated that a time of 16 hours to run CARLOS-3D™ at one frequency would be necessary.

(d) Calculation of near fields using CARLOS-3D™ is possible, even though the user's manual [3] does not state this. However, this option is only available with the bistatic scattering selected. The bistatic scattering option does not allow an incidence angle sweep. This feature (incidence angle sweep with near fields calculations) would allow more efficient generation of data since the excitation vector in the numerical formulation is the only change that needs to be made from one incidence angle to the next. The impedance matrix (which takes most of the cpu time) does not have to be changed. Because of this deficiency in CARLOS-3D™ investigation of the effect of varying incidence angle would have been too time consuming for this study and thus was not accomplished.

(e) In an effort to extend our analysis of this model to 3 GHz, we decided to use the plane of symmetry option. This allows input of data for only half of the problem and CARLOS-3D™ reduces the matrix size to two matrices of 1/4 the size of the full matrix. These are then solved in sequence. Our model, which was segmented assuming a frequency of 3 GHz, produced matrices of 4982 and 5024 elements and a cpu time of a little more than four hours with no disk swapping. The only problem with using this feature is that the calculated fields at 1.5 GHz in the upper cavity region differed significantly from the same fields calculated with the model used without the plane of symmetry option. This problem needs to be corrected in order to extent this type of analysis to higher frequencies.

(f) New features that should be incorporated into CARLOS-3D™ include:

- (1) magnitude and phase of far and near fields,
- (2) dynamic memory allocation to relieve some of the memory problems presented above,
- (3) a figure of merit for the triangulation such as calculations of accumulated charge on patches,
- (4) multi-wire junctions should be handled automatically,
- (5) optional output of the unit vectors in the direction of each current,
- (6) storage and retrieval of filled and/or solved matrices,
- (7) and, capability to read wire geometry from a file.

GEMACS

The GEMACS program (version 5) supports the solution of electromagnetic radiation and scattering from complex perfectly conducting objects using MoM solution of the EFIE, MFIE, and CFIE formulation. It also uses GTD for large perfectly conducting and impedance surfaces and combines GTD and MoM (called MoM/GTD hybrid) for problems where small radiators near large scatterers are modeled. A FD solution is used for closed cavities which when combined with the MoM, GTD or MoM/GTD hybrid can be used for multiple region problems. This code, because of the efficient use of memory in the FD formulation and the availability of the GTD formulation for the high frequency solution of the exterior problem, is the code of choice for this type of study at frequencies where use of CARLOS-3D™ is prohibitive.

Unfortunately, versions of GEMACS for a workstation or one which could access memory above the DOS limit for the PC were not available at the SAC for this study. However, an ongoing effort to make one of these versions available before the end of this study prompted us to use GAUGE [2] to generate input files for our problem. Hopefully, we will use these input files with GEMACS for the higher frequencies in a follow on study.

The analysis of the simplified model of a sensor using GEMACS begins by dividing the problem into three regions (see Figure 1a): (1) an exterior region that includes the excitation source (a plane wave) and the outer shell of the entire sensor plus aperture 1, (2) an intermediate region containing the lower mirror assembly with apertures 1 and

2, and (3) the interior region of the upper cavity. At the higher frequencies of interest (> 3 GHz) the outer region is a GTD problem where energy is coupled into the intermediate region through aperture 1. The intermediate region is an FD problem with energy coupling into the interior region through aperture 2. Finally, the interior region is an FD problem where we want to calculate the fields. Once the fields are known in the interior region and in aperture 2, we can calculate Q in the same manner as we did using CARLOS-3D™.

Summary of Work to be Done

The following is a list of work to be done in a follow-on study:

(1) The use of GEMACS to extend the range of frequencies in this investigation should be the primary focus of a follow-on study.

(2) Variations in incidence angle and the resulting effect on Q, energy stored in and power exiting the cavity should be studied.

(3) Even though we think that the grid size inside the cavity to determine the accurate value of Q is adequate, it should be investigated because of the shapes involved. Preliminary study of the variations of the fields indicate fairly smooth changes with the grid used for this study.

(4) In the transition region of approximately 3 GHz (assuming the problems with the symmetry plane option addressed above are corrected), results from CARLOS-3D™ and GEMACS should be compared.

(5) Segmentation size for both codes should also be studied. The rule of thumb is to have cell sides smaller than 0.1λ . Since computer memory is at a premium for high frequency excitation, this rule of thumb is well worth investigation.

(6) Incorporation into CARLOS-3D™ of the new features mentioned above should be accomplished and validated.

(7) Development or search for a more friendly graphical user interface for CARLOS-3D™ should be accomplished.

(8) Finally, comparison of numerical results with experimental results is necessary.

References

- [1] Ronald R. DeLyser, "An analysis approach to determine quality factors of large, complex cavities," *Final Report, Summer Faculty Research Program*, Phillips Laboratory, Sponsored by The Air Force Office of Scientific Research Bolling Air Force Base, Washington, D.C., September, 1993.
- [2] *Graphical Aids for the Users of GEMACS (GAUGE)*, Rome Air Development Center, AFSC, Griffiss Air Force Base, NY, February 1989.
- [3] J.M. Putnam, L.N. Madgyesi-Mitschang and M.B Gedera, *CARLOS-3DTM Three Dimensional Method Of Moments Code*, McDonnell Douglas Aerospace-East, December 1992.
- [4] *General Electromagnetic Model for the Analysis of Complex Systems (GEMACS) - Version 5*, Rome Air Development Center, AFSC, Griffiss Air Force Base, NY, December 1990.
- [5] Wang, J. J. H. , *Generalized Moment Method In Electromagnetics*, Wiley Interscience, New York, 1991
- [6] Wolfram, S., *Mathematica*, Addison-Wesley, 1991.

UNIDIRECTIONAL RING LASERS AND LASER GYROS
WITH MULTIPLE QUANTUM WELL GAIN MEDIA

Jean-Claude Diels
Professor
Department of Physics and Astronomy

University of New Mexico
800 Yale Blvd. NE
Albuquerque, New Mexico 87131

Final Report for:
Summer Faculty Research Program
Phillips Laboratory

Sponsored by:
Air Force Office of Scientific Research
Bolling Air Force Base, DC

and
Phillips Laboratory

August 1994

UNIDIRECTIONAL RING LASERS AND LASER GYROS
WITH MULTIPLE QUANTUM WELL GAIN MEDIA

Jean-Claude Diels
Professor
Department of Physics and Astronomy

University of New Mexico
800 Yale Blvd. NE
Albuquerque, New Mexico 87131

ABSTRACT

Very thin (compared to the wavelength) gain and dielectric layers have similar reflection properties, except for a phase factor of $\pi/2$. This particular difference makes it possible to design non-reciprocal elements, having a zero reflectivity from one direction, and a finite reflectivity from the other direction. This non-reciprocity is exploited to design unidirectional lasers.

UNIDIRECTIONAL RING LASERS AND LASER GYROS WITH MULTIPLE QUANTUM WELL GAIN MEDIA

Jean-Claude Diels

Objective

The short term objective is to demonstrate a unidirectional ring laser with asymmetric reflection properties.

The long term objective is to demonstrate gyro response of a dual ring laser operating on a small cube of semiconductor material.

The non-reciprocal element

A single quantum well has a thickness d much smaller than the wavelength. Let us consider an inverted single quantum well. An electric field of amplitude \vec{E}_i incident from the left, will, after transmission through the layer, become a transmitted field $\vec{E}_t = (1 + \alpha)\vec{E}_i$. The reflected field will be $\vec{E}_r = \alpha\vec{E}_i$. This result is consistent with a simple argument that the emitting layer being much thinner than the wavelength has no information on the direction of the field, hence has equal probability of emission in forward and backward directions.

The single amplifying quantum well can also be represented by a layer of purely imaginary index of refraction $n_g = -i\kappa$.

Let us thus consider a thin dielectric layer, and the combined reflection from both interfaces. It can easily be shown [1] that, in the limit of zero thickness (thickness negligible compared to the wavelength), for an incident field E_i , the reflected field is $E_r = irE_i$, where r is a real quantity, proportional to the discontinuity in index Δn . This result is consistent with the previous one: for a gain medium, $\Delta n = -i\kappa$, and the reflected field should be of the form $E_r = \alpha E_i$.

The pairing of a thin gain layer with a dielectric reflecting layer leads to a structure that is non reciprocal. Let us consider, from left to right, a thin gain layer (transmission $E_t = (1 + \alpha)E_i$; reflection $E_r = \alpha E_i$) followed at a distance $\ell = 3\lambda/8$ by a dielectric layer (reflection $E_r = irE_i$; transmission $E_t = \sqrt{1 - r^2}E_i$). The round trip between the two layers corresponds to a phase factor $\exp\{-2ik\ell\} = i$. Let us neglect for simplicity multiple reflections. The combined reflection from both interfaces, for a beam incident from the left, is: $E_r = (\alpha - r)E_i$, which is zero if $\alpha = r$. For a beam incident from the right: $E_r = i(\alpha + r)E_i$, which is finite if $\alpha = r$. It is important for gyro related applications that this finite reflectivity has a phase factor of $\pi/2$ with respect to the transmission from left to right. Other cases are possible. For instance, if the spacing between the layers is $\ell = \lambda/8$, then it is the reflection from the right that can be made equal to zero. But the non-zero reflection from the left is then in phase (or π out of phase) with the

material	thickness (nm)	index (r)	index (i)	comment
air		1.	0.000	boundary
ZrO ₂	116.25	1.944	0.000	AR coating
Al _{0.3} Ga _{0.7} As	80.00	3.400	0.000	stop etch layer
AlAs	30.00	3.000	0.000	
Al _{0.3} Ga _{0.7} As	106.94	3.400	0.000	
AlAs	23.02	3.000	0.000	reflector
Al _{0.3} Ga _{0.7} As	106.94	3.400	0.000	
AlAs	23.02	3.000	0.000	(2 layers)
Al _{0.3} Ga _{0.7} As	111.95	3.400	0.000	spacer $r - \alpha$
GaAs	9.61	3.64	-0.028	Quantum well
Ga _{0.78} Al _{0.22} As	115.28	3.45	0.000	pump layer
GaAs	9.61	3.64	-0.028	Quantum well
Ga _{0.78} Al _{0.22} As	115.28	3.45	0.000	pump layer
...	16 pairs
GaAs	9.61	3.64	-0.028	Quantum well
Ga _{0.78} Al _{0.22} As	115.28	3.45	0.000	pump layer
GaAs	9.61	3.64	-0.028	Quantum well
Ga _{0.78} Al _{0.22} As	115.28	3.45	0.000	pump layer
GaAs	9.61	3.64	-0.028	Quantum well
Al _{0.3} Ga _{0.7} As	111.95	3.400	0.000	spacer
AlAs	23.02	3.000	0.000	(1 layer)
Al _{0.3} Ga _{0.7} As	106.94	3.400	0.000	
AlAs	23.02	3.000	0.000	
Al _{0.3} Ga _{0.7} As	80.00	3.400	0.000	stop etch layer
ZrO ₂	116.25	1.844	0.000	AR coating

Table 1: Detailed composition of a non-reciprocal structure, free standing, bounded by a GaAs to air AR vacuum deposited $\lambda/4$ coating.

transmission from the right, which is an undesirable situation for laser gyro applications.

If such a pair of elements is used as a gain medium for a ring laser, the finite reflection will re-inject energy from one sense of rotation into the other, which will dominate, make the ring laser nearly unidirectional. Calculations showing the contrast ratio between the two directions of circulation in the cavity will be presented following a description of some specific structures.

The properties of non-reciprocity in reflection can be generalized to more complex multiple quantum well structures. In the calculations that are presented below, a standard matrix calculation is used to calculate the transmissivity and reflectivity of a multiple quantum well structure.

Layer structure

Using standard matrix multiplication techniques, we calculate first the reflection and transmission from both directions for the multilayer structure detailed in table 1. The transmission of the structure outlined in the table above is 1.095 from both directions in the wavelength range from 855 nm to 865 nm. The reflection coefficient drops to 10^{-6} at 860 nm in one direction, while it is roughly constant at 0.8 % for the whole wavelength range in the other direction.

The thickness of the individual (optically pumped) quantum wells is chosen for the wavelength of 860 nm. The larger the gain/quantum well, the larger the non-reciprocity. We have chosen 2 values of gain, and designed accordingly 2 layer structures.

Structure with grown AR coating

It is preferable to have the AR coating included in the multilayer structure grown by MBE or MOCVD, rather than to have an additional manufacturing step. The single ZrO_2 AR coating layer of the table 1 above has been replaced by a multilayer AR coating in the layer design shown in the following two tables (tables 2 and 3).

Phase on reflection The performances of a laser gyro at low speed are affected by backscattering. At each round trip, some small fraction of the radiation of — for instance — the clockwise propagating beam $\tilde{\epsilon}\tilde{\mathcal{E}}_1 \exp\{i[\omega t - kz]\}$ is reflected into the cavity of the counterclockwise propagating beam. If the phase ϕ_t of the backscattering coefficient $\tilde{\epsilon}$ is such that the reflection has a component in phase with the counterclockwise field $\tilde{\mathcal{E}}_2 \exp\{i[\omega t + kz]\}$, the latter will be “injection locked” by the backscattering. There is no injection locking if the backscattering is 90° out of phase with the field $\tilde{\mathcal{E}}_2$.

For use in a ring laser, it is essential that the phase of the reflected wave be at 90° from that of the transmitted wave. This phase relationship will prevent locking of the laser gyro.

Let us consider a structure such as detailed in tables 2 or 3 inserted in a ring cavity, with the clockwise beam incident first upon the face of zero reflection. Let φ_t be the phase shift upon transmission, and φ_r the phase shift upon reflection of the second surface. The resonance condition for the ring cavity is that the phase shift for the light path outside the MQW structure be $-\varphi_t$. The condition that counterclockwise wave reflected at the right interface be 90° out of phase with the transmitted phase is:

$$\begin{aligned} (-\varphi_t) + \varphi_r &= \varphi_t + \frac{\pi}{2} \\ \varphi_r - 2\varphi_t &= \frac{\pi}{2}. \end{aligned} \tag{1}$$

For the high gain structure of table 2, $\varphi_t = -1.13915$; $\varphi_r = -0.70910$; and the difference $\varphi_r - 2\varphi_t = 1.5692$, or an excess of -0.0016 . For the low gain structure of table 3, $\varphi_t = -1.11669$; $\varphi_r = -0.65876$; and the difference $\varphi_r - 2\varphi_t = 1.5746$, or an excess of 0.0038 .

The overall intensity transmission versus wavelength is plotted in Fig. 1. The peak at 857.64 nm does not match exactly the minimum reflectivity wavelength of 858 nm seen in the plot of Fig. 2. From the other direction, the minimum reflection is 0.024, at an even longer wavelength (854.3 nm) as shown in the plot of Fig. 3.

These plots do not reflect the bandwidth of the laser in operation. As the gain saturates, the values of the transmission (gain), and reflection change. As a result, the relative intensities between both directions also change. A complete simulation of the ring laser has to be made to evaluate the gain bandwidth in a ring configuration.

material	thickness (nm)	index (r)	index (i)	comment
air		1.	0.000	boundary
$Al_{0.25}Ga_{0.75}As$	126.30	3.3967	0.000	stop etch layer
$AlAs$	71.90	2.9835	0.000	
$Al_{0.25}Ga_{0.75}As$	63.15	3.3967	0.000	
$AlAs$	71.90	2.9835	0.000	AR
$Al_{0.25}Ga_{0.75}As$	63.15	3.3967	0.000	
$AlAs$	71.90	2.9835	0.000	AR
$Al_{0.25}Ga_{0.75}As$	63.15	3.3967	0.000	
$AlAs$	71.90	2.9835	0.000	AR
$Al_{0.25}Ga_{0.75}As$	35.50	3.3967	0.000	reflector
$AlAs$	33.80	2.9835	0.000	reflector
$Al_{0.25}Ga_{0.75}As$	73.73	3.3967	0.000	spacer $r - \alpha$
$AlAs$	59.85	2.9835	0.000	(2 layers)
$Al_{0.25}Ga_{0.75}As$	73.73	3.3967	0.000	spacer $r - \alpha$
$AlAs$	59.85	2.9835	0.000	(2 layers)
$Al_{0.25}Ga_{0.75}As$	116.00	3.3967	0.000	spacer $r - \alpha$
$GaAs$	10.00	3.6470	-0.028	Quantum well
$Ga_{0.80}Al_{0.20}As$	115.00	3.4130	0.000	pump layer
$GaAs$	10.00	3.6470	-0.028	Quantum well
$Ga_{0.80}Al_{0.20}As$	115.00	3.4130	0.000	pump layer
...	19 pairs total between —
$GaAs$	10.00	3.6470	-0.028	Quantum well
$Ga_{0.80}Al_{0.20}As$	115.00	3.4130	0.000	pump layer
$GaAs$	10.00	3.6470	-0.028	Quantum well
$Ga_{0.80}Al_{0.20}As$	115.00	3.4130	0.000	pump layer
$GaAs$	10.00	3.6470	-0.028	last Quantum well
$Al_{0.25}Ga_{0.75}As$	116.00	3.3967	0.000	spacer
$AlAs$	59.85	2.9835	0.000	(1 layer)
$Al_{0.25}Ga_{0.75}As$	73.73	3.3967	0.000	spacer
$AlAs$	59.85	2.9835	0.000	reflector
$Al_{0.25}Ga_{0.75}As$	121.80	3.3967	0.000	reflector
$AlAs$	71.90	2.9835	0.000	AR
$Al_{0.25}Ga_{0.75}As$	63.15	3.3967	0.000	AR
$AlAs$	71.90	2.9835	0.000	AR
$Al_{0.25}Ga_{0.75}As$	63.15	3.3967	0.000	AR
$AlAs$	71.90	2.9835	0.000	AR
$Al_{0.25}Ga_{0.75}As$	63.15	3.3967	0.000	AR
$AlAs$	71.90	2.9835	0.000	AR
$Al_{0.25}Ga_{0.75}As$	126.30	3.3967	0.000	2nd stop etch
$AlAs$	10.00	2.9835	0.000	1st Stop etch
$GaAs$		3.6470	0.000	substrate

Table 2: Detailed composition of a non-reciprocal structure, free standing in air. An antireflection stack of layers is incorporated in the structure. This structure is optimized for a high gain $\alpha = 4000 \text{ cm}^{-1}$ (imaginary part of index = 0.028).

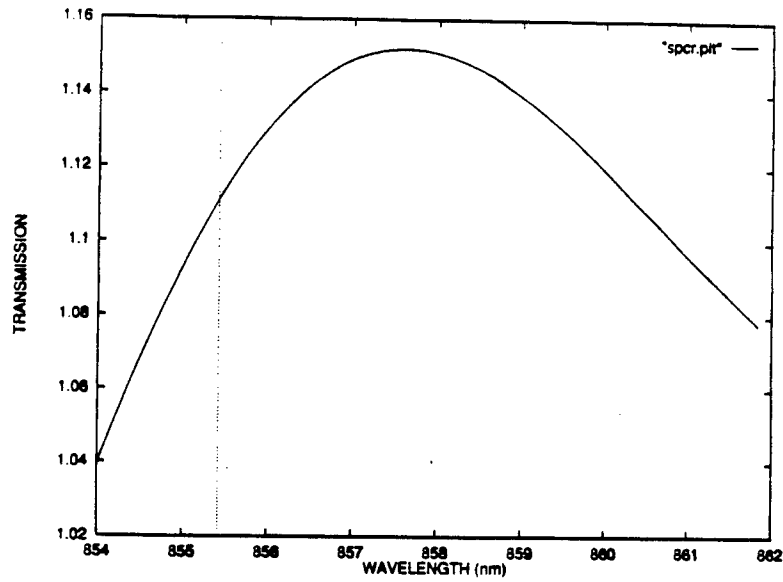


Figure 1: Transmission versus wavelength for the structure presented in table 2.

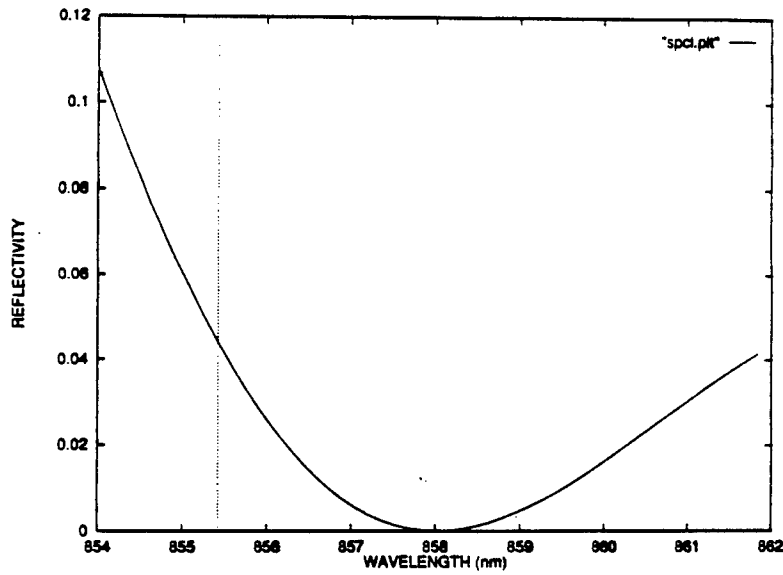


Figure 2: Reflection (left to right) versus wavelength for the structure presented in table 2.

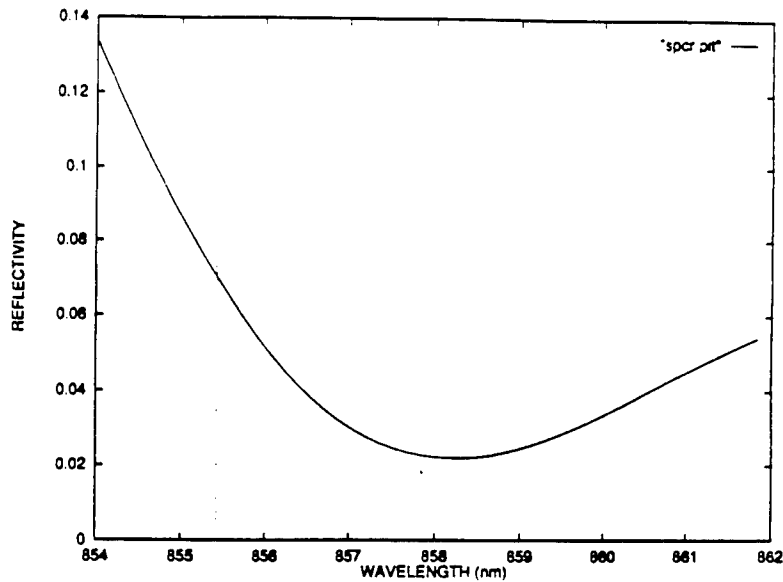


Figure 3: Reflection (right to left) versus wavelength for the structure presented in table 2.

Smaller gain The smaller the gain, the smaller the non-reciprocity. This tendency is obvious from the formulae for the two layer approximation: the smaller the gain, the smaller the reflectivity from right to left $i(\alpha + \tau)$. The next table is for a MQW structure optimized for a smaller gain factor.

Figure 4 shows the reduced minimum reflectivity from right to left for the lower gain structure.

The unidirectional laser structure

The first elements will be made with the GaAlAs structures grown on a GaAs wafer. The substrate, which absorbs the laser radiation, will have to be etched away.

The laser itself will be the simple ring configuration sketched in Fig. 5, pumped by a Ti:sapphire laser.

The next step will be to grow similar structures with InGaAs. Since the substrate is transparent to the laser radiation, it will not have to be etched away.

The laser cube

The laser cube consists of two GaAs 90° turning prisms (Fig. 6a). A nonreciprocal gain layer structure is grown on the hypotenuse face of one prism (InGaAs). The two prisms are thereafter optically contacted to form a cube (Fig. 6b). Depending of the location of the pump spot (pump radiation around 900 nm), the lasing will be clock-wise or counterclock-wise in the cross-section of the cube. With two pump spots at different height in the prisms, lasing can occur in opposite direction in adjacent planes. Since there is no coupling between the cavities, the beat frequency between the two lasing planes should exhibit a perfect gyroscopic response.

material	thickness (nm)	index (r)	index (i)	comment
air		1.	0.000	boundary
$Al_{0.25}Ga_{0.75}As$	126.30	3.3967	0.000	stop etch layer
$AlAs$	71.90	2.9835	0.000	
$Al_{0.25}Ga_{0.75}As$	63.15	3.3967	0.000	
$AlAs$	71.90	2.9835	0.000	AR
$Al_{0.25}Ga_{0.75}As$	63.15	3.3967	0.000	
$AlAs$	71.90	2.9835	0.000	AR
$Al_{0.25}Ga_{0.75}As$	63.15	3.3967	0.000	
$Al_{0.25}Ga_{0.75}As$	48.90	3.3967	0.000	reflector
$AlAs$	29.50	2.9835	0.000	reflector
$Al_{0.25}Ga_{0.75}As$	54.00	3.3967	0.000	spacer $r - \alpha$
$AlAs$	82.35	2.9835	0.000	(2 layers)
$Al_{0.25}Ga_{0.75}As$	54.00	3.3967	0.000	spacer $r - \alpha$
$AlAs$	82.35	2.9835	0.000	(2 layers)
$Al_{0.25}Ga_{0.75}As$	106.70	3.3967	0.000	spacer $r - \alpha$
$GaAs$	10.00	3.6470	-0.014	Quantum well
$Ga_{0.80}Al_{0.20}As$	115.00	3.4130	0.000	pump layer
$GaAs$	10.00	3.6470	-0.014	Quantum well
$Ga_{0.80}Al_{0.20}As$	115.00	3.4130	0.000	pump layer
...	19 pairs total between —
$GaAs$	10.00	3.6470	-0.014	Quantum well
$Ga_{0.80}Al_{0.20}As$	115.00	3.4130	0.000	pump layer
$GaAs$	10.00	3.6470	-0.014	Quantum well
$Ga_{0.80}Al_{0.20}As$	115.00	3.4130	0.000	pump layer
$GaAs$	10.00	3.6470	-0.014	last Quantum well
$Al_{0.25}Ga_{0.75}As$	106.70	3.3967	0.000	spacer
$AlAs$	82.35	2.9835	0.000	(1 layer)
$Al_{0.25}Ga_{0.75}As$	54.00	3.3967	0.000	spacer
$AlAs$	82.35	2.9835	0.000	(1 layer)
$Al_{0.25}Ga_{0.75}As$	110.60	3.3967	0.000	reflector
$AlAs$	71.90	2.9835	0.000	reflector
$Al_{0.25}Ga_{0.75}As$	63.15	3.3967	0.000	AR
$AlAs$	71.90	2.9835	0.000	AR
$Al_{0.25}Ga_{0.75}As$	63.15	3.3967	0.000	AR
$AlAs$	71.90	2.9835	0.000	AR
$Al_{0.25}Ga_{0.75}As$	63.15	3.3967	0.000	AR
$AlAs$	71.90	2.9835	0.000	AR
$Al_{0.25}Ga_{0.75}As$	126.30	3.3967	0.000	etch layer
$AlAs$	10.00	2.9835	0.000	1st etch
$GaAs$		3.6470	0.000	substrate

Table 3: Detailed composition of a non-reciprocal structure, free standing in air. An antireflection stack of layers is incorporated in the structure. This structure is optimized for a low gain $\alpha = 2000 \text{ cm}^{-1}$ (imaginary part of index = 0.014).

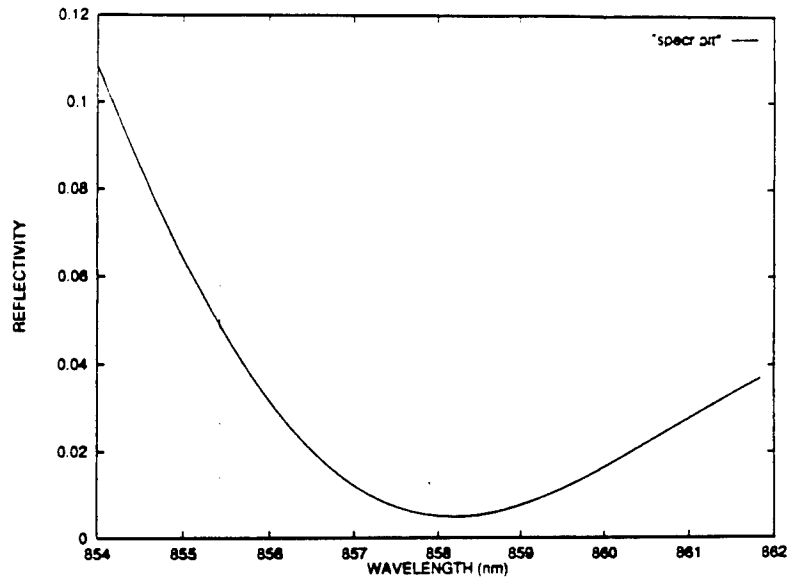


Figure 4: Reflection (right to left) versus wavelength for the structure presented in table II.

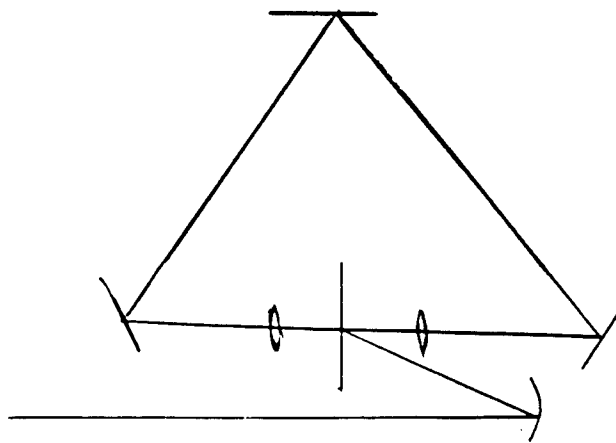


Figure 5: ring laser configuration

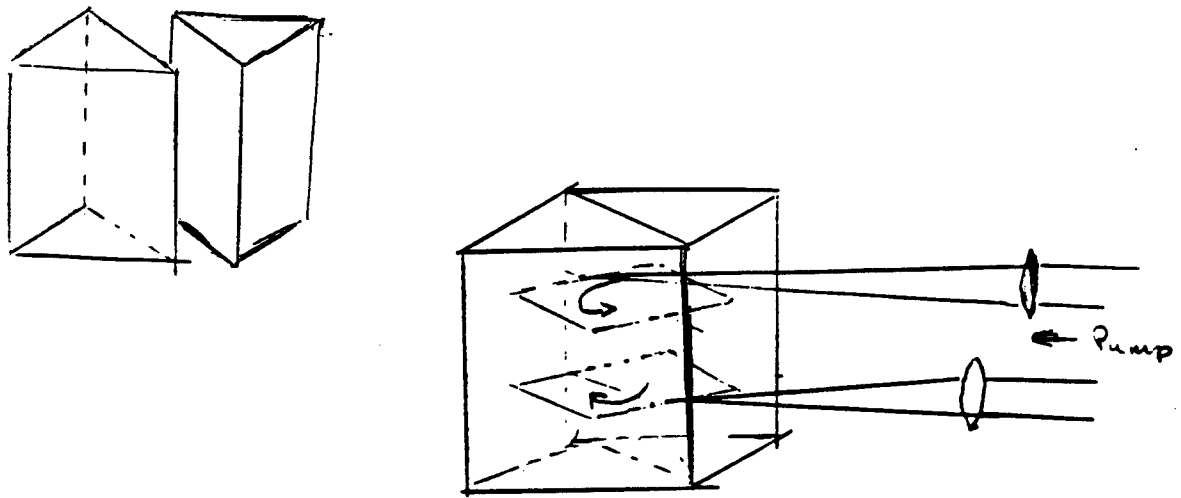


Figure 6: The cubic laser gyro. (a) the two 90° turning prisms that constitute the two halves of the cube. The nonreciprocal layer structure is grown on the hypotenuse plane of one of the cubes. The two prisms are optically contacted. The laser (b) is pumped at two different heights, resulting in unidirectional operation in opposite direction in two parallel planes.

Gyro Properties

Is the ring laser truly unidirectional? The asymmetry is not in transmission, but in a (passive) reflection. In one direction (let us call it (+)), the intensity increases because intensity from the other direction (-) is fed into that direction. There may be a large difference between the intensities I_+ and I_- , but the weak beam (I_-) will never vanish completely. Some of that weak beam is coupled back into the strong beam by the reflection at the dielectric-gain interfaces. Could such a coupling injection lock the stronger beam, eliminating all possibility of gyro response? there is one more fortunate property of this gain-dielectric interface that prevents locking: the coupling of the weak field into the strong one is of the form: $i(r + \alpha)E_-$ and is thus 90° out of phase with the strong field. Injection lock-in does not occur for this particular angle of coupling.

Figure 7 show the evolution with time of the two intensities I_- (a) and I_+ (b) in the cavity. The time is in units of cavity

roundtrip-time. the parameters are:

α	0.080	unsaturated gain factor
α_{loss}	0.040	loss/pass
r	0.038	dielectric reflectivity
I_{sat}	0.100	saturation intensity

With this choice of parameters, in steady-state, the saturated gain is equal to 0.038 (r).

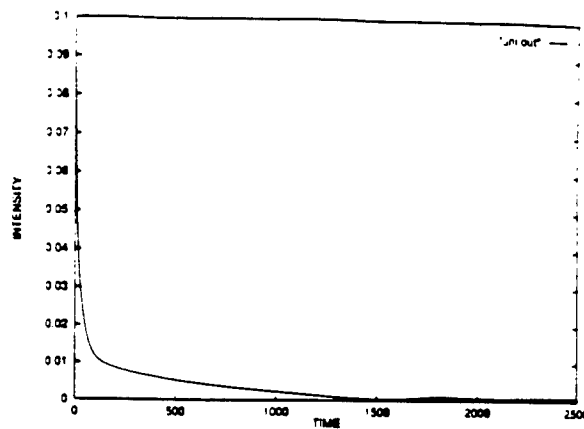
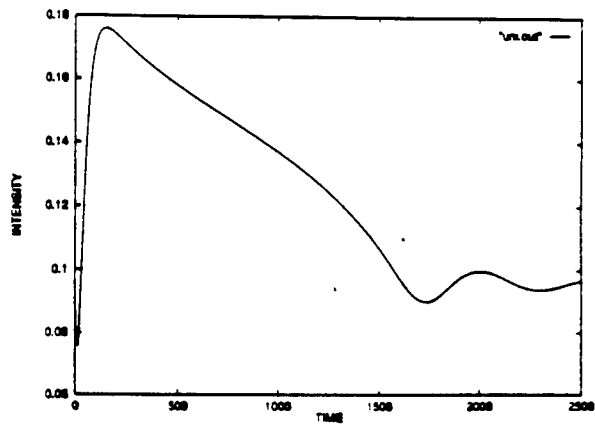


Figure 7: Intensity versus round-trip index for the weak beam I_- (a) and the strong beam I_+ (b).

References

- [1] M. Lai and J.-C. Diels. Backward-stimulated emission and non-reciprocity in optics. *Phys. Rev. A*, A43:2464–2466, 1991.

**AN INVESTIGATION OF HYDROXYLAMMONIUM DINITRAMIDE:
SYNTHESIS, STABILITY, AND COMPATIBILITY**

**Vincent P. Giannamore
Assistant Professor
Department of Chemistry**

**Xavier University of Louisiana
7325 Palmetto Street
New Orleans, LA 70125**

**Final Report for:
Summer Faculty Research Program
Phillips Laboratory**

**Sponsored by:
Air Force Office of Scientific Research
Bolling Air Force Base, DC**

and

Phillips Laboratory

September, 1994

**AN INVESTIGATION OF HYDROXYLAMMONIUM DINITRAMIDE:
SYNTHESIS, STABILITY, AND COMPATIBILITY**

**Vincent P. Giannamore
Assistant Professor
Department of Chemistry
Xavier University of Louisiana**

Abstract

Hydroxylammonium dinitramide (HADN) was prepared from ammonium dinitramide (ADN) by means of an ion exchange reaction to produce dinitramidic acid followed by an acid-base reaction with hydroxylamine yielding HADN. The procedure is, effectively, a one step process. It has several advantages over previously used methods. The stability of the compound and its compatibility with various substances were also examined.

**AN INVESTIGATION OF HYDROXYLAMMONIUM DINITRAMIDE:
SYNTHESIS, STABILITY, AND COMPATIBILITY**

Vincent P. Giannamore

Introduction

Increasing environmental awareness, as well as related public relations and political concerns, have lead the propellants community to consider the environmental impact of its activities. Hazardous waste from manufacturing processes, toxic exhaust, and disposal are all areas of potential concern. A propellant's entire life cycle, from initial research and deveopment through eventual demilitarization, must be considered. Hawkins and Wilkerson [1] have discussed the issues related to environmental propellant.

A principal area of interest is the presence of hydrogen chloride among the exhaust gases. While the total amount of hydrogen chloride vented to the atmosphere in this manner is not large compared to other sources, it is prudent to avoid any such emission where other options are available. This is consistent with EPA priorities which rank reduction of hazardous waste generation ahead of treatment and disposal of waste. Thus, one focus of research in the propulsion industry is the discovery and development of new oxidizers to replace chlorine-containing compounds such as ammonium perchlorate (AP). Another benefit of replacing chlorine-containing oxidizers with chlorine-free oxidizers would be to minimize the signature caused by the propellant exhaust. This makes missile launch harder to detect. However, it is critical that replacement of a hydrogen chloride generating oxidizer with more environmentally benign and lower signature species not involve an unacceptable sacrifice of performance.

One of the most promising chlorine-free oxidizers in development is ammonium dinitramide (ADN). ADN has the advantage of having reduced signature and less environmental impact than AP while having a higher predicted lift capacity. It is also relatively stable. Another dinitramide salt,

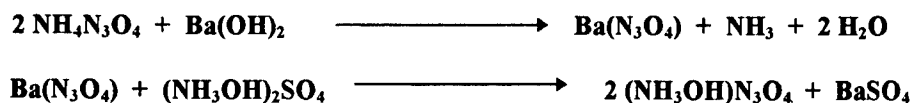
potassium dinitramide (KDN), is being investigated as a phase-stabilizer and performance enhancer for ammonium nitrate (AN) [2]. Several other dinitramide salts have been investigated as well. Another chlorine-free oxidizer under study is hydroxylammonium nitrate (HAN). HAN has been known for many years. However, the development of a stabilized form, S-HAN5, for use as an oxidizer in clean propellant formulations is a recent development.

This paper reports on an investigation of a chlorine-free oxidizer related to ADN and to HAN. Propellants formulated with hydroxylammonium dinitramide (HADN) have been predicted by theoretical calculations to have higher specific impulse values than identical propellants formulated with S-HAN5 [3]. The subject of the current report is primarily the synthesis of HADN. There will also be some discussion of its stability and its compatibility with other materials.

Discussion of Problem

The goals of this study may be conveniently divided into two categories: those associated with the synthesis and those associated with stability and compatibility. The first synthetic goal was to develop an efficient, high yield method for preparing HADN. We also sought to reduce the level of water contaminating the product while using conditions for water removal which did not promote decomposition. Finally, it was considered desirable to avoid the production of barium salts.

Prior to the present work, synthesis of HADN involved two reactions carried out in separate steps. In the first reaction, ADN is treated with barium hydroxide to form barium dinitramide. The barium dinitramide is then reacted with hydroxylammonium sulfate to produce HADN. The equations are shown below:



Notice that water is a byproduct of the first reaction. It is also the major component of the solvent for the second reaction. The intermediate barium dinitramide must be isolated for use in the second reaction. Thus, the synthesis requires two reactions to be worked up. The work-up of the second reaction involves a centrifugation step, followed by a difficult filtration to remove the unwanted barium sulfate. Finally, water was removed by rotary evaporation at 60°C.

There were three goals associated with the stability and compatibility portion of this study. One of these goals was to develop a screening method for predicting stabilizing and destabilizing effects of additives. It was anticipated that changes in the onset temperature of the DSC exotherm of the oxidizer-additive mixture compared to that of the pure oxidizer would be the basis of such a screening method. Another goal was to study the stability of HADN under various conditions and with various additives by empirical observations of small quantities. The third goal was to determine whether addition of certain chemicals, such as buffers, would enhance the stability of HADN. Compounds related to HADN, such as ADN, have been reported to be incompatible with heat and/or light. There is a long list of substances with which S-HAN5 is incompatible. Conversely, it is stabilized and its performance is enhanced by the addition of certain other substances. Since some of these factors might also apply to HADN, the discovery of stabilizing or destabilizing effects is important.

Experimental

Caution: Explosive reactions have been reported to occur when nitric acid and other strong oxidizing agents are mixed with ion exchange resins [4]. Equipment must be designed to prevent rapid build-up of pressure when oxidizers are used with ion exchange resins. Consult knowledgeable sources for information about handling these materials.

Synthesis of Hydroxylammonium Dinitramide

1. Safety trial (Synthesis 1). Dowex 50Wx8 resin (strong acid, proton form, 0.4134 g) was mixed with 10 mL of water. The mixture was stirred and 0.1255 g of ADN dissolved in 10 mL of water was added. About 10 mL of water was used as a wash. The mixture was stirred for 30 minutes. No evidence of any reaction was observed. One milliliter of a 50% aqueous solution of hydroxylamine was added and stirring was continued for another 1.5 h. No evidence of reaction was observed.

2. Synthesis 2. A column was packed with Dowex 50Wx8 resin to the 100 mL mark. The resin was washed with water and then the column was charged with 3.7267 g of ADN (30.040 mmol) in 30 mL of water. The solution was allowed to elute, using water as the eluent, into a stirred solution of 0.9938 g of hydroxylamine (30.086 mmol) in 30 mL of water. Total volume of water in the beaker after elution was ~375 mL. The pH of the resulting solution was 4.14. The mixture was placed on a rotary evaporator at 60 °C for 3 days. The solution was then stirred overnight in a hood under a stream of nitrogen. Portions were then removed periodically and placed on the rotary evaporator. This required 7 more days to complete the process. The product weighed 3.8457 g (91%). Karl Fischer titration showed that it contained 1.6154 % water. All operations after column packing and washing were carried out in the dark or in vessels protected from exposure to light.

3. Synthesis 3. The main purpose of this run was to test the feasibility of using methanol as a solvent. A column was packed with Dowex 50Wx8 resin to the 20 mL mark. The resin was first washed with water and then with methanol. Washing with methanol caused the volume of resin in the column to shrink slightly. The remaining operations were carried out in the dark. The column was then charged with 3.7215 g of ADN (29.998 mmol) in 30 mL of methanol. The column was eluted with an additional 60 mL of methanol with the eluent passing into a stirred solution of 0.9858 g of hydroxylamine (29.846 mmol) in 30 mL of methanol. The methanolic solution of hydroxylamine had been prepared by adding a 50% aqueous solution of hydroxylamine to the methanol. The

reaction mixture was allowed to stir overnight and then stirred for a full day under a flow of nitrogen. At this point Karl Fischer titration revealed it to contain 4.6371% water. The sample was then placed on a rotary evaporator for 6.5 hours. For the first half hour, the temperature of the water bath was maintained at 30 °C. It was then raised to 50 °C for the remaining time. Karl Fischer titration showed it to contain 1.2290% water. Mass of this product was not obtained.

4. Synthesis 4. The column was packed and washed with water and methanol as described for synthesis 3. It was then allowed to stand overnight with the resin covered in methanol. The bed volume was 18 mL. All subsequent operations were conducted in the dark. The column was charged with 3.7180 g of ADN (29.969 mmol) in 30 mL of methanol and was eluted, using an additional 100 mL of methanol into a stirred solution of 0.9929 g of hydroxylamine (30.061 mmol) in 30 mL of methanol. The methanolic solution of hydroxylamine had been prepared by adding a 50% aqueous solution of hydroxylamine to the methanol. This reaction mixture was left stirring under a nitrogen flow overnight and for an additional day. It was then stripped of solvent on a rotary evaporator using a warm water bath for four hours. The yield obtained was 3.0187 g (72%). Karl Fischer titration showed the product to contain 0.9164 % water.

5. Synthesis 5. The column was packed and washed with water and methanol as described for synthesis 3 except that the resin was measured by mass. The mass used was 26.67 g. This was based on the listed "total exchange capacity" of the resin and its moisture content [4]. It is more than twice the amount calculated for a 1:1 ratio of H^+ to NH_4^+ . This approach was used in all of the remaining synthesis although the scale of the reaction was increased. The column was charged with 3.7214 g of ADN (29.997 mmol) in 300 mL of methanol. The large increase in solvent volume compared to previous synthesis was because of a literature recommendation that the concentration of the solution charged to the column be 0.1 N or less [4]. This was abandoned after the next run because such a large volume of solvent was required and the reaction appeared to be no better than it was using higher concentrations and less solvent. The 0.99185 g of hydroxylamine (30.0288 mmol)

was dissolved in 30 mL of methanol as previously. Because of the volume involved, an overnight interruption in the elution of the column was required. An additional 100 mL of methanol was used to wash the column. Solvent was stripped on the rotary evaporator. Because of the volume of solvent involved and the desire to keep the water bath temperature at ~ 30 °C, solvent stripping required several days. It was done in several portions. Originally, as solvent was stripped, more of the solution was added to the original material. However, this was discontinued when it was realized that this would expose that material to heat for a prolonged period. Nevertheless, this product was darker than others and appeared to decompose more rapidly than others. The prolonged period of exposure to heat may have been the cause of its color and relatively short lifetime. The yield was 2.8101 g (67%).

6. Synthesis 6. The column was packed with 26.61 g of the resin in the usual way. It was charged with 3.7214 g of ADN (29.997 mmol) in 300 mL of methanol. The mass of hydroxylamine was 0.9911 g (30.006 mmol). It was dissolved in 100 mL of methanol. Solvent was stripped on a rotary evaporator. At first, the large volume of solvent was reduced in two portions. Then, these portions were combined and the remaining solvent stripped. This was done to avoid the problem of prolonged heating and multiple transferring which occurred in synthesis 5. However, the process had to be interrupted for several days to allow others access to the rotary evaporator. It was stripped for one day at 30 °C before the interruption. After the interruption, it was stripped for an additional hour at the same temperature. Karl Fischer titration showed it to contain 5.1736% water at that point. It was stripped further at 60 °C for 2.5 hours. This resulted in 3.2956 g of product (78%) containing 3.8495% water.

7. Synthesis 7. The column was packed with 63.5312 g of resin in the usual way. It was charged with 8.8569 g of ADN (71.392 mmol) in 100 mL of methanol and eluted into a stirred solution of 2.3587 g of hydroxylamine (71.411 mmol) in 100 mL of methanol. An additional 100 mL of methanol was used to elute the solution at a slow rate and 50 mL more was used to wash the

column at a faster rate. The resulting solution was allowed to stand overnight in an open beaker under a flow of nitrogen gas. On the following day, it was stripped of solvent on the rotary evaporator. This required six hours. The water bath was initially at 45 °C from previous use. It was used at that temperature, but allowed to cool during the run. After three hours it was at room temperature. The temperature was then set to 30 °C for the remainder of the time. The product obtained weighed 9.7180 g (97%) and contained 4.0410% water.

8. Synthesis 8. The column was packed with 63.3980 g of resin in the usual way. It was charged with 8.8788 g of ADN (71.569 mmol) in 100 mL of methanol and eluted into a stirred solution of 2.3577 g of hydroxylamine (71.379 mmol) in 100 mL of ethanol. It was carried out exactly as described for the previous run except that the column was washed with two 80 mL portions of methanol instead of one 100 mL and one 50 mL portion. After the elution and washings were completed, the solution was stirred, under nitrogen, for 1.75 hours. The bulk of the solvent was then stripped on a rotary evaporator at room temperature. The remainder was transferred to a smaller flask and stripped at 30 °C. This process had to be interrupted several times and took longer than expected. A yield of 9.2065 g (92%) was obtained. The sample contained 4.2866% water.

9. Synthesis 9. This was done as in the previous two runs using 64 g of resin, 8.8572 g of ADN (71.394 mmol) and 2.3610 g of hydroxylamine (71.481 mmol). The column was washed with 100 mL of methanol in one portion. This was done at a slow rate for the entire portion. Solvent was stripped on the rotary evaporator leaving 9.2585 g of product (93%) containing 4.8050% water.

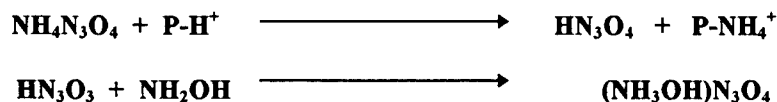
10. Synthesis 10. This was done as in the previous three runs using 63.3 g of resin, 8.8584 g of ADN (71.404 mmol) and 2.3714 g of hydroxylamine (71.794 mmol). After rotary evaporation, the product weighed 9.2622 g (93%) and contained 0.9151% water. The major difference between this and the other runs was that after the bulk of the solvent had been stripped on the rotary evaporator

and the remainder transferred to a smaller flask, the remaining solvent was stripped in a continuous process without interruption for 5.25 hours..

11. Synthesis 11. This was done as in the previous runs using 8.8594 g of ADN (71.412 mmol) and 2.3687 g of hydroxylamine (71.714 mmol). After completion of the reaction, the mixture was allowed to stir overnight under nitrogen. By morning, most of the solvent had evaporated. The remainder was transferred to a smaller flask and stripped of solvent on a rotary evaporator for 7.25 hours. The yield of product was 9.6089 g (96%). It contained 1.1063% water.

Results

A new synthetic method for production of HADN was developed. This method also requires two reactions to transform ADN into HADN. However, the two reactions take place in the context of a single physical procedure. The equations are given below, where P-H⁺ and P-NH₄⁺ refer to the strongly acidic cation exchange resin Dowex 50Wx8 in the original proton form and after exchange of protons with ammonium ions, respectively.



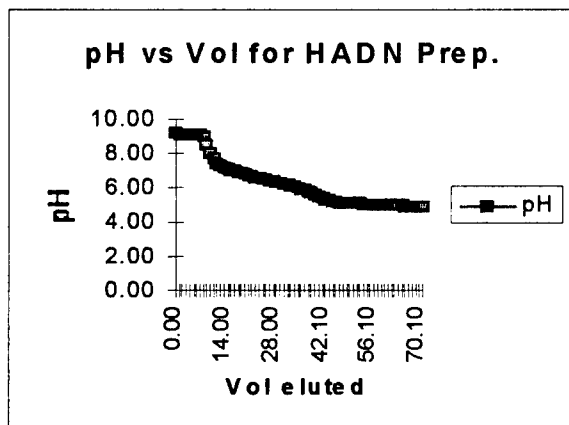
Details of this procedure, including several modifications made in the course of the research, are given in the experimental section. The current procedure can be summarized as follows. First, a column is packed with a slurry of the resin in water and the column is then rinsed with a sufficient volume of methanol to replace the water. Second, a methanol solution of ADN is passed through the column and eluted into a stirred solution of hydroxylamine in methanol. The mixture is then placed on a rotary evaporator. When left on the rotary evaporator for several hours at 30 °C, all of the methanol and most of the water can be removed. The water content of the product can be reduced to approximately 1%. Except for packing and washing the column with methanol, all of the above procedures are carried out in low light.

While on the column, the first reaction takes place and ADN is converted to dinitramidic acid. In the receiving flask, the second reaction, an acid-base reaction between the dinitramidic acid and hydroxylamine, occurs producing the HADN. In the five experimental runs done on the larger scale the average yield was 94.11% with water content averaging 3.03%. The last two runs averaged 1.02% water while yielding 94.34%. These were achieved without any systematic effort to determine the optimum flow rate through the column or the optimum stirring time. So, it is likely that higher yields can be achieved. It appears that a relatively fast flow rate is beneficial and little or no extra stirring time is needed after elution is completed.

This procedure involves no water as solvent. The main source of the water found in the product is from the 50% aqueous solution that is used as the source of the hydroxylamine. There may also be some traces left on the column from the packing step, the solvent, or the ADN. In any event, this procedure, by eliminating the water byproduct and allowing the easily removable solvent methanol to be used in place of water, allows the water to be removed at lower temperatures over a shorter time period than the previous method. This, in turn, appears to prolong the lifetime of the HADN.

This method also has the advantage of needing a work-up procedure only after the second reaction. That work-up is very simple involving only the rotary evaporation of methanol and water. As can be seen from the above, no barium salts are involved. The only waste, other than the methanol, is the spent resin. However, this spent resin can easily be regenerated by treatment with either hydrochloric or sulfuric acid using established procedures [4]. The only byproduct, therefore, is the ammonium salt corresponding to the acid.

Attempts were made to characterize the reaction by following its course using a pH meter and plotting the results similarly to a titration curve. The curve is reproduced below:



Our interpretation of this curve is as follows. The initial, relatively flat portion, represents elution of methanol from the column. The pH is basic due to the hydroxylamine in the receiving beaker where the electrode is placed. The pH then begins to drop sharply as the methanol is displaced and dinitramidic acid begins to elute into the hydroxylamine solution. The slope decreases as an equivalence point is apparently reached. At this point in an ordinary titration the pH would continue to drop as dinitramidic acid continued to elute into the beaker. However, in this case, a 1:1 ratio of hydroxylamine to ADN (and, hence, to dinitramidic acid) was used. Therefore, the curve levels off again as no further dinitramidic acid elutes. All of this appears to be consistent with the ideas about the reaction presented above.

The identification of the product as HADN is based principally on ion chromatography. Both cation and anion analysis were done on several samples. The cation analysis showed a large peak at a retention time known to be that of hydroxylammonium under the conditions. A trace of ammonium was also detected. The concentration of the ammonium in the samples was in the range of 500 ppm. No other cations were detected. The anion analysis showed only dinitramide peaks. Neither nitrate nor nitrite anions, which are common decomposition products of the dinitramide ion, were detected. The samples absorbed at both 214 and 285 nm in the UV. This is typical of dinitramides [3].

Certain quantitative data obtained by ion chromatography, namely the percentages of hydroxylammonium and dinitramide ions in HADN, do not agree completely with the theoretical

values. Presently, there is no explanation for this discrepancy. As stated above, the only other ion present apparently was ammonium. It was not present in sufficient concentration to cause the discrepancy, however. Solvation by water, methanol, or hydroxylamine was considered. However, none of these explain the data correctly. Furthermore, Karl Fischer titration seems to rule out the presence of so much water. The NMR does not show the presence of methanol or hydroxylamine. Work is continuing in this area. It is now suspected that most of the discrepancy may be due to problems with the quantitative analysis rather than with the product.

Proton nuclear magnetic resonance spectra were obtained on a sample of the product and on a sample of ADN. The first spectrum of ADN showed a singlet at 6.3 ppm. The only other peak was the peak due to residual protons in the solvent (CD_3CN). This is consistent with the fact that all protons in ammonium should be equivalent (one singlet). The signal is probably located downfield because the cation's protons are deshielded. A spectrum obtained on the same sample a few days later showed evidence of exchange between the protons of the ammonium cation and the deuterium of the solvent. Both peaks appeared broader, the ammonium signal appeared at a slightly lower position (6.1 ppm) and the relative ratio of ammonium to "residual" protons had decreased considerably. Hydroxylammonium can be expected to show similar behavior upon standing in CD_3CN . The product's proton NMR showed a sharp solvent peak and a slightly broad singlet at 8.9 ppm. There is also a slight "wobble" in the baseline at 6.3 ppm. This is undoubtedly due to the ammonium ion detected to be present in trace amounts by ion chromatography. Addition of ADN to this sample enlarged the size of this peak. The broadness of the peak at 8.9 ppm probably indicates that exchange is taking place. This exchange is probably between the proton on oxygen and those on nitrogen in the hydroxylammonium ion. This exchange probably prevents seeing separate signals for the two types of proton under the conditions of the experiment. The peak became broader when the ADN was added to the sample. This probably indicates additional exchange between protons on the two cations. The position of the signal further downfield than the

ammonium of ADN is consistent with the electron withdrawing effect of the oxygen causing deshielding of the protons. On the whole, the NMR data appears consistent with the presence of hydroxylammonium cation in the sample. Taken together with the IC data, it helps confirm the identification of the cation portion of the product. Furthermore, there is no evidence of any other proton containing species between -4 and 15 ppm, except for the trace of ammonium discussed above.

An FT-IR was also obtained. It appears consistent with a hydroxylammonium compound. The samples prepared by the current method appear similar to those prepared by the previous method, but no data from the other method is available for comparison except DSC which appears similar. Density and index of refraction were obtained on a single sample. They are 1.7324 g/mL and 1.5825, respectively.

Screening for stability and compatibility by the use of differential scanning calorimetry (DSC) was the subject of the research of high school apprentice Chris Amos. Details of this work may be found in his report [5]. The DSC results were mixed. The onset temperature of the DSC exotherm for HADN in the absence of any additives varied slightly between runs. The value appeared to cluster about two temperatures. No explanation for this was discovered. Therefore, slight changes in the onset temperature caused by additives would not be detected. Nevertheless, significant changes should have been apparent. None were detected. Thus, if the method is valid, none of the additives tested appeared to destabilize HADN, but none stabilized it either.

Systematic empirical studies are still in progress. It appears that elevated temperatures hasten the eventual decomposition of HADN. Those samples worked up at ~ 60 °C on the rotary evaporator did not last as long as those worked up at ~ 30 °C. Samples stored in a freezer at -34.4 °C have not yet decomposed. However, storage of samples in the freezer was not done early in the project, so all of the data is relatively recent. More time is needed before any definite statement can be made about temperature effects on stability of HADN. Since ADN is reported to be sensitive to

light, especially sunlight and fluorescent light, we have treated HADN as if it were also. This needs to be shown systematically also, and the study has been started. Because the emphasis was placed on the DSC studies earlier, these empirical studies were not started until relatively late. Regular laboratory personnel will complete them.

Conclusion

An efficient, high yield synthesis of HADN has been developed. Although some questions may yet have to be answered concerning the quantitative ion chromatography data, it appears that this should allow the production of good quality samples of HADN for further study. Questions about the compatibility of HADN with other substances and the effects of those substances on HADN's stability are among the studies that need to be pursued. When these studies have been sufficiently advanced, concerns such as propellant formulation and testing can be pursued.

References

1. Hawkins, T.W. and Wilkerson, B. E., Environmental Propellant: Current Issues and Assessment, 1992 JANNAF Propulsion Meeting.
2. Borman, S., "Advanced Energetic Materials Emerge For Military and Space Applications", Chemical & Engineering News, January 17, 1994, p. 18.
3. Losey, Matthew, personal communication.
4. Rohm and Haas Ion Exchange Laboratory Guide, Rohm and Haas Company, Philadelphia, PA 19105.
5. Amos, Chrisopher, "Thermal Analysis of HADN and S-HAN5", Final Report for High School Apprenticeship Program, 1994.

A NEW MISSION FOR THE
AIR FORCE PHILLIPS LABORATORY MALABAR TEST FACILITY

James E. Harvey
Associate Professor
The Center for Research and Education in Optics and Lasers (CREOL)
Department of Electrical and Computer Engineering

The University of Central Florida
12424 Research Parkway
Orlando, Florida 32826
(407) 658-6818
FAX 658-6880

Final Report for:
Summer Faculty Research Program
Air Force Phillips Laboratory

Sponsored by:
Air Force Office of Scientific Research
Bolling Air Force Base, DC

and

Air Force Phillips Laboratory

October 1994

A NEW MISSION FOR THE AIR FORCE PHILLIPS LABORATORY MALABAR TEST FACILITY

James E. Harvey, Associate Professor
The Center for Research and Education in Optics and Lasers (CREOL)
Department of Electrical and Computer Engineering
The University of Central Florida

Abstract

In spite of a long history of valuable support to a wide variety of DoD and NASA programs, the Air Force Malabar Test Facility in Palm Bay, Florida is currently suffering from a rather serious decline in funded technical activity, and therefore in manpower and capability. This applied research and strategic planning project provides an assessment of the Malabar Test Facility and identifies a new mission related to the commercialization of space in the United States. Four significant opportunities for future Malabar participation include: a major role in the Eastern Range Modernization and Automation Program, an enhanced role in dual-use research and operations, technology transfer to the commercial space launch business, and as a major participant in a University Center of Excellence in Space Education and Research.

A NEW MISSION FOR THE
AIR FORCE PHILLIPS LABORATORY MALABAR TEST FACILITY

James E. Harvey

Introduction

In spite of a long history of valuable support to a wide variety of DoD and NASA programs, the Air Force Malabar Test Facility in Palm Bay, Florida (see Appendix for brief description) is currently suffering from a rather serious decline in funded technical activity, and therefore in manpower and capability. Civil government positions are down from nine(9) a few years ago to five(5), site contractor positions are down from approximately fifty (50) to thirteen (13), and military personnel (A. F. Officers) are down from four (4) to zero (maybe one). Funding from the Ballistic Missile Defense Organization (formerly SDIO) is down from \$2-3 Million/year a few years ago to a negligible sum. Tasking from NASA to monitor Space Shuttle launches has dropped to zero. The Atlantic Laser Ground Station (ALGS) program was canceled. The Nuclear Detection System (NDS) was transferred to AFTAC. There is still some support of Titan rocket launches and minimal visiting experiments.

Due partially to the virtual shut-down of the U. S. Space Program for the three years following the Space Shuttle Challenger disaster, the United States, who pioneered the exploration of space with the phenomenally successful Apollo Program, currently has only approximately fifteen percent (15%) of the world market in commercial space launches. France has captured a fifty-five percent (55%) market share, and both China and Russia are pursuing aggressive space launch programs.

The severe decline in the traditional role of the Air Force Malabar Test Facility in supporting classified DoD programs coincides with the recognition by both government and industry leaders that the commercialization of space should be a national priority. The current status of the commercial launch industry in the United States is summarized in Figure 1 as a collage of headlines and articles recently published in *Space News*.

Significant developments include the new government policy that provides for the commercialization of remote-sensing imagery. This specialized market is expected to grow from the current \$400 Million/year to \$2 Billion/year by the turn of the century. However, this will be dwarfed by the space communications business as the information highway becomes a reality. As you can see from the headlines in Figure 2, investors are growing bullish on space, and four states have formed commercial spaceports to promote the commercialization of space and the local economic growth it promises. Critical issues include launch cost and schedule

dependability, with emphasis upon *schedule dependability*. User friendliness of the government facility is also extremely important to commercial users.



Figure 1 Current status of the space launch industry in the United States.

The 45th Space Wing of the U.S. Air Force Space Command is currently involved in a major multi-year Range Automation and Standardization Program to modernize the Eastern Range. This program is intended to up-grade the facilities on the Range to permit cost effective commercial and military launches of space vehicles. Approximately \$1 Billion will be spent on this effort over the next decade.

Figure 2 illustrates that both NASA and U. S. industry realizes that education is crucial to the successful commercialization of space.

It is in response to these and other national needs that we propose the formation of a University Center of Excellence in Space Education and Research which will utilize Malabar as an operational laboratory for pilot programs involving the test and evaluation of new technologies on actual launch vehicles.

NASA Programs Add Space To Classroom Education

By WILLIAM BOYER
Special to Space News

ANAHEIM, Calif. — NASA is bringing space into the classroom with special programs, speakers, internships and free educational materials designed to inspire students into pursuing science, mathematics and aerospace careers.

From the elementary school to the university, the agency's educational outreach programs teaching resources and levels, often putting teachers in NASA

for NASA news and educational material. Or, turn on NASA Select for daily television programming broadcast by NASA.

Teacher Programs

Two of the most popular enrichment programs by the space agency are the NASA Teacher Resource Center(s)

For students in NASA's annual Student

3-12. ence 7 is 7m

Where To Contact NASA For Education Programs

NASA Teacher Resource Center(s)

Contact the education officer at the NASA field center serving your area.

Ames Research Center, Moffett Field, Calif. 94035. (Alaska, Arizona, California, Hawaii, Idaho, Montana, Nevada, Oregon, Utah, Washington, Wisconsin, Wyoming)

Center, Greenbelt, Md. 20771. (Connecticut, Delaware, Florida, Georgia, Illinois, Indiana, Iowa, Kansas, Kentucky, Louisiana, Maine, Maryland, Massachusetts, Michigan, Minnesota, Missouri, Nebraska, New Hampshire, New Jersey, New Mexico, New York, North Carolina, North Dakota, Ohio, Oklahoma, Pennsylvania, Rhode Island, South Carolina, South Dakota, Tennessee, Texas, Virginia, West Virginia, Wisconsin, Wyoming)

Arizona, Kansas, Dakota, Texas) in Puerto Rico,

San, Va. 23065. (out Virginia) Cleveland, Ohio Wisconsin)

Space Companies Hope To Reap What They Sow Through Education

Thursday evenings to help local math and science homework. ■ corporate and employee contributing \$450,000 from McDonnell Douglas for a three-year program for students in Math and Science. ■ funding of \$1 million for the Los Angeles high-achieving program.

Space Firms Push Educational Efforts

ANAHEIM, Calif. — Tomorrow's scientists and engineers getting help today with elementary and secondary

Figure 2. Education is crucial to the successful commercialization of space.

Space-related National Needs

In addition to previously mentioned need to upgrade the national launch facilities, the Air Force also has a requirement to develop facilities and techniques to identify space objects orbiting in space. These objects may be small pieces of debris or malfunctioning vehicles and satellites.

Other national needs related to space is the need to develop stand-off surveillance systems for civilian and military applications including drug interdiction and theater missile defense.

The nation also needs to develop technology for beaming energy to orbiting satellites, possibly using laser beams from the ground. This would permit communication satellites to have a significantly longer life-time, thereby being more cost-effective.

These national needs are summarized below:

- Upgrade National Launch Facilities
- Space Object Identification (USAF)
- Stand-off Surveillance Systems (BMDO)
- Laser Power beaming to Space Vehicles (NASA)
- Small Satellite Development (Commercial Industrial)
- Education and Research in Launch Technology and Space Science and Technology

If the above needs are to be satisfied, there will be a continuing requirement for technical manpower trained in the areas of electro-optic sensors, precision tracking and imaging radar, space-launch technology, and the fabrication of mechanical structures in space.

The Spaceport Florida Authority

The Spaceport Florida Authority (SFA) was established by the Florida State Legislature in 1990 for the expressed purpose of promoting economic growth and space-related industry in the State of Florida. Their main charter is to develop launch technologies for commercial applications using Pad 46 at Cape Canaveral Air Station (CCAS), and to interface with private industry and the public in promoting commercial applications of space. A second charter is to increase the state's involvement in space science and research. The University of Central Florida (UCF) can aid in the accomplishment of this mission by joining forces with the SFA and forming a Center of Excellence in space-related research and education.

The Florida Space Center

The Florida Space Center (FSC) will be a synergistic consortium of Florida universities and colleges, government laboratories, and state agencies. As illustrated schematically in Figure 3, the FSC will be hosted at the University of Central Florida some 30 miles west of Kennedy Space Center. The other university and colleges participating in the FSC will be the Florida Institute of Technology (FIT) for space sciences and engineering, Brevard Community College (BCC) for space technology for undergraduates; and Bethune-Cookman College for undergraduate science education. The State agencies participating will be Spaceport Florida Authority, Enterprise Florida, and the Technological Research and Development Authority (TRDA). Other Florida universities will participate through the Florida Space Grant Consortium.

The FSC will be an education and research center. The emphasis of the work will be to test concepts and technologies in the field with real assets in the normal operations of the Eastern Range. The FSC will work to support the surveillance and sensor development mission of BMDO; development of technology for the Air Force mission of space object identification and space debris tracking; the development of technology for the commercial, DoD, and NASA space-launch industry; and the development of engineering launch technologies for the Eastern Range.

The objectives of the Florida Space Center will be to provide a practiced-based education and experience for students in actual projects involving space technology. The space

community at Kennedy Space Center and the Cape Canaveral Air Force Station is the world's premiere space launch facility. The students will have the opportunity to be involved in the actual work of launching this nation's space vehicles and to work with the people who conduct this nation's space business.

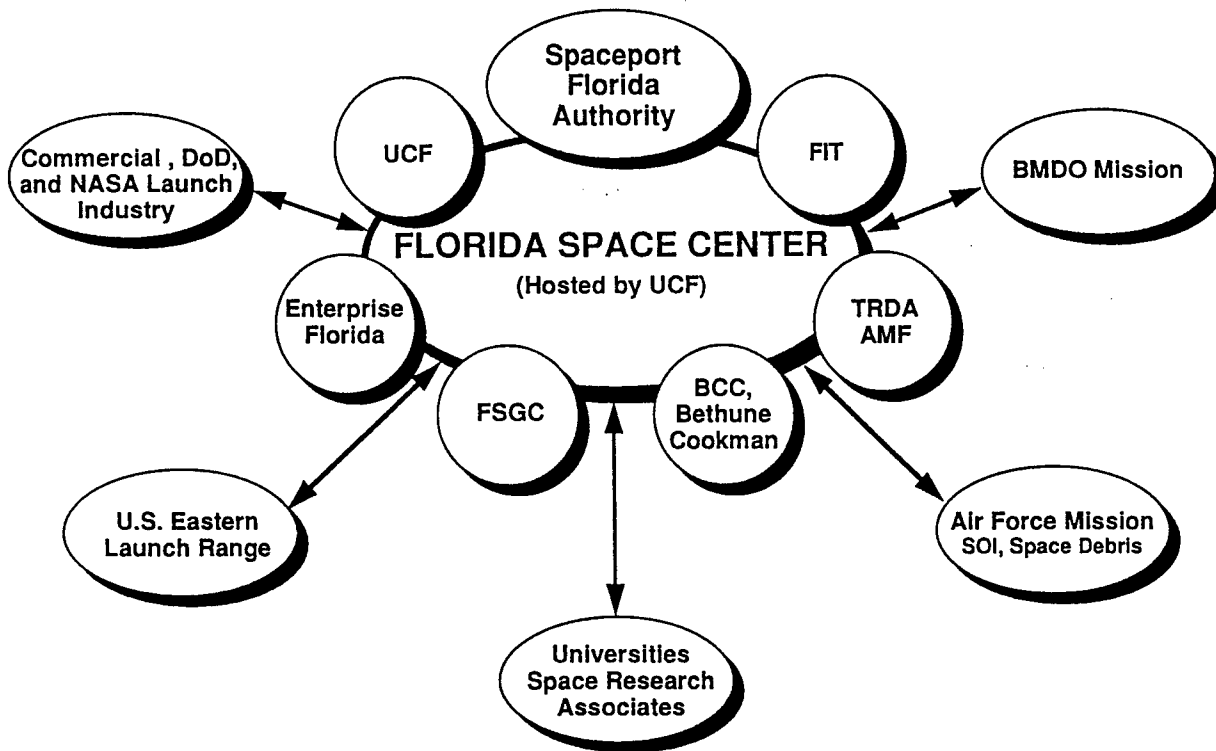


Figure 3 The Florida Space Center, a synergistic consortium of Florida universities and colleges, government laboratories, and state agencies.

Initially the Florida Space Center will work to develop new space and atmospheric sensing technology and space-launch technology for dual-use commercial and defense applications. The FSC will also serve as a technology transfer conduit from formerly classified programs and national laboratories to industrial applications, exercising a measured and disciplined approach to transferring formally classified technology into the industrial marketplace through the education and research programs of the center.

In addition to the Spaceport Florida Authority which has a charter from the State of Florida to promote space-related industry, there are a number of other elements and assets already in place which promise to make the formation of the Florida Space Center a success.

The Center for Research and Education in Optics and Lasers (CREOL) at UCF is a world class research center in the area of electro-optics and lasers. Currently there are some 40 faculty, 85 graduate students, and 30 visiting scientists and post-doctoral students working at CREOL.

The Space Education and Research Center (SERC) at UCF is a collection of faculty and academic departments at UCF that have developed a classroom curriculum for space technology. This Center also promotes space related research primarily through NASA. UCF also participates in the Florida Space Grant Consortium (FSGC) which is a consortium of Florida universities that sponsor small space related research projects for students and faculty. Space-related education and training degree programs also already exist at Brevard Community College (BBC) and the Florida Institute of Technology (FIT).

The Florida state Technological Research and Development Authority (TRDA) receives funds from the Florida Department of Education and from the sale of Challenger license plates. The TRDA supports space-related educational and research projects at universities throughout Florida.

BMDO has a laser-optical tracking facility on Merrit Island at Kennedy Space Center (see Figure 4). The facility is part of BMDO's Innovative Science and Technology Office and is called the Innovative Science and Technology Experimental Facility (ISTEF). The mission of ISTEf is to provide a field laboratory where the equipment and systems developed under the funding from BMDO can be integrated and field tested with real rockets and space objects. The world's premier adaptive optical instrument with a one-meter beam director, built by Thermo Trex Corporation of San Diego, is to be installed at ISTEf in 1995. Over \$20 Million has been invested in it by BMDO and ARPA. Approximate value of physical assets at ISTEf is \$60 Million. UCF has had a contractual relationship providing technical expertise in the area laser radar technology to the ISTEf facility for approximately seven (7) years.

The Malabar Test Facility of the U. S. Air Force Phillips Laboratory, some 40 miles south of Cape Canaveral (see Figure 4), is an optical tracking and telescope station at Palm Bay, Florida. This facility has been in place for some 30 years and has conducted some of the first experiments on laser tracking of launched rockets and space satellites as well as optical communications from ground to space. The primary resources Malabar Test Facility includes two optical trackers (a 48 inch Itek wide FOV telescope and a 24 inch Itek telescope with support instruments), two laser transmitters, major computer facility to handle data and control the telescope sensors, and image and data processing capabilities to support such missions as launches from KSC and the Eastern Range, offshore operations, and on-orbit observations. See the Appendix for a more complete description of the Malabar Test Facility. The value of physical assets is approximately \$120 Million. FIT has conducted research at the Malabar

Facility for several years, with both faculty and students benefiting from "hands-on" research projects.

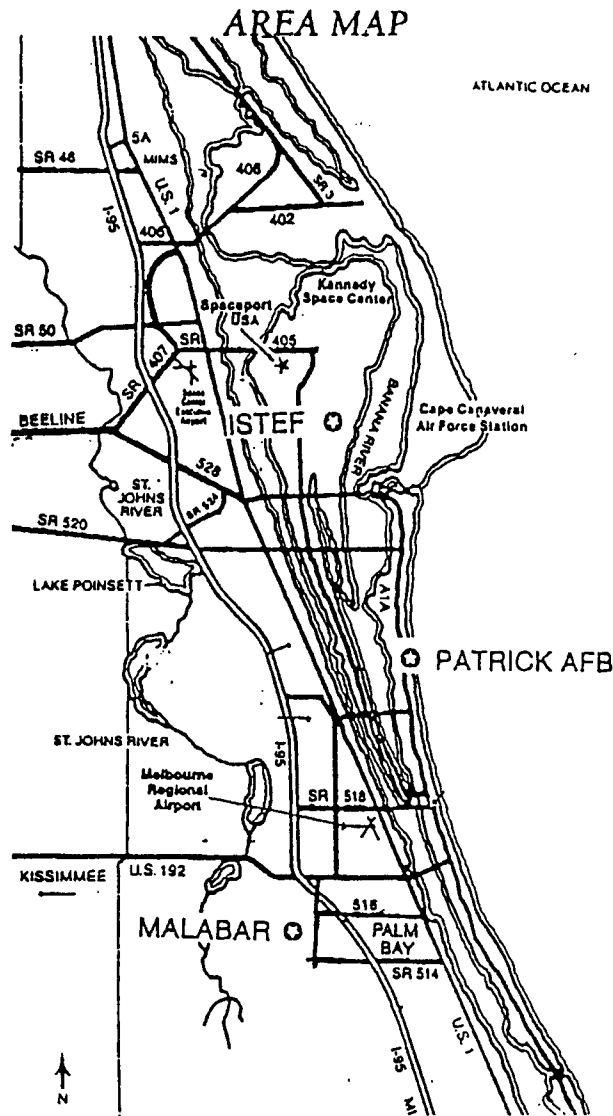


Figure 4. Area map showing the strategic location of ISTEf and Malabar relative the U. S. launch facilities at Kennedy Space Center and Cape Canaveral Air Station.

A New Mission for Malabar

Malabar is ideally positioned to provide an extensive remote sensing capability for launch vehicle health monitoring, space object identification, and atmospheric studies.

Since the Eastern Range is now an *operation* and no longer has a charter to do test and evaluation, Malabar can serve a valuable function as an operational laboratory for pilot programs involving the test and evaluation of new technologies on actual launch vehicles. Technical support to Malabar can be provided by the Florida Space Center which is less than

an hour drive from Malabar. The Florida Space Center can also serve as a conduit for technology transfer to the commercial launch industry through its relationship with the Spaceport Florida Authority.

Phillips Laboratory technology applicable to the range modernization program includes:

- Hyperspectral Imaging
- Laser Radar
- Local Wind Velocity Monitoring
- Precision Optical Tracking
- Adaptive Optics
- Unconventional Imaging

Figure 5 illustrates how the Air Force Material Command can fulfill its responsibility to satisfy the Eastern Range modernization and automation requirements by transferring newly developed technologies from the Phillips Laboratory to Malabar for test and evaluation at Malabar (by Florida Space Center Personnel) before being delivered to the Eastern Range as operational turn-key instrumentation.

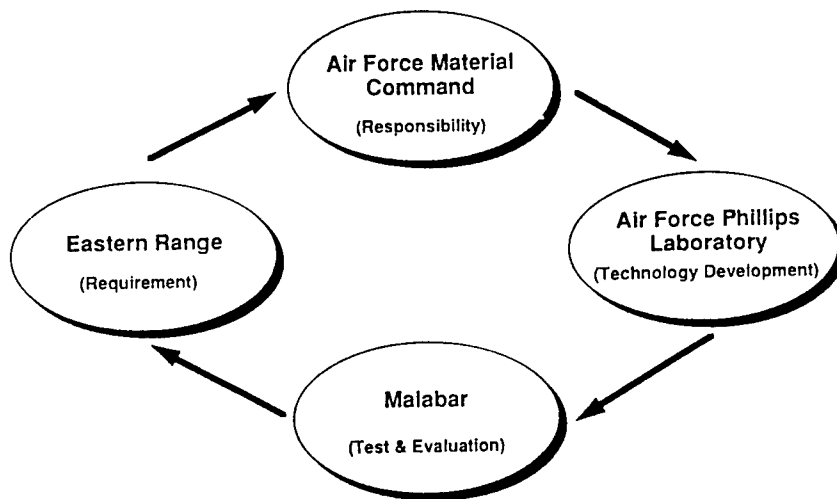


Figure 5 Eastern Range modernization and automation requirements provide research and development opportunities for the Phillips Laboratory as well as a mission for Malabar as an operational laboratory for the test and evaluation of new remote sensing instrumentation.

With faculty and student participation in these test and evaluation operations at Malabar, technology transfer to the commercial launch industry will occur through the close relationship of the Florida Space Center with the Spaceport Florida Authority and its commercial customers at Launch Complex 46. Also the educational charter will be fulfilled by having university students actively involved and getting hands-on experience in the test and

evaluation operations at Malabar. The transfer of technology from Phillips Laboratory research and development programs will be complete and highly effective as these students graduate and join the technical work force in the commercial launch industry.

Specific needs in the area of launch vehicle health monitoring include

- Early Detection of Launch Anomalies
- Recording and Archiving Anomalous Behavior
- Verification of Launch trajectory and Orbit Insertion
- Verification of Satellite Orientation and Stabilization
- Monitoring Rocket Exhaust for Environmental Studies
- Providing a Database for Potential Commercial Users

Hyperspectral imaging is a good example of a new technology currently under development at the Phillips Laboratory¹ that could be combined with the new developments in laser radar at ISTE² to achieve a truly revolutionary remote sensing capability. The basic remote sensing functions include the following:

- Target Search, Acquisition, and Tracking
- Radiometry (Intensity Measurements)
- Spectroscopy (Spectral Measurements)
- Imaging (Spatial Measurements)
- Laser Radar (Position and Velocity Measurements)

The combination of a radiometer and a spectroscope allows one to make spectral radiometry measurements as illustrated in Figure 6. Similarly, the combination of spectroscopy and imaging has been utilized for years to obtain multi-spectral images³⁻⁵; however, with state-of-the-art mosaic focal plane technology the field of hyperspectral imaging⁶⁻⁸ is rapidly being developed. And finally, the field of coherent laser radar (ladar) array receivers^{9,10} allows one to do high resolution image reconstruction from the amplitude and phase measurements from sparse arrays. Thus we have imaging ladar.

If we combine all of the basic remote sensing functions with the new hyperspectral imaging technology, we could create the new field of *radiometric hyperspectral imaging ladar* which results in a hyperdimensional data set. This data set would include one dimension of intensity information, one dimension of spectral information, two or three dimensions of imaging information, three dimensions of information concerning the position of the target, and six dimensions (three translational and three rotational) of information concerning the target

velocity. This hyper-dimensional remote sensing capability is illustrated schematically in Figure 6.

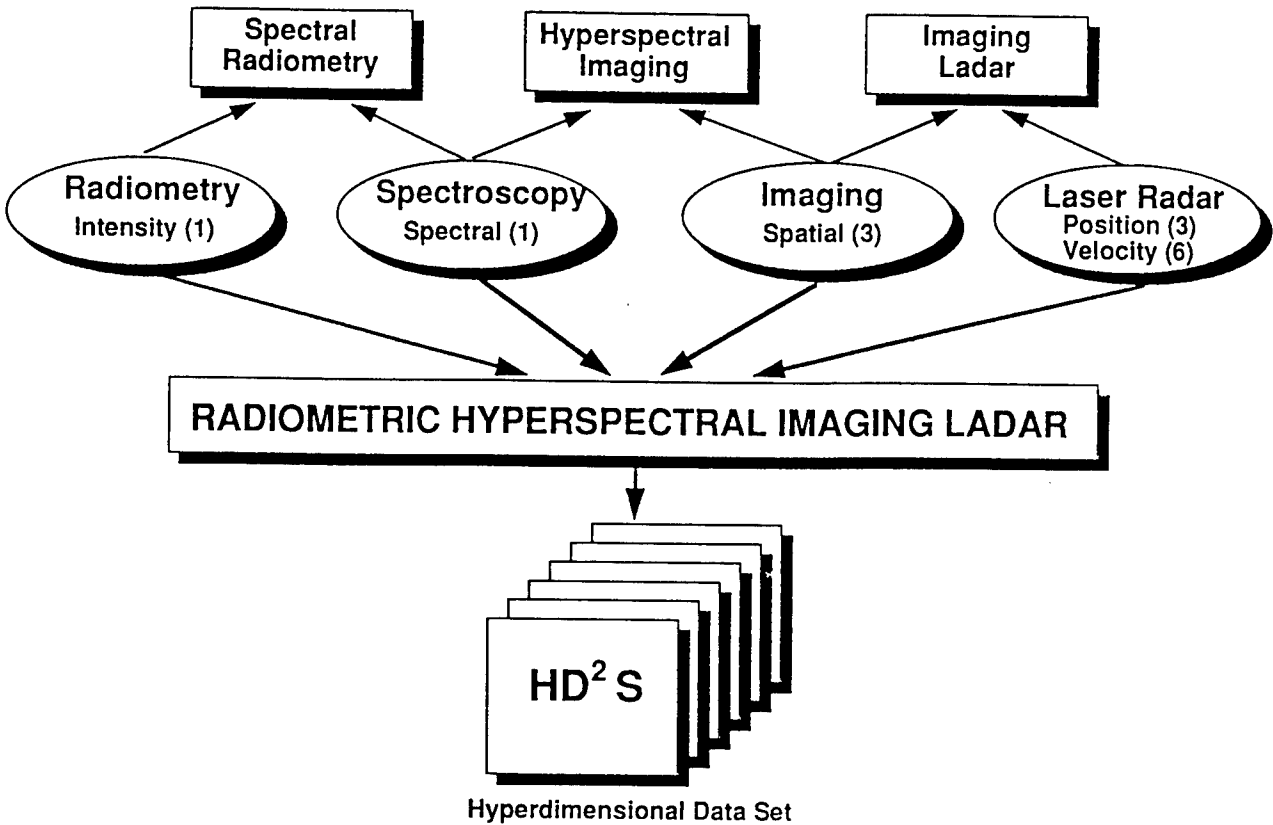


Figure 6. Hyper-dimensional remote sensing for launch vehicle health monitoring.

This significant advancement in remote sensing technology is merely one example of a specific project that could be carried out by collaboration between the academic participants of the Florida Space Center and the Air Force Phillips Laboratory using Malabar as the operational laboratory for test and evaluation of these advanced systems on real launch vehicles.

Clearly this type of remote sensing capability would be applicable to a wide range of applications in addition to launch Vehicle health monitoring

- Launch Vehicle Health Monitoring
- Space Object Identification
- Earth Resource Surveys
- Weather Analysis and Forecasting
- Reconnaissance and Surveillance
- Environmental Monitoring
- Search and Rescue Missions

- Atmospheric and Ocean Sciences

Florida Space Center Funding Plan

All of the participants will share in the cost and benefit from the results of the Florida Space Center. The Florida state university system (SUS) will contribute to the cost by funding tenure-track faculty lines and recruiting and hiring the best people in the industry to lead the research and teaching activities of the FSC. They will benefit by becoming recognized for the best academic program in the country in space-related technologies. The local launch industry will share in the cost by funding graduate student stipends and research projects of specific interest. They will benefit by staying at the cutting edge of technology and by taking advantage of the highly qualified manpower labor pool generated by the experience-based academic program. The Spaceport Florida Authority will provide FSC infrastructure support. The BMDO and Air Force Phillips Laboratory will contribute Facilities and Equipment (i.e., the ISTEf and Malabar Sites) and some contract funds for specific projects related to their particular missions. The Air Force 45th Space Wing and NASA will provide operational launch support. The federal government will provide TRP funds to get the FSC established. And after some initial period of time the FSC should become self-supporting through a variety of federal and private industry contract support.

- SUS ----- Faculty Lines
- Launch Industry ----- Graduate Student Stipends
- Spaceport Florida Authority -- FSC Infrastructure Support
- TRDA ----- FSC Infrastructure Support
- BMDO/Phillips Lab ----- Facilities and Equipment
- 45th Space Wing ----- Operational Launch Support
- Federal Government ----- TRP Funds
- NSF, DOT, AFSOR, NRAD ----- Contract Support
NASA, ARMY, Private Industry

Summary

We have performed a preliminary assessment of the Air Force Malabar Test Facility and identified a new mission related to the commercialization of space in the United States. Four significant opportunities for future Malabar participation include: 1.) a major role in the Eastern Range Modernization and Automation Program, 2.) an enhanced role in dual-use research and operations, 3.) technology transfer to the commercial space launch business, and 4.) a major participant in a University Center of Excellence in Space Education and Research.

We have also described a synergistic consortium of universities, state agencies, government laboratories, and private industry that will all benefit from the formation of the Florida Space Center (FSC). This academic research and educational center of excellence in space-related technologies will help to upgrade our national launch facilities and capture a major market share of the burgeoning commercial launch business. Malabar would become an operational laboratory for pilot programs involving the test and evaluation of new technologies on actual launch vehicles. A hyper-dimensional remote sensing capability for launch vehicle health monitoring has been identified and described as one particular technical project with high potential pay-off. A preliminary funding plan for getting the FSC established has been outlined .

References

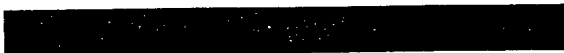
1. S. E. Durham and T. E. Payne, "Hyperspectral Imaging for Space Object Imaging", *Proc. SPIE 2308-01* (July 1994).
2. P. Gatt, J. E. Harvey, A. R. Weeks, H. Mylar, C. M. Stickley, and R. Mongeon, "CREOL Laser Radar Activities at ISTEf", *17th International Laser Radar Conference, IEEE, Sendai, Japan* (July 1994).
3. A. Goetz and G. Vane, "Imaging Spectrometry of Earth Remote Sensing", *Science*, Vol. 228, No. 4704, p. 1147 (1985).
4. W. Porter and H. Enmark, "A System Overview of the Airborne Visible/Infrared Imaging Spectrometer (AVIRIS)", *Proc. SPIE*, Vol 834, p. 22 (1987).
5. G. Vane and A. Goetz, "Terrestrial Imaging Spectroscopy", *Remote Sensing of the Environment*. Vol. 24, p. 1-29 (1988).
6. R. Basedow, P. Silverglate, et. al., "The HYDICE Instrument Design", *Proc. of the International Symposium on Spectral Sensing Research*, Vol. 1, p. 430-445 (1992).
7. R. Birk and T. McCord, "Airborne Hyperspectral Sensor Systems", *Proc. of 47th National Aerospace and Electronics Conference*, Dayton, OH (1994).
8. B. Braam, et. al., "AISI a New Versatile Tool for Hyperspectral Remote Sensing", *Proc SPIE 2318-09* (July 1994).
9. P. Gatt, W. P. Perez, D. A. Heimmermann, and C. M. Stickley, "Coherent Laser Radar Array Receivers: Theory and Experiment", *OSA 7th Conference on Coherent Laser Radar*, Paris France (July 1993).
10. P. Gatt, W. P. Perez, and C. M. Stickley, "Applications of Diversity Reception Techniques to Coherent Laser Radar", *Annual LEOS Conference*, Boston, MA (Nov 1992).



FACILITIES AVAILABLE FOR EXPERIMENTAL USE



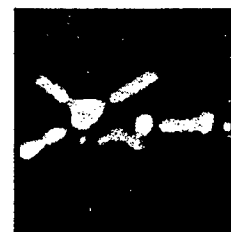
U.S. AIR FORCE
PHILLIPS LABORATORY
OL-AG
MALABAR TEST FACILITY
PALM BAY, FLORIDA



PHILLIPS LABORATORY MALABAR TEST FACILITY

The Malabar Test Facility in Palm Bay, Florida is a remote site of Phillips Laboratory (headquartered at Kirtland Air Force Base, New Mexico) one of the Air Force's largest research and development organizations. The research and development areas supported by Phillips Laboratory encompass geophysics, propulsion, space and missile technology, lasers and imaging, advanced weapons and survivability, and space experiments. The Malabar facility is part of the *lasers and imaging* branch.

Mission: Malabar conducts optical and electro-optical research and development activities in support of Air Force space programs and other government organizations. Malabar can provide space and launch vehicle imagery, on-orbit calibration of space sensors, and support of anomaly investigations. In addition, Malabar can provide software development, image processing and analysis, and optical design services to customers. Malabar's resources consist of proven equipment, qualified personnel, and excellent geographical location for customer's experiments. Some of Malabar's customers are DoD agencies, commercial agencies, and foreign governments.



Centaur Upper Stage and Skylab

Location: Malabar's geographical location on the space coast provides unique chances for observing over 20 launches per year as "targets of opportunity." Malabar is located 30 miles south of Cape Canaveral launch sites and 55 miles east

of Orlando. In conjunction with a sister facility (the Maui Optical Site), Malabar can provide unique resources and coverage through a networking of optical sites.

Equipment: Primary optical systems available are shown in Table 1. The optical systems include two receivers and one laser beam director.

R1	48-inch telescope Four main focus points 3.5-degree WFOV 20-inch LATS
R2	24-inch telescope for UV and IR 3 - 5 micron MWIR 10-inch LWIR telescope
T1	24-inch afocal beam director 6X beam expander

Table 1 Malabar Optical Systems

The lasers available for active illumination include a kilowatt continuous wave YAG (Yttrium Aluminum Garnet) laser, two pulsed frequency-doubled YAG lasers (500 millijoules and 100 millijoules), and a 100-microjoule modulated YAG laser.

Sensors available for collecting data are shown in Table 2. The visible sensors (excluding the photometer and the spectral imager) can be used at various focal positions (120, 240, 480, 480 to 4800-inch) of the 48-inch receiver. The ultraviolet and Infrared sensors share the prime focal position (96-inch) of the 24-inch receiver. The intensified CID and CCD cameras are used to support night time imaging operations. These cameras are equipped with adjustable exposures and fast gating circuits to capture special events and backscatter light from laser-illuminated space objects.

Ultraviolet:	CCD, .32 - .36 μ meters
Visible:	ISIT 3-chip color CCD Single-chip color CCD Megapixel (1024 X 1024) CCD Slow scan megapixel CCD 40 mm ICID 25 mm ICID Photometer Spectral Imager
Infrared:	InSb, 3.0 - 5.2 μ meters SIAs, 9.5 - 11.5 μ meters

Table 2 Malabar Sensors

Other supporting equipment includes two Recognition Concepts realtime recording image processors, one Silicon Graphics image processor, three microVAX III's, three Sun workstations, and general purpose calibration equipment.

Tracking Capabilities: The tracking mounts are elevation-over-azimuth types that use 25-bit absolute position encoders. The mounts are computer driven in realtime to give a pointing accuracy of less than 2 arcseconds, a tracking velocity of 15° per second, and an acceleration of 2° per second². The realtime program that drives the mounts has been refined over many years to produce highly reliable tracking. Tracking may be performed by hand, digital tracker, radar drive, or vectors generated on-site.

Present Programs:

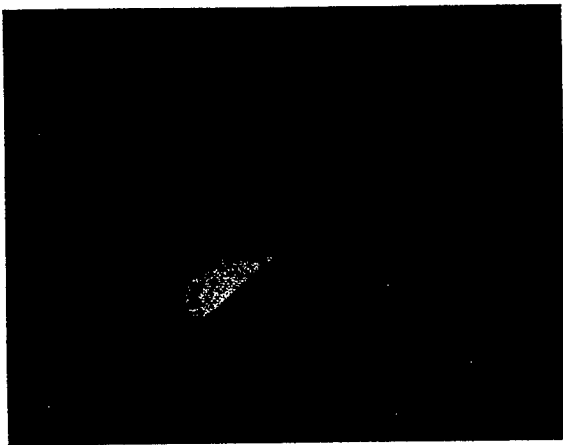
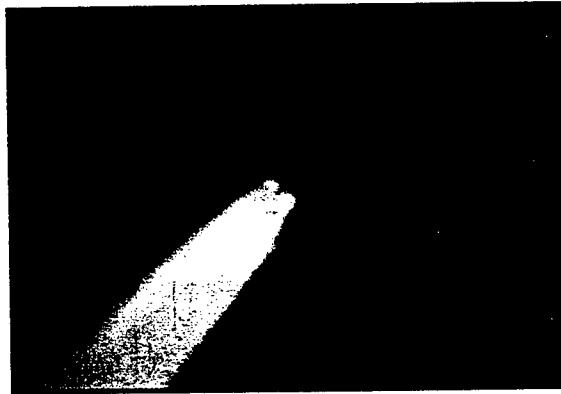
- 1) Supporting classified space experiments
- 2) Tracking and recording commercial and government launches
- 3) Laser illuminating and tracking space objects for developing and refining laser ranging and laser communications capabilities

Past Programs:

- 1) Tracking space debris for classifying space objects
- 2) Tracking, video taping, and transmitting video and critical data on specific space objects for space object identification
- 3) Developing and testing a digital tracker
- 4) Autonomous tracking of boosting and thrusting space vehicles
- 5) Collecting data for plume phenomenology and discrimination studies in support of the Ballistic Missile Defense Organization
- 6) Building and testing a mount control system to replace systems at other Air Force installations

Personnel: In addition to the civilian group at the Malabar facility, the following contractor groups provide on-site operational and engineering support:

- Orion International Technologies**
- United Technologies**
- Florida Institute of Technology**



Laser Illuminating a Vehicle

For more information on the Malabar Test Facility, contact:



Branch Chief
OL-AG, Phillips Laboratory
Malabar Test Facility
5600 Minton Road
Palm Bay, FL 32907
Phone: (407) 723-3100
Internet: info@malabar.fl.us
info@malabar.mlb.fl.us



Dr. Stan Heckman
Report Not Available

HIGH RESOLUTION RANGE DOPPLER IMAGERY AND DATA FOR
SPACE OBJECT IDENTIFICATION AND ANALYSIS

James M. Henson
Assistant Professor
Department of Electrical Engineering

University of Nevada
Reno, Nevada 89557

Final Report for:
Summer Faculty Research Program
Phillips Laboratory

Sponsored by:
Air Force Office of Scientific Research
Bolling Air Force Base, DC

and

Phillips Laboratory

July 1994

HIGH RESOLUTION RANGE DOPPLER DATA AND IMAGERY FOR SPACE OBJECT IDENTIFICATION AND ANALYSIS

James M. Henson
Assistant Professor
Department of Electrical Engineering
University of Nevada

Abstract

The following pages describe the raw data available from radar sites such as HAYSTACK, ALCOR, and MMW as well as several data processing and presentation options including Range Time Intensity (RTI) and Doppler Time Intensity (DTI) strips and Range Doppler (ISAR) imagery. Several image sequences are provided to demonstrate the effects of a) Angular Sampling Interval, b) Angle of Integration, c) Zero Padding of signals in the Range and Doppler Dimensions, d) Center or Operating Frequency, and e) Signal Bandwidth. These variables represent a minimal set of parameters necessary for both site characterization and image understanding. A thorough understanding of the image formation process represents a necessary and prerequisite step to automated or manual object identification and analysis.

HIGH RESOLUTION RANGE DOPPLER IMAGERY AND DATA FOR
SPACE OBJECT IDENTIFICATION AND ANALYSIS

James M. Henson

Introduction

It is the goal of Phillips Laboratory WSAT to develop a multispectral, workstation based, image/data fusion and analysis tool for automated Space Object Identification (SOI), mission characterization, and health assessment. The radar frequency regime of interest includes operating frequencies in the 10 to 95 GHz range with bandwidths ranging from 500 to 1024 MHz. Also of interest is Narrowband data available from geographically diverse sites at similar operating frequencies. Due to the relative importance of two-dimensional range Doppler imagery much of the following discussion is dedicated to a presentation of such imagery and those radar and signal processing parameters that control image fidelity. A well engineered automatic SOI system must accept both narrowband and wideband input data at range resolutions commensurate with various system bandwidths and at Doppler resolutions related to angular sampling rate, object dimensions, operating frequency, and angular period of integration. The current study, made possible by the AFOSR and Phillips Laboratories, serves as necessary and critical to the development of the radar related portion of the planned ASOI system.

Range Doppler Data

As shown below, the raw data signal from a wideband radar is a continuous waveform due to a single target aspect. As the target moves with respect to the fixed radar position additional aspect sensitive signals, $V_i(t)$, are received. The data is processed to achieve resolution in the range dimension as shown in Figure 1.

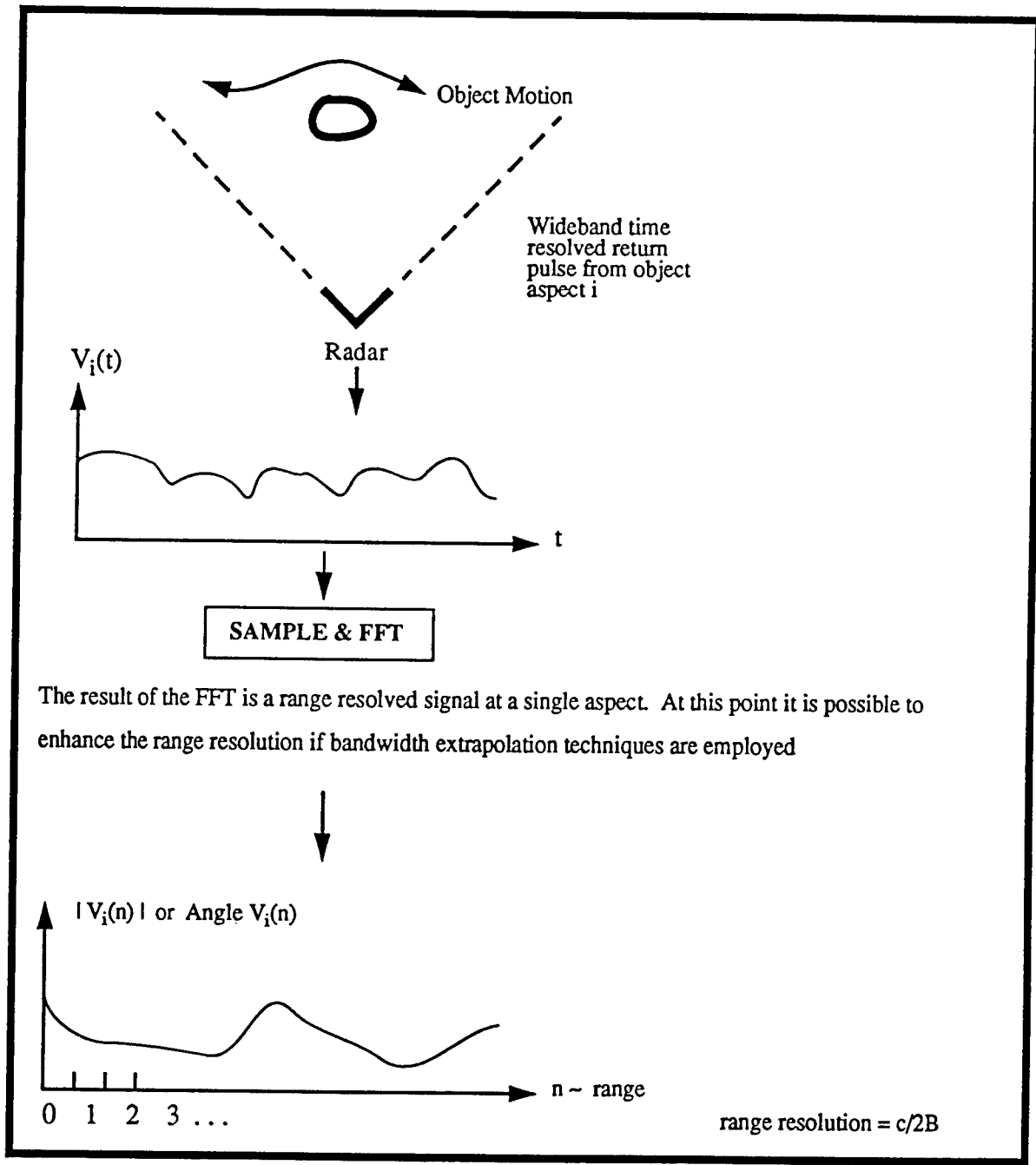


Figure 1

$V_i(n)$ may be thought of as the range 'signature' of the object when illuminated at aspect angle i .

This discrete signal can be displayed graphically as a function of n or as an image intensity strip. Discrete range resolved signals displayed in this fashion are called Range Time Intensity (RTI) strips.

As the object rotates some incremental amount, $\Delta\theta$, to aspect $i + 1$, a second signal $V_{i+1}(n)$ may be generated. If these strips are stacked vertically, grey level intensity at a set of constant ranges may be observed in the vertical (aspect) dimension as shown schematically in Figure 2. Phase Time Intensity plots (strips) may also be created using phase rather than magnitude data.

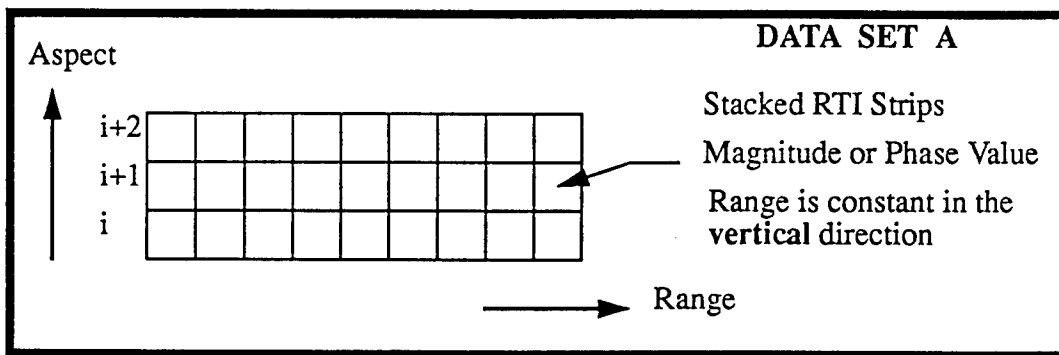


Figure2

In this way a complex valued high resolution range signal is generated for each target aspect. The number of distinct angles available for further processing depends on the motion of the object as well as the true pulse width and PRF of the radar system used to collect the data.

Let's define this information, $V_i(n)$, $i = 1, 2, \dots, m$, as Data Set A. It is a complex set of values - one complex value for each range, R , and aspect angle, Θ

$$V_c(R, \Theta) = (a(R, \Theta) + jb(R, \Theta))$$

Now suppose that we repeat this data collection process using a Narrowband Pulse, that is, a pulse with

$$\Delta R = \frac{C}{2B} = \frac{C\tau}{2} \quad \text{on the order of the dimension of the object. Then at each aspect we will have only one return,}$$

$$V_i(t) = a \cos(\omega_c t + \Psi) \quad \text{where } \omega_c \text{ is the narrowband carrier frequency. The Transform of this signal is}$$

$$a\pi \left[e^{-j\Psi} \delta(\omega - \omega_c) + e^{j\Psi} \delta(\omega + \omega_c) \right] .$$

If we 'stack' this data (intensity $a\pi$, or phase ψ) in a **horizontal** fashion or plot it as a function of aspect angle, we

have the following data display possibilities:

- 1) intensity versus aspect strip images
- 2) intensity versus aspect plots (These are usually called RCS plots)
- 3) phase versus aspect strip images
- 4) phase versus aspect plots

Suppose that we now take the DFT of $i = 1, 2, \dots, N$ of these complex narrowband signal values, $V_i(\omega)$, where

$$N = \frac{\Theta_{Total}}{\Delta\Theta}$$

$$\Theta_{Total} \leq \sqrt{\frac{\lambda}{2R}}$$

$$\Delta\Theta \leq \frac{\lambda}{4R}$$

R = Radius of "Rotating" object

In this fashion one can create a series of Doppler intensity strips or plots as shown in **Figure 3**.

If these one dimensional doppler image strips (intensity or phase) are stacked vertically we form what are known as stacked Doppler Time Intensity (DTI) strips. Doppler Phase Strips can also be created if the phase data is used.

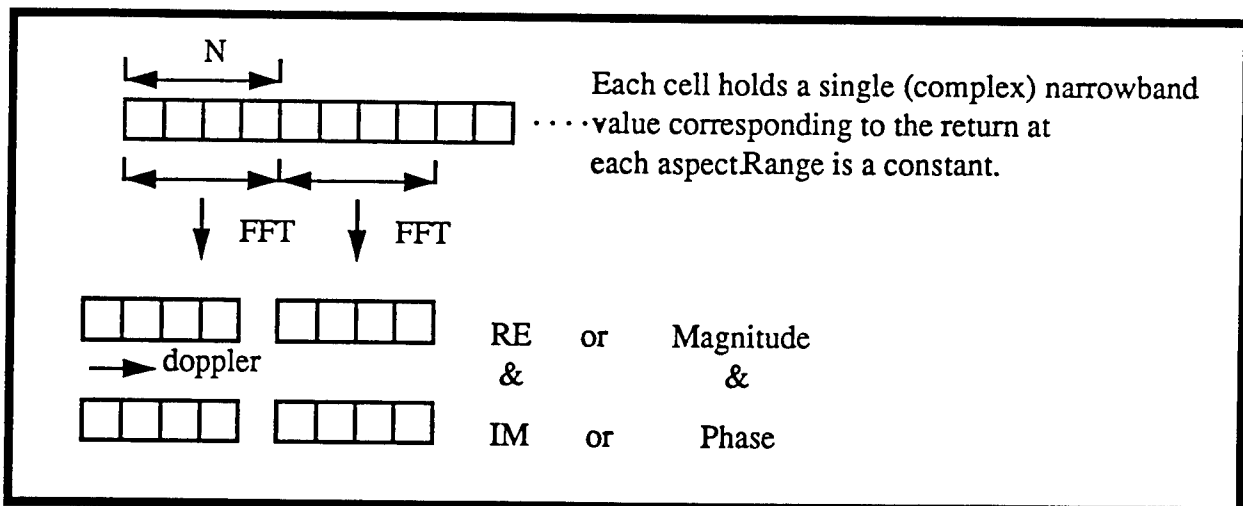


Figure 3

Each group of N values (in the horizontal direction) corresponds to a single cross range 'image' of the object. These images (intensity or phase) are one dimensional in the range dimension but resolved in the Doppler or cross range direction.

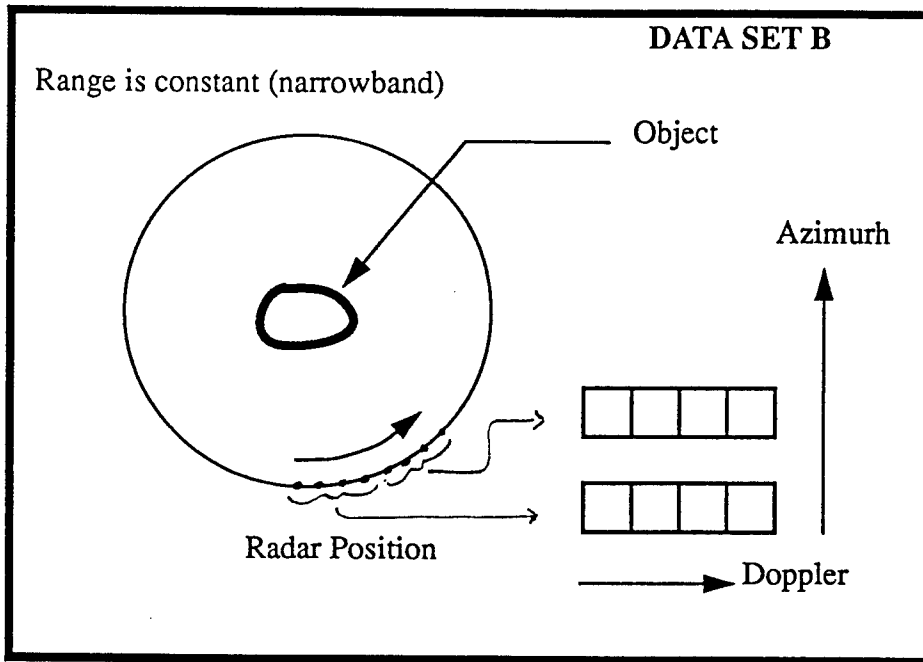


Figure 4

Let's define this information as Data Set B. It consists of a set of complex valued doppler (or cross range) arrays. Each one dimensional array corresponds to a particular object aspect. The data is depicted in Figure 4. Notice that the Narrowband DTI information of data set B can be created from data set A as follows.

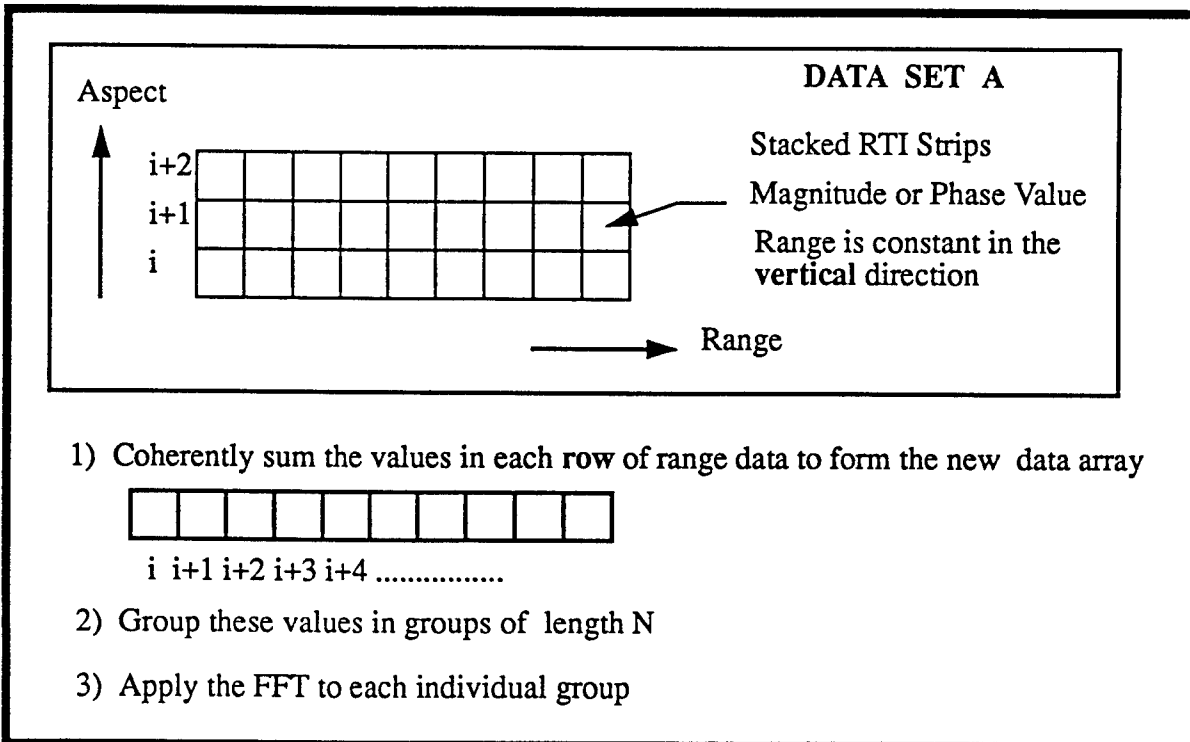


Figure 5

In other words, the narrowband information is recoverable from the wideband data. Actually, the narrowband and wideband range data represent the two range resolution extremes.

Finally, if the one dimensional FFT is applied to the columns of Data Set A (the complex wideband range resolved data) one can form true two dimensional range doppler (cross range) intensity and phase imagery. Note, however, that a single column of data may consist of range return data from any number of unique aspect increments, $i, i+1, \dots, i+M$, where the optimal increment is given theoretically as $\Delta\theta \leq \frac{\lambda}{4R}$. The optimal number of column

elements used to form a cross range (doppler) image strip at a given range is $N = \frac{\theta_{Total}}{\Delta\theta}$, where $\theta_{Total} \leq \sqrt{\frac{\lambda}{2R}}$

is the angle of integration for a single image. Thus a total of $\frac{M+1}{N}$ images may be formed by this process. The

basic processing is shown in Figure 6.

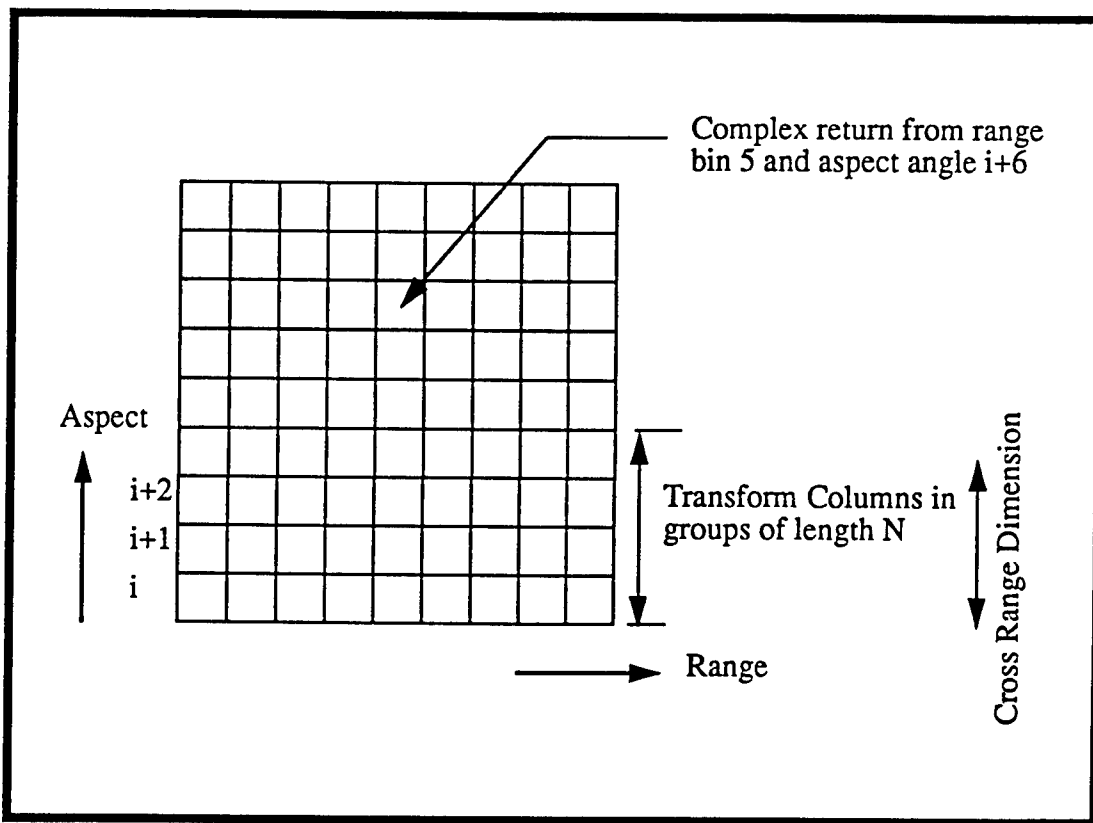


Figure 6

It should be noted that while the full wideband signal information content is available in the range Doppler Imagery, RTI and DTI strips and plots are expected to be of value in the satellite feature information extraction process. A related MFR is planned to address this issue.

Range Doppler Imagery and Related Phenomena

The imagery that follows in this section was generated using certain of the Lincoln Laboratories RCS Toolbox simulation software. In the discussion that follows reference is made to a number of user controlled variables in the software related setup files `.setupptd` and `setupimagetbl`. In **Figure 7** the object on the turntable (x/y plane) is assumed to be stationary while the radar moves around the object along a circular arc in discrete angular increments of length $\Delta\theta = \frac{\lambda}{4R}$ radians or $\Delta\theta = \frac{45\lambda}{\pi R}$ degrees. λ is the center frequency of the radar and R should be set to the known or estimated maximum radius of the object about its center of rotation (i.e. the z axis of the turntable). In actual processing terms the variable $\Delta\theta$ controls the processing interval or sampling rate.

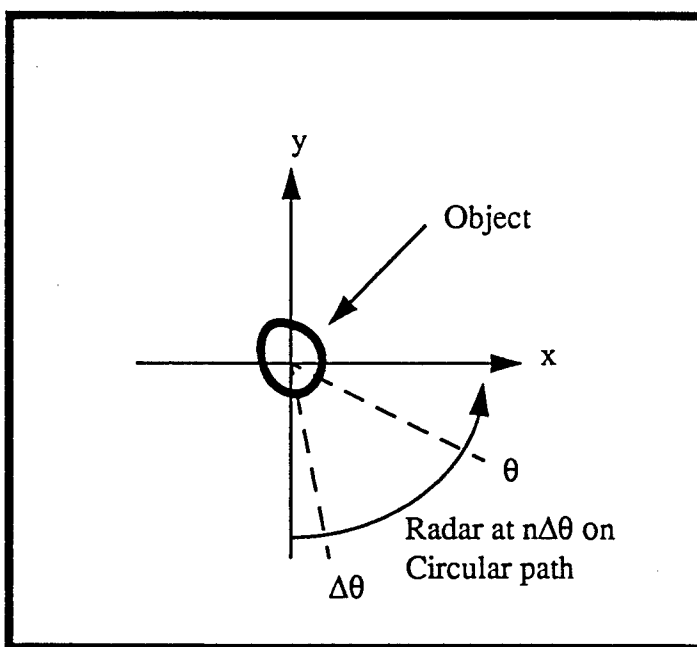


Figure 7

The value the user enters for 'number of samples' controls the number of discrete increments of length $\Delta\theta$, over which the radar will be moved. Note that moving the radar along a circular arc as shown in **Figure 1** is entirely equivalent to holding the radar in a fixed position and rotating the object about the the z (turntable) axis..

If $\Delta\theta = 0.5$ degrees and $N=100$ samples, 50 range waveforms will be generated -- at viewing angles 0, 0.5, 1.0, 1.5, ..., 50 degrees. The variable θ shown in the figure is associated with the program `setupimagetbl` where it is called the 'angle of integration'. NOTE that the LL Users Guide to the RCS Toolbox (Version 3.0) incorrectly defines the

angle of integration, θ , as $\Delta\theta$. The correct value (for optimal linear cross range focusing) is $\theta = \frac{180}{\pi} \sqrt{\frac{\lambda}{2R}}$

degrees. Together, θ and $\Delta\theta$ control the linearly focused cross range (or Doppler) resolution, $\Delta x \geq \sqrt{\frac{\lambda R}{2}}$. If the

angle of integration is taken such that $\theta < \sqrt{\frac{\lambda}{2R}}$, Δx increases correctly within the limits of the linear focusing

approximation. If $\theta > \sqrt{\frac{\lambda}{2R}}$, Δx theoretically decreases. However, the resulting imagery will be blurred (incorrectly

focused) due to scattering centers 'walking' between resolution cells. Figures 8, 9, 10, and 11 are included to demonstrate the phenomenon. The cross range blurring of the object in Figure 8 is due to an integration angle which is too small.

Figure 9 shows the object processed at the optimal integration angle. The blurring in Figure 10

(which shows the effect of a 25 degree integration angle) is a result of the linear focusing approximation (FFT) which decouples the relation between frequency and angle. Figure 11 is just an enlargement of the image of Figure

10. Notice that even with the blur caused by scattering centers walking between resolution bins in Figure 10, cross range resolution is still enhanced. The result suggests that variable angle of integration angle processing may be of value in the recognition/assessment process. Note however that the LL software will not accept integration angles that exceed $\theta = 256(\Delta\theta)$. This is because the software is limited to radix-2 FFT's of size 256. A future study is anticipated on the topic of focusing approximation and 'Extended Coherent Processing' techniques which provide more accurate focusing and enhanced cross range resolution.

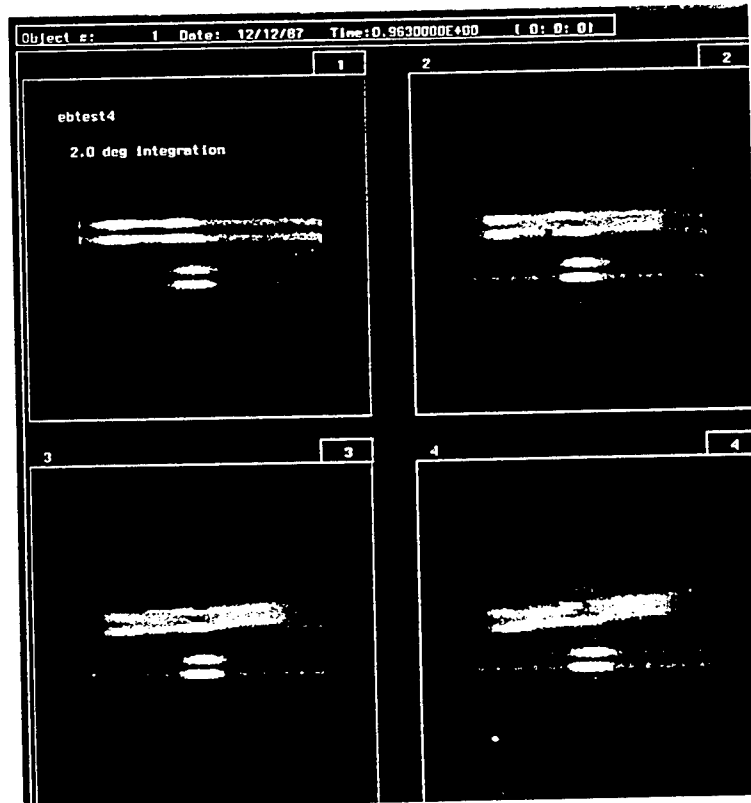


Figure 8

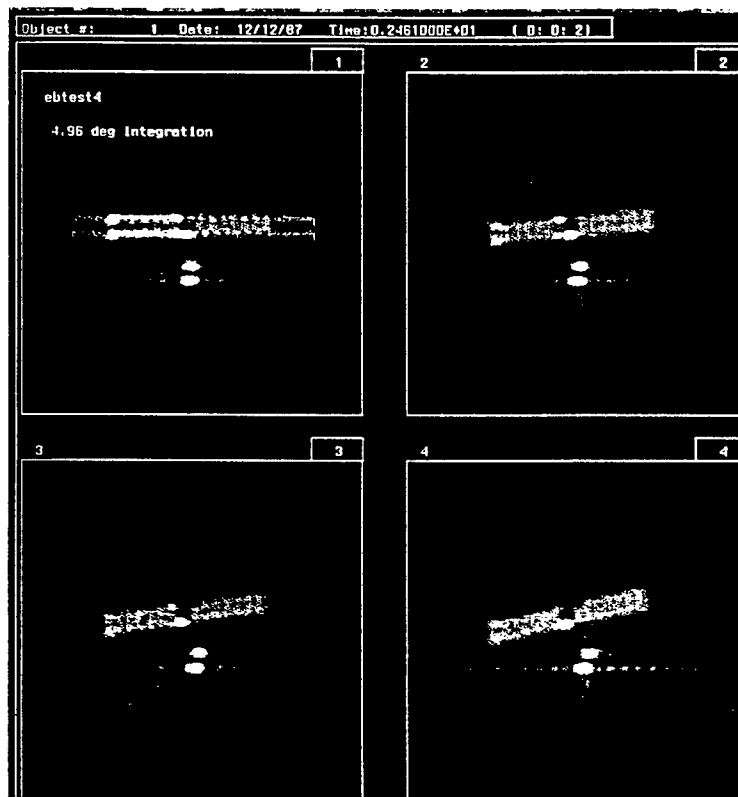


Figure 9

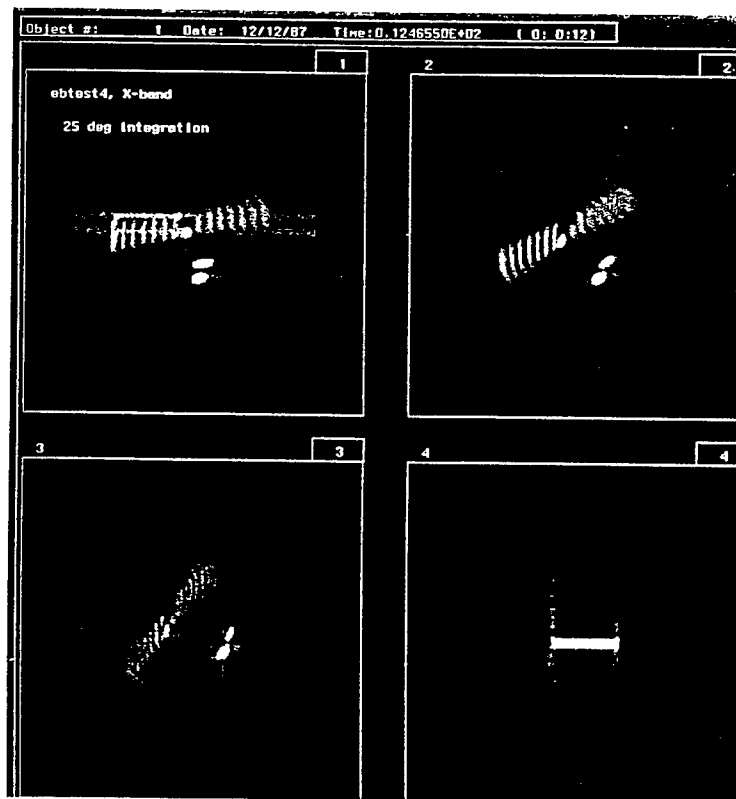


Figure 10

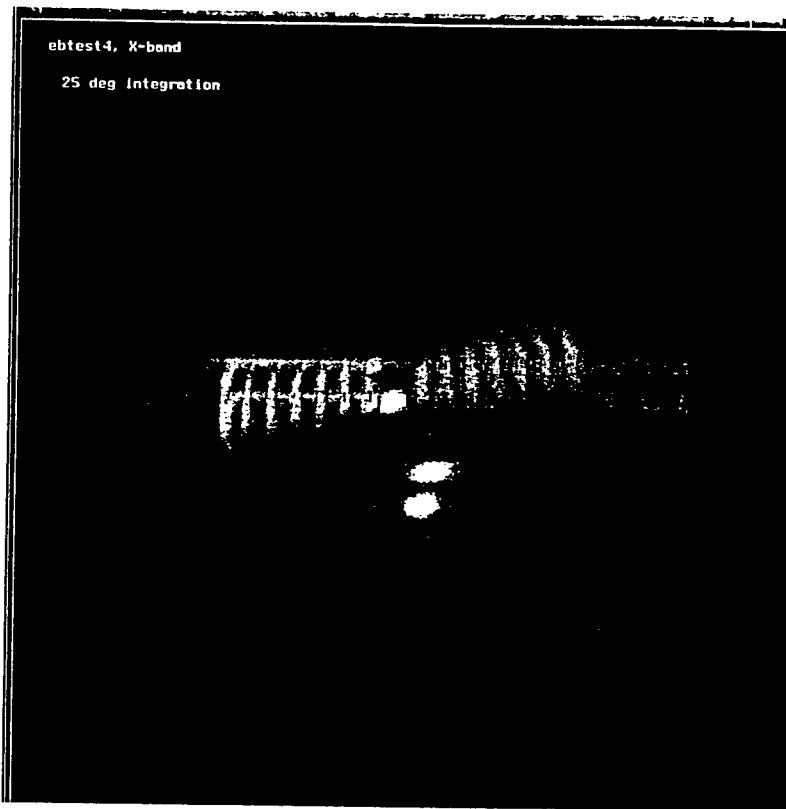


Figure 11

Our experience with the RCS Toolbox also indicates that $\Delta\theta$ (as given above) must be reduced by a factor of approximately one half to avoid FFT aliasing effects which are manifested as cross range pixel values corresponding to large Doppler shifts being 'wrapped' between sides of an image. These effects can always be avoided in simulated imagery but may be present in actual imagery if the radar PRF is not adequate to properly sample the motion of the object. These effects are the result of undersampling and the periodicity of the Discrete Fourier Transform or FFT. Figures 12 and 13 demonstrate the effect of an incorrect integration increment, $\Delta\theta$. In Figure 13 $\Delta\theta$ is too large. The image of Figure 12 results when $\Delta\theta$ is selected correctly.

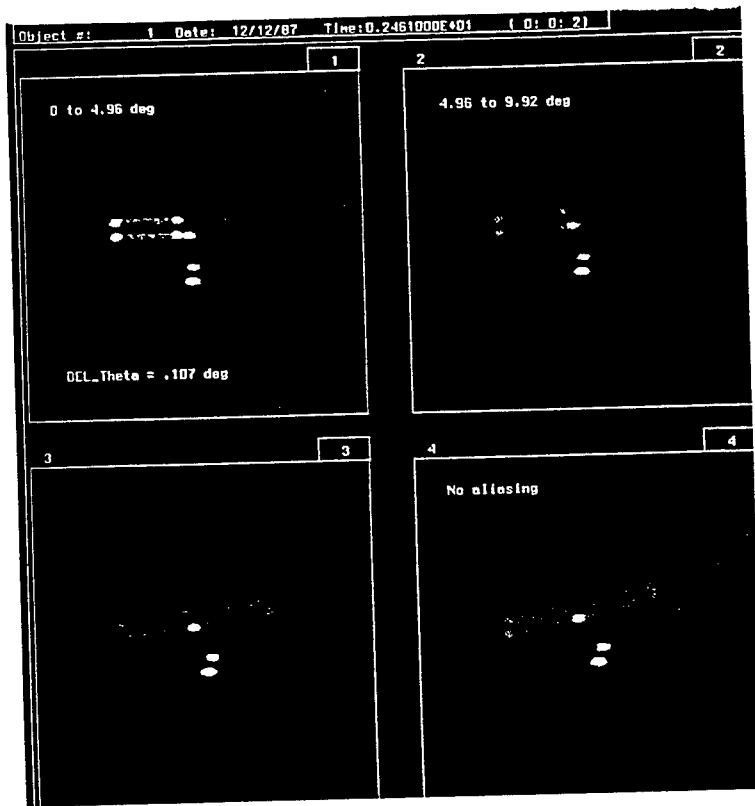


Figure 12

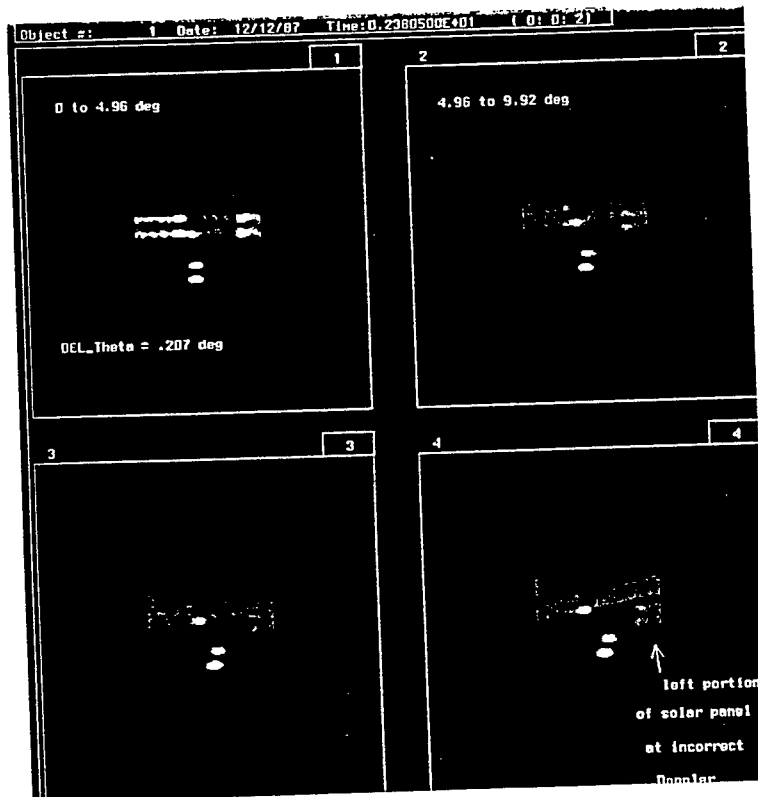


Figure 13

The 'zero padding' option refers to the number of zeros one wishes to append to each row of aspect sensitive (constant range bin) data prior to cross range FFT. A 64 point FFT of the sequence $x[n]$ will produce 64 values in the transform domain with uniform spacing inversely proportional to the sampling period used to produce $x[n]$. The distance between samples in the frequency domain is of course the cross range resolution, Δx . If zeroes (say 64) are appended to $x[n]$, the corresponding transform will be of length 128. This may seem to suggest a new cross range resolution of $\Delta x/2$. This is, however, NOT the case. The actual effect is to create additional frequency samples by interpolating between the original samples with a Sinc function. The new values may be completely erroneous. FFT resolution cannot be enhanced by appending zeroes to a function $x[n]$ unless the function is in fact zero valued over the interval where the zeroes are appended. The only sure way to increase the resolution is to increase the angle of integration, θ . Unfortunately, θ is limited as discussed previously. Figures 14 and 15 are included to demonstrate the effect of padding the wideband range return (at each $\Delta\theta$) with 16 zeroes. Figure 14 represents the image prior to zero padding. Figure 15 is the result after zero padding.

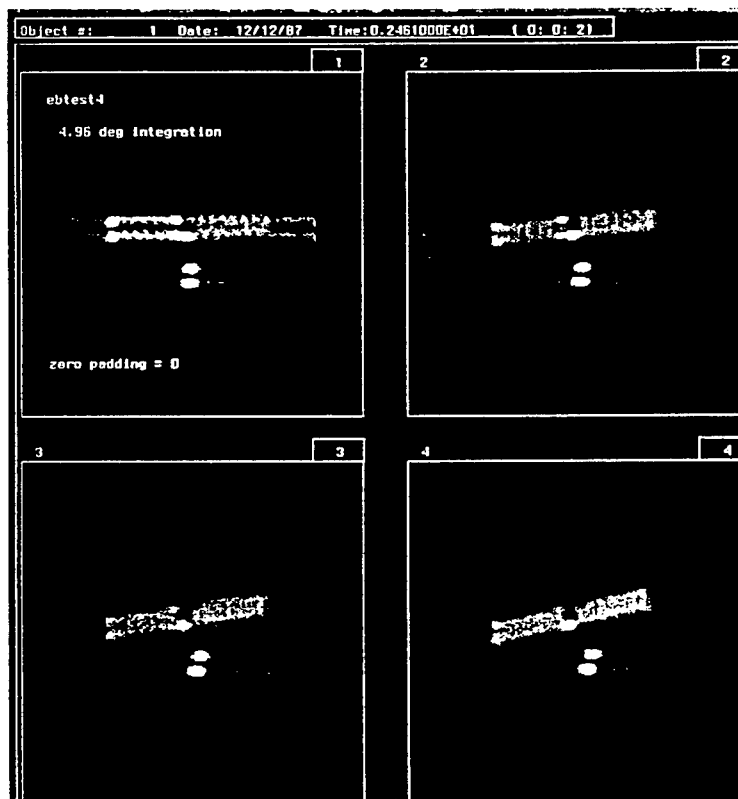


Figure 14

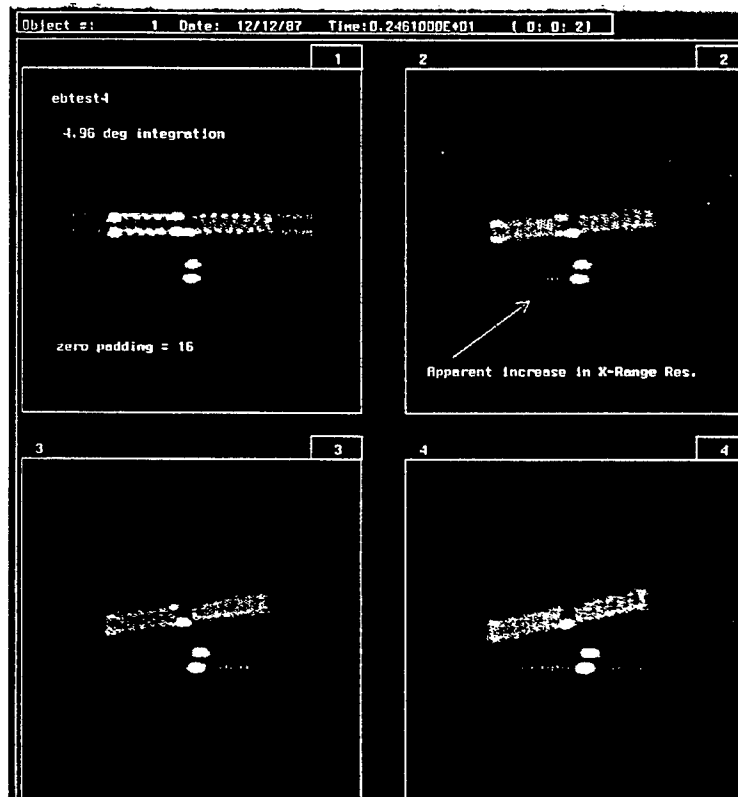


Figure 15

The variable 'bandwidth' controls the cross range resolution according to $\Delta r \cong \frac{c}{2B}$ where B is the bandwidth of the interrogating radar. Thus the bandwidth the user enters in the program `setupptdtable` must be used to compute the 'delta value for the range', Δr , in the program `setupimagnetbl`. According to LL personnel the variable `SRCSL` must be less than or equal to Δr . This suggests that it plays a role similar to the zero padding variable. For example, if $\Delta r = 0.1$ and we set `SRCSL = 0.05`, an appropriate number of zeroes are appended to the wideband return signal prior to the range FFT. Again, this cannot enhance the range resolution. It is only an interpolation process. However, recently developed Bandwidth Extrapolation techniques may be useful for enhancing the range resolution. Such techniques attempt to extrapolate unknown signal values (beyond the signal window) using various autoregression or maximum entropy methods. Figures 16 and 17 show the effect of setting `SRCL` less than the attainable range resolution. The image in Figure 16 was processed using `SRCSL = 0.146`, the range resolution for a 1024 MHz bandwidth. The image of Figure 17 was processed using `SRCSL = 0.1m`. The apparent increase in range resolution is clear.

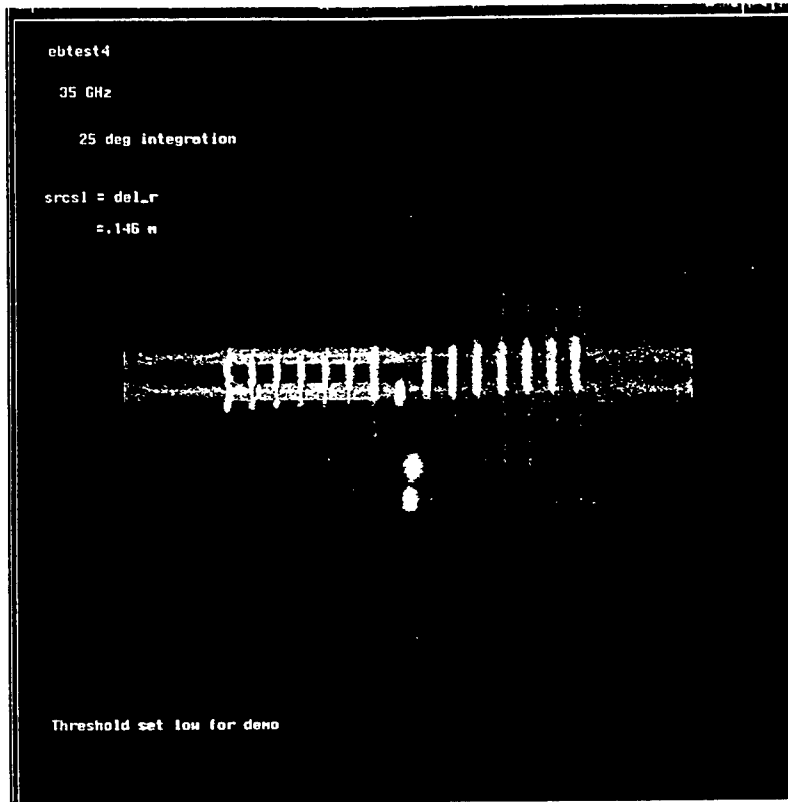


Figure 16

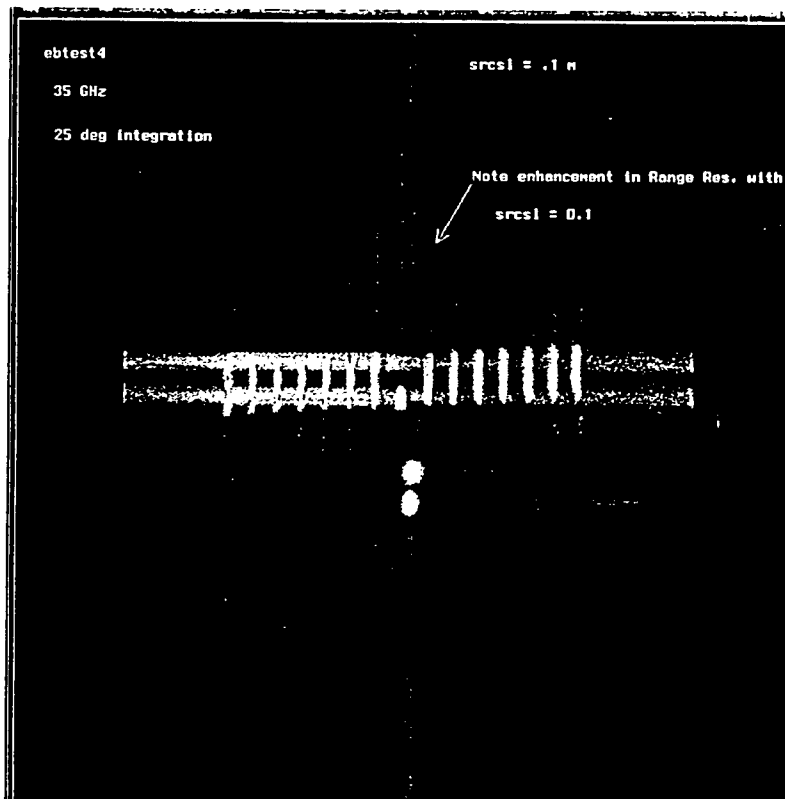


Figure 17

The variable 'center frequency', in the .setupptd file can have considerable effect on wideband imagery -- particularly the scattering regimes and the cross range resolution. ALCOR and HAYSTACK are X-Band systems (center frequency = 10 GHz) while MMW is a millimeter wave system (center frequency 35 GHz). Figures 18 and 19 indicate the difference between image quality at X-Band and MMW. Figure 14 gives the corresponding X-Band image, with an angle of integration of 4.96 degrees, and a processing increment, $\Delta\theta = 0.107$ degrees. Figure 18 is the result at a frequency of 35 GHz, an angle of integration of 1.96 degrees, and $\Delta\theta = 0.03$ degrees. The changes in θ and $\Delta\theta$ are necessary since both are a function of center frequency. Notice the increased resolution in the cross range dimension evidenced in the image of Figure 18 -- even at an integration angle of less than half the integration angle of the X-band image. Figure 19 shows the result of the millimeter wave center frequency with an angle of integration of 7.6 degrees (the program limit). Notice the improvement in the cross range resolution when compared with Figure 18. The expected range walk focusing error, while noticeable, may not be disagreeable -- especially with respect to the feature extraction and recognition process.

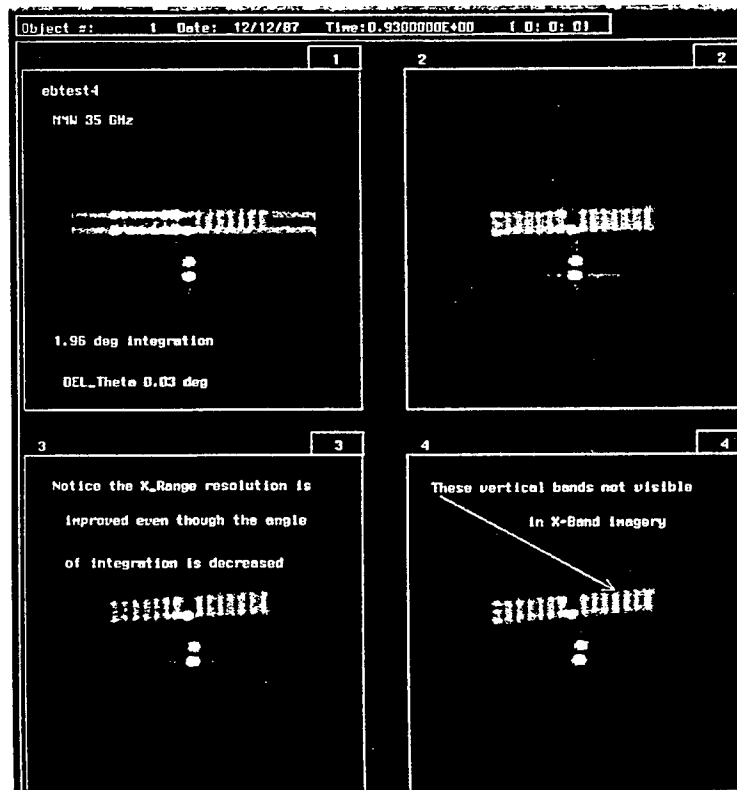


Figure 18

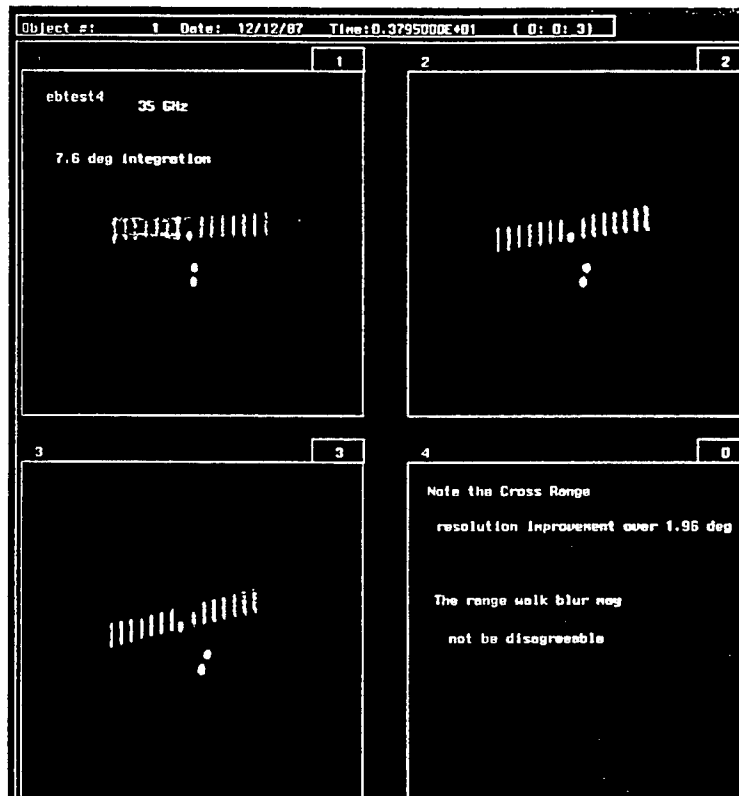


Figure 19

Finally, Figures 20 through 22 are included to demonstrate differences in image quality for several actual radar systems. The image of Figure 20 corresponds to an ALCOR (C-Band, 512 MHz bandwidth, optimal integration angle) simulation. Figure 21 shows the same object when interrogated by HAYSTACK (X-Band, 1024 MHz bandwidth, optimal integration angle). Figure 22 is a MMW (95 GHz, 1000 MHz bandwidth, optimal integration angle) version of the object. Notice the radical differences in resolution.

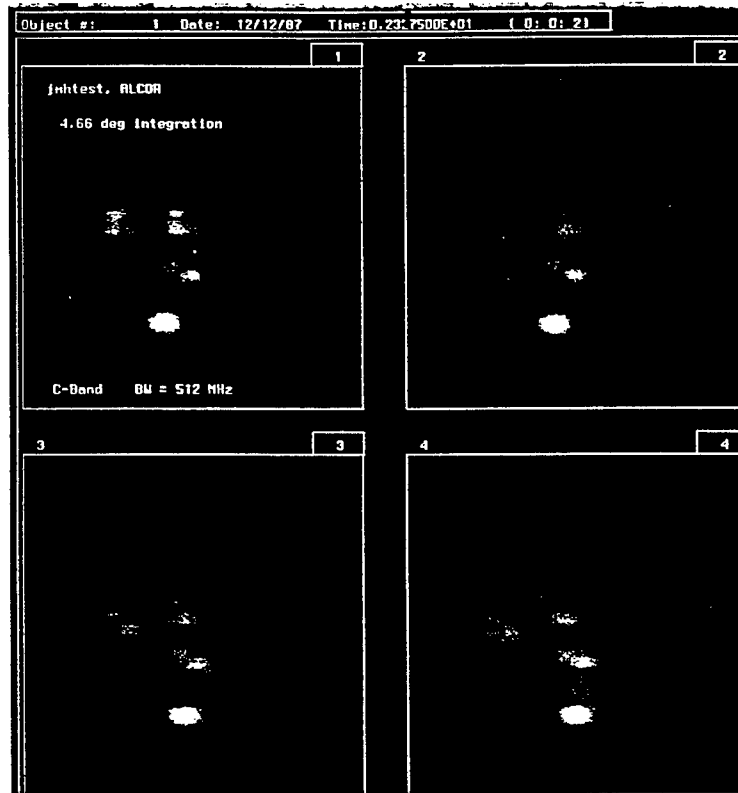


Figure 20

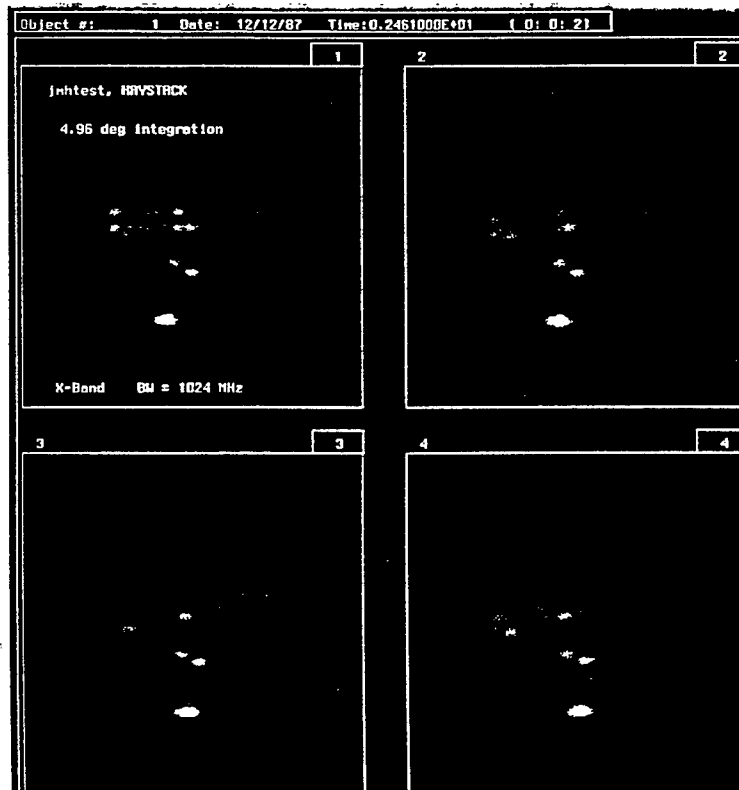


Figure 21

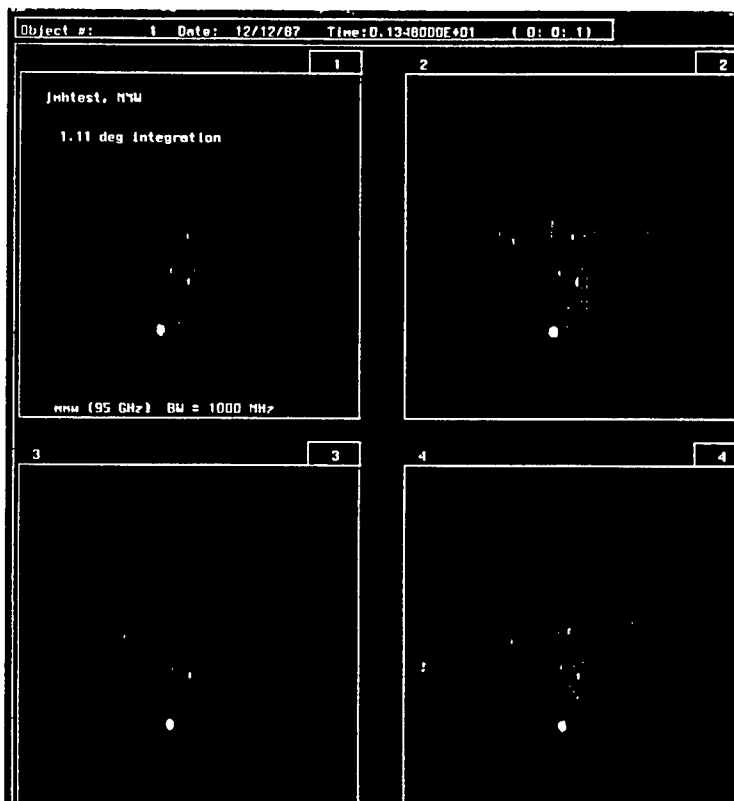


Figure 22

REVERSE-FLOW GAS GENERATOR STUDY FOR H₂/O₂ ROCKETS

DR. SAN-MOU JENG
ASSOCIATE PROFESSOR

AEROSPACE ENGINEERING AND ENGINEERING MECHANICS

UNIVERSITY OF CINCINNATI
MAIL LOCATION #70
309 RHODES HALL
CINCINNATI, OH 45221-0070

FINAL REPORT FOR:
SUMMER FACULTY RESEARCH PROGRAM
AIR FORCE PHILLIPS LABORATORY

SPONSORED BY:
AIR FORCE OFFICE OF SCIENTIFIC RESEARCH
BOILING AIR FORCE BASE, WASHINGTON, D.C.

SEPTEMBER, 1994

REVERSE-FLOW GAS GENERATOR STUDY FOR H₂/O₂ ROCKETS

DR. SAN-MOU JENG

ASSOCIATE PROFESSOR

AEROSPACE ENGINEERING AND ENGINEERING MECHANICS

ABSTRACT

A preliminary study, using the ALLSPD CFD code (developed by NASA Lewis Research Center), on a proposed reverse-flow gas generator for full-flow staged H₂/O₂ rocket engines was conducted. Two-dimensional CFD simulations at different operating conditions were investigated. The mixing quality between combustion products from the preburner, which is operated at O/F=64, and the pure hydrogen diluent, which has temperature of 300 °K, was summarized in this report. The computational results indicated that at least five recirculation bubbles exist in the gas generator, and the temperature and species distributions are nearly uniform at the gas generator outlet. The results also implied that the center body of this gas generator may be overheated. This study concluded that the three-dimensional CFD simulation is needed to provide a better design guidance for the on-going Air Force gas generator program.

REVERSE-FLOW GAS GENERATOR STUDY FOR H₂/O₂ ROCKETS

DR. SAN-MOU JENG

I. INTRODUCTION

The SSME main engine uses the fuel-rich combustion products to drive both fuel and oxidizer high pressure pumps. Recently, concept of using fuel-rich combustion products to drive the fuel pump and using oxidizer-rich combustion products to drive the oxidizer pump have been re-examined. This is not a new concept, both the United States and Russian have experience on these engine cycles.

Several advantages can be gained from this approach. The turbine of the proposed engine cycle will be operated at lower temperature and higher flow rate to drive the propellant pump. This would increase the turbopump life expectancy which also allows the larger throttling on the engine thrust. Also, sealing of the flow passage within the turbo-pump system can be easily handled and a small flow leakage within the system should not generate a catastrophic failure mode as in the current SSME main engine.

Air Force Phillips Laboratory is currently conducting an experimental study on a gas generator to provide the design information for future rockets. The considered gas generator consists of two major components: the first component (preburner) burns hydrogen and oxygen at near stoichiometric conditions; and

the second component (mixer) mixes the preburner combustion products with pure oxygen or hydrogen and generates the uniform, low temperature, oxygen rich or fuel rich combustion products for the turbo-pump system.

Two gas generators are required for each full-staged combustor. The gas generator for the fuel turbopump has a fuel-rich preburner and pure hydrogen diluent in the mixer. Similarly the gas generator to drive the oxidizer pump has an oxidizer-rich preburner and pure oxygen diluent in the mixer. The mixer of the considered gas generator at Air Force Phillips Laboratory is shown in figure 1. Hot gas from the preburner enters from the left entrance (either fuel rich or fuel lean combustion products) and mixes with cold hydrogen or oxygen issued from three individual injectors.

In this study, the evaluation of a CFD code, ALLSPD, to predict the flowfield of the hot gas generator is conducted. Under the AFOSR summer faculty fellowship program, the flowfield within the mixer, based on two-dimensional assumptions, has been successfully calculated. The predictions indicate that the considered gas generator can provide a uniform flow for the turbopump system. From the parametric study, the centerbody used in the gas generator may be overheated and may therefore require active wall cooling.

II. GOVERNING EQUATIONS

Although the ALLSPD CODE can perform the liquid spray combustion

analysis, the reported calculations are based on the assumptions that the propellant injection into the mixer is gaseous with the assigned temperature. The two-dimensional, unsteady, compressible, time averaged Navier-Stokes equations and species transport equation were used to solve the mixer flows. The low Reynolds number k-e turbulence model was considered. The chemical reaction was assumed frozen since very little chemical reaction may occur in the mixer.

Under above assumptions, the governing equations in generalized body-fitted coordinate can be expresses as

$$\frac{\partial \bar{Q}}{\partial \tau} + \frac{\partial (\bar{E} - \bar{E}_v)}{\partial \xi} + \frac{\partial (\bar{F} - \bar{F}_v)}{\partial \eta} = \bar{H}_c \quad (1)$$

where the vectors Q, E, F, E_v, F_v and H_c are defined as

$$\begin{aligned} \bar{Q} &= \frac{Y^\delta}{J} Q, \\ \bar{E} &= \frac{Y^\delta}{J} [\xi_\tau Q + \xi_x E + \xi_y F], \\ \bar{F} &= \frac{Y^\delta}{J} [\eta_\tau Q + \eta_x E + \eta_y F], \\ \bar{E}_v &= \frac{Y^\delta}{J} [\xi_x E_v + \xi_y F_v], \\ \bar{F}_v &= \frac{Y^\delta}{J} [\eta_x E_v + \eta_y F_v], \\ \bar{H}_c &= \frac{1}{J} H_c \end{aligned} \quad (2)$$

and $\tau, \xi,$ and η are the time and spatial distance in the generalized coordinate, J is the transformed Jacobian. When $\delta=0$ is two dimensional and $\delta=1$ is axisymmetric case. The vectors $Q, E, F,$

F_v and F_v in the equation 2 are

$$\begin{aligned}
 Q &= (\rho, \rho u, \rho v, \rho E, \rho \kappa, \rho \epsilon, \rho Y_1, \dots, \rho Y_{N-1})^T, \\
 E &= (\rho u, \rho u u + p, \rho u v, (\rho E + p) u, \rho u \kappa, \rho u \epsilon, \rho u Y_1, \dots, \rho u Y_{N-1})^T, \\
 F &= (\rho v, \rho u v, \rho v v + p, (\rho E + p) v, \rho v \kappa, \rho v \epsilon, \rho v Y_1, \dots, \rho v Y_{N-1})^T, \\
 E_v &= (0, \tau_{xx}, \tau_{xy}, u \tau_{xx} + v \tau_{xy} + Q_{xe}, \tau_{xx}, \tau_{xy}, Q_{x1}, \dots, Q_{x,N-1})^T, \\
 F_v &= (0, \tau_{xy}, \tau_{yy}, u \tau_{xy} + v \tau_{yy} + Q_{ye}, \tau_{yx}, \tau_{ye}, Q_{y1}, \dots, Q_{y,N-1})^T,
 \end{aligned} \quad (3)$$

and the source term vector, H_c , is

$$H_c = \begin{array}{c} 0 \\ -\frac{2}{3} \delta \frac{\partial [\mu_e v]}{\partial x} \\ \delta [p - \tau_{\theta\theta} - \frac{2}{3} \frac{\partial \mu_e v}{\partial y}] \\ -\frac{2}{3} \delta \left[\frac{\partial [\mu_e u v]}{\partial x} + \frac{\partial \mu_e v v}{\partial y} \right] \\ y^\delta [\psi - \rho \epsilon] - \frac{2}{3} \delta \mu_t v \left[\frac{\partial u}{\partial x} + \frac{\partial v}{\partial y} \right] \\ y^\delta \left[(c_1 f_1 \psi - c_2 f_2 \rho \kappa) \frac{\epsilon}{\kappa} + \Lambda \right] - \frac{2}{3} \delta \mu_t v \left[\frac{\partial u}{\partial x} + \frac{\partial v}{\partial y} \right] c_1 f_1 \frac{\epsilon}{\kappa} \\ y^\delta S_1 \\ \cdot \\ \cdot \\ y^\delta S_{N-1} \end{array} \quad (4)$$

III. NUMERICAL METHODS

The ALLSPD code used the compressible flow algorithm and is capable of solving the flowfield with any mach number. To circumvent the two well known numerical difficulties: roundoff error of the pressure gradient term in the momentum equations and the disparity of the system eigenvalues, the approach developed by Merkle and Chow (1), and Shuen et al. (2) was incorporated. A time preconditioning term was used to rescale the system eigenvalues while the pressure variable was decomposed into a constant

reference part and a gauge pressure part. The resulting Navier-Stokes equation in a conservative form are

$$\mathbf{T} \frac{\partial \overline{Q}^*}{\partial \tau^*} + \frac{\partial \overline{Q}}{\partial \tau} + \frac{\partial (\overline{E} - \overline{E}_v)}{\partial \xi} + \frac{\partial (\overline{F} - \overline{F}_v)}{\partial \eta} = \overline{H}_c, \quad (5)$$

where the primitive variable vector Q and Γ are given as

$$\overline{Q}^* = \frac{y^\delta}{J} \begin{bmatrix} p_g \\ u \\ v \\ h \\ \kappa \\ \epsilon \\ Y_1 \\ \cdot \\ \cdot \\ Y_{N-1} \end{bmatrix} \quad (6)$$

$$\mathbf{T} = \begin{bmatrix} \frac{1}{\beta} & 0 & 0 & 0 & 0 & 0 & \cdot & \cdot & \cdot & \cdot & 0 \\ \frac{u}{\beta} & \rho & 0 & 0 & 0 & 0 & \cdot & \cdot & \cdot & \cdot & 0 \\ \frac{v}{\beta} & 0 & \rho & 0 & 0 & 0 & \cdot & \cdot & \cdot & \cdot & 0 \\ \frac{h}{\beta} - 1 & \rho u & \rho v & \rho & 0 & 0 & \cdot & \cdot & \cdot & \cdot & 0 \\ \frac{\kappa}{\beta} & 0 & 0 & \cdot & \rho & 0 & \cdot & \cdot & \cdot & \cdot & 0 \\ \frac{\epsilon}{\beta} & 0 & 0 & \cdot & \cdot & \rho & 0 & \cdot & \cdot & \cdot & 0 \\ \frac{Y_1}{\beta} & 0 & 0 & \cdot & \cdot & \cdot & \rho & 0 & \cdot & \cdot & 0 \\ \cdot & \cdot & \cdot & \cdot & \cdot & \cdot & \cdot & \rho & \cdot & \cdot & 0 \\ \cdot & \cdot & \cdot & \cdot & \cdot & \cdot & \cdot & \cdot & \rho & \cdot & 0 \\ \cdot & \cdot & \cdot & \cdot & \cdot & \cdot & \cdot & \cdot & \cdot & \rho & 0 \\ \frac{Y_{N-1}}{\beta} & \cdot & \cdot & \cdot & \cdot & \cdot & \cdot & \cdot & \cdot & \cdot & \rho \end{bmatrix} \quad (7)$$

where τ^* is the pseudo-time, β is the parameter for rescaling the eigenvalues of the new system of equations. The definition of vectors in Eq. (5) is identical to those in Eq. (2) except that the pressure term in the momentum equations are replaced by the gauge pressure, p_g .

A dual-time stepping integration method was used to get time-accurate solutions. At each time-accurate physical time step, the solutions converge in the pseudo-time domain by iteration methods. Since the interest in this work is to provide the steady-state solutions, the physical time term in the equation can be dropped and the solution can be marched in the pseudo-time domain until convergence of the marching process is reached.

After linearization and applying a first order time differencing, the finite difference equation can be expressed in the following form:

$$\begin{aligned}
 & [T - \Delta\tau^* D + \Delta\tau^* \left(\frac{\partial A}{\partial \xi} - \frac{\partial}{\partial \xi} R_{\xi\xi} \frac{\partial}{\partial \xi} \right) + \Delta\tau^* \left(\frac{\partial B}{\partial \eta} - \frac{\partial}{\partial \eta} R_{\eta\eta} \frac{\partial}{\partial \eta} \right)]^p \Delta \bar{Q} = -\Delta\tau^* (R)^p \\
 & R^p = \frac{\partial(\bar{E} - \bar{E}_v)^p}{\partial \xi} + \frac{\partial(\bar{F} - \bar{F}_v)^p}{\partial \eta} - \bar{H}^p_c - \bar{H}^p_1
 \end{aligned} \tag{8}$$

where p denotes the previous iteration level, D is the Jacobian for chemical and turbulent source terms. A and B are the inviscid term Jacobians and $A_{\xi\xi}$ and $B_{\eta\eta}$ are the viscous term Jacobians. Central differencing was used to discretize all spatial variables in the above equations. The resulted algebraic equations are solved using

MSIP method proposed by Schneider and Zedan (3).

IV. TEST CONDITIONS

Figure 1 shows the preburner/mixer geometry similar to that considered at Air Force Phillips Laboratory. Detailed design of the preburner is not illustrated, which was originally designed for space station keeping purpose and has been extensively studied at NASA Lewis Research Center. In the current study the gas generator was assumed axisymmetric, and the considered geometry is shown in figure 2. The preburner was replaced by a straight cylinder at the left hand side of figure 2. It was assumed that the preburner produced complete combustion and provided the uniform flow coming into the left entrance of the considered gas generator.

The combustion at the preburner was assumed oxygen rich and the pure oxygen was injected into the mixer. Three injectors (ring injector for two-dimensional simulation) were aimed at the center of the mixing sphere. A backflow plate (splash plate), located near the exit of the mixing sphere, was also used to improve the flow mixing efficiency.

This study (two-dimensional simulation) considered that the preburner was operated at an O/F ratio of 64 and the combustion products entered the mixer with a uniform velocity. The combustion products were assumed thermodynamic equilibrium and were calculated by the NASA SP-273 computer program. The oxygen leaving the

injectors was assumed to be 300 K, with uniform velocity.

V.RESULTS AND DISCUSSION

Figure 2 shows the body-fitted grid system used in the computations. The figure also illustrates the isothermal contours after 200 iterations in pseudo-time.(about three thousand iterations to reach converged solution) The computational mesh consists of 34 by 169 nodes and clustered near the wall in order to resolve the turbulent boundary layer.

Figure 3 shows the velocity vectors, temperature contours and species contours of the considered test conditions. The temperature contours and species contours indicated that the mixer provides excellent mixing between hot and cold fluids as evident by the little temperature and species variations along the mixer exit. Enlarged views of the velocity vectors at four different locations are depicted in figure 4 while figure 5 shows the temperature contours at the same four locations. Two small recirculation zones exists near the oxygen injector which are due the finite thickness of the injector wall. The finite thickness of the splash plate also generates a recirculation bubble. The flow path from the preburner exit to the splash plate generally follows the mixer centerline. The majority of the fluid then bends and flows along the surface of the splash plate. This indicates that the mixing between the injector fluid and the preburner fluid near the centerline ahead of the splash plate may be slow. The hot fluid, which may have similar

temperature as the preburner combustion products, may impinge the center of the splash plate. Overheating of the plate may be a potential problem and active cooling on the splash plate is suggested.

The existence of the recirculation zones in the mixer provides fast mixing among the fluids. The impact of flow recirculation is illustrated in figure 6. The temperature, species concentration fraction and velocity variations along two vertical lines starting from leading and trailing edges of the splash plate are plotted. These two lines roughly corresponds the starting and ending positions of the recirculation zone generated from the finite thickness of the plate. The temperature variations (standard deviations) along these lines are excellent indicators of the mixing quality. Although the plate thickness is small compared to the mixer dimension, the derived recirculation zone improves the flow mixing significantly.

The three dimensional simulations on the gas generator was not attempted in this study, but efforts in generating the three-dimension grids was conducted. The computational mesh system was generated by the EAGLE VIEW software. It considered three fuel injectors (120° apart) as well as the three spacers holding the splash plate. Figure 6 show the generated mesh viewed from different angles. It is multi-block system and contains 300,000 grid points. The ALLSPD code with the generated grid system is

recommended for future study in order to predict the realistic gas generator performance.

VI. CONCLUSIONS

It has been demonstrated that the ALLSPD code can calculate the performance of the proposed gas generator, which has a very complicated geometry. Two-dimensional simulations have been conducted and the grid system for the three-dimensional gas generator have been generated. The computational results indicated the mixer can provide cold and uniform flow to drive the turbopump for the full- staged combustion system. The results also indicated that the splash plate thickness has significant impact on the mixing quality. The splash plate may be overheated and active wall cooling is suggested.

VII. SUGGESTED STUDY

In order to improve the performance of the proposed gas generator and to reduce the number of experimental tests during the developmental stage, a theoretical study with following emphasis is recommended:

1. Three dimensional simulations with various operating conditions (variable thrust, O/F ratio) to define the operating boundaries of the designed gas generator.
2. Perturbation study on the gas generator geometry to

maximize the gas generator performance and to guide the gas generator design for the full size rocket booster.

3. Evaluation of new gas generator (injectors, mixing augmentation,..) to explore opportunities for the best designed gas generator.

REFERENCES

1. C. L. Merkle and D. Choi, *AIAA J.* 3, 1518 (1985)
2. J Shuen, K. Chen and Y. Choi, *J. Comp. Phys.* 106. 306 (1993).
3. G. E. Schneider and M. Zedan, *Numer. Heat Transf.* 4. 10 (1981).

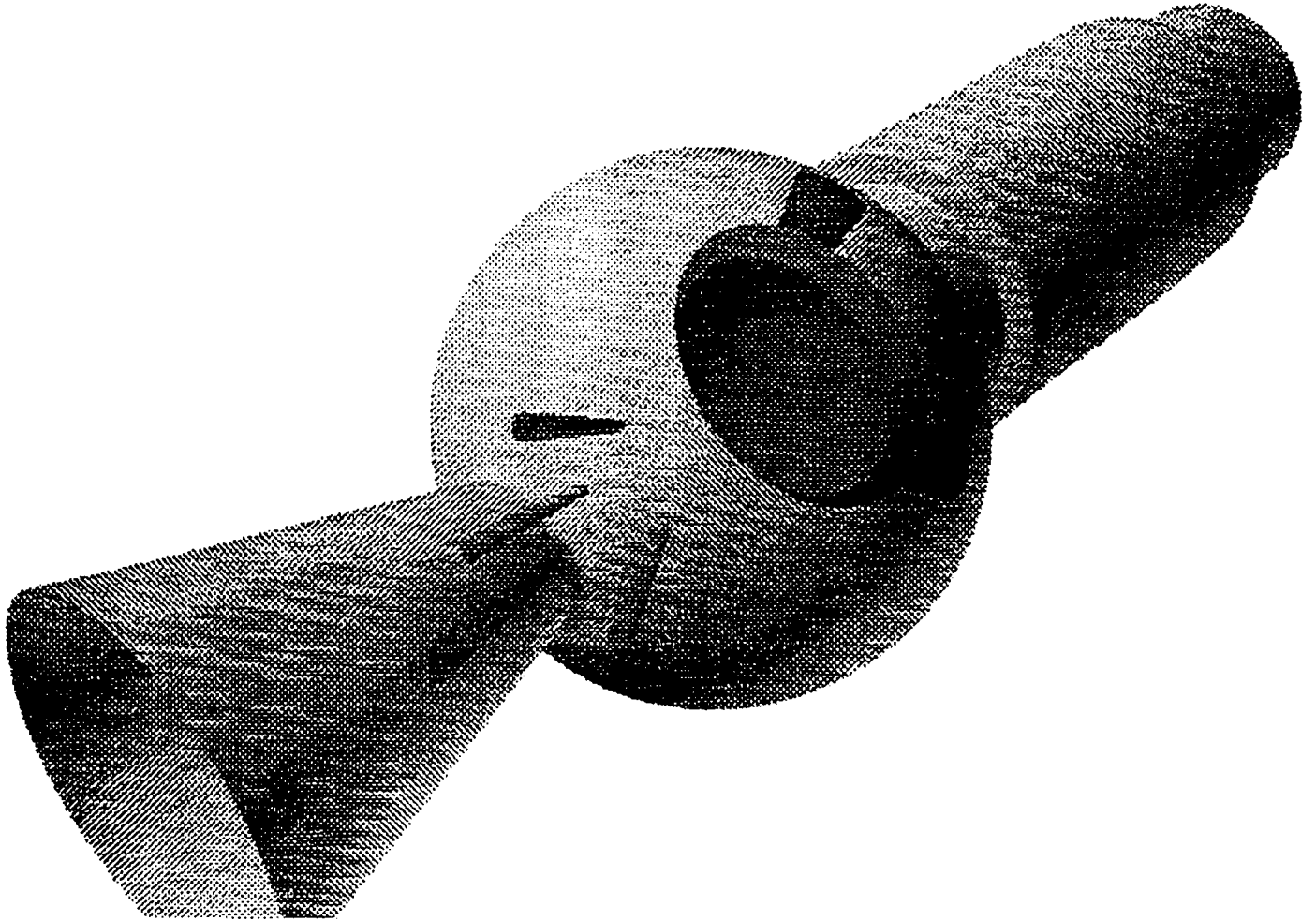


FIGURE 1. SKETCH OF A REVERSE FLOW GAS GENERATOR

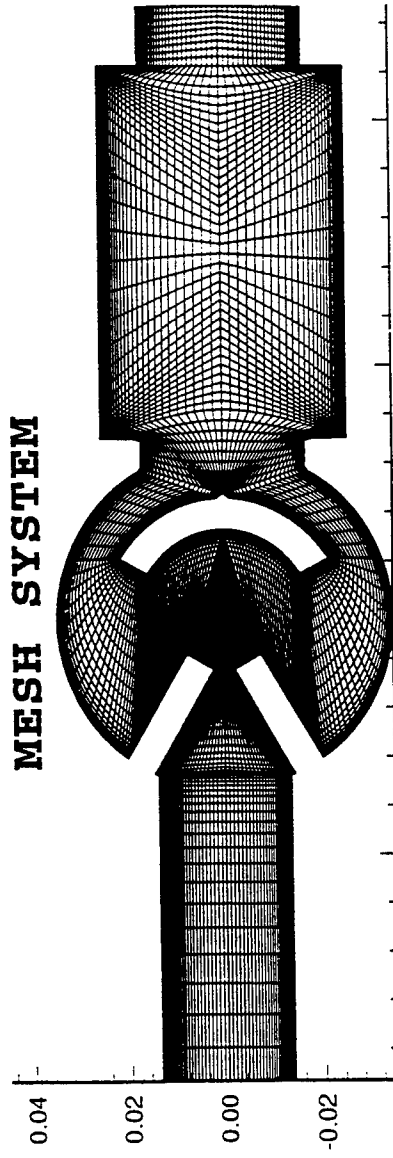
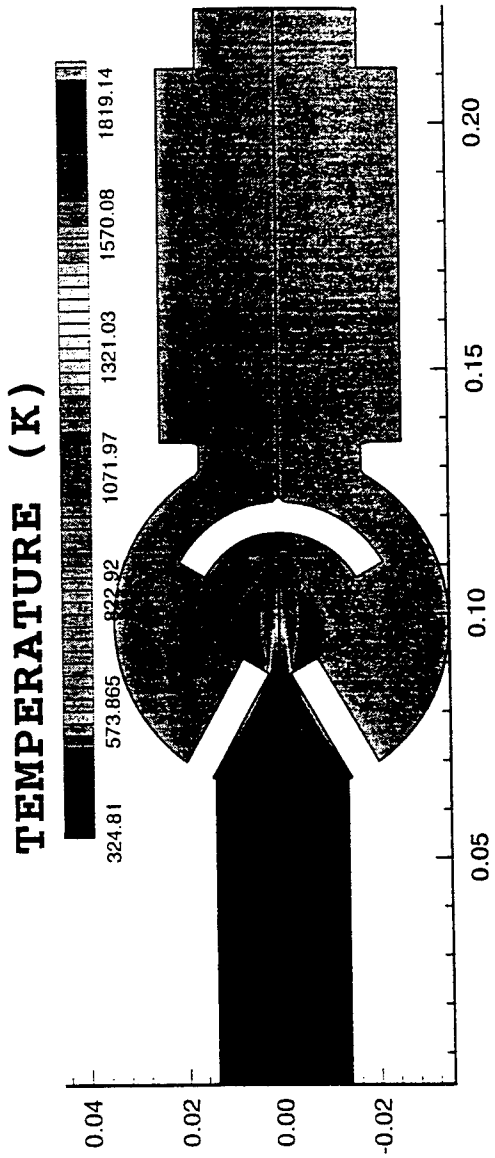


FIGURE 2. COMPUTATIONAL MESH SYSTEM AND THE TEMPERATURE DISTRIBUTION AT 200 ITERATIONS

REVERSE-FLOW GAS GENERATOR

-- MIXING BETWEEN HOT COMBUSTION PRODUCTS (O/F=64) AND PURE OXYGEN

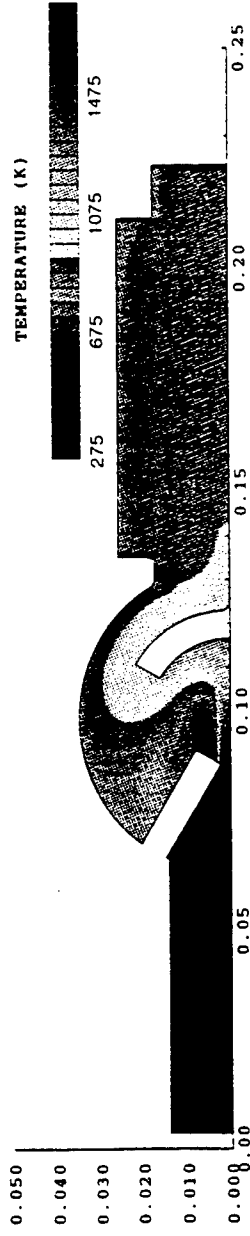
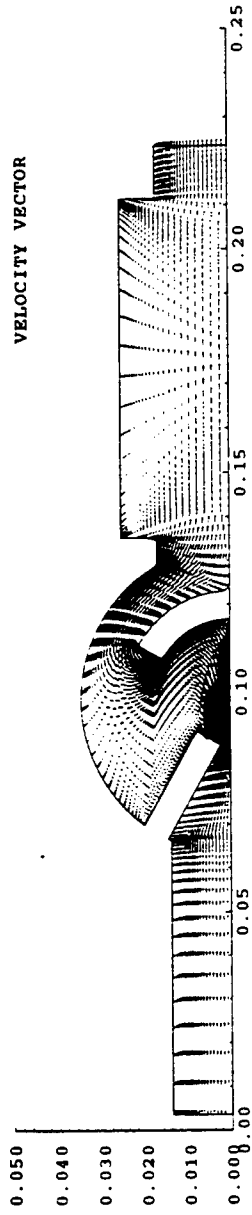
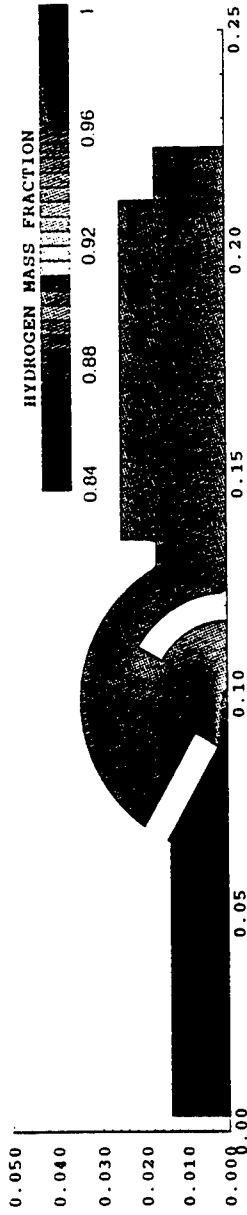


FIGURE 3. TEMPERATURE CONTOURS, VELOCITY VECTORS AND H₂ MASS FRACTION CONTOURS OF THE GENERATOR (O/F=64 PRODUCTS MIXED WITH PURE O₂)

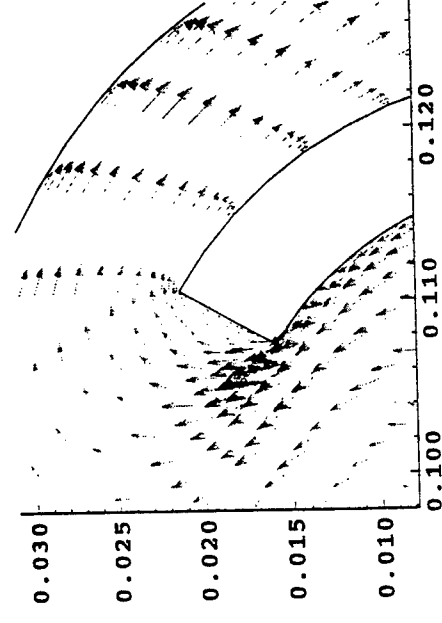
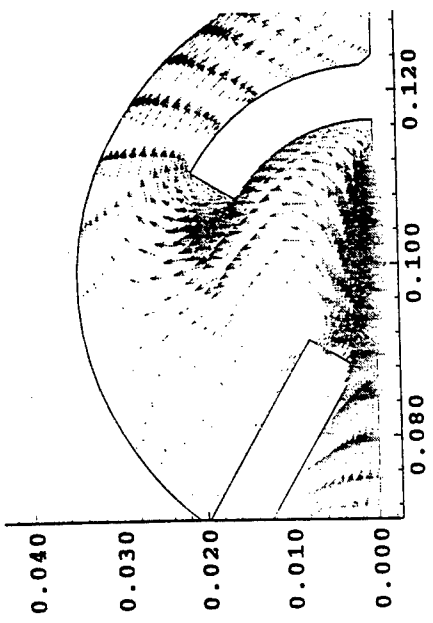
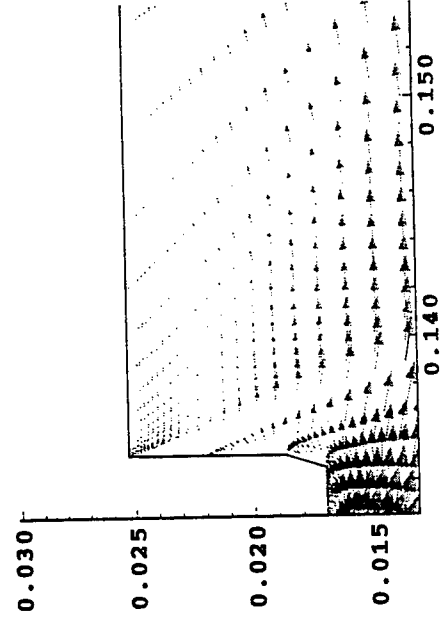
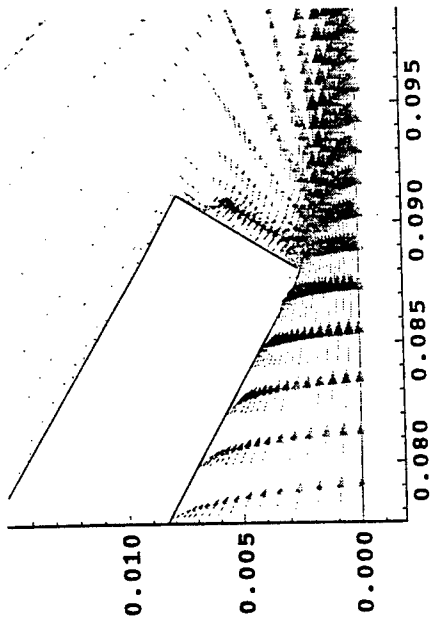


FIGURE 4. VELOCITY VECTORS AT FOUR DIFFERENT LOCATIONS

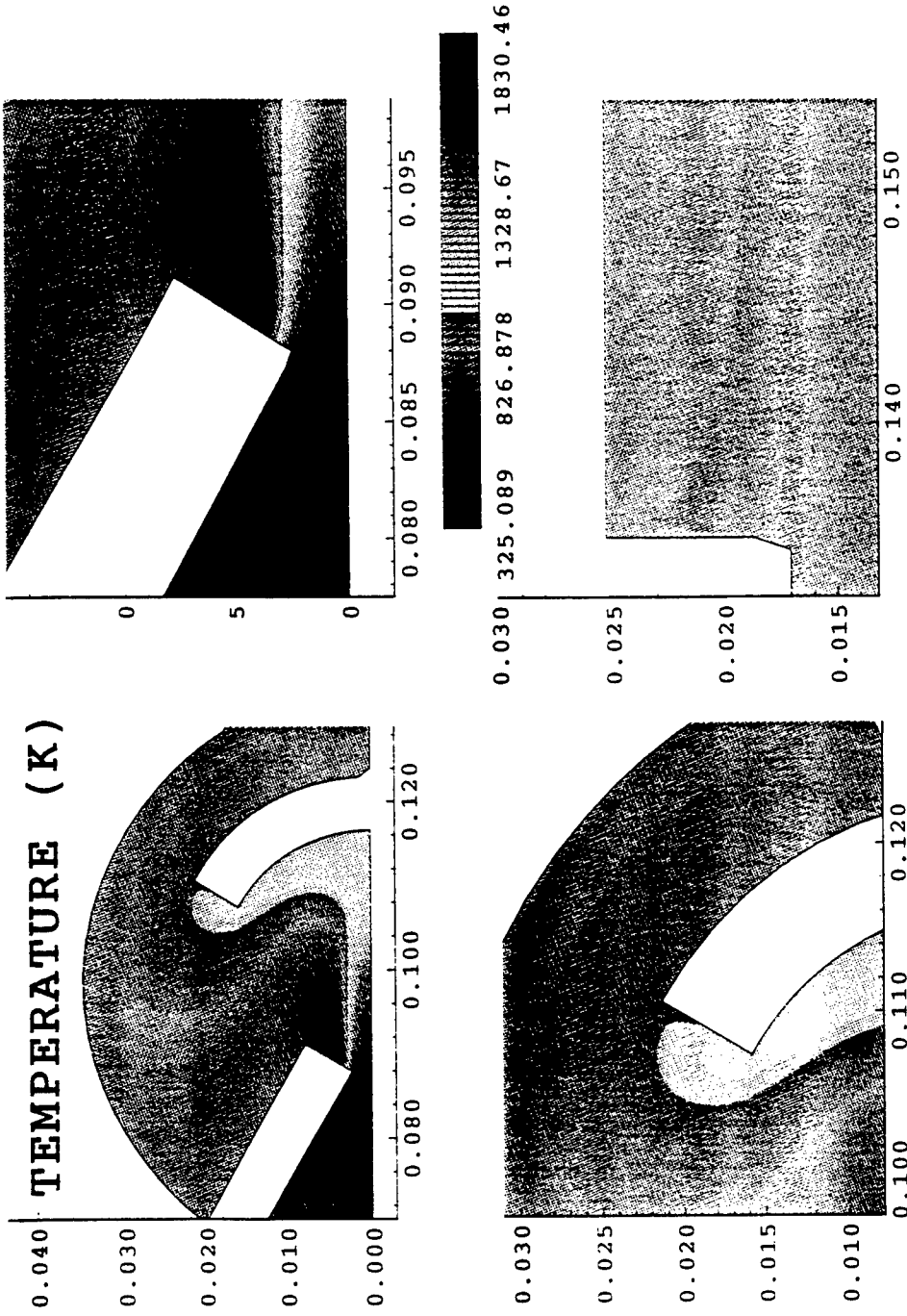


FIGURE 5. TEMPERATURE CONTOURS AT FOUR DIFFERENT LOCATIONS

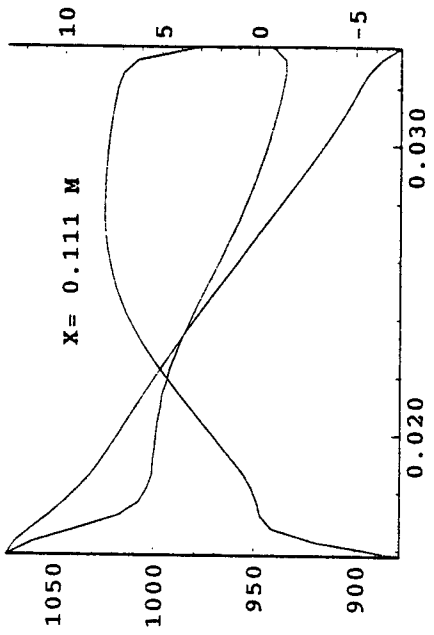
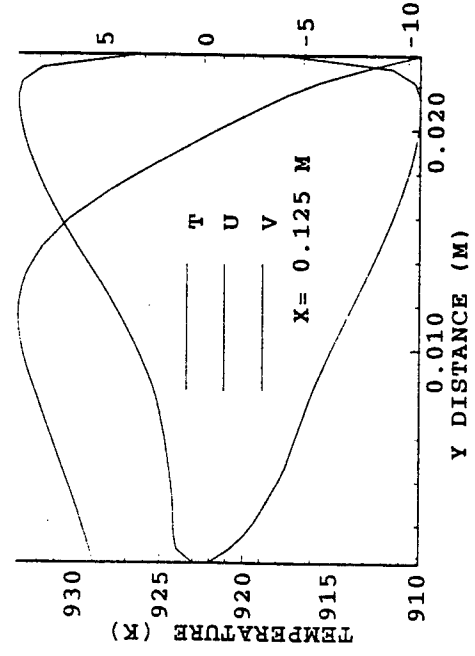
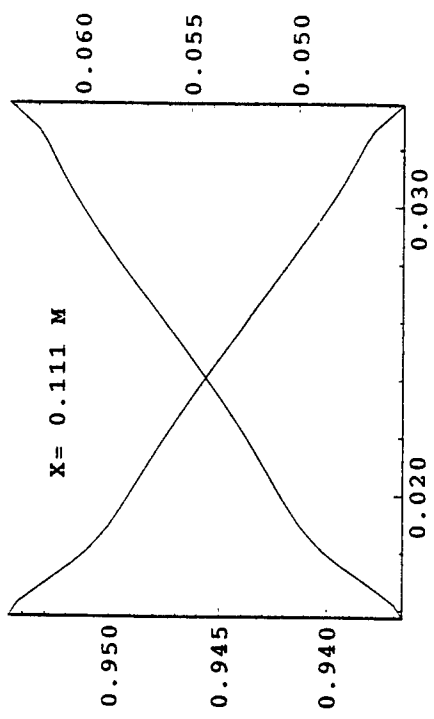
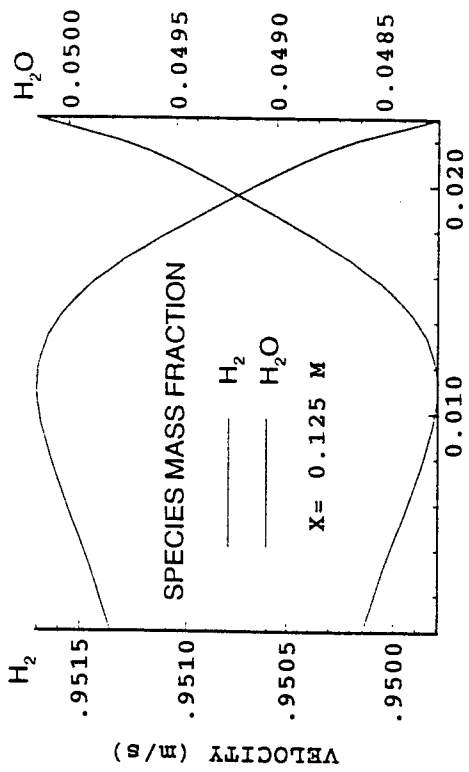
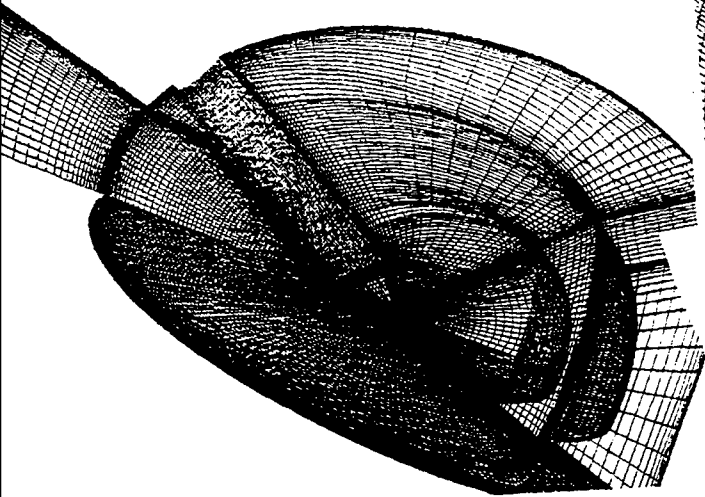
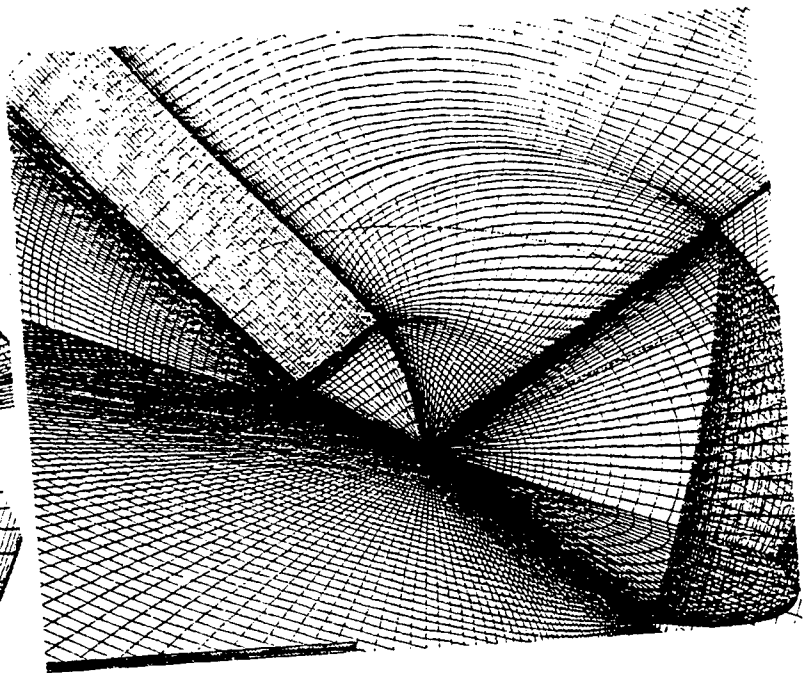


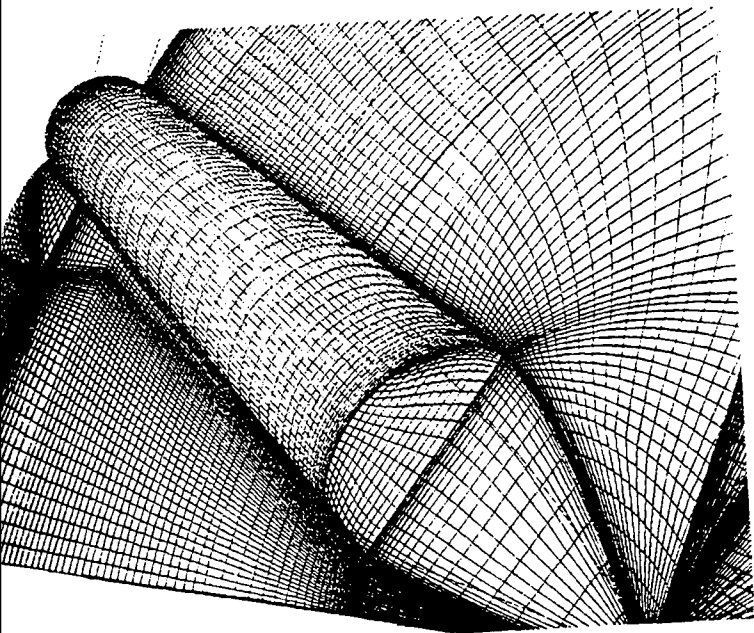
FIGURE 6. VELOCITIES, TEMPERATURE AND SPECIES MASS FRACTION VARIATIONS



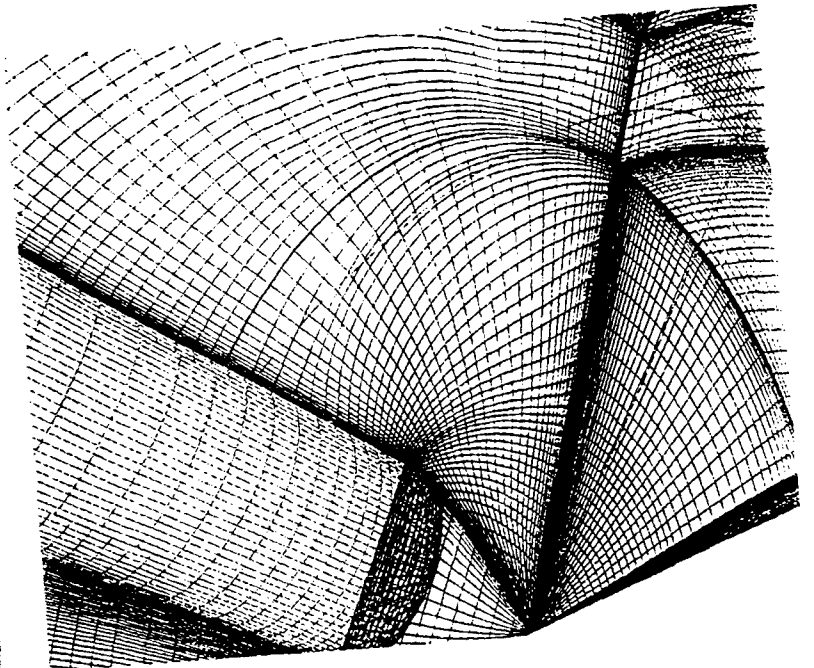
3D View # 1



3D View # 2



3D View # 3



3D View # 4

PHYSICAL WAVELETS FOR RADAR AND SONAR

Gerald Kaiser
Professor
Department of Mathematical Sciences

University of Massachusetts at Lowell
1 University Avenue
Lowell, MA 01854

Final Report for:
Summer Faculty Research Program
Phillips Laboratory
Hanscom Air Force Base, MA

Sponsored by:
Air Force Office of Scientific Research
Bolling Air Force Base, DC

August, 1994

PHYSICAL WAVELETS FOR RADAR AND SONAR

Gerald Kaiser
Professor

Department of Mathematical Sciences
University of Massachusetts at Lowell
Lowell, MA 01854
email: kaiserg@woods.uml.edu

Abstract

Physical wavelets are localized functions in space-time \mathbf{R}^4 which (a) behave like typical wavelets in the sense that they generate bases or frames by translations and dilations, and (b) satisfy certain physical differential equations. For example, electromagnetic wavelets satisfy Maxwell's equations and acoustic wavelets satisfy the scalar wave equation. A class of such wavelets was defined and studied in [3], where some applications to radar and scattering were also proposed. Here we extend the theory by showing that physical wavelets can be generated by any one-dimensional function $\phi(\tau)$ satisfying some mild conditions. This opens the possibility for implementing the theory developed here through efficient computational algorithms such as multiresolution analysis.

PHYSICAL WAVELETS FOR RADAR AND SONAR

Gerald Kaiser

1. General Physical Wavelets

Our construction of physical wavelets is based on the following generalization of the wavelet transform [2, 3]: Let $\phi(\tau)$ be a (possibly) complex-valued function of a real variable. Let $F(\mathbf{x}, t)$ be a function of space and time representing a physical field such as an acoustic or electromagnetic wave. (F may be real-valued, complex-valued or vector-valued, depending on the kind of physical field represented by F . For definiteness we suppose here that it is real-valued.) We use the compact notation $x \equiv (\mathbf{x}, t)$, $F(x) \equiv F(\mathbf{x}, t)$. Define a new function $F_\phi(x, y)$ of the *eight* real variables

$$x = (\mathbf{x}, t) \in \mathbf{R}^4, \quad y = (\mathbf{y}, s) \in \mathbf{R}^4, \quad \text{with } s > 0,$$

by

$$F_\phi(x, y) \equiv \int_{-\infty}^{\infty} d\tau \phi(\tau)^* F(x + \tau y) = \int_{-\infty}^{\infty} d\tau \phi(\tau)^* F(\mathbf{x} + \tau \mathbf{y}, t + \tau s), \quad (1)$$

where the asterisk denotes complex conjugation. One way to motivate this is to think of $\phi(\tau)^*$ as the "impulse response" of a small (point) instrument and of $F_\phi(x, y)$ as the result of measuring the field at \mathbf{x} at time t with this instrument while moving along the straight line in space-time parameterized by

$$x(\tau) = x + \tau y, \quad \text{i.e.,} \quad \begin{cases} \mathbf{x}(\tau) = \mathbf{x} + \tau \mathbf{y} \\ t(\tau) = t + \tau s. \end{cases}$$

The significance of s is that it is a *scale parameter*. For example, if $\phi(\tau)$ vanishes outside the interval $0 \leq \tau \leq T$ and $\int d\tau \phi(\tau) = 1$, then $F_\phi(x, y)$ is a weighted average of F over the time interval $t \leq \tau \leq t + sT$. The significance of \mathbf{y} is that the velocity of the instrument is

$$\mathbf{v} = \frac{d\mathbf{x}(\tau)}{dt(\tau)} = \frac{\mathbf{y}}{s}. \quad (2)$$

The mapping $F(x) \rightarrow F_\phi(x, y)$ will be interpreted as a wavelet transform with respect to a family of wavelets $\Phi_{x,y}(x')$ defined on space-time. In that context, s will be reinterpreted as the *duration* of the wavelet, and \mathbf{v} as its *center velocity*. To see that F_ϕ is a generalization of the usual one-dimensional wavelet transform, note that the change of variables $u \equiv t + \tau s$ gives

$$F_\phi(x, y) = \int_{-\infty}^{\infty} du s^{-1} \phi\left(\frac{u-t}{s}\right)^* F(\mathbf{x} + (u-t)\mathbf{v}, u), \quad (3)$$

where we have used (2). If $\mathbf{v} = 0$, this is indeed just a (continuous) wavelet transform of $F(\mathbf{x}, t)$ in the time variable, with $\phi(\tau)$ as the basic wavelet.

Now let us specialize to the case where $F(x)$ represents an acoustic wave, i.e., a solution of the homogeneous wave equation

$$(c^2 \nabla^2 - \partial_t^2) F(\mathbf{x}, t) = 0, \quad (4)$$

where c is the propagation speed. If the instrument moves with a speed less than that of sound, (2) implies

$$|\mathbf{y}| < cs, \quad (5)$$

hence y belongs to the *future sound cone* in space-time, which we denote by V'_+ :

$$V'_+ = \{y = (\mathbf{y}, s) \in \mathbf{R}^4 : |\mathbf{y}| < cs\}.$$

(In the electromagnetic case, F and f are vector-valued and (5) necessarily holds, where c now stands for the speed of light.) Since we allow, in principle, all initial positions and times $x = (\mathbf{x}, t) \in \mathbf{R}^4$ and all vectors $y = (\mathbf{y}, s) \in V'_+$, $F_\phi(x, y)$ is defined on the set

$$\mathcal{T}_+ \equiv \{(x, y) \in \mathbf{R}^8 : x \in \mathbf{R}^4, y \in V'_+\},$$

called the *future tube*. The eight parameters in \mathcal{T}_+ give the position, time, velocity, and scale associated with the measurement. Thus \mathcal{T}_+ plays the role of an extended *phase space*.

A general solution can be written as a superposition of plane waves with spatial wave vector $\mathbf{p} \in \mathbf{R}^3$ and frequency $\omega = \pm c|\mathbf{p}|$, as required by the wave equation. $F(x)$ can be written as the real part of a complex-valued solution, which we denote by the same symbol:

$$F(\mathbf{x}, t) = (2\pi)^{-3} \int_{\mathbf{R}^3} d^3\mathbf{p} e^{i\omega t - i\mathbf{p}\cdot\mathbf{x}} f(\mathbf{p}), \quad \omega \equiv c|\mathbf{p}|. \quad (6)$$

It is convenient to write

$$p \cdot x \equiv \omega t - \mathbf{p} \cdot \mathbf{x} \quad (7)$$

for the the (indefinite) Lorentzian inner product of the four-vectors $p \equiv (\mathbf{p}, \omega)$ and $x \equiv (\mathbf{x}, t)$, so that (6) can be written in the compact form

$$F(x) = (2\pi)^{-3} \int_{\mathbf{R}^3} d^3\mathbf{p} e^{ip \cdot x} f(\mathbf{p}). \quad (8)$$

To construct the wavelets, we need a *Hilbert space* of solutions. Therefore define the *norm* $\|F\|$ of F by

$$\|F\|^2 \equiv (2\pi)^{-3} \int_{\mathbf{R}^3} \frac{d^3\mathbf{p}}{\omega^{a-2}} |f(\mathbf{p})|^2, \quad (9)$$

where a is an as yet arbitrary real parameter. (The usual energy corresponds to $a = 2$, but we will find it necessary to require $a > 2$.) The set of all solutions of the form (8) with finite norm will be called \mathcal{H}_a :

$$\mathcal{H}_a \equiv \{F(x) : \|F\|^2 < \infty\}. \quad (10)$$

\mathcal{H}_a is a Hilbert space under the inner product corresponding to the norm (9), i.e.,

$$\langle G, F \rangle \equiv (2\pi)^{-3} \int_{\mathbf{R}^3} \frac{d^3\mathbf{p}}{\omega^{a-2}} g(\mathbf{p})^* f(\mathbf{p}). \quad (11)$$

Combining (1) with (8) and denoting the Fourier transform of $\phi(\tau)$ by $\hat{\phi}(\xi)$, we obtain

$$\begin{aligned} F_\phi(x, y) &\equiv \int_{-\infty}^{\infty} d\tau \phi(\tau)^* F(x + \tau y) \\ &= (2\pi)^{-3} \int_{-\infty}^{\infty} d\tau \phi(\tau)^* \int_{\mathbf{R}^3} d^3\mathbf{p} e^{ip \cdot (x + \tau y)} f(\mathbf{p}) \\ &= (2\pi)^{-3} \int_{\mathbf{R}^3} d^3\mathbf{p} e^{ip \cdot x} f(\mathbf{p}) \int_{-\infty}^{\infty} d\tau e^{i\tau p \cdot y} \phi(\tau)^* \\ &= (2\pi)^{-3} \int_{\mathbf{R}^3} d^3\mathbf{p} e^{ip \cdot x} \hat{\phi}(p \cdot y)^* f(\mathbf{p}) \\ &= (2\pi)^{-3} \int_{\mathbf{R}^3} \frac{d^3\mathbf{p}}{\omega^{a-2}} e^{ip \cdot x} \omega^{a-2} \hat{\phi}(p \cdot y)^* f(\mathbf{p}) \\ &= \langle \Phi_{x, y}, F \rangle, \end{aligned} \quad (12)$$

where the solution $\Phi_{x,y}(x')$ is defined in the Fourier domain by the coefficient function

$$\phi_{x,y}(\mathbf{p}) \equiv e^{-i\mathbf{p}\cdot\mathbf{x}} \omega^{a-2} \hat{\phi}(\mathbf{p}\cdot\mathbf{y}). \quad (13)$$

Thus in the space-time domain $\Phi_{x,y}$ is given by

$$\begin{aligned} \Phi_{x,y}(x') &\equiv (2\pi)^{-3} \int_{\mathbf{R}^3} d^3\mathbf{p} e^{i\mathbf{p}\cdot\mathbf{x}'} \phi_{x,y}(\mathbf{p}) \\ &= (2\pi)^{-3} \int_{\mathbf{R}^3} d^3\mathbf{p} e^{i\mathbf{p}\cdot(\mathbf{x}'-\mathbf{x})} \omega^{a-2} \hat{\phi}(\mathbf{p}\cdot\mathbf{y}) \\ &= (2\pi)^{-3} \int_{\mathbf{R}^3} d^3\mathbf{p} e^{i\mathbf{p}\cdot(\mathbf{x}'-\mathbf{x})} \omega^{a-2} \int_{-\infty}^{\infty} d\tau e^{-i\tau\mathbf{p}\cdot\mathbf{y}} \phi(\tau) \\ &= \int_{-\infty}^{\infty} d\tau \phi(\tau) K(x' - x - \tau\mathbf{y}), \end{aligned} \quad (14)$$

where $K(x)$ is the (generalized) function

$$K(x) \equiv (2\pi)^{-3} \int_{\mathbf{R}^3} d^3\mathbf{p} e^{i\mathbf{p}\cdot\mathbf{x}} \omega^{a-2}. \quad (15)$$

The solutions $\Phi_{x,y}(x')$ are, by definition, the *acoustic wavelets* generated by $\phi(\tau)$. The last equality in (12) shows that $F_{\phi}(x, y)$ can be interpreted as the wavelet transform with respect to these wavelets.

Although the wavelets $\Phi_{x,y}$ depend on the choice of ϕ , there is a “canonical” choice which determines all others in the same way that a Green function determines all solutions subject to a given set of boundary conditions. The canonical ϕ which governs *all* the wavelets $\Phi_{x,y}$ is the *Cauchy kernel* $\kappa(\tau)$, defined by

$$\kappa(\tau)^* \equiv \frac{1}{2\pi i(\tau - i)} = \frac{1}{2\pi(1 + i\tau)}. \quad (16)$$

Then a contour integration gives

$$\hat{\kappa}(\xi) = -\frac{1}{2\pi i} \int_{-\infty}^{\infty} \frac{d\tau}{\tau + i} e^{-i\xi\tau} = \begin{cases} e^{-\xi} & \text{if } \xi > 0 \\ 0 & \text{if } \xi < 0 \end{cases} = \theta(\xi)e^{-\xi}, \quad (17)$$

where $\theta(\xi)$ is the unit step function. The physical wavelets generated by $\kappa(\tau)$ will be called *Cauchy wavelets*. By (14), they are given by

$$K_{x,y}(x') = (2\pi)^{-3} \int_{\mathbf{R}^3} d^3\mathbf{p} \theta(\mathbf{p}\cdot\mathbf{y}) e^{i\mathbf{p}\cdot(\mathbf{x}'-\mathbf{x}+i\mathbf{y})} \omega^{a-2}. \quad (18)$$

We claim that the right-hand side is an *analytic function* of $x' - x + iy$, as long as y belongs to the future cone V'_+ . To see this, note that by Schwarz's inequality,

$$\mathbf{p}\cdot\mathbf{y} = \omega s - \mathbf{p}\cdot\mathbf{y} \geq |\mathbf{p}|(cs - |\mathbf{y}|) > 0$$

for all $\mathbf{p} \neq \mathbf{0}$. Hence $\theta(\mathbf{p}\cdot\mathbf{y}) \equiv 1$ identically. Furthermore, the exponential factor $e^{-\mathbf{p}\cdot\mathbf{y}}$ decays rapidly in all directions in \mathbf{p} (though least rapidly when \mathbf{p} is parallel to \mathbf{y}), and this results in analyticity of the integral. Therefore, comparing with (15), we have

$$K_{x,y}(x') = (2\pi)^{-3} \int_{\mathbf{R}^3} d^3\mathbf{p} e^{i\mathbf{p}\cdot(\mathbf{x}'-\mathbf{x}+i\mathbf{y})} \omega^{a-2} = K(x' - x + iy), \quad (19)$$

where $K(z)$ is the *analytic continuation* of $K(x)$ to the complex space-time domain $\{z = x + iy : x \in \mathbf{R}^4, y \in V_+^t\}$, which is just the future tube \mathcal{T}_+ , now regarded as a domain in \mathbf{C}^4 . (The above argument proves that $K(z)$ is analytic in $z \in \mathcal{T}_+$.) Therefore it suffices to compute $K(iy)$ and then find $K_{x,y}(x')$ by analytic continuation. We find

$$K(iy) = \frac{\Gamma(a)}{4\pi^2 c^2 |y|} \left[\frac{1}{(s - |y|/c)^a} - \frac{1}{(s + |y|/c)^a} \right], \quad y \neq 0, \quad (20)$$

and the case $y = 0$ is obtained by taking the limit. To find $K_{x,y}(x')$ we must, according to (18), substitute $y \rightarrow y - i(x' - x)$. Thus

$$s \rightarrow s - i\tau \text{ and } |y| \equiv \sqrt{y^2} \rightarrow \sqrt{(y - i\mathbf{r})^2}, \quad \text{where } \tau \equiv t' - t, \quad \mathbf{r} \equiv \mathbf{x}' - \mathbf{x}. \quad (21)$$

The simplest expression is obtained when $y = 0$. Then $|y| \rightarrow -i|\mathbf{r}| \equiv -i\mathbf{r}$, so

$$K_{x,y}(x') = \frac{\Gamma(a)}{4\pi^2 c^2 i\mathbf{r}} \left[\frac{1}{(s - i\tau - i\mathbf{r}/c)^a} - \frac{1}{(s - i\tau + i\mathbf{r}/c)^a} \right], \quad y = 0. \quad (22)$$

Thus $K_{x,y}$ splits up naturally as

$$K_{x,y}(x') = K_{x,y}^-(x') + K_{x,y}^+(x'), \quad (23)$$

where

$$K_{x,y}^\pm(x') = \pm \frac{i\Gamma(a)}{4\pi^2 c^2 \mathbf{r}} \frac{1}{(s - i\tau \pm i\mathbf{r}/c)^a}. \quad (24)$$

- $K_{x,y}^-(x')$ is a *converging wavelet absorbed* at $x' = x$
- $K_{x,y}^+(x')$ is a *diverging wavelet emitted* at $x' = x$.

These partial wavelets no longer satisfy the homogeneous wave equation. Instead, they satisfy the *inhomogeneous* wave equations

$$(c^2 \nabla_{\mathbf{x}'}^2 - \partial_{t'}^2) K_{x,y}^\pm(x') = \pm \frac{c^{-2} \Gamma(a)}{i\pi (s - i\tau)^a} \delta(\mathbf{r}) = \pm \kappa_{s,t}^a(t') \delta(\mathbf{x}' - \mathbf{x}), \quad (25)$$

where

$$\begin{aligned} \kappa_{s,t}^a(t') &\equiv \frac{c^{-2} \Gamma(a)}{i\pi (s - i\tau)^a} = s^{-a} \kappa^a \left(\frac{t' - t}{s} \right), \\ \kappa^a(\tau) &\equiv \frac{c^{-2} \Gamma(a)}{i\pi (1 - i\tau)^a} = \frac{c^{-2}}{i\pi} \int_0^\infty d\xi \xi^{a-1} e^{-\xi(1-i\tau)}. \end{aligned} \quad (26)$$

Therefore

$$\hat{\kappa}^a(\xi) = -2ic^{-2} \theta(\xi) \xi^{a-1} e^{-\xi} = -2ic^{-2} \xi^{a-1} \hat{\kappa}(\xi). \quad (27)$$

The Cauchy kernel $\kappa(\tau)$ generates a canonical family of time wavelets $\kappa_{s,t}^a(t')$. When $\kappa_{s,t}^a(t')$ is used as a stationary source localized at $\mathbf{x} \in \mathbf{R}^3$ and centered at time t , the resulting acoustic wave is the Cauchy wavelet $K_{x,y}^+(x')$ with $x = (\mathbf{x}, t)$ and $y = (0, s)$. Similarly, $-\kappa_{s,t}^a(t')$ acts as a sink for $K_{x,y}^-(x')$.

It can be shown [3] that if $a > 2$, then the $K_{x,y}$'s with $y = 0$ and $t = \text{constant}$ are complete in \mathcal{H}_a

and the $\kappa_{s,t}^a$'s are complete in $L^2(\mathbf{R})$. That is, every solution $F(x)$ can be written as a superposition of $K_{x,y}$'s and every finite-energy time signal $g(t)$ can be written as a superposition of $\kappa_{s,t}^a$'s. Thus (25) induces, by linearity, a fundamental connection between *general* time signals and the physical waves they generate.

As promised, the scale parameter s can now be interpreted as measuring the *duration* of the pulses $K_{x,y}^\pm(x')$. Cauchy wavelets with $\mathbf{y} \neq 0$ are similarly interpreted as being associated with a source or sink moving with velocity $\mathbf{v} = \mathbf{y}/s$. This means that rather than having *concentric* spherical wave fronts (corresponding to a stationary source), the centers of their wave fronts move with velocity \mathbf{v} . They are, therefore, *Doppler-shifted versions* of the stationary wavelets. This feature makes the physical wavelets particularly attractive for sonar and radar applications.

What about wavelets generated by ϕ other than the Cauchy kernel? By (14), they can be obtained from the Cauchy wavelets by a limiting process

$$\Phi_{x,y}(x') = \lim_{y' \rightarrow 0} \int_{-\infty}^{\infty} d\tau \phi(\tau) K(x' + iy' - x - \tau y), \quad (28)$$

where $y' \rightarrow 0$ in V_+^+ . The splitting $K(z) = K^-(z) + K^+(z)$ therefore induces a splitting

$$\Phi_{x,y}(x') = \Phi_{x,y}^-(x') + \Phi_{x,y}^+(x'), \quad (29)$$

and $\Phi_{x,y}^\pm(x')$ have a similar interpretation as absorbed and emitted wavelets. Again, $(x, y) \in \mathcal{T}_+$ are interpreted as extended phase-space parameters associated with the source or sink function for $\Phi_{x,y}^\pm(x')$.

2. Applications to Radar and Sonar

The Cauchy wavelets $K_{x,y}^\pm(x')$ are "elementary" acoustic waves. Aside from the fact that they act as "bases" or building blocks for general acoustic waves, this means that they have a particularly simple behavior under scattering, in particular under reflections. This simple behavior is based on the transformation properties of the wavelets under the 15-dimensional *conformal group* of space-time [3]. The more general wavelets $\Phi_{x,y}^\pm(x')$ can be expected to have similar reflection properties, provided their generating function ϕ is sufficiently reasonable. This is one of the topics I hope to explore in the near future.

3. Multiresolution Analysis using Physical Wavelets

A possible advantage of the more general physical wavelets $\Phi_{x,y}$ over the Cauchy wavelets $K_{x,y}$ is that by choosing the generator $\phi(t)$ to be the scaling function associated with a multiresolution analysis [1, 3], it may be possible to induce a space-time multiresolution analysis based on the physical wavelets $\Phi_{x,y}$. This would give fast algorithms for space-time wavelet analyses in acoustics and electromagnetics, possibly resulting in real-time codes for radar and sonar applications. Such applications are currently under investigation.

References

- [1] I Daubechies, *Ten Lectures on Wavelets*, SIAM, Philadelphia, 1992.
- [2] G Kaiser and RF Streater, Windowed Radon transforms, analytic signals, and the wave equation, in *Wavelets: A Tutorial in Theory and Applications*, CK Chui, ed., Academic Press, New York, 1992.
- [3] G Kaiser, *A Friendly Guide to Wavelets*, Birkhäuser-Boston, 1994.

BACKSCATTER FROM A PLASMA PLUME DUE TO
EXCITATION OF SURFACE WAVES

Dikshitulu K. Kalluri
Professor
Department of Electrical Engineering

University of Massachusetts Lowell
Lowell, MA 01854

Final Report for:
Summer Faculty Research Program
Philips Laboratory / Geophysics Directorate

Sponsored by:
Air Force Office of Scientific Research
Bolling Air Force Base, DC
and
Philips Laboratory / Geophysics Directorate

September 1994

BACKSCATTER FROM A PLASMA PLUME DUE TO EXCITATION OF SURFACE WAVES

Dikshitulu K. Kalluri
Professor
Department of Electrical Engineering
University of Massachusetts Lowell
Lowell, MA 01854

Abstract

Experiments conducted by Air Force Laboratories showed that considerable unexpected electromagnetic backscatter from a plasma plume is occurring in a certain intermediate frequency band. A plausible explanation for the backscatter is offered based on the excitation of surface waves.

For source frequency f less than plasma frequency f_p , the surface of the plasma column is an interface between free space and an overdense plasma which behaves like a conductor. The turbulent outer radial layer behaves like a rough surface. The plasma column is thus capable of supporting a TM surface wave.

The surface wave on the plasma column is analogous to a current wave along a wire antenna in the end-fire mode. When it encounters a spatial discontinuity in the properties of the medium in the axial direction of the column, it is reflected. The reflected wave gives rise to the backscatter.

The theory is illustrated through a sample calculation made at $f = 600$ MHz.

BACKSCATTER FROM A PLASMA PLUME DUE TO EXCITATION OF SURFACE WAVES

Dikshitulu K. Kalluri

I. Introduction

Dr. Keith Groves, my focal point at PL/GP for the Air Force Office of Scientific Research Summer Faculty Research Program (1994), suggested I investigate the following problem: Experiments conducted by Air Force Laboratories showed that considerable unexpected electromagnetic backscatter from a plasma plume is occurring in a certain intermediate frequency band.

Figures 1 and 2 show the electron density and collision frequency numbers in the plasma plume. The plume is a cylindrical inhomogeneous lossy plasma column. The maximum electron density N_{0m} on the axis ($r = 0$) is $3E13$ ($\#/cm^3$) corresponding to angular plasma frequency (Note: for convenience, the computer notation $E_{xx} = 10^{xx}$ will be used occasionally.):

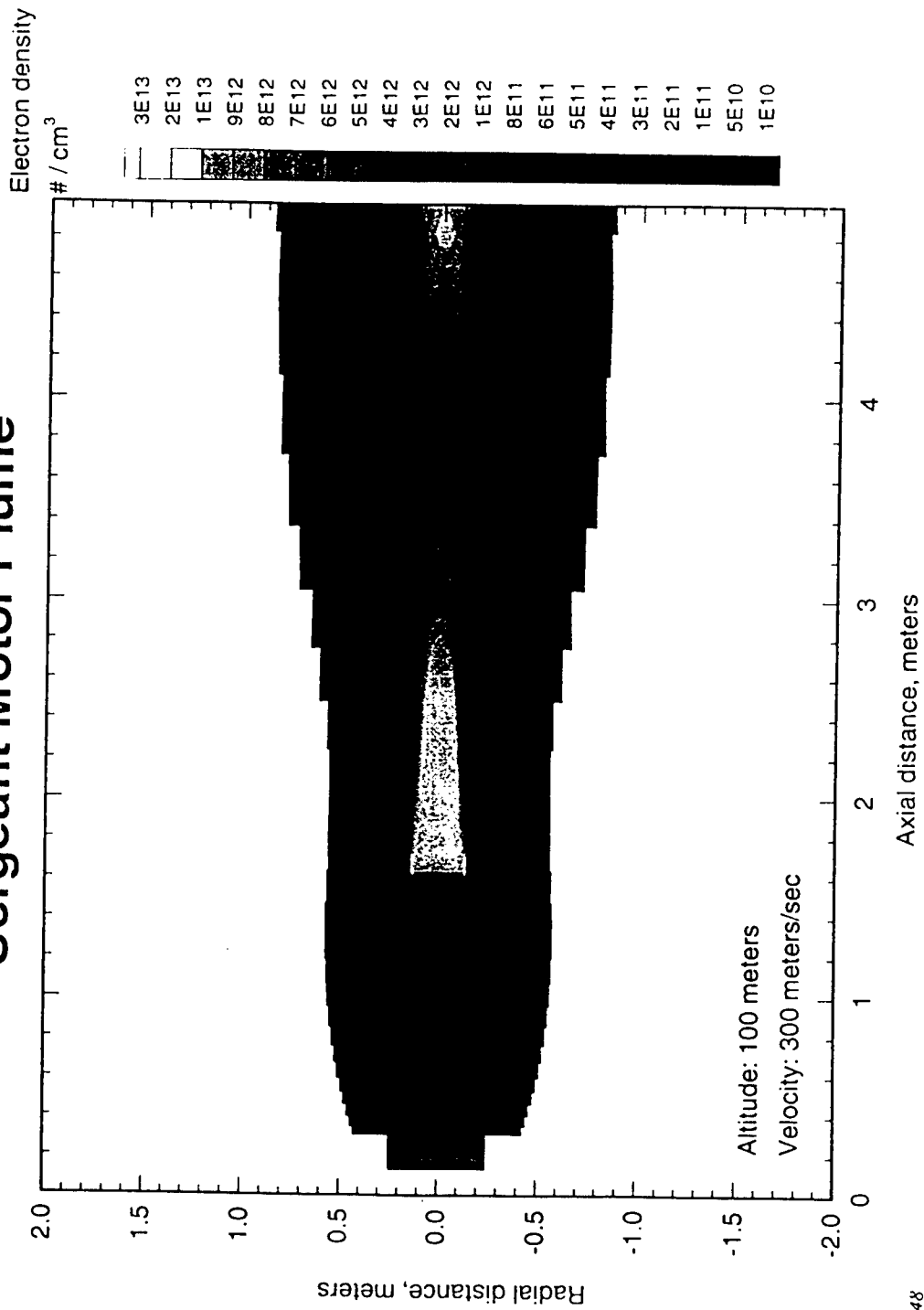
$$\omega_{pm} = \sqrt{\frac{N_{0m} e^2}{m \epsilon_0}} = 3 \times 10^{11} \text{ (rad/s)} \quad (1)$$

and $f_{pm} = \omega_{pm} / 2\pi = 47.75$ GHz. Here m and e are the mass and absolute value of the charge of an electron, and $\epsilon_0 = 8.854E-12$ (F/m) is the permittivity of free space. The collision frequency (ν) also varies with r ranging in value from $6E11$ to $1E11$ (rad/s). Scattering of an electromagnetic wave, in the frequency range of $f = 50$ MHz to 10 GHz, by such an inhomogeneous and lossy plasma plume is the object of this investigation.

II. Problem Classification based on Plasma Parameters

- (1) Plasma radius a is of the order of 0.5 m; The normalized value $a/\lambda_{pm} = af_{pm} / c = 83.3$. In this sense the column may be classified as thick.

Sergeant Motor Plume



CS942748

Figure 1

Sergeant Motor Plume

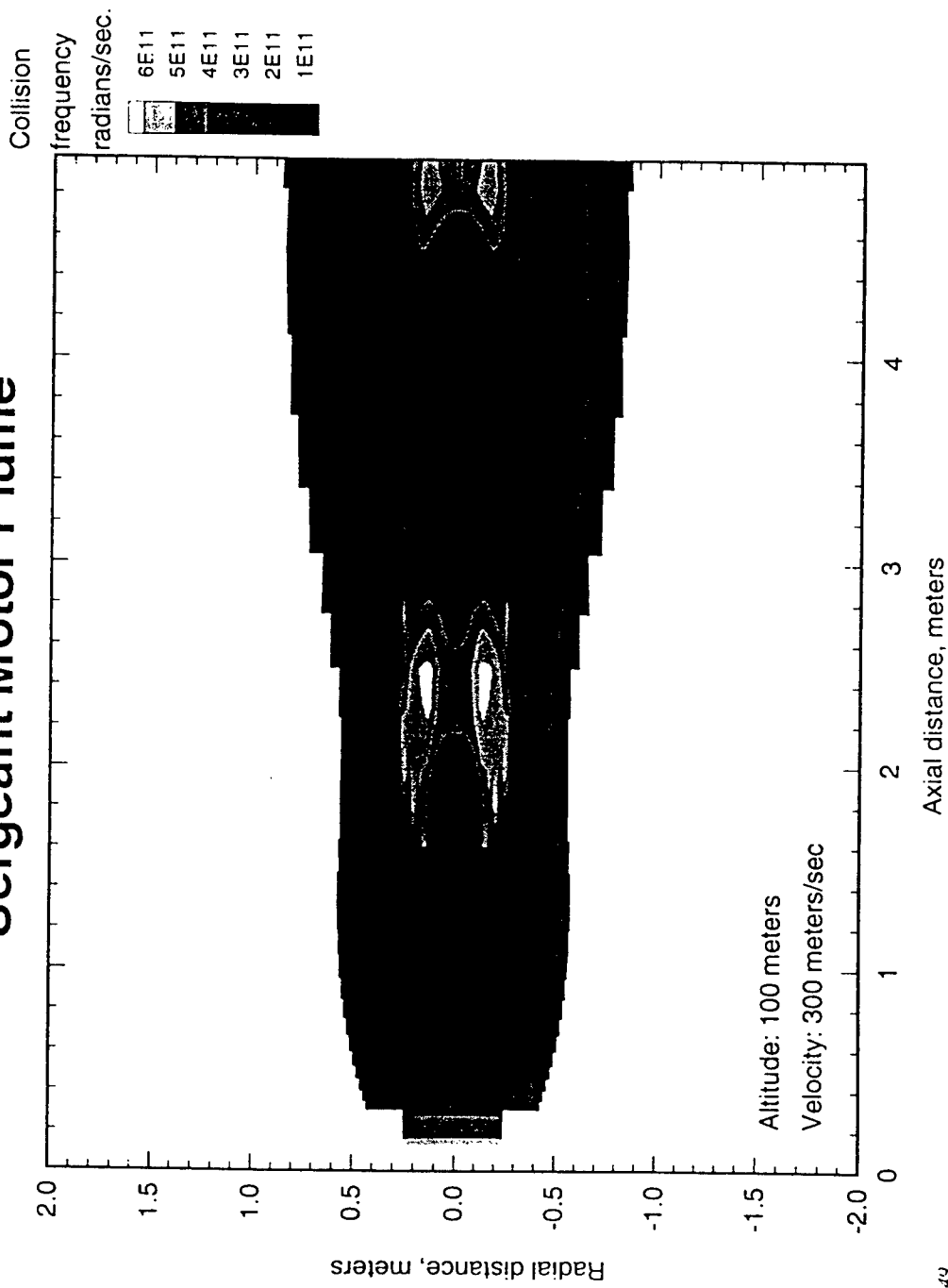


Figure 2

C5942749

Here c is the velocity of light = 3×10^8 m/s and λ_{pm} is the free space wave length of the corresponding plasma frequency.

- (2) The normalized value $a/\lambda = af/c$ varies from 8.3×10^{-2} to 16.67 as f varies from 50 MHz to 10 GHz respectively.
- (3) The collision frequency (ν) is quite high and is of the order of plasma frequency on the axis. The plasma has to be classified as highly collisional.
- (4) The outer layer around $r = a$ has a turbulent character.
- (5) Apart from the outer layer, the rest of the column behaves like an overdense plasma (good conductor), for the frequency range 50 MHz to 10 GHz.
- (6) The fact that $r > a$ is free space and $r < a$, overdense plasma that behaves like a conductor suggests that the column is capable of supporting TM surface waves. The outer edge near $r = a$, being turbulent, behaves like a rough surface [1] for $f < f_p$.

The author of this report (henceforth will be referred to as the author) is strongly influenced by his experience with the study of surface plasmons at optical frequencies and wondered whether their excitation in this case will result in backscatter. However before launching a full investigation into this aspect, the author wanted to understand the absorption of the high frequency electromagnetic radiation by the highly collisional inhomogeneous plasma. This aspect is discussed in the next section.

III. Absorption of TM wave

The problem of the absorption of the electromagnetic wave by the highly collisional plasma column is studied by modeling the column as an inhomogeneous lossy plasma slab of width $d = 2a$. Figure 3 shows this model, where the inhomogeneity is

mathematically modeled, for illustrative purposes, by a trigonometric function given below:

$$\omega_p(z) = \omega_{pm} (\sin \pi z/d)^{m/2} \quad (2)$$

By changing the value of m , the profile may be altered to fit the experimental profile approximately.

In the region $0 < z < d$, the equations satisfied by the time-harmonic fields are given below:

$$\nabla \times \bar{E} = -j\omega\mu_0 \bar{H} \quad (3)$$

$$\nabla \times \bar{H} = -N_0 e \bar{v} + j\omega\epsilon_0 \bar{E} \quad (4)$$

$$j\omega m \bar{v} = -e \bar{E} - m v \bar{v} \quad (5)$$

Here E , H , and v are the electric, the magnetic, and the velocity field respectively. The other symbols have the usual meaning. Assuming the field quantities vary as

$$F(x, z, t) = F(z) e^{j(\omega t - Sx)} \quad (6)$$

the first order coupled differential equations satisfied by the state variables E_x and ($\eta_0 H_y$) of a TM wave are obtained:

$$-\frac{1}{jk_0} \frac{dE_x}{dz} = \frac{C^2 - X/U}{1 - X/U} (\eta_0 H_y) \quad (7)$$

$$-\frac{1}{jk_0} \frac{d(\eta_0 H_y)}{dz} = (1 - X/U) E_x \quad (8)$$

Here $S = \sin \theta$, $C = \cos \theta$, θ is the angle of incidence (angle with z axis), $k_0 = \omega/c$, η_0 is the characteristic impedance of free space $= (\mu_0 / \epsilon_0)^{1/2} = 120\pi$ and the symbols X and U (notation used in magnetoionic theory) are:

$$X(z) = (\omega_p(z) / \omega)^2 \quad (9a)$$

$$U = 1 - jZ, Z(z) = v(z) / \omega \quad (9b).$$

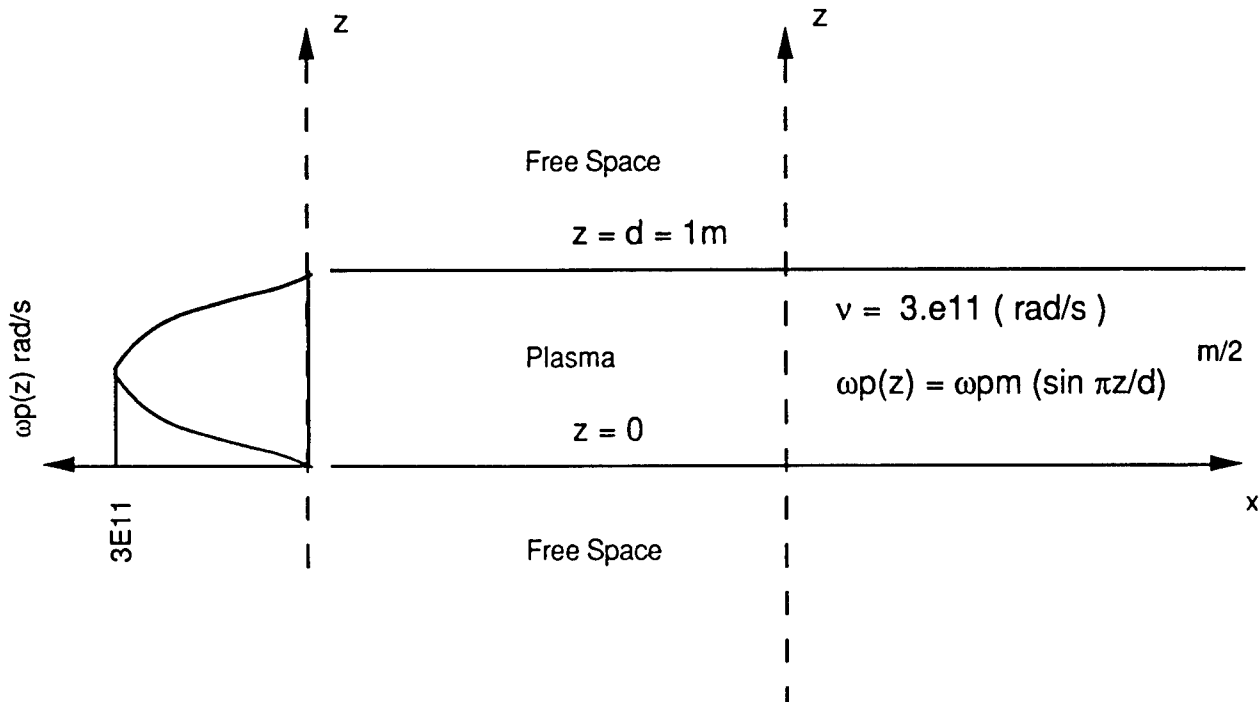


Figure 3

The following numerical method is devised to obtain the absorption coefficient.

- (1) Assume a suitable arbitrary complex value K_x for E_x at $z = d$ i. e. $E_x(d) = K_x = E_x^T$. It follows that $(\eta_0 H_y)$ at $z = d$ is K_x / C .
- 2) Starting with these initial values, solve, numerically the first order coupled differential equations (7) and (8) by integrating downwards and obtain $E_x(0) = a_x$ and $\eta_0 H_y(0) = b_y$.
- (3) Calculate the reflection and transmission coefficients:

$$R_{11} = \frac{E_x^R}{E_x^I} = \frac{a_x - C b_y}{a_x + C b_y} \quad (10)$$

$$|T_{11}| = \left| \frac{E_x^T}{E_x^I} \right| = \left| \frac{2 K_x}{a_x + C b_y} \right| \quad (11)$$

Here the superscripts I, R, T refer to incident, reflected, and transmitted fields respectively. The subscript 11 refers to the parallel (TM) polarization of the incident wave.

(4) Calculate the absorption coefficient :

$$A = 1 - \rho - \tau = 1 - |R_{11}|^2 - |T_{11}|^2 \quad (12)$$

where ρ and τ are power reflection and transmission coefficients.

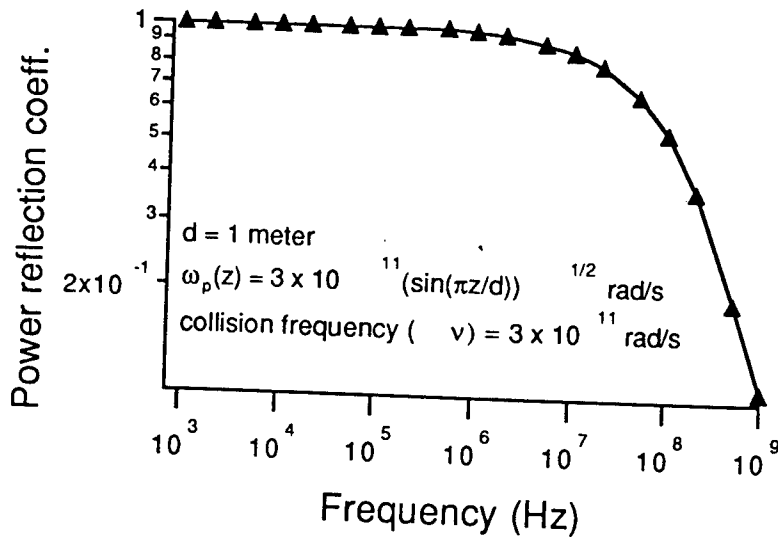


Figure 4a

Figures 4a, 4b and 4c are graphs for ρ , τ and A vs f for an angle of incidence of 60° . Here ν is assumed constant and equal to $3E11$ (rad/s). From these graphs, it is clear absorption increases with frequency. This result may be qualitatively explained by noting that the depth of penetration of the source wave increases with frequency since the value of z at which $\omega_p(z) = \omega$ increases with increase of f . In passing, It may be

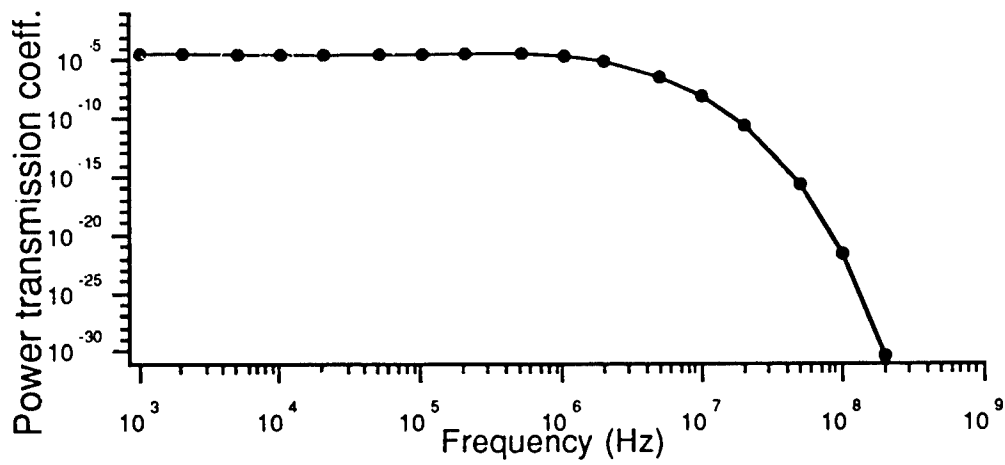


Figure 4b

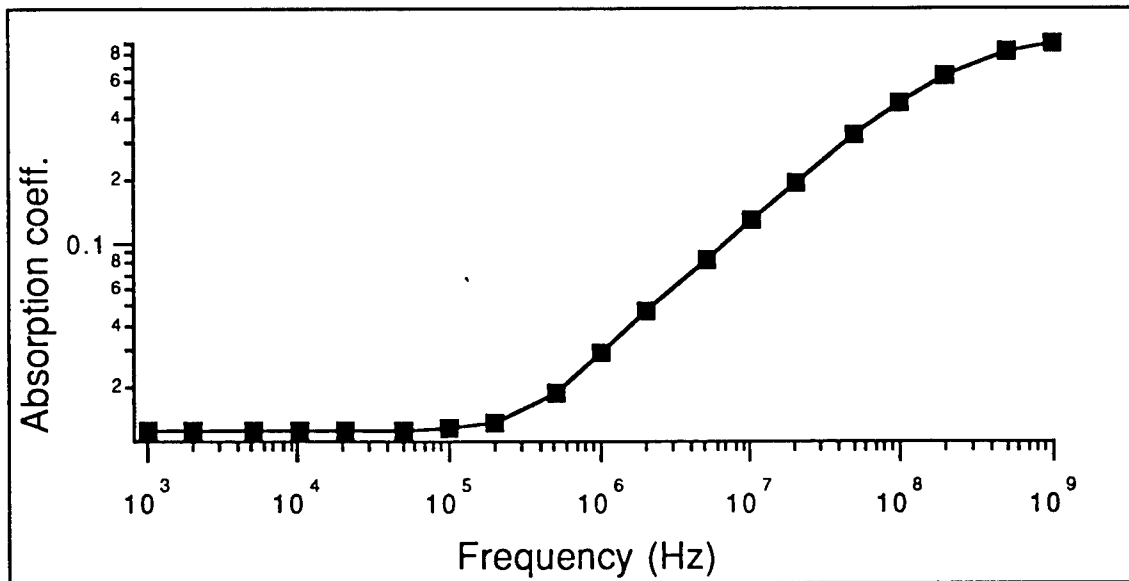


Figure 4c

noted that a pseudo Brewster angle exists for the TM case under consideration and shown in Figure 5.

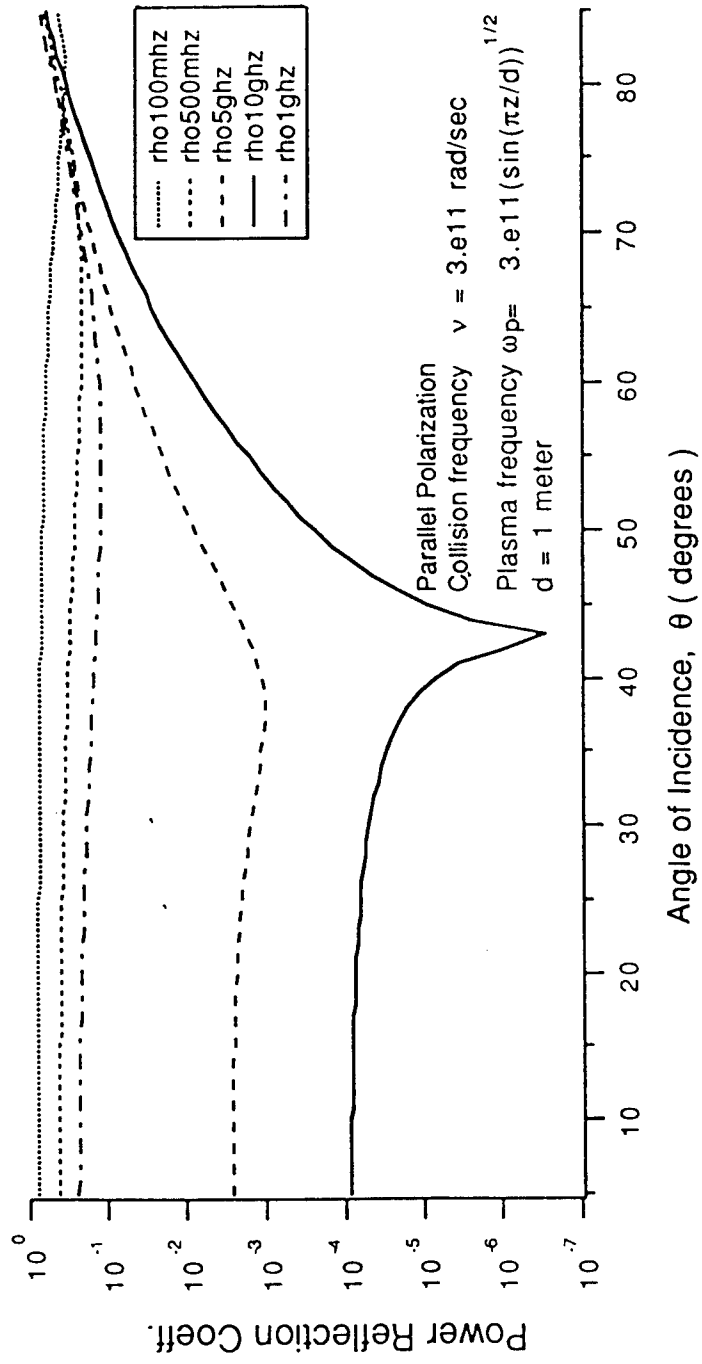


Figure 5

In conclusion, a theory based on only specular reflection and associated physics assumed above does not perhaps explain the increased back scatter in an intermediate frequency range. This led us to consider incorporating new physics into our model.

Turbulence present in the outer layers perhaps plays some part. Since for the frequency range under consideration, the plasma is overdense, the turbulent layer is modeled as a rough surface. The inner layers behave like a gaseous conductor. These thoughts led the author to consider the aspect of surface wave excitation.

IV. Review of Surface Waves

A surface wave [2], [3] propagates along the surface $x = 0$ (see Figure 6), with a phase velocity $V_{ph} = \omega/k_z$. Its fields attenuate for $|x| > 0$. An interface between two dielectrics can support such a wave provided their dielectric constants are of opposite sign and $\epsilon_{r1} < -\epsilon_{r2}$. If medium 2 is free space and medium 1 is a

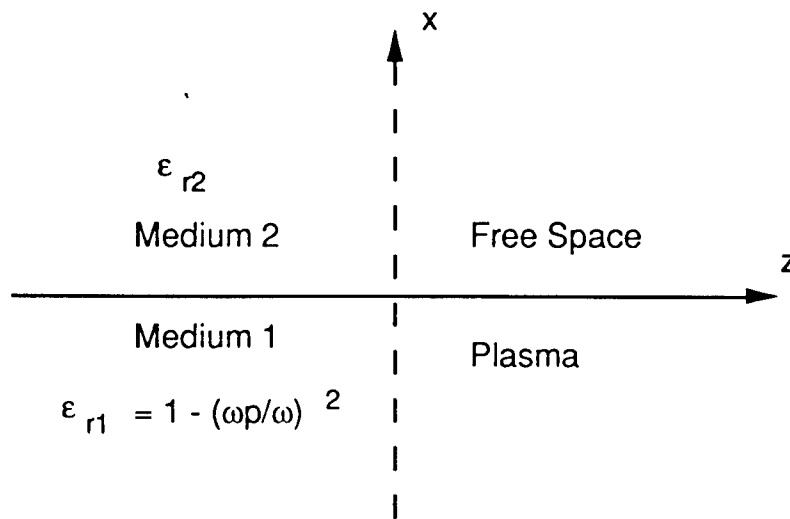


Figure 6

plasma whose plasma frequency is such that $\epsilon_{r1} = (1 - \omega_p^2/\omega^2) < -1$, the

conditions for the support of a surface wave at the interface are satisfied. Such a surface wave is called surface plasmon. For optical frequencies, medium 1 is a metal which behaves like a plasma with negative dielectric constant.

However, an electromagnetic wave in free space incident at any angle on the interface can not excite the surface wave since the dispersion characteristic of the surface wave (k_z vs ω) lies to the right of the light line (see Figure 9 b for an illustrative graph in which β is the real part of k_z). In optics, the required additional Δk_z is obtained by using a ATR Coupler or a Grating Coupler or a rough surface.

V. Excitation of Surface waves on Plasma Plume

From the material presented in sections II and IV, it is clear that conditions exist for the excitation of a surface wave on the surface of the plasma plume. In this section, the equations needed to obtain the dispersion relation [3], [4] of the surface plasmons are discussed. Refer to Figure 7.

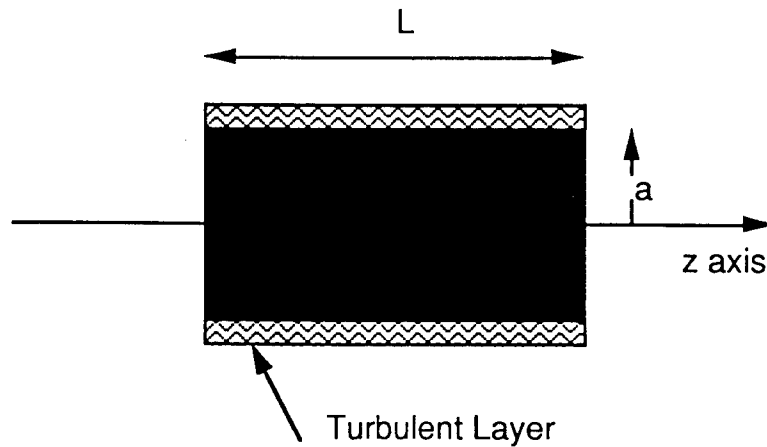


Figure 7

Plasma region ($0 < r < a$)

$$\epsilon_p(r) = 1 - \frac{\omega_p^2(r)}{\omega(\omega - j\nu)} \quad (13a)$$

Let

$$E_z^p(r, \phi, z, t) = A G(r) e^{j(\omega t - k_z z)} \quad (14)$$

where

$$-k_{tp}^2(r) + k_z^2 = k_0^2 \epsilon_p(r), \quad k_0 = \omega/c \quad (15)$$

and $G(r)$ satisfies the differential equation:

$$\frac{d^2 G}{dr^2} + \left[\frac{1}{r} + \frac{k_z^2}{k_{tp}^2(r)} \frac{d\epsilon_p/dr}{\epsilon_p(r)} \right] \frac{dG}{dr} - k_{tp}^2(r) G = 0 \quad (16)$$

Other field components of this TM wave can be expressed in terms of the z component of the electric field.

$$E_r^p = -\frac{j}{k_{t0}^2} k_z \frac{\partial E_z^p}{\partial r} \quad (17a)$$

$$H_\phi^p = -\frac{j}{k_{t0}^2} \omega \epsilon_0 \epsilon_p \frac{\partial E_z^p}{\partial r} \quad (17b)$$

$$Z_{TM}^z = \frac{E_r}{H_\phi} = \frac{k_z}{\omega \epsilon_0 \epsilon_p} \quad (17c)$$

Free Space Region ($a < r < \infty$)

$$\frac{d^2 E_z^0}{dr^2} + \frac{1}{r} \frac{dE_z^0}{dr} - k_{t0}^2 E_z^0 = 0 \quad (18)$$

$$-k_{t0}^2(r) + k_z^2 = k_0^2 \quad (19)$$

$$E_z^0(r, \phi, z, t) = B K_0(k_{t0} r) e^{j(\omega t - k_z z)} \quad (20)$$

$$E_r^0(r, \phi, z, t) = j B \frac{k_z}{k_{t0}} K_1(k_{t0} r) e^{j(\omega t - k_z z)} \quad (21a)$$

$$H_{\phi}^0(r, \phi, z, t) = \frac{jB}{k_{t0}} \omega \epsilon_0 K_1(k_{t0}r) e^{j(\omega t - k_z z)} \quad (21b)$$

Here K_0 and K_1 are the modified Bessel functions of the second Kind [5]. From the boundary conditions of continuity of E_z and H_{ϕ} at $r = a$, the following dispersion relation is obtained:

$$\frac{k_{tp}^2(a)}{\epsilon_p(a)} \frac{G(a)}{G'(a)} + k_{t0} \frac{K_0(k_{t0}a)}{K_1(k_{t0}a)} = 0 \quad (22)$$

In these equations while ω is real, k_z and several other quantities are complex and the complex mode is to be used for computations. In particular, let us denote:

$$k_z = \beta - j\alpha \quad (23)$$

where β the phase constant and α the attenuation constant are real. The propagation velocity of the surface wave is given by

$$V_{ph} = \omega / \beta \quad (24)$$

VI. Numerical Method for obtaining the Dispersion Relation

The above equations are used to compute the complex value of k_z for a given real value of ω . Numerical mode of the software Mathematica is used. The method consists of iterating between the two steps outlined below till convergence is obtained:

- Step 1 Starting with a guessed value for k_z , the differential equation (16) for G is numerically solved, with the initial conditions $G(0) = 0$ and $G'(0) = 0$. The singularity at $r = 0$ has to be handled with care. Thus the values of $G(a)$ and $G'(a)$ are obtained.
- Step 2 The dispersion relation which is a nonlinear algebraic equation is now solved for k_z .

Since the cylinder is thick it is possible that for some values of ω , $G(a)$ and $G'(a)$ are both large though their ratio is not large. To cover this aspect an alternative numerical method is also developed. The second order differential equation for G is converted to a first order nonlinear differential equation by defining a new variable $Y = G'/G$, which has the initial condition $Y = 0$:

$$\frac{dY}{dr} + \left[\frac{1}{r} + \frac{k_z^2}{k_{tp}^2(r)} \frac{d\epsilon_p/dr}{\epsilon_p(r)} \right] Y + Y^2 - k_{tp}^2(r) = 0 \quad (25)$$

Once again the singularity at $r = 0$ has to be handled with care.

VII. Back Scatter

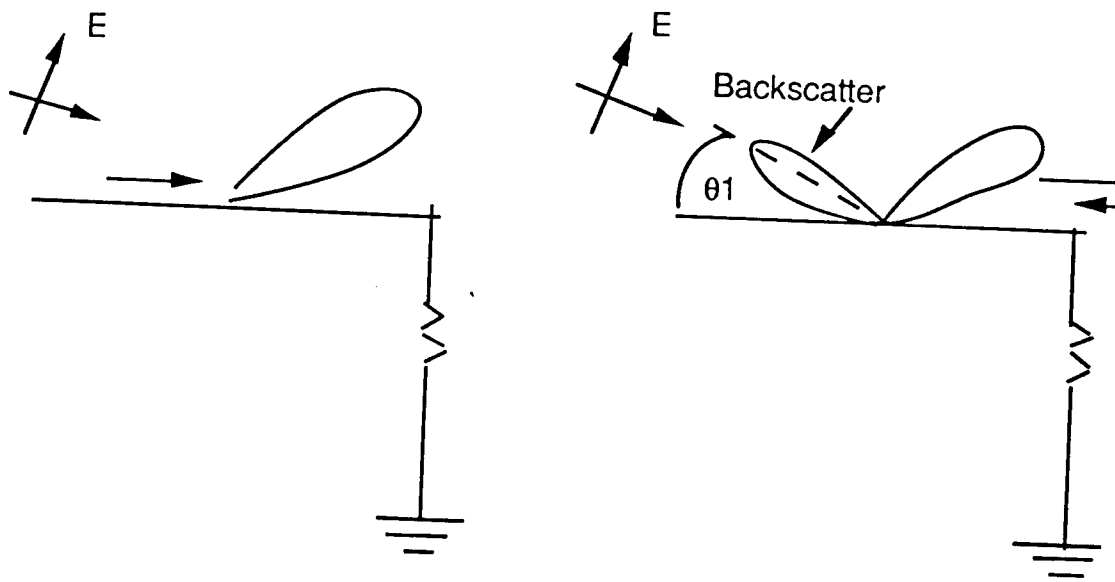


Figure 8

The surface traveling wave on the plasma plume is analogous to a current wave along thin wire antennas [6] in the end-fire mode. It travels with a velocity close to that of light. The far radiated field

$$E_r = -A j k_0 L \sin\theta_1 \frac{\sin\left[\frac{1}{2p} k_0 L (1 - p \cos\theta_1)\right]}{\frac{1}{2p} k_0 L (1 - p \cos\theta_1)} \quad (26)$$

where A is a constant with respect to θ_1 and L , θ_1 is the angle of the point of observation away from the axis of the plume and p is the propagation velocity divided by c . p is close but slightly less than the number 1. The surface traveling wave traveling a distance L along the axis is reflected when it encounters a spatial discontinuity in the properties of the medium at $z = L$. It is the reflected wave that gives rise to the backscatter. Figure 8 gives a qualitative explanation [6] for the backscatter. For p close to 1, the first maximum in the pattern [5] occurs at

$$\theta_1 = 49.35 \sqrt{\lambda/L} \text{ (degrees)} \quad (27)$$

VIII. Sample Calculation

The electron density is assumed to be varying radially as a Bessel function of the first kind of zero order. Consequently the square of the plasma frequency is given by

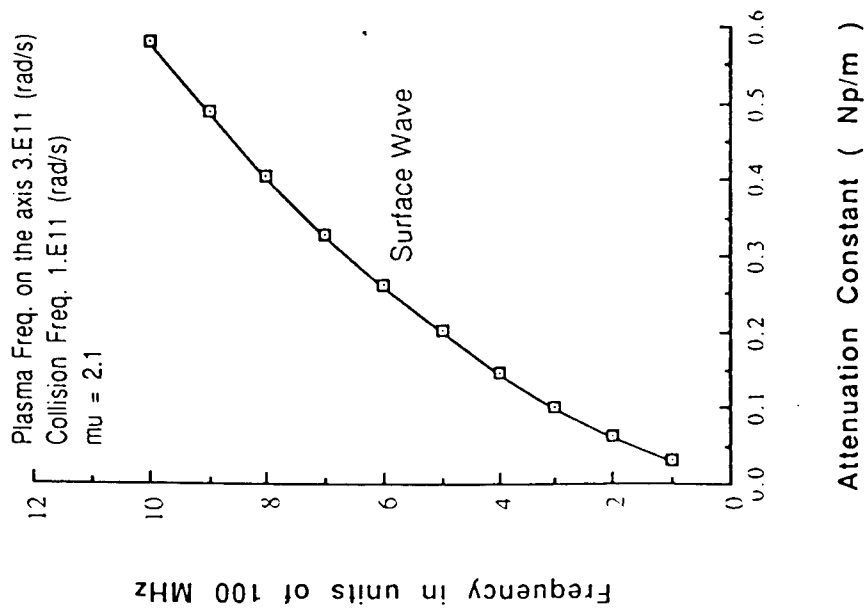
$$\omega_p^2(r) = \omega_{pm}^2 J_0^2(\mu r/a) \quad (28)$$

If $\mu = 0$, we have the homogeneous case and if $\mu = 2.405$ the plasma density at the edge $r = a$ is zero. For the sample calculation we chose $\mu = 2.1$. Thus

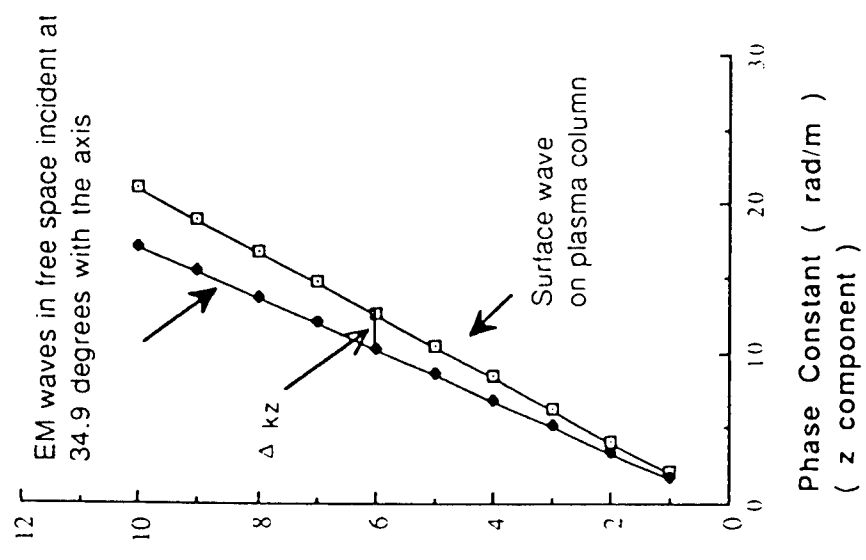
$$\omega_p(a) = \omega_{pm} \sqrt{J_0(2.1)} = 0.4082 \omega_{pm} \quad (29)$$

Choosing further $\omega_{pm} = 3 \text{ E11 (rad./s)}$, plasma frequency $f_p(a) = 19.51 \text{ GHz}$.

For the purpose of illustration, let the turbulent layer be described by $0.4 < r < 0.5$, thus $a = 0.4 \text{ m}$. The collision frequency ν is taken to be 1 E11 (rad/m) which is the value in the outer layers. Using these parameters α vs f and β vs f are obtained numerically as described in section V1. Figure 9 shows these results. The value of $L = 1 \text{ meter}$ is assumed where from Figure 2, there appears to be a discontinuity in the properties of



(a)



(b)

Figure 9

the medium. For an illustrative value of $f = 600\text{MHz}$, $\lambda = 0.5$ meters and from (27), $\theta_1 = 34.9^\circ$. The line to the left of the dispersion curve marked as Surface wave on plasma column is the light line for a EM wave in free space incident at 34.9° with the axis. This curve is a straight line described by the equation:

$$k_{z0} = k_0 \cos 34.9^\circ \quad (30)$$

The horizontal line marked as $\Delta k_z = 2.29$ is proportional to the z component of the momentum (in the language of photonics) that is supplied by the turbulent rough surface. Superposition of the spectrum of plasma turbulence will lead to the frequency band of the surface waves that can be excited. Figure 9a permits us to calculate the attenuation suffered by the surface wave in traveling a distance L before it reaches the point of discontinuity. At 600 MHz $\alpha = 0.26119$ and $\exp (- 2 \alpha L) = 59.3\%$. Thus 60% of power is still in tact for backscattering. All the numbers were obtained assuming p is nearly equal to 1 and this may be verified by calculating ω/β at $f = 600$ MHz. This gives a propagation velocity of $2.9767e8$ m/s confirming $p \approx 1$.

IX. Results and Conclusions

Based on the results obtained so far, the following observations can be made with reference to the various parameters.

Effect of Frequency: At low frequencies the radiation field given in (26), which is inversely proportional to λ , is weak. At high frequencies the attenuation constant is high and the surface wave is dissipated before it reaches the discontinuity and therefore the backscattering is weak.

Effect of L: As L increases, the radiation field increases as seen from (26) but the aspect angle θ_1 decreases, Δk_z decreases facilitating easier excitation of the surface waves. There is no change in α or β . However the wave attenuation increases because of the increase in L. Perhaps the center of the frequency band of significant backscatter moves towards higher frequencies as L increases.

Effect of Polarization: The model assumed TM waves, since surface plasmons can be

excited only when the wave electric field has a z component.

X. Scope for Future Work

A theory based on the excitation of surface waves on a plasma plume is constructed to offer a plausible explanation for increased backscatter in an intermediate frequency band. Sample calculations are made based on a simple model and approximate data. The theory will be improved and more accurate calculations will be made based on some more experimental data. Spectrum of the turbulent plasma will be incorporated into the model when the experimental data on this aspect becomes available. The author intends to submit summer research extension proposal to complete this work.

REFERENCES

- [1] A. R. Hochstin and C. P. Martens, *Proceedings of Symposium on Turbulence of Fluids and Plasmas*, Polytechnic Press, 1968, p. 187.
- [2] H. Raether, *Surface PLasmons*, Springer- Verlag, 1988.
- [3] A. D. Boardman (ed), *Electromagnetic Surface Modes*, John Wiley, 1982.
- [4] M. Zethoff, U. Kortshagen, Vol. 25, *J. Phys. D: Applied Physics*, 1992, p. 187
- [5] M. Abramowitz and I. A. Stegun (ed), *Handbook of Mathe matical Functions*, Dover Publications, 1965.
- [6] E. F. Knott, J. F. Shaeffer and M. T. Tuley, *Radar Cross Section*, Artech House, i985, p. 148.

INVESTIGATION OF ATMOSPHERIC HEATING AND COOLING BALANCE USING
MODTRAN3

Lucia M. Kimball
Instructor
Department of Mathematics

Worcester Polytechnic Institute
100 Institute Road
Worcester, MA. 01609

Final Report For:
Summer Faculty Research Program
Phillips Laboratory

Sponsored by:
Air Force Office of Scientific Research
Bolling Air Force Base, Washington, DC

and

Phillips Laboratory

August 1994

INVESTIGATION OF ATMOSPHERIC HEATING AND COOLING BALANCE USING
MODTRAN3

Lucia M. Kimball
Instructor
Mathematics Department
Worcester Polytechnic Institute

Abstract

Recent modifications to MODTRAN3, a 2 cm^{-1} resolution radiative transfer model, have permitted its transformation into a full flux divergence algorithm. It is now possible to calculate heating and cooling rates arising from both thermal and solar sources. The thermal calculations have been validated against benchmark line-by-line (LBL) calculations provided as an outgrowth of the InterComparison of Radiation Codes used in Climate Models (ICRCCM), organized by Ellingson and colleagues. The MODTRAN3 comparisons for separate species (H_2O , CO_2 , and O_3) were all of sufficient quality, usually falling within the range of LBL comparisons, to warrant the extension to other species. MODTRAN3 now includes improved band model formulations, particularly for O_3 , a new solar irradiance, absorption cross sections in the ultraviolet (SO_2 and NO_2) and infrared (CFC-11, -12, -13, -14, -21, -22, -113, -114, and -115, plus N_2O_5 , HNO_4 and CCL_4), derived from the HITRAN92 data base. Coupled with the standard

MODTRAN3 options, it is now possible to calculate extensive IR thermal cooling rates as well as balancing UV/Vis solar heating. Calculations for standard atmospheric conditions as well as the roles of single scattering are presented.

INVESTIGATION OF ATMOSPHERIC HEATING AND COOLING BALANCE USING
MODTRAN3

Lucia M. Kimball

Introduction

In the past MODTRAN3, a moderate resolution radiative transfer code, has been used to calculate clear sky thermal cooling rates due to each of the separate species H_2O , CO_2 , and O_3 . Comparisons with prior line-by-line(LBL) cooling rate calculations (*Clough, 1992*) are excellent. *Bernstein (1994)* has shown that MODTRAN3 can replicate LBL computations to within a few percent.

The latest modifications to MODTRAN include an updated band model, a new solar irradiance, and the inclusion of new absorption cross sections in the ultraviolet and the infrared. A more extensive investigation of atmospheric heating and cooling rates is now possible.

Flux Calculation

Upwelling and downwelling vertical fluxes are defined as the normal component of the radiance integrated over the upper and lower hemisphere, respectively (*Liou, 1980*). Therefore the upward

and downward fluxes can be expressed as

$$F_v^+ = \int_0^{2\pi} \int_0^1 I_v(\mu, \phi) \mu d\mu d\phi$$

$$F_v^- = \int_0^{2\pi} \int_{-1}^0 I_v(\mu, \phi) \mu d\mu d\phi$$

where μ is the zenith direction cosine, $I_v(\mu, \phi)$ is the monochromatic radiance at wavenumber v , and ϕ is the azimuthal angle. For the present case, we assume the integrals are azimuthally independent and the fluxes become

$$F_v^\pm = \pm 2\pi \int_0^{\pm 1} I_v(\mu) \mu d\mu.$$

In this study, the angular integration was done using a two point, first moment Gaussian quadrature with weights and path zenith angles given by $w_1 = 0.18196$, $w_2 = 0.31804$, $\theta_1 = 69.203$, and $\theta_2 = 32.334$ (Abramowitz and Stegun, 1972). Now we can write

$$F_v^+ = 2\pi \sum_i w_i I_v(\cos(\theta_i))$$

$$F_v^- = 2\pi \sum_i w_i I_v(\cos(180 - \theta_i)) .$$

It has been shown (Clough, et. al., 1992) that a two point Gaussian integration converges the flux to within 99.5% of its fully numerically converged value.

In the solar case, formulation of the upwelling and downwelling fluxes involves an instantaneous sun angle. We can express the downward monochromatic heat flux in the following

way,

$$F_v^- = I_v^s \mu \exp\left(-\frac{\tau_v}{\mu}\right)$$

where μ is the cosine of the solar zenith angle, I_v^s is the solar intensity at the top of the atmosphere and τ_v is the optical depth. Assuming a Lambertian surface with albedo α , the upwelling flux is given by

$$F_v^+ = \alpha \mu \exp\left(-\frac{\tau_v}{\mu}\right) .$$

Integration over solar day gives the average daily effect. An estimate of the average daily effect can be computed by assuming an average sun angle and a daily-weighted multiplication factor. Values for mean cosine of the solar zenith angle and length of daytime in parts of 24 hours can be found in *Manabe, et. al., 1961*.

The net flux $F_{v,\ell}$ at any atmospheric level ℓ is the difference between the upwelling and downwelling fluxes at that level $F_{v,\ell} = F_{v,\ell}^+ - F_{v,\ell}^-$.

Heating and Cooling Rate Calculations

The cooling/heating rate in an atmospheric layer defined by levels ℓ and $\ell-1$ is defined as the divergence of the net flux across the layer. The average cooling rate, Q , for the layer can be expressed in terms of temperature change by the following finite difference formula:

$$Q \approx \frac{\Delta T}{\Delta t} = \frac{g}{C_p} \frac{F_\ell - F_{\ell-1}}{P_\ell - P_{\ell-1}}$$

where F_l is the net flux for level l , P_l is the pressure at level l , g is the gravitational constant, and C_p is the specific heat of air at constant pressure. As in *Ridgway et. al.*, 1991 a value of $8.422 \text{ mb}^\circ\text{K-m}^2/\text{W-day}$ is used for the constant $\frac{g}{C_p}$.

Integrating the monochromatic cooling rates over frequency provides a measure of the total atmospheric heating/ cooling at a given level. If we represent integrated heating due to solar contributions by Q_s and the integrated thermal contribution by Q_t , then the sum, Q_s+Q_t , represents the atmospheric heating/cooling balance.

MODTRAN3 Radiance Calculations

MODTRAN3, the latest version of MODTRAN, was used to calculate the thermal radiances and solar irradiances used in the cooling/heating rate computations.

In MODTRAN3, four model parameters are derived for each molecular species based on the 1992 HITRAN database (*Rothman, et. al.*, 1992). These parameters are the interval average absorption coefficient (S/d), line density parameter (1/d), pressure broadening line width (α_c), and line tail continuum absorption coefficient (C) due to the tails of lines originating outside the interval. A band model parameter data file is created which tabulates these parameters at 1 cm^{-1} intervals from 1 to $17,900 \text{ cm}^{-1}$ at five temperatures (200, 225, 250, 275, and 300 K). Parameter values at intermediate temperatures are interpolated

during the radiative transfer computation. The transmittance, T , for a spectral bin Δv is given by

$$T = \left(\frac{2}{\Delta v} \int_0^{v/2} e^{-s u b(v)} dv \right)^n$$

where $b(v)$ is the Voigt line shape function, u is the absorber amount, s and n are defined in terms of the band model parameters as

$$s = \frac{(s/d)}{(1/d)}, \quad n = (1/d) \Delta v,$$

$$(s/d) = \left(\frac{1}{\Delta v} \right) \sum S_i, \quad (1/d) = \left(\frac{1}{\Delta v} \right) \left(\sum \sqrt{S_i} \right)^2 / \sum S_i$$

where S_i is the integrated line strength of line i , and the sum is over N lines whose center are contained in a bin of width Δv . The effective optical depth τ_v is derived from the log ratios of the full path transmittances between adjacent layers.

The monochromatic radiance seen by an observer looking along a particular directional path is the sum of contributions from all sources along the line-of-sight. The sources include gaseous emission, transmitted extraterrestrial (solar/lunar) emission and radiation scattered into the line of sight by aerosols or molecules. The radiance due to thermal sources is found by summing over each optical path the product of the layer-specific black body function and the transmittance between that layer and the observer. The radiance contributed by scattering sources is produced by summing the product of the source function and the transmittance along the optical path.

MODTRAN3 Results

For each of the MODTRAN3 calculations a 60-layer atmosphere was used with 30 layers between 1013 and 85 mbar and the remaining 30 layers distributed between 85 mbar and $1.e-4$ mbar. Results presented are for the spectral range 0-50,000 cm^{-1} , calculated at 1 cm^{-1} intervals and subsequently degraded to 50 cm^{-1} resolution for plotting. All gases currently supported by MODTRAN3 are included. H_2O , CO_2 , O_3 , N_2O , CO , CH_4 , O_2 , NO , SO_2 , NO_2 , NH_3 , and HNO_3 are incorporated through band models, and the chlorofluorocarbons (CFCs) are included through cross sections. Similarly, in the visible and UV spectral ranges O_3 , O_2 , SO_2 , and NO_2 are also incorporated as cross sections.

In order to include the effects of both directly transmitted solar irradiance and singly scattered solar contributions to the path radiances, it is necessary to run two separate cases. Path radiances including direct thermal contributions, scattered thermal contributions, ground reflected solar contributions and singly scattered solar contributions are obtained by running MODTRAN3 in the single scattered radiance mode. The directly transmitted solar contribution can be obtained by running in the directly transmitted solar mode. The energy distribution from the two approaches can be summed together because (1) the thermal and direct solar contributions arise from two different sources and (2) the scattered solar energy is considered a loss term when calculating the transmittance of the direct solar component, so

its reintroduction as a scattered component does not entail duplication.

Results are presented for both a clear sky and cloudy tropical (15 N latitude) atmospheres. An average sun angle of 50 degrees corresponding to day 120 of the year in a tropical atmosphere is used. The corresponding daily solar weighting factor from *Manabe, et. al.*, (1961) is 0.5. The surface albedo is 0.1 for all frequencies. Spectral cooling and heating rate results are given in units of $^{\circ}\text{mK}/\text{day}/\text{cm}^{-1}$ and integrated results are in terms of $^{\circ}\text{K}/\text{day}$. In this paper cooling rates are given as positive numbers and heating rates are negative. Figure 1 presents the spectral heating and cooling rates for the clear sky tropical atmosphere including contributions from both solar and thermal sources. In figure 1a heating contours are given by the dotted lines and cooling contours are indicated by the solid line. Figure 1b shows the magnitude of the heating/cooling corresponding to figure 1a. Both figures employ a pseudo-logarithmic abscissa, derived by adding 1000 cm^{-1} to the actual frequency before logarithmic plotting. The true frequency identifications are then mapped onto the appropriate locations. This facilitates seeing the whole spectral range ($0\text{-}50,000\text{ cm}^{-1}$) in one figure, minimizing the dominance of higher frequencies (as would occur on a linear scale) while permitting the inclusion of 0 cm^{-1} . The ordinate is log pressure, where 100, 1 and 0.01 mbar denote the approximate locations of the tropical tropopause, stratopause and mesopause.

Most of the cooling takes place in the 0 - 3000 cm^{-1} range due to the presence of the CO_2 15 μm (centered at 666 cm^{-1}) and O_3 9.6 μm (near 1040 cm^{-1}) bands. The combination of maximum cooling occurs at the stratopause where the spectrally integrated CO_2 and O_3 cooling between 0 and 3000 cm^{-1} amounts to about 13°K/day, 10°K from CO_2 and 3°K from O_3 . The tropospheric radiative cooling over the same spectral range derives primarily from H_2O bands, yielding an integrated 3-4°K/day. All of these values agree well with those found in the ICRCM studies of *Ridgway (1991)*, *Ellingson and Fouquart (1991)*, *Clough et al (1992)*, and *Bernstein et al (1994)*. The maximum cooling (loss of energy within the layer) for the clear sky can be expected to occur where the temperature is high and the opacity low, the configuration at the stratopause.

The actual identified maximum cooling of 80.88°mk/day/ cm^{-1} occurs at 650 cm^{-1} , the center of the CO_2 band at this resolution. Interestingly, the maximum heating, -27.39°mk/day/ cm^{-1} , also occurs at 650 cm^{-1} at a pressure of 0.013 mbar. This is not unrelated to the reasoning for the maximum cooling at the stratopause in that the heating is near the mesopause, the coldest region of the atmosphere, where radiation is being absorbed from the surrounding warmer layers. Such radiative heating can also be seen in the CO_2 band at 100 mb, the cold tropical tropopause. The mesopause heating values are only coarse estimates of the appropriate radiative forcing in that MODTRAN3 does not include

important non-LTE effects. The heating at the tropopause, on the other hand, is a realistic representation.

The prior discussion has centered on the thermal radiation and its relative cooling and heating. Additional discussion could be provided on the apparent role of green house gases (HNO_3 , CFC-11 and -12, O_3 , and CO_2) in the spectral range between 500 and 3000 cm^{-1} , readily apparent in Fig. 1. However, switching to the calculations of direct and scattered solar irradiance as a heating source, one must look primarily at the frequencies between 3000 and 50,000 cm^{-1} . Ozone predominates as the heating agent, particularly in the UV between 30,000 and 50,000 cm^{-1} , the sight of the weak Huggins and strong Hartley bands. Both lead to dissociation of O_3 , with subsequent direct heating of approximately 12-13°K/day, maximizing at the stratopause, again in agreement with the ICRCM-related studies. These values approximately balance the IR cooling at the same altitudes. The much weaker O_3 Chappuis bands (.45-.7 μm or 14,000-22,000 cm^{-1}) contributes a significantly smaller but discernible heating in the middle stratosphere.

Integrating by frequency, we obtain the energy balance shown in figure 2. As expected, the heating and cooling balance is close to zero throughout the middle atmosphere with maximum total cooling of approximately 4°K per day at the surface and maximum total heating of approximately 2.5°K per day just below 1 mbar. The imbalance at the top and bottom of the atmosphere could be due to the approximation of the solar day integral. According

to Cogley, et. al., (1976) the technique of choosing the mean solar angle and multiplying by a daily weighting factor can lead to large errors. This error could also arise because of the assumption of single scattering for solar irradiance. The multiple scattering capability, when implemented, will provide a more correct estimate, but will also impose major time penalties not warranted for this preliminary study.

The effect of a 1.1 km thick cirrus cloud present at 15km on the spectral cooling rate profile can be seen in figure 3. As in figure 1, dotted lines represent heating and solid lines represent cooling with the magnitude of heating/cooling given in figure 3b. In the presence of the the cirrus cloud layer, the maximum cooling still occurs at 650 cm^{-1} with a magnitude of $80.88^{\circ}\text{mK/day/cm}^{-1}$ but the maximum heating occurs in the cloud layer at 850 cm^{-1} with a value of $-31.1^{\circ}\text{mK/day/cm}^{-1}$. This heating is in the window region between the strong CO_2 and O_3 absorption bands.

The heating and cooling balance given in figure 4 shows a total heating of approximately 6°K/day at the bottom of the cloud and additional cooling of approximately 16°K/day at the top of the cloud. The cloud also causes a slight additional cooling for layers above the cloud up to approximately 1 mbar and additional heating between the ground to the cloud bottom.

Conclusions

Separating and/or isolating the regions of optimum heating and cooling as a function of both altitude and frequency provides the research community with an important tool for recognizing the potential impact of any natural or artificial (e.g. manmade) contaminant. The ability of MODTRAN3 to provide full path, full frequency transmittance and radiance calculations in seconds makes it a suitable choice for the required flux divergence calculations.

References

Abramowitz, M., and I. A. Stegun, Handbook of Mathematical Functions, 1046 pp., National Bureau of Standards, Applied Mathematical Series 55, Wash., D.C., 1972.

Berk, A. L., L. S. Bernstein, and D. C. Robertson, MODTRAN: A Moderate Resolution Model for LOWTRAN7, Rep. GL-TR-89-0122, Air Force Geophysics Lab., Bedford, MA., 1989.

Bernstein, L.S., A. Berk, P. K. Acharya, D. C. Robertson, G. P. Anderson, J. H. Chetwynd, and L. M. Kimball, Very Narrow Band Model Calculations of Atmospheric Fluxes and Cooling Rates Using The MODTRAN Code, in preparation for submission to *J. Geophys. Res.*, 1194.

Clough, S. A., M. J. Iacono, and J.-L. Moncet, Line-by-line Calculations of Atmospheric Fluxes and Cooling Rates: Application to Water Vapor, *J. Geophys. Res.*, 97, 15761-15785, 1992.

Cogley, A. C., and Borucki, W. J., Exponential Approximation for Daily Average Solar Heating or Photolysis, *J. Atmos. Sci.*, 33, 1347-1356, 1976.

Ellingson, R. G. and Y. Fouquart, The Intercomparison of Radiation Codes Used in Climate Models: longwave Results, *J. Geophysical Research*, 96, 8929 - 8953, 1991.

Liou, K. N., *An Introduction to Atmospheric Radiation*, Academic Press, Inc., San Diego, 1980.

Manabe, S. and Moller, F., On the Radiative Equilibrium and Heat Balance of the Atmosphere, *Monthly Weather Review*, Vol. 89, 12, 503-530, 1961.

Ridgway, W. L., Harshvardhan, and A. Arking, Computation of Atmospheric Cooling Rates by Exact and Approximate Methods, *J. Geophys. Res.*, 96, 8969-8984, 1991.

Rothman, L. S., R. R. Gamache, A. Goldman, L. R. Brown, R. A. Toth, H. M. Pickett, R. L. Poynter, J. M. Flaud, C. Camy-Peyret, A. Barbe, N. Husson, C. P. Rinsland, and M. A. H. Smith, The HITRAN molecular database: editions of 1991 and 1992, *J. Quant. Spectrosc. Radiat. Transfer*, 48, 469-507, 1992.

TROPICAL HEATING AND COOLING RATES

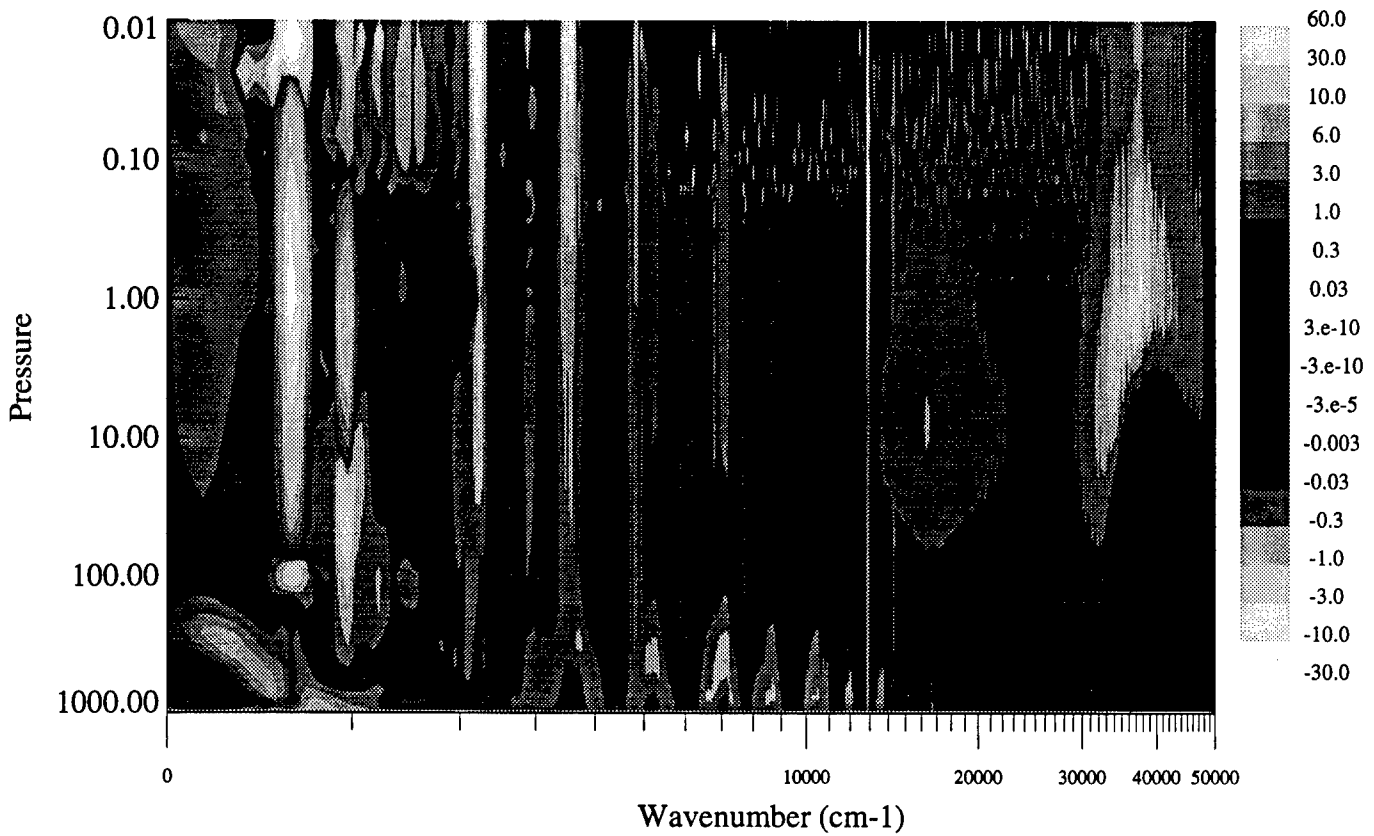
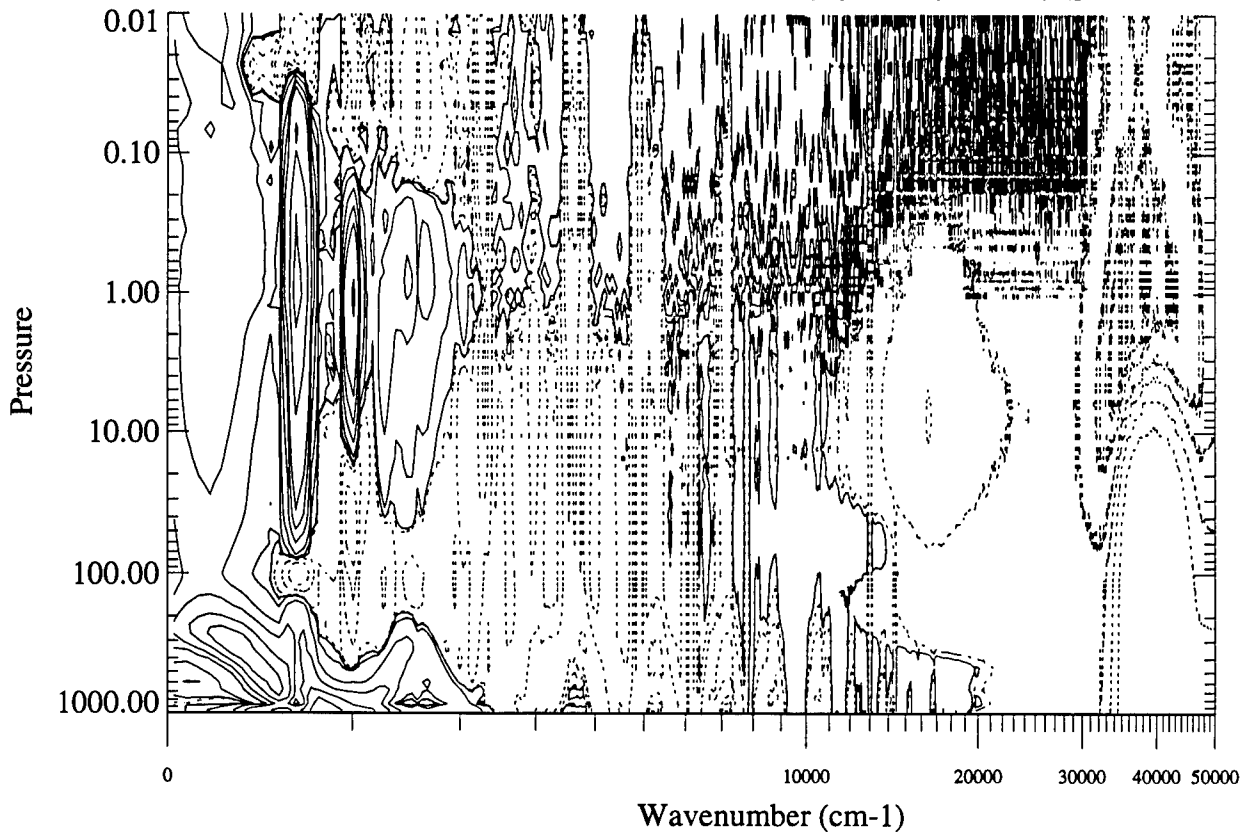


Figure 1: 1a (top) and 1b (bottom)
19-16

TROPICAL HEATING AND COOLING

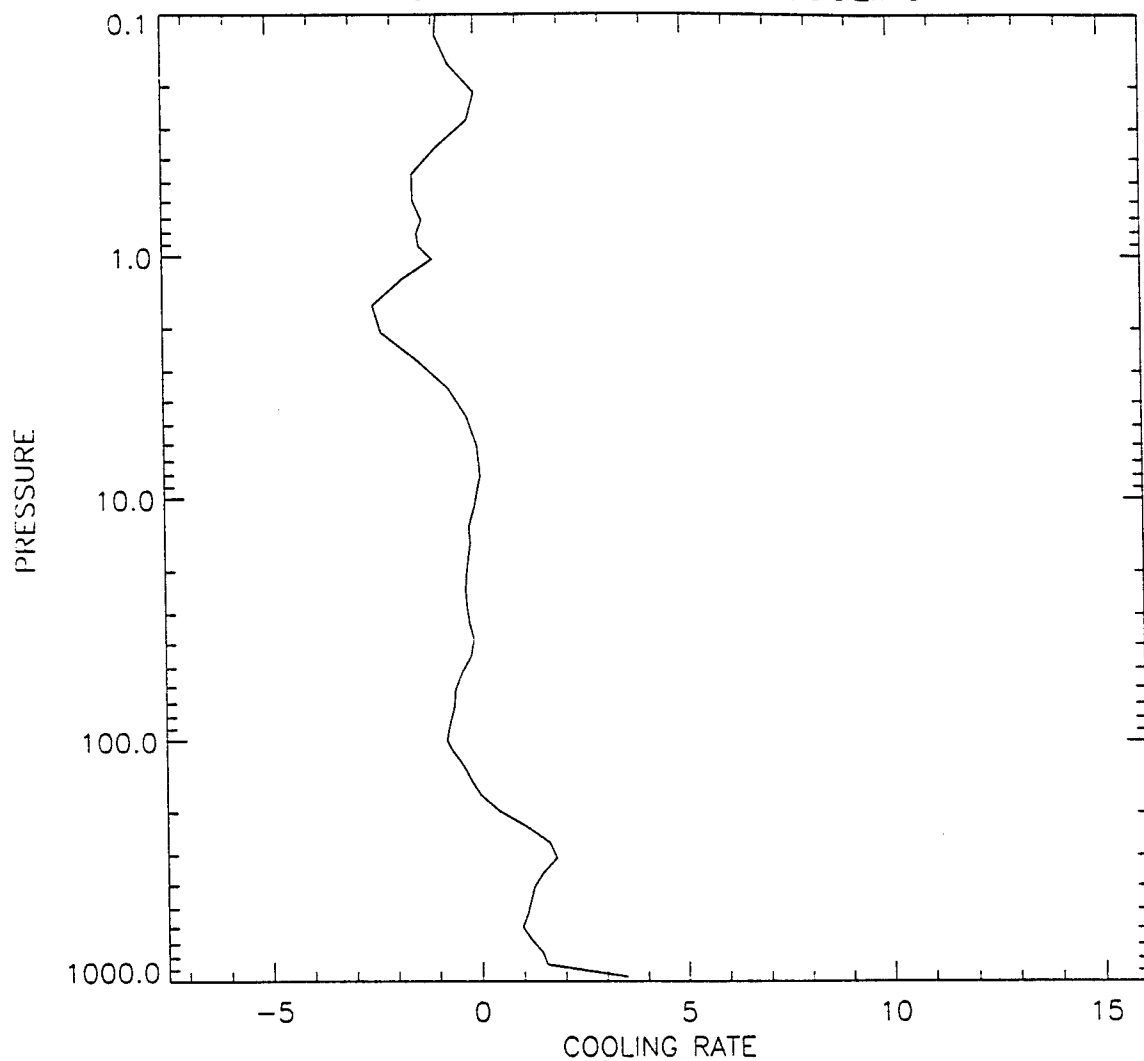


Figure 2

TROPICAL HEATING AND COOLING RATES CIRRUS CLOUD AT 15KM

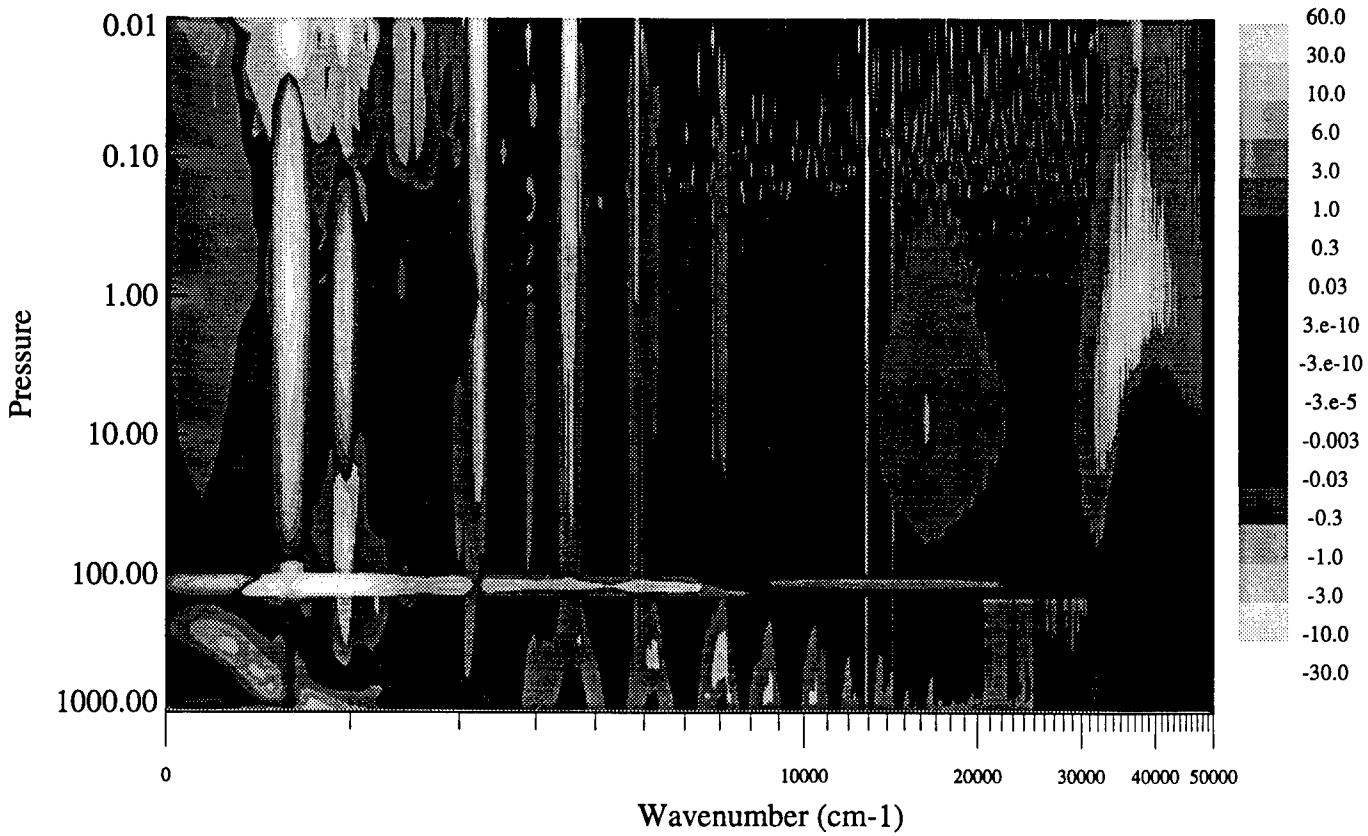
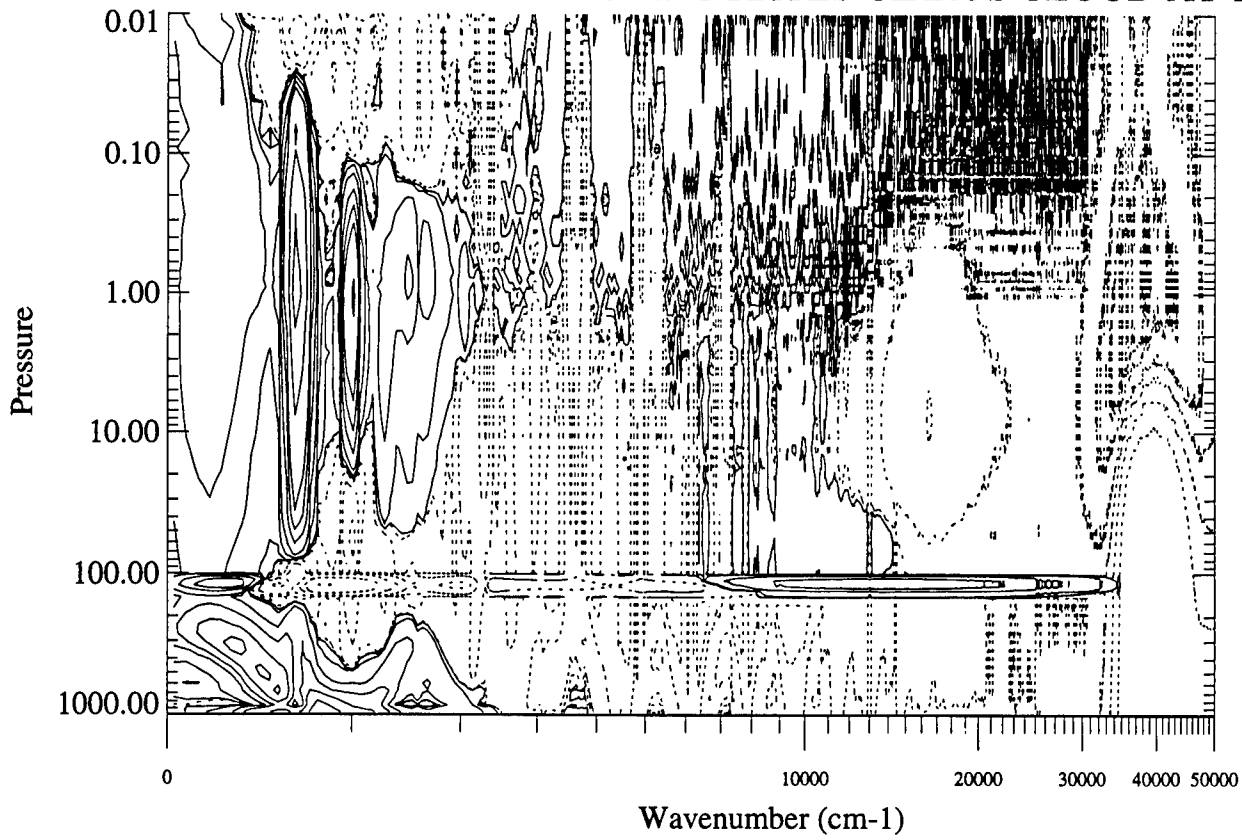


Figure 3: 3a (top) and 3b (bottom)
19-18

TROPICAL HEATING AND COOLING

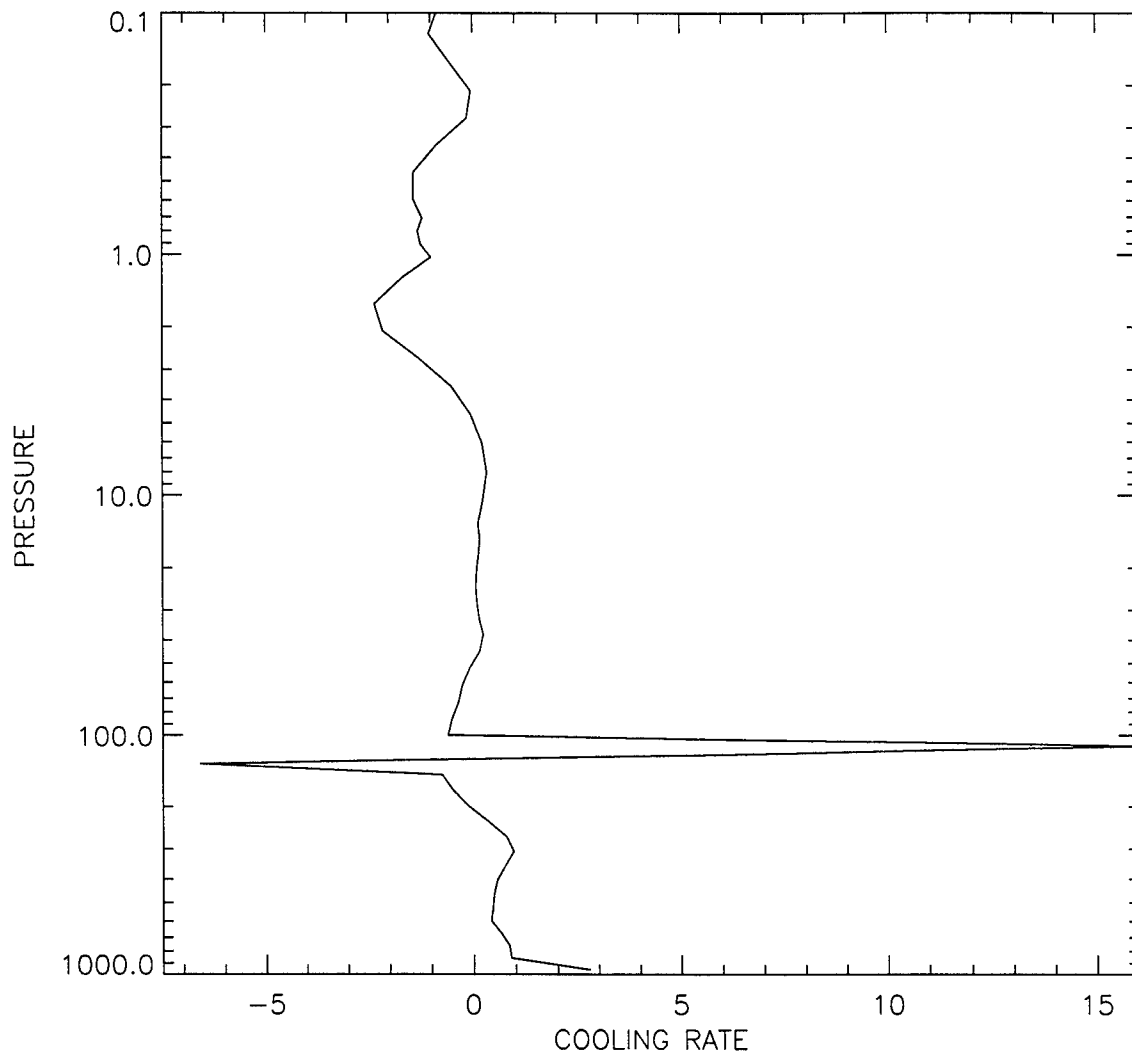


Figure 4